

Collisions in Global Gyrokinetic Simulations of Tokamak Plasmas using the Delta-f Particle-In-Cell Approach: Neoclassical Physics and Turbulent Transport

THÈSE N° 5638 (2013)

PRÉSENTÉE LE 18 JANVIER 2013
À LA FACULTÉ DES SCIENCES DE BASE
CRPP - THÉORIE
PROGRAMME DOCTORAL EN PHYSIQUE

ÉCOLE POLYTECHNIQUE FÉDÉRALE DE LAUSANNE

POUR L'OBTENTION DU GRADE DE DOCTEUR ÈS SCIENCES

PAR

Thibaut VERNAY

acceptée sur proposition du jury:

Prof. O. Schneider, président du jury
Prof. L. Villard, Dr S. Brunner, directeurs de thèse
Dr S. Coda, rapporteur
Prof. P. Helander, rapporteur
Prof. B. McMillan, rapporteur



ÉCOLE POLYTECHNIQUE
FÉDÉRALE DE LAUSANNE

Suisse
2013

À mes parents, Philippe et Marian, pour leur soutien constant.

ABSTRACT

The present work takes place within the general context of research related to the development of nuclear fusion energy. More specifically, this thesis is mainly a numerical and physical contribution to the understanding of turbulence and associated transport phenomena occurring in tokamak plasmas, the most advanced and promising form of magnetically confined plasmas.

The complexity of tokamak plasma phenomena and related physical models, either fluid or kinetic, requires the development of numerical codes to perform simulations of the plasma behaviour under given conditions defined by the magnetic geometry as well as density and temperature profiles. The studies presented in this work are based on electrostatic kinetic simulations, taking advantage of a reduced kinetic model (the gyrokinetic model) which is particularly suitable for studying turbulent transport in magnetically confined plasmas, in effect solving an approximate form of the Vlasov equation for the distribution function of each species (electrons, ions) along with a reduced form of the Poisson equation providing the self-consistent electric fields.

The main tool of this work, the gyrokinetic ORB5 code making use of numerical particles according to the Particle-In-Cell (PIC) method, has been upgraded during this thesis with different linearized collision operators related to both ions and electrons. The BIRDIE code, enabling to study collisional effects on the evolution of Langmuir waves in an unmagnetized plasma, has been written in order to serve as a test-bed for the collision operators ultimately implemented in ORB5. Some essential algorithms related to collisional simulations have been jointly implemented, such as the two-weight scheme which is extensively described in this work. The collision operators in ORB5 have been further carefully tested through neoclassical simulations and benchmarked against other codes, providing reliable levels of collisional transport. Together with different procedures controlling the numerical noise, the collision operators have then been applied to the study of collisional turbulent transport in two different regimes, the Ion-Temperature-Gradient (ITG) regime and the Trapped-Electron-Mode (TEM) regime requiring a trapped electron kinetic response. Although not dominant in core tokamak plasmas, collisional effects nevertheless lead to interesting modifications in the turbulence behaviour which are not captured by the often considered collisionless gyrokinetic models. The so-called coarse-graining procedure, a noise-control algorithm which is suitable for collisional gyrokinetic simulations with particles, is shown to enable carrying out relevant simulations over many collision times. Consequently, reliable conclusions regarding turbulent transport in the presence of collisions could be drawn in this thesis. Namely, the turbulent transport in the ITG regime is found to be enhanced by ion collisions through interactions with so-called zonal flows associated to axisymmetric modes, while it is reduced by electron collisions in the TEM regime through electron detrapping processes. The zonal flow dynamics in collisionless and collisional ITG turbulence simulations is studied, emphasizing the limitation of the zonal flow level due

to Kelvin-Helmoltz-type instabilities. Additionally, some purely collisionless issues related to tokamak physics are discussed, such as the finite plasma size effects in TEM-dominated regime which are found to be important in non-linear simulations but unimportant in linear simulations. The role of zonal flows in temperature-gradient-driven TEM turbulence saturation is confirmed to be weak, in agreement with previous studies. Finally, a realistic global gyrokinetic simulation, accounting for a proper TCV tokamak magnetic equilibrium and related experimental profiles, has been successfully carried out thus demonstrating the relevance of the ORB5 code for predictions related to physics of real tokamaks. A good agreement with GAM experimental measurements is indeed obtained.

KEYWORDS: plasma, tokamak, fusion, gyrokinetics, turbulence, transport, collisions.

RÉSUMÉ

La présente thèse se place dans le contexte de la recherche scientifique liée au développement de l'énergie de fusion nucléaire. Plus précisément, ce travail est une contribution numérique et physique à la compréhension de la turbulence et des phénomènes de transport se produisant dans les plasmas de tokamak, la forme la plus avancée et prometteuse de plasmas confinés magnétiquement.

La complexité des phénomènes relatifs aux plasmas de tokamak, ainsi que des modèles physiques associés, qu'ils soient fluides ou cinétiques, nécessite le développement de codes numériques afin d'effectuer des simulations du comportement du plasma sous certaines conditions de géométrie, densité et température. Les études proposées dans ce travail sont menées par le truchement de simulations gyrocinétiques électrostatiques, tirant avantage d'un modèle cinétique réduit qui se trouve être particulièrement approprié pour les plasmas de tokamak et permet de résoudre l'équation de Vlasov pour la fonction de distribution d'une espèce donnée, avec une forme réduite de l'équation de Poisson qui fournit les champs électriques auto-cohérents.

L'outil principal de ce travail, le code gyrocinétique ORB5, utilise des particules numériques suivant la méthode 'Particule-en-Cellule' (ou PIC, selon l'acronyme de l'appellation anglaise 'Particle-In-Cell'). Pour cette thèse, ORB5 est amélioré grâce à différents opérateurs de collision linéarisés, qui affectent aussi bien les ions que les électrons. Un petit code pour plasmas homogènes et non-magnétisés, BIRDIE, a été écrit afin de servir de laboratoire pour tester les opérateurs de collision, au travers de leurs effets sur les ondes de Langmuir, avant leur mise en œuvre dans ORB5. Quelques algorithmes fondamentaux liés aux simulations collisionnelles sont également nouvellement mis en œuvre, comme par exemple le schéma à deux poids qui est décrit en détail dans ce travail. Les opérateurs de collision sont soigneusement testés au travers de simulations néoclassiques et sont comparés avec ceux d'autres codes, fournissant des niveaux de transport collisionnel considérés comme fiables. Accompagnés par diverses procédures pour contrôler le bruit numérique, les opérateurs de collision sont ensuite utilisés pour étudier le transport turbulent en présence de collisions, et ce dans deux régimes différents : le régime du gradient de température ionique (Ion-Temperature-Gradient ou ITG) et le régime des modes d'électrons piégés (Trapped-Electron-Mode ou TEM), ce dernier nécessitant une réponse cinétique des électrons piégés. Bien que plutôt faibles dans les plasmas chauds de tokamak, les effets collisionnels peuvent néanmoins mener à d'intéressantes modifications dans le comportement de la turbulence qui ne sont pas décrites par les modèles gyrocinétiques sans collisions, souvent considérés. La procédure de l'espace grossièrement grenelé (coarse-graining), un algorithme de contrôle du bruit approprié pour les simulations gyrocinétiques collisionnelles avec particules, démontre sa capacité à fournir des résultats pertinents. En conséquence, des conclusions fiables peuvent être esquissées concernant le transport turbulent en présence de collisions. Concrètement, le transport turbulent dans le régime ITG est augmenté par les collisions des ions, au travers d'interactions avec les écoulements zonaux, alors que le transport

est réduit dans le régime TEM par les collisions des électrons qui génèrent un processus de dépiégeage. Les effets de la taille finie du plasma sur la turbulence d'électrons piégés sont aussi étudiés, apparaissant importants pour les simulations non-linéaires mais faibles pour les simulations linéaires. En accord avec de précédentes études, il est montré que l'effet de cisaillement de l'écoulement zonal sur la saturation de la turbulence est faible dans un régime TEM soutenu par le gradient de température. Finalement, une simulation gyrocinétique globale basée sur un équilibre expérimental du tokamak TCV a été menée avec succès, démontrant la fiabilité du code ORB5. Un bon accord avec des mesures expérimentales sur le tokamak TCV est notamment obtenu.

MOTS-CLEFS : plasma, tokamak, fusion, gyrocinétique, turbulence, transport, collisions.

Contents

1	Introduction	1
1.1	Nuclear fusion as a source of abundant energy	1
1.2	Anomalous transport due to microturbulence as a critical problem for tokamak physics	2
1.3	Codes for simulating microturbulence	3
1.4	Contributions of this thesis	5
1.5	Outline	6
2	Basic tokamak concepts	9
2.1	Introduction	9
2.2	Coordinate systems and safety factor	10
2.3	Magnetic equilibrium	11
2.4	Particle motion in the unperturbed tokamak plasma	12
2.4.1	Larmor motion	12
2.4.2	Constants of motion	13
2.4.3	Trapped and passing particles	14
2.4.4	Diamagnetic drifts	16
2.5	Microinstabilities	17
2.5.1	General considerations on ITG instabilities	18
2.5.2	General considerations on TEM instabilities	22
2.6	Transport in a tokamak	24
2.6.1	Collisional transport: Classical and neoclassical treatment	24
2.6.2	Transport due to microturbulence	26
3	The electrostatic ORB5 collisional model	29
3.1	The ORB5 code	29
3.2	Statistical treatment	30
3.3	The gyrokinetic equation	32
3.4	The δf method	36
3.5	ORB5 models for ions	39
3.6	ORB5 models for electrons	40
3.7	The quasi-neutrality equation	40
3.7.1	Ion contribution	41
3.7.2	Electron contribution and final form	42

3.8	Physical parameters	42
3.9	Temperature and density profile initialization	43
3.10	Transport diagnostics	45
4	ORB5 numerical schemes: the δf Particle-In-Cell (PIC) approach	47
4.1	Introduction	47
4.2	Collisionless marker trajectories	47
4.3	Collisional marker trajectories	48
4.4	The two-weight δf -scheme	48
4.4.1	Collisionless weight equations	50
4.4.2	Collisional weight equations	52
4.4.3	Interpretation of marker weights	53
4.4.4	The background switching scheme	55
4.5	Parallelization	57
4.6	The solver for the quasi-neutrality equation	57
4.7	Initial conditions: Loading the markers and the weights	60
4.8	Controlling the numerical noise: Fourier-filtering, Krook operator and coarse-graining procedure	60
4.8.1	Coarse-graining: 1) binning	61
4.8.2	Coarse-graining: 2) smoothing	62
4.9	Numerical parameters	64
4.9.1	Number of markers	64
4.9.2	Time step	64
4.9.3	Configuration space grid	65
5	Linearized collision operators for a δf Particle-In-Cell code	67
5.1	Introduction	67
5.2	Phenomenology of Coulomb collisions	68
5.3	Suitable expression for collision operators	68
5.4	Collisions on a Maxwellian background and linearization	70
5.5	The self-collision operator	72
5.6	The Lorentz approximation	74
5.7	The electron-ion collision operator	75
5.8	The Langevin approach for solving the Fokker-Planck equation	76
5.9	δf PIC implementation of the Lorentz e-i collision operator	77
5.10	δf PIC implementation of the self-collision operator	78
5.10.1	Handling the test particle operator $C[f_{LM}, \delta f_{LM}]$	78
5.10.2	Handling the background reaction operator $C[\delta f_{LM}, f_{LM}]$	79
5.10.3	Field-aligned binning for the background reaction	81
5.11	Basic tests	84

5.11.1	Lorentz operator for electron-ion collisions	84
5.11.2	Self-collisions: conservation of moments	86
5.11.3	Electrical Spitzer conductivity	88
5.12	Gyrokinetic corrections for collision operators	88
5.12.1	Analytical expressions	90
5.12.2	In a PIC code with magnetic coordinates	91
6	Neoclassical studies using ORB5	93
6.1	Introduction	93
6.2	Neoclassical ordering	94
6.2.1	Zeroth-Order equation	94
6.2.2	First-Order equation	95
6.3	Some features of neoclassical fluxes	96
6.4	Collisionless and collisional contributions to the parallel current	98
6.4.1	Trapped particle contribution	99
6.4.2	Passing particle contribution	101
6.4.3	Numerical results	103
6.5	Benchmarks for neoclassical transport, no electric field	104
6.5.1	Electron transport	104
6.5.2	Ion transport	105
6.6	Global neoclassical ion transport with self-consistent electric field	106
6.6.1	Zonal flow damping: Rosenbluth-Hinton test	107
6.6.2	Ion transport and neoclassical equilibrium with adiabatic electrons	109
6.6.3	Adding collisional kinetic electrons	112
6.6.4	Breakdown of the standard neoclassical approximation	114
6.7	Towards gyrokinetic turbulent simulations	114
6.7.1	The coarse-graining procedure in neoclassical simulations	114
6.7.2	Neoclassical tests of the local/canonical Maxwellian background switching scheme	115
6.8	Conclusions	118
7	Collisional Ion-Temperature-Gradient (ITG) turbulence and zonal flows	121
7.1	Introduction	121
7.2	Linear studies and ion-ion collisions	122
7.3	Non-linear global ITG simulations with no heat sources	123
7.4	Quasi-stationary collisional turbulence simulations started from a neoclassical equilibrium	125
7.4.1	Temperature gradient and collisionality effects on heat diffusivity	128
7.4.2	Zonal flows in collisional ITG turbulence simulations	130

7.4.3	Details of the Dimits shift softening mechanism	136
7.5	Relevance of the pitch angle scattering approximation	138
7.6	Effects of the coarse-graining procedure on ITG turbulence	140
7.7	Effects of trapped electron kinetic response on ITG turbulence	142
7.8	A simple predator-prey model for studying zonal flow-turbulence interactions	143
7.9	ITG simulations considering MHD equilibria	144
7.10	Conclusions	146
8	Global gyrokinetic studies of collisionless and collisional Trapped-Electron-Modes (TEMs)	149
8.1	Introduction	149
8.2	ORB5 simulations of TEM instabilities: model and physical cases	150
8.3	Importance of background reaction term $C_{ee}[\delta f_{LM,e}, f_{LM,e}]$ and associated binning	153
8.4	Linear simulations: Convergence with the number of markers	154
8.5	Different contributions to the TEM instabilities	154
8.6	ORB5-GENE linear TEM benchmark	155
8.7	Comparison of noise-control methods	156
8.8	Linear and non-linear ρ^* effects in TEM regime	157
8.9	Effects of axisymmetric modes on temperature-gradient-driven TEM turbulence	159
8.10	Varying the electron temperature gradient in TEM regime	160
8.11	Linear and non-linear collisional effects in TEM regime	162
8.12	Effects of electron collisions on zonal flows	166
8.13	Realistic simulation of microturbulence related to the TCV shot # 45353	166
8.14	Conclusions	168
9	Conclusions and outlook	171
A	Potential energy flux in turbulence simulations	173
B	A collisional δf PIC code for unmagnetized plasmas	175
B.1	Description	175
B.2	Linear studies	178
B.2.1	Analytical considerations	178
B.2.2	Linear benchmark	180
B.2.3	Convergence studies	181
B.3	Non-linear studies	181
B.3.1	Energy conservation	182
B.3.2	Collisionless entropy conservation	182
B.3.3	Non-linear evolution of the perturbation	183

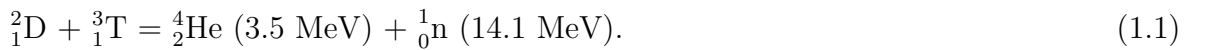
Bibliography	185
Remerciements	193
Publications & Conferences	196
Curriculum Vitae	201

Chapter 1

Introduction

1.1 Nuclear fusion as a source of abundant energy

One of the main challenges related to the future of mankind is the quest for appropriate energy sources, satisfying criteria such as safety, efficiency and sustainability. Among the various energy production modes matching these requirements, the most promising candidate is probably the control of nuclear fusion on Earth. Like in the sun, fusion reactions between light nuclei take place within a hot ionized gas called plasma, when temperatures are high enough in order for the nuclei to overcome the Coulomb repulsion between two positively charged particles, and when densities are high enough in order for a nucleus to collide often enough with other nuclei. Various reactions between different light nuclei may be considered in view of a future reactor. However, according to the combination of the fusion reaction cross-section, the corresponding energy released and the element availability, the most promising reaction turns out to be a fusion between two Hydrogen isotopes, Deuterium and Tritium, formally written as:



Note that Deuterium is easily extracted from water, while Tritium can be generated by bombarding Lithium with neutrons. The walls of future fusion reactors are planned to contain Lithium, in order to generate directly Tritium from neutrons produced by the fusion reactions and hitting the walls. The total mass of the fusion reaction products, a Helium nucleus and a neutron, is slightly lower than the total mass of the reactants. The missing mass is turned into kinetic energy carried by the fusion reaction products, according to the relation $E = mc^2$. Per D-T reaction, a total of 17.6 [MeV] is released in this way. Obtaining a sufficiently hot and dense plasma for a sufficiently long time, where fusion reactions can occur at a significant rate and release energy, is related to the quality of the so-called 'plasma confinement'. The Lawson criterion [1] states that the triple product: electron density $n_e \times$ plasma temperature $T \times$ confinement time τ_E has to reach a given value for the produced energy (through nuclear fusion reactions) to exceed the energy required for operating the tokamak:

$$n_e T \tau_E \geq 10^{21} [\text{keV s/m}^3]. \quad (1.2)$$

In the sun, the confinement is ensured by gravitational forces, an aid which is not (sufficiently) available on Earth. Alternative techniques are thus required for plasma confinement on Earth with the purpose of producing energy. There are mainly two potential approaches for producing energy from nuclear fusion that are currently subjects of intense research activity. The first approach involves inertially confining a high density, low confinement time plasma pellet thanks to laser light [2], which compresses and heats the fuel target through shock waves. The present work deals with the second approach, the magnetic confinement which makes use of strong magnetic fields to confine a low density, high confinement time plasma in a given device. In both approaches, the plasma temperature is expected to be $T \sim 15[\text{keV}]$. While the inertial confinement approach is potentially able to confine a plasma of density $n_e \sim 10^{30}[\text{m}^{-3}]$ for a time $\tau_E \sim 10^{-9}[\text{s}]$, the magnetic confinement approach aims at confining a plasma of density $n_e \sim 10^{21}[\text{m}^{-3}]$ for a time $\tau_E \sim 1[\text{s}]$. Note that both approaches can match the Lawson criterion (1.2).

The first attempts to magnetically confine a plasma were performed within cylinder-shaped linear machines, featuring either a longitudinal magnetic field (so-called θ -pinch machines) or a poloidal magnetic field (so-called z -pinch machines). The main problem related to linear machine configurations is the "loss cone", i.e. the loss of particles at the ends of the machine. This problem is logically solved by closing the magnetic field lines in a toroidal topology, forming magnetic surfaces. The present thesis is actually dedicated to the most advanced device related to plasma magnetic confinement, the tokamak, a toroidal device which will be described in some detail in Chapter 2. The other type of toroidal device which is currently under investigation for fusion through magnetic confinement is the stellarator in which the whole magnetic field is produced by coils with complicated helical geometry. The main advantage of a stellarator configuration is its absence of induced toroidal currents, avoiding the risk of toroidal current disruptions and the periodic stresses of pulsed operation.

1.2 Anomalous transport due to microturbulence as a critical problem for tokamak physics

Important developments have been achieved in the field of tokamak physics over the last decades. A few tokamak devices are currently under operation throughout the world, aiming at studying complex plasma phenomena in toroidal configuration with closed magnetic surfaces, such as macroinstabilities or electromagnetic microturbulence, along with real-time plasma control and several engineering issues. Note that current tokamaks serve as research devices and generally do not produce any energy. The state-of-the-art machines, currently at the front of research, are for instance JT-60U (Japan), DIII-D (USA), NSTX (USA), ALCATOR C-MOD (USA), ASDEX-UPGRADE (Germany), TCV (Switzerland), MAST (England) and the largest one JET (England), which came closest to break-even related to energy production through nuclear fusion in magnetically confined plasmas in 1997, when $\simeq 16[\text{MW}]$ of fusion power have been obtained during a D-T campaign for $\simeq 22[\text{MW}]$ of input heating power. Note that earlier, the TFTR tokamak in Princeton produced $10.7[\text{MW}]$ of fusion power from a D-T plasma in 1994. In order to definitely prove the viability of a commercial reactor relying on nu-

clear fusion, a large project called International Thermonuclear Experimental Reactor (ITER) has been initiated. Thanks to its size much larger than for any existing tokamak and the intensity of its magnetic field, the ITER tokamak is supposed to satisfy the Lawson criterion and open the way towards the first true reactor called DEMO.

According to the Lawson criterion, obtaining a high temperature is crucial in a future tokamak reactor. The plasma is naturally heated by the toroidal current through the Joule effect, as an electrical current going through the wire of a light bulb heats it and the environment. The plasma resistivity η , correlated to the efficiency of the Joule effect, decreases however when the temperature T increases ($\eta \sim T^{-3/2}$), finally leading to the inefficiency of the Joule effect for reaching the required temperatures (typically of $T \simeq 15[\text{keV}] \simeq 150 \cdot 10^6[^\circ\text{C}]$ in ITER). Additional heating systems are thus considered, like a Neutral-Beam-Injector (NBI) system for ion heating and an Electron-Cyclotron-Resonance-Heating (ECRH) system for heating electrons through injection of high frequency electromagnetic waves which enter in resonance with the electron Larmor motion (see Chapter 2). Ideally, the *ignition* regime would be reached, where the plasma heats itself by the Helium nuclei it produces through fusion reactions. But the energy confinement time and thus the temperature in a tokamak are limited by radial heat losses (towards the wall of the tokamak vessel). Regarding the issue of density, critical as well through the Lawson criterion, the main limitation comes from the Greenwald density limit [3], including radial particle losses.

The value of the Lawson triple product is thus fundamentally affected by transport phenomena occurring in a tokamak plasma. Collisions between charged particles provide an intrinsic particle and/or heat transport in a tokamak, called neoclassical transport. Some basic elements of neoclassical transport theory in a tokamak will be explained in Chapter 6. After the first tokamak plasma experiments, it however quickly appeared that the relatively low collisional transport levels were unable to explain the observed degradation of the confinement time. The actual heat and particle losses, unexpectedly high in practice, naturally affect the ability of a plasma to reach the Lawson criterion and thus represent one of the major obstacles in achieving nuclear fusion in magnetically confined plasmas. Those high transport levels which cannot be explained by collisions alone are gathered under the single name of *anomalous transport*. Since the main mechanism responsible for anomalous transport is at this point widely accepted to be related to electromagnetic microturbulence, the name of *turbulent transport* is often used as well.

1.3 Codes for simulating microturbulence

Electromagnetic microturbulence (or its electrostatic limit as addressed in this thesis) defines the non-linear evolution of microinstabilities driven by plasma pressure gradients towards a turbulent regime (see Chapter 2). Plasma microturbulence shares some common features with turbulence in neutral fluids, like energy cascades, but is governed by more complex kinetic models involving furthermore Maxwell's equations. Actually, the system of equations that needs to be solved in order to properly address the issue of plasma microturbulence, called the Vlasov-Poisson system in its electrostatic limit and partly detailed in this thesis (see Chapter

3), is a very demanding set of equations due to its non-linearity combined with its *a priori* 6-dimensionality. The gyrokinetic model [4], allowing to reduce the dimensionality of the problem from 6 to 5, is briefly described in Chapter 3. The gyrokinetic model relies essentially on strong magnetic fields and small fluctuation levels compared to plasma background temperature. Note that this thesis addresses the issue of microturbulence in the core of tokamak plasmas, where the gyrokinetic model assumptions are fully valid. Large pressure gradients in the plasma edge, forming the pedestal region related to H-mode (high confinement mode) plasmas [5], are responsible for other plasma instabilities which are not described here.

Although some elegant analytical work may be performed related to the Vlasov-Poisson system in low-dimensionality plasmas [6], obtaining reliable solutions describing accurately the related microturbulence in tokamak configuration is only possible through numerical simulations [7]. The most accurate simulation codes for studying microturbulence currently rely on the gyrokinetic model presented in Chapter 3, which in the electrostatic limit provides a modified Vlasov-Poisson system combining the gyrokinetic equation with the quasi-neutrality equation. Note that a code can consider a global geometry, i.e. accounting for the full torus configuration, or can be limited to a local (flux-tube) geometry, accounting for a limited plasma volume in the vicinity of a given magnetic field line. A local code is naturally less demanding in terms of computer resources than a global code. However, a local code does not account for temperature and density profile variations and is thus in particular inappropriate for simulating small tokamak plasmas where characteristic gradient length scales and turbulence correlation length scales are not clearly separated. For large tokamak plasmas of future reactors, the accuracy of a local model may nevertheless be satisfying. Another crucial feature of a gyrokinetic code is its treatment of electrons, which can range from the adiabatic assumption (the computationally cheapest model) to a fully kinetic electron response (the computationally most expensive model). In addition to the latter models, a gyrokinetic code can consider a hybrid model for electrons, partly adiabatic, partly kinetic, as described in this thesis.

Several numerical approaches are used for solving the gyrokinetic model equations. Currently, the most popular way of numerically handling the gyrokinetic model is the Eulerian approach, where the equations are discretized on a fixed grid in the 5D gyrokinetic phase space and solved through finite difference schemes. The most prominent Eulerian-based gyrokinetic codes are GS2 [8], GENE [9] [10], GYRO [11], GKW [12] and GT5D [13]. This thesis is mainly dedicated to the global gyrokinetic code ORB5 [14] [15] [16], described in detail in Chapters 3 and 4. ORB5, like the tokamak code GTC [17] and the stellarator code EUTERPE [18], is based on the alternative common approach for gyrokinetic codes, the Particle-In-Cell (PIC) approach, thoroughly described throughout this work and which requires the introduction of numerical particles. The PIC approach, based on a Lagrangian representation, is more intuitive and in certain cases less costly (in terms of computer resources) than a Eulerian-based approach thanks to its grid limited to the 3D configuration space, but suffers from the numerical noise due to the finite number of numerical particles used for representing the statistical distribution functions of particles. The issue of numerical noise is addressed in this thesis. Note that a third approach, the semi-Lagrangian method, is used by the GYSELA code [19] and consists of integrating the gyrokinetic equation over each time step along trajectories starting from the

mesh points of a fixed phase space grid. The semi-Lagrangian method is however costly from a numerical point of view and has not allowed so far to obtain simulation results accounting for kinetic electron response.

1.4 Contributions of this thesis

The starting point of this thesis is the code ORB5, described in Chapters 3 and 4. The original ORB5 model [15] was fully collisionless and electrostatic, featuring a single weight scheme. As a preparatory work, linearized Landau collision operators [20], both for pitch angle scattering of electrons off the ions and self-collisions, were first implemented and tested in the two-weight PIC code BIRDIE, written especially for this purpose and described in Appendix B. More precisely, the collision operators were validated and benchmarked considering the particular case of electron collision effects on Langmuir waves (also referred to as electron plasma waves). A similar two-weight scheme [21] was implemented in ORB5, as a necessary requirement before the introduction of collisional effects. The linearized collision operators, namely the pitch angle scattering operator for electrons and the self-collision operator both for ions and electrons, were then included in ORB5 (see Chapter 5). A long testing phase followed, during which both basic properties of the collision operators, such as conservation properties, as well as several neoclassical aspects were addressed. Many careful neoclassical benchmarks were performed, which have shown the reliability of the collision operator implementation [16]. Insights into neoclassical physics were obtained, like the breakdown of the neoclassical approximation close to the magnetic axis or the effects of poloidally asymmetric modes on neoclassical transport. A new scheme, called the background switching scheme, was written in order to run collisional simulations accounting for a canonical Maxwellian as background distribution function. The latter scheme was used in order to prepare relevant neoclassical equilibria from which the ITG turbulence simulations with collisions were systematically started, a novelty in the frame of gyrokinetic simulations.

A new scheme for controlling the numerical noise, the coarse-graining procedure [22], was implemented in the code by B. McMillan. This contribution was especially important since the coarse-graining procedure turns out to be the only practical noise-control scheme compatible with collisions, opening the way towards collisional simulations over turbulence time scales. Following previous studies [23] [24], ion-ion collision effects on ITG-dominated turbulence were extensively studied through their interactions with zonal flows associated to axisymmetric modes and acting as an important mechanism in ITG turbulence self-organization [17] [25]. A general increase in ITG turbulence levels due to ion collisions was emphasized, along with the collisional softening of the Dimits shift region. The topic of zonal flow stability and saturation in collisionless and collisional ITG simulations completed the study of the ITG-dominated turbulent regime in tokamak plasmas carried out in this thesis [26].

A kinetic electron response was then considered in order to study the TEM-dominated (driven by electron temperature gradient) turbulent regime. A successful linear and collisionless benchmark against the global GENE code [10] in the TEM regime was performed, accounting for a fully kinetic electron response. The effects of finite plasma size in the TEM regime were

investigated, appearing to be weak in linear simulations but strong in non-linear simulations. The zonal flows were shown to play no role in temperature-gradient-driven TEM turbulence saturation, contrary to ITG turbulence, confirming previous studies related to this controversial subject [27] [28] [29]. Regarding collisional simulations, the reduction of the TEM instability mechanism by electron collisions through detrapping processes was emphasized [30].

Meanwhile, a new electromagnetic, multi-ion species version of the ORB5 code called NEMORB was written by A. Bottino [31]. The collision operators were successfully merged into this new version of the code. Collisional simulations of electromagnetic microturbulence are however not possible yet, due to the (temporary) incompatibility between the two-weight scheme and the electromagnetic solver.

Finally, a new interface between ORB5 and the equilibrium code CHEASE [32] was written during this thesis. This has allowed us to perform the first global gyrokinetic ORB5 turbulence simulation of a TCV shot characterized by a TEM-dominated regime (see Sec. 8.13).

1.5 Outline

The present thesis is organized as follows: Chapter 2 presents the general frame of tokamak physics and related microinstabilities. The transport phenomena in a tokamak, already mentioned in the current introduction, are also briefly summarized. Chapter 3 starts with a general history of the ORB5 code and provides details about the gyrokinetic formalism, the physical model on which the code ORB5 relies, along with the appropriate forms of related equations. Chapter 4 explains the numerical algorithms which translate the equations of the gyrokinetic formalism into code routines. Different numerical methods for controlling the numerical noise, inherent to the PIC approach, are presented as well. Chapter 5 is dedicated to the collision operators, addressing both their analytical and discretized forms and showing some basic tests of the collision operator properties. A brief discussion related to Finite-Larmor-Radius effects in collision operators is provided as well. Chapter 6 briefly presents the general framework of the neoclassical transport theory. A model for calculating the collisionless current in a tokamak associated to Finite-Orbit-Width effects in the presence of a pressure gradient is described and compared to ORB5 simulations. Neoclassical benchmarks are carried out, both for electron and ion transport, either neglecting or accounting for an axisymmetric electric field. Some limitations of the neoclassical assumptions are exhibited, and the noise-control schemes are already tested within the frame of neoclassical simulations in order to prepare for the turbulence studies. Chapter 7 deals with ITG-dominated turbulence simulations and especially focuses on ion-ion collision effects on ITG turbulence through interactions with zonal flows. Zonal flow stability is addressed both in collisionless and collisional simulations. The validity of the Lorentz approximation (pitch angle scattering) for self-collisions is studied in ITG turbulence simulations. The noise-control efficiency in ITG turbulence simulations through the coarse-graining procedure is carefully checked. The effects of kinetic electron response on ITG turbulence are briefly discussed as well. A simple predator-prey model is shown to be able to recover some basic features of collisionless and collisional ITG turbulence in the presence of zonal flows. Finally, a few simulations are performed accounting for realistic MHD equilibria.

Chapter 8 addresses the TEM-dominated turbulence driven by electron temperature gradient by considering the kinetic response of trapped electrons. In order to validate the code for TEM studies, a linear benchmark accounting for a fully kinetic electron response is presented. Linear scans are performed, both with and without collisions. The effects of finite plasma size on TEM turbulence are addressed, along with the effects of zonal flow shearing on turbulence saturation. Comparisons with ITG turbulence are sketched. Electron collision effects both on linear growth rates and turbulence levels related to TEM instabilities are investigated. Finally, a simulation including a kinetic response of trapped electrons and accounting for a realistic magnetic equilibrium corresponding to the TCV tokamak is discussed. The general conclusions of the thesis are summarized in Chapter 9. Additionally, the role of potential energy fluxes in turbulence simulations is mentioned in Appendix A. Finally, the BIRDIE code for unmagnetized homogeneous plasmas, serving as a test-bed for the collision operators, is presented in Appendix B.

Chapter 2

Basic tokamak concepts

2.1 Introduction

The tokamak (see Figure 2.1) is a toroidal device whose purpose is to confine a plasma, a quasi-neutral gas of individually charged particles, through magnetic field lines lying on nested toroidal magnetic surfaces. The equilibrium magnetic field \mathbf{B} of a tokamak is decomposed in a toroidal component \mathbf{B}_φ produced by external coils, where φ stands for the toroidal angle, and a poloidal component \mathbf{B}_{pol} mainly produced by the toroidal plasma current \mathbf{j}_φ . The plasma current is generated by induction (Ohmic regime) and/or by injection of radio-frequency waves or a beam of neutral particles. Note that the poloidal magnetic field \mathbf{B}_{pol} is also partly produced by poloidal field coils (see Figure 2.1) which serve to stabilize and shape the plasma cross-section. The magnetic axis, near the center of the tokamak vessel, is such that its magnetic field is purely toroidal: $\mathbf{B} = \mathbf{B}_0 = \mathbf{B}_\varphi$. Note that the quasi-neutrality of a plasma is broken at small scale, within a sphere of radius $\lambda_D = \sqrt{\epsilon_0 T / ne^2}$, where n and T are the density and the temperature of the plasma respectively. λ_D is called the Debye length and is typically of the order $\sim 2 \cdot 10^{-5}[\text{m}]$ for a tokamak plasma.

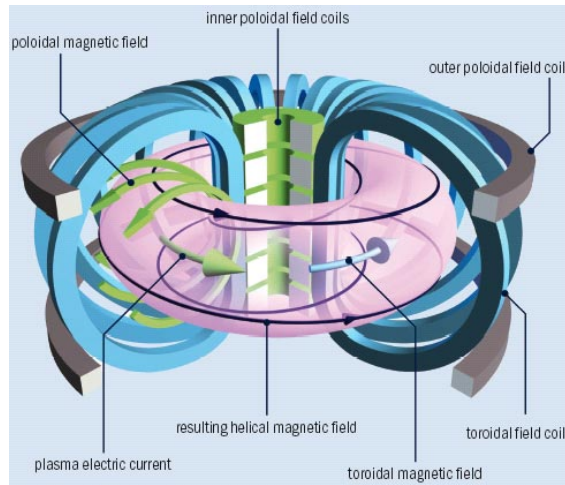


Figure 2.1: The tokamak device. Figure courtesy of [33].

2.2 Coordinate systems and safety factor

In order to describe a tokamak, a cylindrical coordinate system (R, φ, Z) is first introduced with respect to the symmetry axis of the device. A toroidal coordinate system (r, φ, θ) is defined and is related to the cylindrical system by the following relations:

$$R = R_0 + r \cos \theta, \quad (2.1)$$

$$Z = r \sin \theta, \quad (2.2)$$

where R_0 stands for the position R of the magnetic axis and is called the major radius. $r \in [0, a]$, where a is called the minor radius. The local inverse aspect ratio of a tokamak is defined by $\epsilon = r/R_0$, while the global inverse aspect ratio is given by $\epsilon_{\text{glob}} = a/R_0$. Typically $\epsilon_{\text{glob}} \sim 1/3$ and for analytical derivations one often makes the assumption $\epsilon \ll 1$.

One introduces the poloidal magnetic flux $\Psi = \int_S \mathbf{B} \cdot d\boldsymbol{\sigma}/2\pi$, where the edge of the surface S lies on a circular path defined by $R, Z = \text{const}$. Note that, due to the incompressibility of the magnetic field ($\nabla \cdot \mathbf{B} = 0$), $\mathbf{B} \cdot \nabla \Psi = 0$, so that \mathbf{B} is tangent to $\Psi = \text{const}$, which thus defines a magnetic surface. The safety factor $q_s(\Psi)$ of a tokamak magnetic equilibrium (as defined in Sec. 2.3), constant on each magnetic surface, is related to the twist of the field line (number of toroidal turns for one poloidal turn of the magnetic field) and is expressed as follows:

$$q_s(\Psi) = \frac{1}{2\pi} \oint \left. \frac{d\varphi}{d\theta} \right|_{\text{along B}} d\theta = \frac{1}{2\pi} \int_0^{2\pi} \frac{\mathbf{B} \cdot \nabla \varphi}{\mathbf{B} \cdot \nabla \theta} d\theta. \quad (2.3)$$

The magnetic shear \hat{s} is furthermore introduced and defined by:

$$\hat{s}(\Psi) = \frac{\rho(\Psi)}{q_s} \frac{dq_s}{d\rho(\Psi)}, \quad (2.4)$$

where $\rho(\Psi)$ is a label for a given magnetic surface, for instance $\rho(\Psi) = r$ for a circular plasma cross-section. A modified poloidal angle, the called straight-field-line poloidal angle θ^* , is defined such that the magnetic pitch $d\varphi/d\theta^*|_{\text{along B}} = q_s(\Psi)$ is constant on a given magnetic surface Ψ , leading to:

$$\theta^*(\theta) = \frac{1}{q_s(\Psi)} \int_0^\theta \frac{\mathbf{B} \cdot \nabla \varphi}{\mathbf{B} \cdot \nabla \theta'} d\theta'. \quad (2.5)$$

The straight-field-line magnetic coordinate system $(\Psi, \theta^*, \varphi)$ is finally introduced. The Jacobian $J_{\Psi\theta^*\varphi}$ of the magnetic coordinate system takes the following form:

$$J_{\Psi\theta^*\varphi} = \frac{1}{|(\nabla \Psi \times \nabla \theta^*) \cdot \nabla \varphi|} = \frac{Rq_s}{B_\varphi}. \quad (2.6)$$

The area of the flux surface $S(\Psi)$ is computed by:

$$S(\Psi) = \int_0^{2\pi} \int_0^{2\pi} |\nabla \Psi| J_{\Psi\theta^*\varphi} d\theta d\varphi. \quad (2.7)$$

Note that the alternative magnetic coordinate system (s, θ^*, φ) , where $s = \sqrt{\Psi/\Psi_{\text{edge}}}$, may be used as well. The different coordinate systems are presented in Figure 2.2 (a).

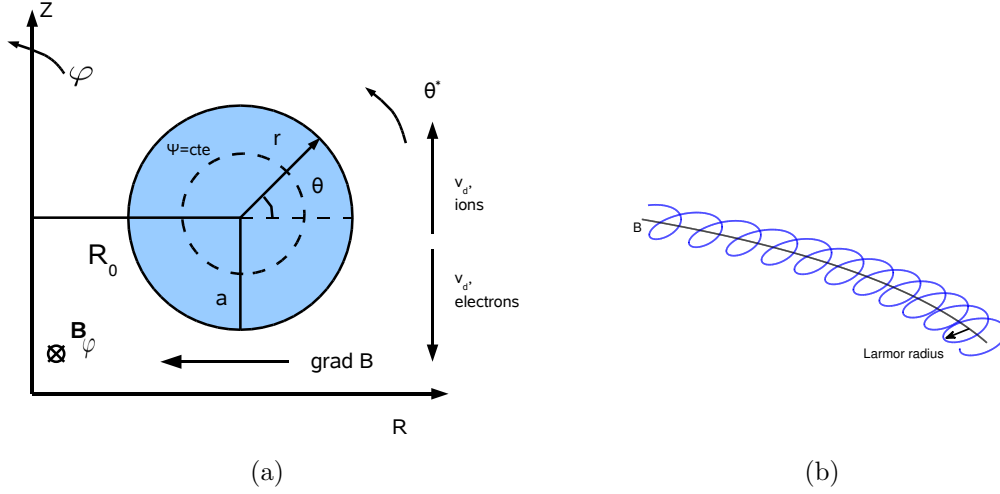


Figure 2.2: (a) ORB5 coordinate systems and circular tokamak configuration, with ion and electron magnetic drift velocities arising from the magnetic field curvature. (b) Typical motion of a charged particle along and around a magnetic field line.

2.3 Magnetic equilibrium

The tokamak is designed in order to be axisymmetric, such that $\partial/\partial\varphi = 0$ for any equilibrium scalar quantity. The most general axisymmetric field \mathbf{B} satisfying $\nabla \cdot \mathbf{B} = 0$ has the following form:

$$\mathbf{B} = \mathbf{B}_\varphi + \mathbf{B}_{\text{pol}} = F(\Psi)\nabla\varphi + \nabla\Psi \times \nabla\varphi, \quad (2.8)$$

where $F(\Psi) = RB_\varphi$ is the poloidal current flux function. The magnetic axis is defined as the region of the tokamak where the magnetic surface reduces to a toroidal magnetic field line (with $\mathbf{B}_{\text{pol}} = \mathbf{0}$). Let $p(\Psi)$ stand for the plasma pressure profile. Combining the force balance relation between the magnetic force and the plasma pressure $\nabla p = \mathbf{j} \times \mathbf{B}$ with Ampère's law $\nabla \times \mathbf{B} = \mu_0 \mathbf{j}$ leads to the Grad-Shafranov equation:

$$R \frac{\partial}{\partial R} \left(\frac{1}{R} \frac{\partial \Psi}{\partial R} \right) + \frac{\partial^2 \Psi}{\partial Z^2} = -F(\Psi) \frac{dF}{d\Psi} - R^2 \mu_0 \frac{dp}{d\Psi}. \quad (2.9)$$

For given $F(\psi)$ and $p(\Psi)$ profiles, the Grad-Shafranov equation (2.9) provides $\Psi(R, Z)$ and thus the full magnetic equilibrium through Eq. (2.8). The safety factor profile $q_s(\Psi)$ is obtained from Eq. (2.3). The important parameter $\beta = 2\mu_0 p/B^2$ is introduced, measuring the ratio between the kinetic pressure p and the magnetic pressure $B^2/2\mu_0$. Standard tokamaks typically feature a ratio $\beta \ll 1$. Note that the main tool of this work, the code ORB5 described in Chapters 3 and 4, provides an interface with the equilibrium code CHEASE [32] which is able to solve the Grad-Shafranov equation in order to obtain an ideal MagnetoHydroDynamics (MHD) axisymmetric

equilibrium.

Instead of solving the Grad-Shafranov equation (2.9) in order to obtain an ideal MHD equilibrium, an analytical equilibrium may be used, which is an approximation of a true solution to the Grad-Shafranov equation (2.9). The considered *ad hoc* equilibrium consists of toroidal, axisymmetric, nested magnetic surfaces with circular, concentric, poloidal cross-sections. In this case, we assume $\Psi = \Psi(r)$ with $d\Psi/dr = rB_0/\bar{q}(r)$, as well as $F = RB_\varphi = R_0B_0$, so that the axisymmetric magnetic field is given by:

$$\mathbf{B} = \frac{B_0R_0}{R} \left(\hat{e}_\varphi + \frac{r}{R_0\bar{q}(r)} \hat{e}_\theta \right), \quad (2.10)$$

where \hat{e}_φ and \hat{e}_θ are the unit vectors in the toroidal and poloidal directions, respectively. At zeroth-order in ϵ , $B \sim 1/R$. The region close to the tokamak axis of symmetry is thus called the high-field-side of the torus, the opposite region being called the low-field-side. The \bar{q} profile, called here the pseudo-safety factor profile, is chosen quadratic or quartic:

$$\bar{q}(r) = \bar{q}_0 + (\bar{q}_{\text{edge}} - \bar{q}_0) \frac{r^2}{a^2}, \quad (2.11)$$

$$\bar{q}(r) = \bar{q}_0 + \bar{q}_1 \frac{r}{a} + \bar{q}_2 \frac{r^2}{a^2} + \bar{q}_3 \frac{r^3}{a^3} + \bar{q}_4 \frac{r^4}{a^4}, \quad (2.12)$$

and through Eq. (2.3) is related to the safety factor profile $q_s(r)$ by the following relation:

$$\bar{q}(r) = \sqrt{1 - \epsilon^2} q_s(r). \quad (2.13)$$

Considering a large aspect ratio tokamak ($\epsilon \ll 1$), we clearly have $\bar{q} \simeq q_s$. The standard safety factor profile used along with the *ad hoc* equilibrium and corresponding to the so-called CYCLONE case (see Sec. 3.8) is the quadratic profile given by Eq. (2.11) with $\bar{q}_0 = 0.854$ and $\bar{q}_{\text{edge}} = 3.038$.

2.4 Particle motion in the unperturbed tokamak plasma

2.4.1 Larmor motion

Let us consider a particle in the tokamak plasma, of mass m and charge q . The velocity \mathbf{v} of the particle is split into a contribution parallel to the magnetic field $v_\parallel = \mathbf{v} \cdot \hat{\mathbf{b}}$, where $\hat{\mathbf{b}} = \mathbf{B}/B$ is introduced, and a contribution perpendicular to the magnetic field $\mathbf{v}_\perp = \mathbf{v} - \mathbf{v}_\parallel$. We consider here an unperturbed tokamak plasma, i.e. considering no perturbed fields and only the tokamak stationary magnetic field of equilibrium \mathbf{B} . The basic equation of motion for a particle is given by Newton's *lex secunda*:

$$\frac{d\mathbf{v}}{dt} = \frac{q}{m} \mathbf{v}_\perp \times \mathbf{B} = \mathbf{v}_\perp \times \boldsymbol{\Omega}, \quad (2.14)$$

the cyclotron frequency $\boldsymbol{\Omega} = q\mathbf{B}/m$ being defined. Eq. (2.14) leads to the so-called Larmor motion or gyromotion, i.e. a circular motion in the perpendicular plane around the field line.

The radius of the Larmor motion relative to the field line is $\rho_L = v_\perp/\Omega$. The vectorial form of the Larmor radius reads $\boldsymbol{\rho}_L = \mathbf{B} \times \mathbf{v}/B\Omega$. The phase of the Larmor motion is described by the so-called gyroangle α . The gyroaverage operation $\langle \cdot \rangle$, crucial in the frame of the gyrokinetic theory introduced in Chapter 3, is defined by:

$$\langle \cdots \rangle = \frac{1}{2\pi} \int_0^{2\pi} \cdots d\alpha. \quad (2.15)$$

The perpendicular Larmor motion added to the parallel motion along the field line forms essentially the trajectory of a charged particle in the presence of a magnetic field, as presented in Figure 2.2 (b). In the presence of magnetic field curvature, as is the case in a tokamak, a charged particle drifts perpendicularly to the magnetic field line in addition to the parallel motion and the Larmor motion, as explained in Sec. 2.4.2.

2.4.2 Constants of motion

The magnetic moment of a charged particle in a magnetic field \mathbf{B} is defined by $\mu = IdS = q\pi\rho_L^2\Omega/2\pi = mv_\perp^2/2B$, where I is the current carried by the particle and dS the circular surface defined by the Larmor motion. The kinetic energy of a particle, written $\mathcal{E} = mv_\parallel^2/2 + mv_\perp^2/2 = mv_\parallel^2/2 + \mu B$, is naturally a constant of motion in the unperturbed system since:

$$\frac{d\mathcal{E}}{dt} = m\mathbf{v} \cdot \frac{d\mathbf{v}}{dt} = q\mathbf{v} \cdot (\mathbf{v} \times \mathbf{B}) = 0. \quad (2.16)$$

In case of spatially slowly varying magnetic field \mathbf{B} over the Larmor scale ($|\boldsymbol{\rho}_L \cdot \nabla B|/B \ll 1$), the magnetic moment $\mu = mv_\perp^2/2B$ is an adiabatic constant of motion of the unperturbed system, associated to the periodic Larmor motion. A third constant of motion related to the axisymmetric configuration may be derived. Making use of the cylindrical coordinates (R, φ, Z) , the unperturbed Lagrangian of a single plasma particle reads:

$$\mathcal{L} = \frac{m}{2} \left(\dot{R}^2 + R^2 \dot{\varphi}^2 + \dot{Z}^2 \right) + q \left(A_R \dot{R} + A_\varphi R \dot{\varphi} + A_Z \dot{Z} \right), \quad (2.17)$$

where $\mathbf{A} = A_R \hat{e}_R + A_\varphi \hat{e}_\varphi + A_Z \hat{e}_Z$ is the magnetic potential such that $\mathbf{B} = \nabla \times \mathbf{A}$. Since $\partial\mathcal{L}/\partial\varphi = 0$ due to the axisymmetry, φ is a cyclic variable and the associated conjugate momentum, called the toroidal canonical momentum Ψ_0 , is a constant of motion:

$$\Psi_0 = \frac{1}{q} \frac{\partial\mathcal{L}}{\partial\dot{\varphi}} = \underbrace{RA_\varphi}_{\Psi} + \frac{m}{q} R^2 \dot{\varphi} = \Psi + \frac{m}{qB_\varphi} (RB_\varphi) v_\varphi = \Psi + \frac{F(\Psi)v_\parallel}{\Omega}. \quad (2.18)$$

The term $\Delta\Psi = F(\Psi)v_\parallel/\Omega$ represents actually the excursion in Ψ of the particle from a given magnetic surface Ψ , due to drift velocities associated to the magnetic field curvature and gradient. The drift velocities are treated systematically in the frame of the gyrokinetic approach in Chapter 3, but the main idea underlying their derivation is presented here. Generally, a charged particle in a magnetic field \mathbf{B} submitted to an external force \mathbf{F} undergoes a drift velocity $\mathbf{v}_d = \mathbf{F} \times \mathbf{B}/qB^2$. In a tokamak, the curvature and the gradient of the magnetic field

both generate an external force, $\mathbf{F}_c = -m_{||}v_{||}^2\hat{\mathbf{b}} \cdot \nabla\hat{\mathbf{b}}$ and $\mathbf{F}_{\nabla B} = -\mu\nabla B$ respectively, giving rise to perpendicular drifts. Here $\hat{\mathbf{b}} = \mathbf{B}/B$. The drift velocities appear through the gyroaverage of the non-Larmor velocity $\mathbf{v} - d\boldsymbol{\rho}_L/dt$, giving the so-called guiding-center velocity \mathbf{v}_{GC} . For an inhomogeneous magnetic field, it reads:

$$\mathbf{v}_{GC} = \left\langle \mathbf{v} - \frac{d\boldsymbol{\rho}_L}{dt} \right\rangle = \mathbf{v}_{||} + \mathbf{v}_{\nabla B} + \mathbf{v}_c. \quad (2.19)$$

where $\mathbf{v}_{\nabla B} = (mv_{\perp}^2/2qB^3)(\mathbf{B} \times \nabla B)$ is the ∇B drift velocity related to the magnetic inhomogeneity and $\mathbf{v}_c = (mv_{||}^2/qB^2)\mathbf{B} \times [\hat{\mathbf{b}} \cdot (\nabla\hat{\mathbf{b}})]$ is the curvature drift velocity related to the centrifugal force which a particle undergoes in a tokamak. In the case of a low β plasma, $\beta \ll 1$, these two drifts can be combined: $\mathbf{v}_{\nabla B} + \mathbf{v}_c \simeq m/qB^3(v_{\perp}^2/2 + v_{||}^2)\mathbf{B} \times \nabla B$. The difference between the parallel motion and the guiding-center motion leads to an excursion from the magnetic surface on which the particle is in principle located. Due to the charge dependence of the magnetic drifts, the ions and electrons drift in opposite directions in a tokamak, mainly upwards or downwards (see Figure 2.2). The charge dependence in the magnetic drift velocities thus prevents any confinement with a purely toroidal magnetic field to be possible. The poloidal field \mathbf{B}_{pol} in a tokamak, although much smaller than the toroidal field \mathbf{B}_{φ} , is crucial in this respect, in order to prevent the mentioned charge separation from occurring. The excursions from magnetic surfaces associated to magnetic drift velocities are much smaller for electrons than for ions, due to the difference between electron and ion Larmor motions. Note that considering an electric field \mathbf{E} in the tokamak yields another drift velocity $\mathbf{v}_{E \times B} = \mathbf{E} \times \mathbf{B}/B^2$ related to the electric force, central in the frame of microturbulence studies since the drift velocity $\mathbf{v}_{E \times B}$ is believed to drive the anomalous transport of heat and particles. There can also be an axisymmetric \mathbf{E} field related to the neoclassical equilibrium. The total drift velocity is written $\mathbf{v}_d = \mathbf{v}_{\nabla B} + \mathbf{v}_c + \mathbf{v}_{E \times B}$. In a typical tokamak configuration $\nabla B/B \sim 1/R_0$, giving an ordering for the drift velocity of the unperturbed system: $v_d/v_{th} \sim \rho_L/R_0 \ll 1$. Here the thermal velocity $v_{th} = \sqrt{T/m}$ is introduced.

The three constants of motion derived above, associated with the axisymmetry of a tokamak, lead to particle trajectories which are closed in the poloidal plane. Note that collisions break the magnetic moment conservation and thus lead to trajectories in the poloidal plane which are not necessarily closed.

2.4.3 Trapped and passing particles

The parallel velocity of any particle is obtained from kinetic energy \mathcal{E} and magnetic moment μ :

$$v_{||} = \sqrt{\frac{2}{m}(\mathcal{E} - \mu B)}. \quad (2.20)$$

A particle is called trapped at the position (s, θ) if its magnetic moment μ is large enough in order to cancel its parallel velocity before reaching the maximum magnetic field $B_{\max}(s)$ on the magnetic surface $s = \text{const.}$ on which the trajectory lies (neglecting here at first radial

excursions from magnetic surfaces), i.e. if $\mu B_{max} \geq \mathcal{E}$, leading to:

$$\frac{v_{||}}{v_{\perp}} < \sqrt{\frac{B_{max}}{B(s, \theta)} - 1} \simeq \sqrt{\epsilon(1 + \cos \theta)}. \quad (2.21)$$

The parallel velocity of a trapped particle thus remains low, typically of the order $|v_{||}| \sim \sqrt{\epsilon} v_{th}$, and periodically changes its sign when the particle reaches the high-field-side region, leading to the so-called banana orbit in the poloidal plane (s, θ) . A particle which is able to overcome the magnetic barrier on the high-field-side is called passing and is clearly such that its parallel velocity never vanishes.

The excursion from the magnetic surface due to drift velocities described in Sec. 2.4.2 is on average larger for trapped than for passing particles. For a trapped particle, the excursion is given by the so-called banana width $\Delta r_b = |\Psi_0 - \Psi|/|\nabla \Psi|$. Estimating $\nabla \Psi \simeq RB_{pol}$ and using Eq. (2.18), the banana width for a trapped particle is given by:

$$\Delta r_b \simeq \frac{RB_{\varphi}}{RB_{pol}} \frac{|\Delta v_{||}|}{\Omega} \sim \frac{q_s}{\epsilon} \frac{|v_{||}|}{\Omega} \sim \frac{q_s}{\sqrt{\epsilon}} \rho_L, \quad (2.22)$$

having furthermore invoked $q_s \simeq rB_{\varphi}/RB_{pol}$. The bounce frequency ω_b , i.e. the frequency of the banana motion, is estimated by:

$$\omega_b \simeq \frac{v_d}{\Delta r_b} \simeq \sqrt{\epsilon} \frac{v_{th}}{q_s R_0} \simeq \sqrt{\epsilon} \omega_t, \quad (2.23)$$

where $\omega_t = v_{th}/q_s R_0$ is the transit frequency, the poloidal motion frequency of a passing particle. The excursion of a passing particle from its magnetic surface Δr_t is smaller by a factor $\sqrt{\epsilon}$ than the excursion of a trapped particle Δr_b :

$$\Delta r_t \simeq \frac{v_d}{\omega_t} \simeq q_s \rho_L \ll \Delta r_b. \quad (2.24)$$

Typical motions in the poloidal plane for trapped and passing particle guiding centers are shown in Figure 2.3.

The fraction of trapped electrons depends on the considered magnetic surface. The local fraction is obtained by the following expression, in the limit $\epsilon \ll 1$:

$$\alpha_b(\Psi, \theta) = \frac{\int_{\text{trapped}} d^3v}{\int d^3v} = \sqrt{1 - \frac{B(\Psi, \theta)}{B_{\max}(\Psi)}} \simeq \sqrt{1 - \frac{1 - \epsilon \cos \theta}{1 + \epsilon}} \simeq \sqrt{\epsilon(1 + \cos \theta)}. \quad (2.25)$$

In the large aspect ratio limit $\epsilon \ll 1$, a rough estimate of the flux-surface-averaged fraction of trapped electron $\langle \alpha_b \rangle_S(\Psi)$ is thus provided by:

$$\langle \alpha_b \rangle_S(\Psi) \simeq \frac{\sqrt{\epsilon}}{2\pi} \int_0^{2\pi} \sqrt{1 + \cos \theta} d\theta = \frac{2\sqrt{2}}{\pi} \sqrt{\epsilon} \simeq 0.9 \sqrt{\epsilon}, \quad (2.26)$$

which clearly indicates that there are more trapped particles on the outer magnetic surfaces than close to the magnetic axis where $\epsilon \rightarrow 0$.

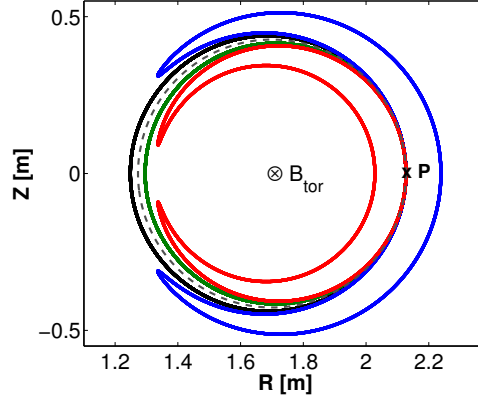


Figure 2.3: Different trajectories in the tokamak poloidal plane for an ion guiding center starting from the point P : passing particle with $v_{\parallel} > 0$ and $v_{\parallel} < 0$ (black and green curve, respectively), trapped particle with $v_{\parallel} > 0$ and $v_{\parallel} < 0$ (blue and red curve, respectively). The magnetic surface on which lies the point P is shown by the dashed grey line.

2.4.4 Diamagnetic drifts

Besides the individual guiding-center drifts due to magnetic inhomogeneities and possible electric fields mentioned in Sec. 2.4.2, a collective diamagnetic drift velocity may be generated by plasma pressure gradients [34]. Considering the orthonormal right-handed system $(\hat{e}_x, \hat{e}_y, \hat{e}_z = \hat{b})$ with a uniform magnetic field $\mathbf{B} = B\hat{e}_z$, a stationary distribution function f_0 to the Vlasov equation for a given species (mass m , charge q) may be built as a function of constants of motion. Let us consider for instance a near-Maxwellian distribution, function of the kinetic energy \mathcal{E} and the guiding-center position $X = x + v_y/\Omega$, both being constants of motion:

$$f_0(\mathbf{r}, \mathbf{v}) = \frac{n(X)}{(2\pi T(X)/m)^{3/2}} \exp -\frac{\mathcal{E}}{T(X)}. \quad (2.27)$$

Expanding to first order in the Larmor parameter $\delta = \rho_L/L_c$, where $1/L_c \sim d \ln n/dx, d \ln T/dx$, gives:

$$f_0 = \left[1 + \frac{v_y}{\Omega} \left(\frac{d \ln n}{dx} + \frac{dT}{dx} \frac{\partial}{\partial T} \right) \right] f_{LM}(x, \mathcal{E}) + \mathcal{O}(\delta^2), \quad (2.28)$$

where $f_{LM}(x, \mathcal{E})$ is a local Maxwellian distribution function:

$$f_{LM}(x, \mathcal{E}) = \frac{n(x)}{(2\pi T(x)/m)^{3/2}} \exp -\frac{\mathcal{E}}{T(x)}. \quad (2.29)$$

The average velocity over the distribution (2.28) (in a fluid sense) provides the diamagnetic drift:

$$\mathbf{v}_{\text{dia}} = \frac{1}{n} \int f_0 \mathbf{v} d^3v = -\frac{\nabla \mathbf{p} \times \mathbf{B}}{nqB^2} + \mathcal{O}(\delta^2). \quad (2.30)$$

The diamagnetic drift takes thus the classical form $\mathbf{F} \times \mathbf{B}/qB^2$, where $\mathbf{F} = -\nabla p/n$ is the macroscopic force related to temperature and density gradients. As further discussed in the next section, the inhomogeneous magnetized plasmas may carry so-called drift waves or microinstabilities traveling essentially perpendicularly to \mathbf{B} with velocity $\sim \mathbf{v}_{\text{dia}}$. One thus defines the corresponding diamagnetic drift frequency ω^* of a given mode by $\omega^* = \mathbf{k} \cdot \mathbf{v}_{\text{dia}}$, where \mathbf{k} is the mode wavevector. The diamagnetic drift frequency can be decomposed in a density drift frequency and a temperature drift frequency: $\omega^* = \omega_n + \omega_T$, where $\omega_n = k_\theta T \nabla n / nqB$ and $\omega_T = k_\theta \nabla T / qB$, k_θ being the poloidal wavenumber. The diamagnetic drift is the main source of electrostatic microinstabilities, a class of instabilities first introduced in Sec. 2.5 and further studied in Chapters 7 and 8.

2.5 Microinstabilities

A tokamak plasma houses a lot of electromagnetic and electrostatic instabilities, featuring a wide range of wavelengths and frequencies. The microinstabilities studied in this work are driven either by ion temperature gradients (ITG-type instability) or by the interplay of temperature/density gradients with the specific dynamics of trapped particles such as in the case of the Trapped-Electron-Mode instability (TEM). These microinstabilities are essentially of electrostatic nature and thus provide no perturbation to the tokamak magnetic field. An electrostatic instability takes thus the form of a perturbed electrostatic potential, solved through the quasi-neutrality equation (a reduced form of the Poisson equation). Note that the subject of electromagnetic microinstabilities, such as the Kinetic Ballooning Modes (KBMs) and the Neoclassical Tearing Modes (NTMs), is not addressed in this work. Several thorough studies related to the physical properties of microinstabilities have been performed, for instance in [35] or [34]. Some physical features of ITG and TEM instabilities are reminded in this thesis, in Secs. 2.5.1 and 2.5.2 respectively. In particular, these waves are characterized by a slow frequency, typically of the order $\omega \sim \omega^* \sim 10^{-3}\Omega_i$, where Ω_i is the ion cyclotron frequency. They can thus be comparable to MHD instabilities with respect to the time scale. However, while an MHD instability has a typical wavelength comparable to the macroscopic size of the plasma ($\sim 1[m]$), the wavelength of an ITG or TEM microinstability is of the order of the ion Larmor radius ρ_{Li} ($\sim [mm]$), i.e. between 10^2 and 10^3 times smaller than a MHD instability wavelength. A single fluid model such as the MHD model is not appropriate for representing the instabilities in this range of wavelengths, which require a kinetic or gyrokinetic model, as detailed in this work.

In a toroidal system, any perturbation field ϕ can be represented as a superposition of poloidal and toroidal Fourier modes m and n respectively:

$$\phi(\Psi, \theta^*, \varphi) = \sum_{n,m} \phi_{nm}(\Psi) e^{im\theta^* + in\varphi}. \quad (2.31)$$

The relation $\nabla \phi \sim i\mathbf{k}\phi$ provides the wavevector \mathbf{k} associated to a given Fourier mode (m, n) :

$\mathbf{k} = m\nabla\theta^* + n\nabla\varphi$. The parallel wavenumber k_{\parallel} is thus:

$$k_{\parallel} = \frac{\mathbf{k} \cdot \mathbf{B}}{B} = \frac{1}{BJ_{\Psi\theta^*\varphi}}(nq_s - m) \simeq \frac{1}{R_0q_s}(nq_s - m), \quad (2.32)$$

while the poloidal wavenumber is computed by:

$$k_{\theta^*} = m|\nabla\theta^*| \simeq \frac{m}{r} \simeq k_{\theta}. \quad (2.33)$$

The field-aligned modes ($k_{\parallel} \simeq 0 \implies m \simeq nq_s$) thus have the phase dependence $\phi \sim \exp[in(\varphi + q_s\theta^*)]$, with associated wavevector:

$$\mathbf{k} = n \left[\frac{dq_s}{dr} \theta^* \nabla r + q_s \nabla\theta^* + \nabla\varphi \right]. \quad (2.34)$$

For field-aligned modes, the perpendicular wavevector \mathbf{k}_{\perp} is thus related to the poloidal wavenumber k_{θ^*} as follows:

$$\mathbf{k}_{\perp} = \frac{nq_s}{r}(\hat{e}_{\theta^*} + \hat{s}\theta^*\hat{e}_r) = k_{\theta^*}(\hat{e}_{\theta^*} + \hat{s}\theta^*\hat{e}_r), \quad (2.35)$$

where \hat{s} is defined by Eq. (2.4). Typically $k_{\parallel} \sim 1/R_0q_s$ for ballooning modes, while $k_{\theta}\rho_{Li} \simeq k_{\perp}\rho_{Li} \sim 1$.

Through a time dependence $\sim \exp(-i\omega_R t + \gamma t)$, a microinstability is furthermore associated to a real frequency ω_R and a growth rate γ computed from the field energy E_{field} . The field energy is defined as follows, taking into account the contributions from all the particle species σ , with associated charge q_{σ} and perturbed density $\delta n_{\sigma}(\mathbf{x}, t)$:

$$E_{\text{field}}(t) = \sum_{\sigma} \frac{q_{\sigma}}{2} \int \delta n_{\sigma}(\mathbf{x}, t) \phi(\mathbf{x}, t) d^3x. \quad (2.36)$$

The growth of the instability and the associated growth rate γ are given by the time variation of the field energy as follows:

$$\gamma = \frac{1}{2E_{\text{field}}} \frac{dE_{\text{field}}}{dt}. \quad (2.37)$$

2.5.1 General considerations on ITG instabilities

An Ion-Temperature-Gradient (ITG) mode is an instability driven by the temperature gradient of ions. The ITG-type waves are non-resonant waves and may thus be described by a fluid model, contrary to the purely density gradient drift wave instability. Note that a kinetic electron response is not required in order to study ITG instabilities, since it is an ion-type instability. Electrons entering the ITG model through an adiabatic response in the quasi-neutrality equation are thus appropriate, although considering kinetic electrons may lead to different ITG growth rates. The so-called slab-ITG mode, an ion-acoustic-wave driven unstable by ion temperature gradients, develops in a plasma with a uniform magnetic field. Let us point out that ORB5 allows to study the toroidal-ITG instabilities, first identified in Ref. [36] and

resulting from a combination between the ion temperature gradient and the toroidal geometry of the magnetic field which modifies the slab-ITG to an interchange-like mode, whose nature is similar to the so-called Rayleigh-Taylor instability occurring when a fluid with a higher density is above a fluid with a lower density. The basic mechanism of the toroidal-ITG microinstabilities is elegantly described and illustrated in [37]. In the low-field-side region of the torus (outer mid-plane), the combination of a pressure perturbation with the mainly vertical ∇B drift velocity generates a charge separation such that the resulting electric field convects hotter plasma in the hot spot of the perturbation, as well as colder plasma in the cold spot of the perturbation. The effect of the electric field is opposite in the high-field-side region (inner mid-plane). The latter basic mechanism is illustrated in Figure 2.4. This explains why ITG microinstabilities, through the properties of their dispersion relations, are unstable ($\gamma > 0$) only if $\nabla p \cdot \nabla B > 0$, i.e. only on the low-field-side of the torus. This latter fact is illustrated by Figure 2.5 which shows the typical structure of a linear ITG perturbed electrostatic potential ϕ in the poloidal plane of a tokamak, both for an *ad hoc* equilibrium and an ideal MHD equilibrium, solution of the Grad-Shafranov equation (2.9).

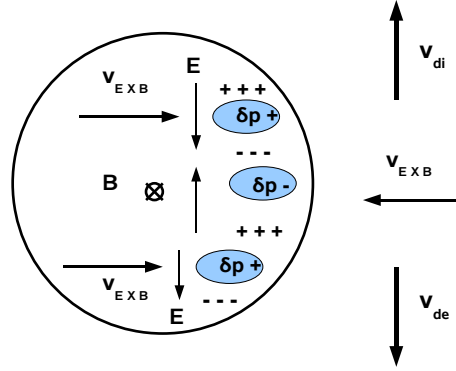


Figure 2.4: Basic mechanism of ITG instability. $\delta p+$ is a region with higher density and temperature, while $\delta p-$ is a region with lower density and temperature. The drift velocity $\mathbf{v}_{E \times B}$ reinforces the instability by bringing dense and hot plasma to the $\delta p+$ regions, while less dense and colder plasma is brought to the $\delta p-$ regions.

Note that the specific trapped ion dynamics is in general not important for ITG instabilities, except for modes whose frequency ω falls below the ion bounce frequency ω_{bi} . In this latter case, a Trapped-Ion-Mode (TIM) develops, similar to the Trapped-Electron-Modes (TEMs) addressed in Sec. 2.5.2 and Chapter 8.

The starting point to derive a linear ITG dispersion relation is a kinetic model for ions, as developed in Chapter 3, and more precisely a linear form of the electrostatic gyrokinetic equation (3.34) with no collisions ($C = 0$) and no source ($S = 0$) which reads [38]:

$$\left(\frac{\partial}{\partial t} + \mathbf{v}_G \cdot \frac{\partial}{\partial \mathbf{R}} \right) \left(\delta f_i + \frac{q f_{LM} \phi}{T_i} \right) = \frac{q}{T_i} f_{LM} \frac{\partial \langle \phi \rangle}{\partial t} + \frac{\partial f_{LM}}{\partial \Psi} \frac{\mathbf{B} \times \nabla \Psi}{B^2} \cdot \nabla \langle \phi \rangle, \quad (2.38)$$

where f_{LM} is a local Maxwellian background distribution for ions of temperature T_i and density n_i , δf_i is the perturbed part of the full ion distribution, \mathbf{v}_G is the ion guiding-center velocity as

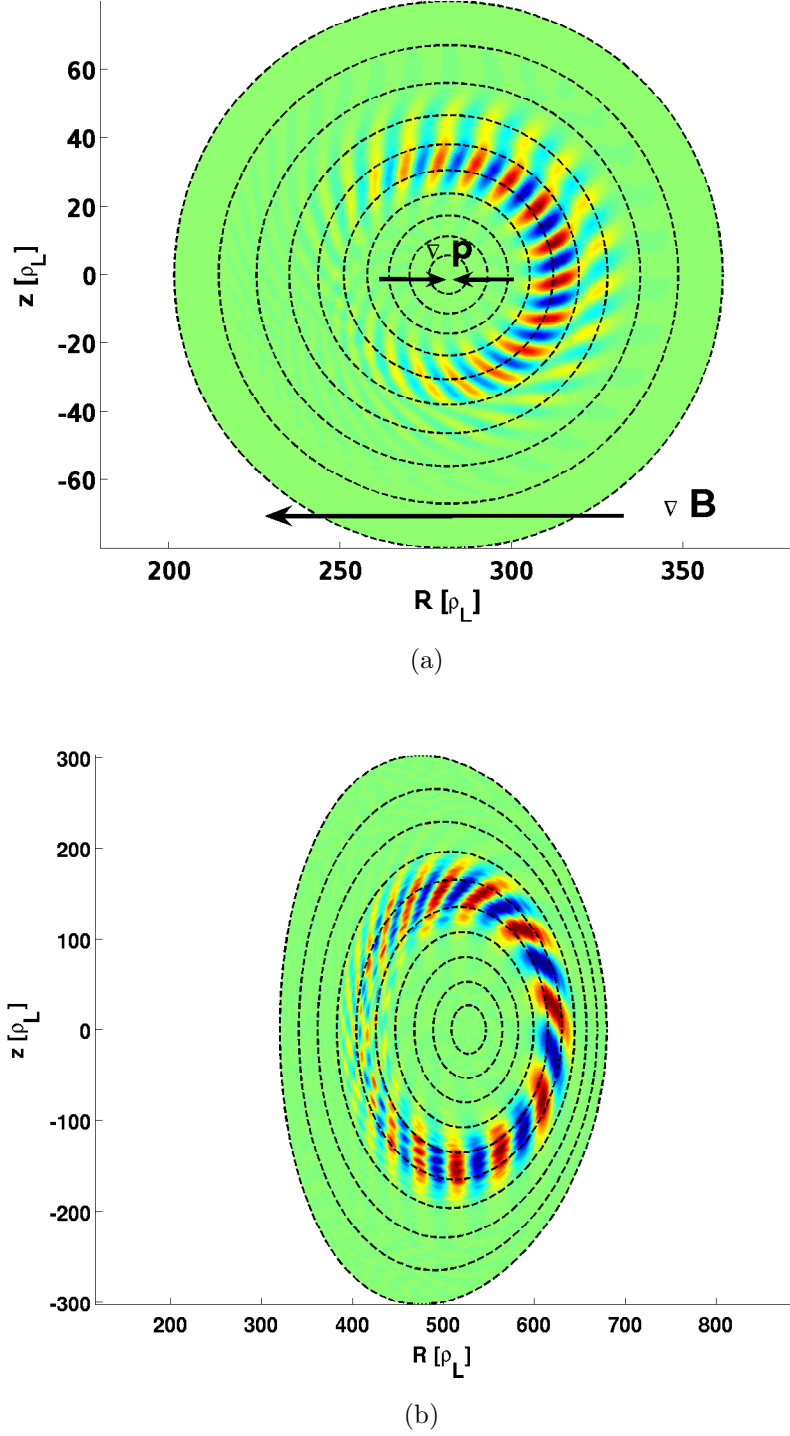


Figure 2.5: Typical structure of perturbed electrostatic potential field ϕ of a linear ITG mode, in the poloidal plane of a tokamak for (a) a circular plasma (*ad hoc* equilibrium), mode ($n = 16, m \simeq q_s n \simeq 22$), and (b) an elongated plasma (MHD equilibrium solution of the Grad-Shafranov equation (2.9)), mode ($n = 9, m \simeq q_s n \simeq 11$).

given by Eq. (3.22) and $\langle \phi \rangle$ is the gyroaveraged electrostatic potential. Assuming an adiabatic

electron response, $|\omega/\Omega| \ll 1$ and $k\lambda_D \ll 1$ so that the quasi-neutrality can be invoked:

$$Z\delta n_i = Z \int \delta f_i d^3v = \delta n_e = \frac{n_i e \phi}{T_e}, \quad (2.39)$$

the relevant dispersion relation for studying the toroidal-ITG instability is derived in [39] and reads:

$$\epsilon(\mathbf{k}, \omega) = \frac{1}{k^2 \lambda_{De}^2} + \frac{1}{k^2 \lambda_{Di}^2} \left[1 + (\omega - \omega_{ni} - \omega'_{Ti}) \int d^3v \frac{f_{LM,i}}{n_i} \frac{J_0^2\left(\frac{k_\theta v_\perp}{\Omega}\right)}{k_{||} v_{||} + \omega_{Fi} - \omega} \right] = 0, \quad (2.40)$$

where $\epsilon(\mathbf{k}, \omega)$ is the dielectric function and J_0 is the Bessel function of the first kind, related to Finite-Larmor-Radius effects and defined by:

$$J_0(x) = \frac{1}{2\pi} \int_{-\pi}^{\pi} \exp(ix \sin y) dy. \quad (2.41)$$

The temperature drift frequency operator $\omega'_{Ti} = (k_\theta T_i \nabla T_i / qB) \partial / \partial T_i$ is introduced in Eq. (2.40). Moreover, the curvature drift frequency ω_{Fi} , related to the magnetic field curvature, is $\omega_{Fi} = \mathbf{k} \cdot (\mathbf{v}_{\nabla B} + \mathbf{v}_c)$. Taking the fluid-like limit $|\omega / (k_{||} v_{thi})| \gg 1$ and assuming $|\omega / \omega_F| \gg 1$ as well as lowest order Finite-Larmor-Radius effects ($k_\theta \rho_{Li} \ll 1$), the dispersion relation (2.40) becomes:

$$\frac{T_i}{Z T_e} + \frac{\omega_{ni}}{\omega} - \left(1 - \frac{\omega_{ni} + \omega_{Ti}}{\omega} \right) \left[\left(\frac{k_{||} v_{thi}}{\omega} \right)^2 + \frac{\langle \omega_{Fi} \rangle}{\omega} - k_\theta^2 \rho_{Li}^2 \right] = 0, \quad (2.42)$$

where $\langle \omega_{Fi} \rangle = 2T_i k_\theta |\nabla_\perp \ln B| / eB$. Considering a homogeneous plasma ($\omega_{Ti} = \omega_{ni} = 0$) confined by a uniform magnetic field ($\omega_{Fi} = 0$), Eq. (2.42) becomes:

$$\omega^2 = \frac{k_{||}^2 c_s^2}{1 + k_\theta^2 c_s^2 / \Omega^2}, \quad (2.43)$$

where $c_s = \sqrt{Z T_e / m_i}$ is the sound speed. Eq. (2.43) in fact results from lowest order Finite-Larmor-Radius dispersion relation of an ion-acoustic-wave accounting for the polarization drift effect. Considering now a finite ion temperature gradient ($\omega_{Ti} \neq 0$), but still no density gradient ($\omega_{ni} = 0$), and neglecting all the Finite-Larmor-Radius effects, the following dispersion relation is obtained:

$$1 - \left(1 - \frac{\omega_{Ti}}{\omega} \right) \left[\left(\frac{k_{||} c_s}{\omega} \right)^2 + \frac{T_e}{T_i} \frac{\langle \omega_{Fi} \rangle}{\omega} \right] = 0. \quad (2.44)$$

In the case of a uniform magnetic field ($\omega_{Fi} = 0$), Eq. (2.44) is the dispersion relation of the slab-ITG mode. It leads to finding zeroes of a cubic polynomial which for $k_{||} c_s < k_{||, \text{crit}} c_s \simeq \omega_{Ti}$ in particular include a conjugate complex pair, providing an instability:

$$\omega_{ITG} \simeq \gamma_{ITG} \simeq (\omega_{Ti} (k_{||} c_s)^2)^{1/3} \underset{k_{||} \rightarrow k_{||, \text{crit}}}{\simeq} \omega_{Ti}. \quad (2.45)$$

In the case of a non-uniform magnetic field ($\omega_{Fi} \neq 0$), the presence of $\mathbf{F} = \mathbf{F}_{\nabla B} + \mathbf{F}_c$ changes the nature of slab-ITG to interchange-like mode, essentially aligned with \mathbf{B} ($k_{\parallel} \simeq 0$). Assuming $|\omega| \ll |\omega_{Ti}|$ and $k_{\parallel} \simeq 0$, the dispersion relation (2.44) includes the toroidal-ITG branch and has the solutions:

$$\omega = \pm \sqrt{-\frac{T_e}{T_i} \omega_{Ti} \langle \omega_{Fi} \rangle} = \pm \sqrt{-\frac{2k_{\theta}^2 T_i T_e}{e^2 B^2} \frac{\nabla T_i \cdot \nabla B}{T_i B}}, \quad (2.46)$$

assuming $Z = 1$. The toroidal-ITG mode is thus unstable only if $\nabla T_i \cdot \nabla B > 0$, as already mentioned, and is therefore located on the low-field-side of the tokamak (so-called bad curvature region), leading to the ballooning structure shown in Figure 2.5.

Figure 2.6, obtained by solving numerically the dispersion relation (2.40), shows the real frequency ω_r as well as the linear growth rate γ of a toroidal-ITG instability versus the perpendicular wavenumber k_{\perp} . The Finite-Larmor-Radius roll-over provides a maximum linear growth rate at $k_{\perp} \rho_{Li} \simeq 0.5$, leading to a typical ITG wavelength $\lambda_{ITG} = 2\pi/k_{\perp}$ of the order of a few ion Larmor radii.

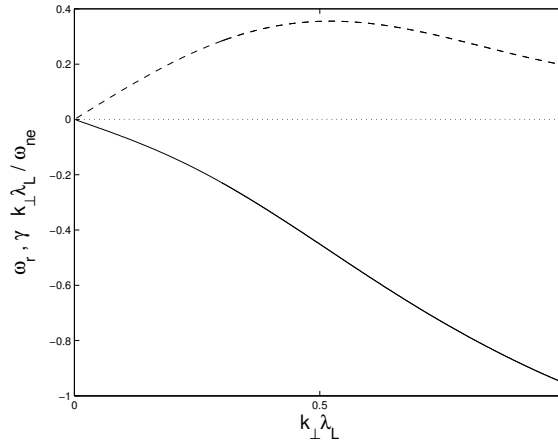


Figure 2.6: Typical k_{\perp} -dependence of both the linear growth rate γ (dashed line) and the real frequency ω_r (full line) associated to a toroidal ITG mode. λ_L is the ion Larmor radius. Figure courtesy of [34].

2.5.2 General considerations on TEM instabilities

A Trapped-Electron-Mode (TEM) is an instability closely related to trapped electron dynamics. Its frequency ω falls below the electron bounce frequency $\omega_{be} \sim \sqrt{\epsilon} v_{the}/q_s R_0$, which allows a trapped particle to carry out multiple banana orbits over the typical mode time scale. More precisely, the drive of the mode is the precessional drift velocity $\langle \dot{\phi} \rangle_b$, i.e. the net toroidal motion of the trapped particle after a banana orbit is completed, which enters in resonance with the perturbation. $\langle \rangle_b$ stands here for the bounce average, defined as:

$$\langle \dots \rangle_b = \frac{\omega_b}{2\pi} \int_{\text{orbit}} \dots \frac{dl}{v_{\parallel}}, \quad (2.47)$$

the drift motion perpendicular to the magnetic field being here neglected in a first approximation. The starting point to derive a linear TEM dispersion relation is again a linear form of the gyrokinetic equation for electrons, similar to Eq. (2.38) but where all the Finite-Larmor-Radius effects are neglected, i.e. the linear drift-kinetic equation:

$$\left(\frac{\partial}{\partial t} + \mathbf{v}_G \cdot \frac{\partial}{\partial \mathbf{R}} \right) \delta f_e = \frac{\nabla \phi \times \mathbf{B}}{B^2} \cdot \frac{\partial f_{LM}}{\partial \mathbf{R}} - e \mathbf{v}_G \cdot \nabla \phi \frac{\partial f_{LM}}{\partial \mathcal{E}}, \quad (2.48)$$

where the local Maxwellian f_{LM} is the electron background distribution and δf_e the fluctuating part of the electron distribution. Using the characteristic TEM frequency range $\omega \ll \omega_{be}$, an average procedure is performed with respect to the ω_{be} periodicity from the drift-kinetic equation (2.48), providing the so-called linear electrostatic bounce-averaged equation:

$$\left(\frac{\partial}{\partial t} + \langle \dot{\varphi} \rangle_b \frac{\partial}{\partial \varphi} \right) \left(\delta f_e - \frac{e f_{LM} \phi}{T_e} \right) = -\frac{e}{T_e} f_{LM} \frac{\partial \langle \phi \rangle_b}{\partial t} - \frac{\partial f_{LM}}{\partial \Psi} \frac{|\nabla \Psi|}{B_{pol}} \hat{e}_\varphi \cdot \nabla \langle \phi \rangle_b, \quad (2.49)$$

where $\langle \phi \rangle_b$ is the bounce-averaged electrostatic potential. The linear dispersion relation for TEM is provided again by the quasi-neutrality equation, considering the bounce-averaged equation (2.49) for electrons and neglecting the ion drive in the ion drift-kinetic response in order to isolate the pure TEM mode. Moreover, the bounce-averaged electrostatic potential $\langle \phi \rangle_b$ is approximated by ϕ , assuming a field-aligned (flute-like) structure. Defining $\omega_\varphi = \omega_{ne} L_n / R_0$, where $L_n = n / |\nabla n|$, the TEM linear dispersion relation reads:

$$0 = \frac{T_i}{T_e} + \frac{2T_i \alpha_b}{T_e \omega_\varphi} \left[\left(\omega - \omega_{ne} \left(1 - \frac{3}{2} \eta_e \right) \right) W(z_{be}) - \omega_{ne} \eta_e \left(\frac{\omega}{\omega_\varphi} W(z_{be}) + \frac{1}{2} \right) \right] + \frac{\omega_{ni}}{\omega}, \quad (2.50)$$

where $\eta_e = d \ln T_e / d \ln n_e$ and $z_{be} = \text{sign}(\omega_\varphi) \sqrt{2\omega / \omega_\varphi}$. α_b is the trapped electron fraction on the low-field-side of the tokamak where the TEM instability develops (local approximation) and $W(z)$ is the plasma dispersion function defined as:

$$W(z) = \frac{1}{\sqrt{2\pi}} \int_{-\infty}^{+\infty} \frac{x}{x - z} \exp\left(-\frac{x^2}{2}\right) dx, \quad \text{Im}(z) > 0. \quad (2.51)$$

Assuming $|\omega_\varphi / \omega| \ll 1$ as well as $T_e = T_i$ and retaining lowest order terms provide the following dispersion relation for TEM [34]:

$$\underbrace{1}_{\text{adiab. el.}} + \alpha_b \underbrace{\left[-1 + \frac{\omega_{ne} - 3\omega_\varphi/2}{\omega} + \frac{3}{2} \frac{\omega_\varphi \omega_{ne} (1 + \eta_e)}{\omega^2} \right]}_{\text{non adiab. trap. el.}} \underbrace{- \frac{\omega_{ne}}{\omega}}_{\text{ions}} = 0. \quad (2.52)$$

The real frequency of a TEM is typically of order $\omega_{TEM} \sim \omega_{ne}$. If $T_e = T_i$, the density drift frequency is estimated by $\omega_{ne} = k_\theta \rho_{Li} v_{thi} / L_n$. For the growth rate, the following rough approximation is obtained, for $\eta_e \gg 1$:

$$\gamma_{TEM, \text{no coll}} \simeq \omega_{ne} \sqrt{\frac{\epsilon^{1/2} L_n \eta_e}{R_0}}. \quad (2.53)$$

Note that the TEM growth rate increases with ϵ , i.e. with the fraction of trapped electrons as expected. The order of the growth rate is typically $\gamma_{TEM, \text{no coll}} \lesssim \omega_{ne}$. However, in order to get a better accuracy for the growth rate estimate, it is possible to solve numerically the analytical linear dispersion relation (2.50). Note that the TEM frequency range is similar to the ITG frequency range. The ion diamagnetic velocity being of the order of the electron diamagnetic velocity, the typical TEM perpendicular wavelength is expected to be close to the typical ITG perpendicular wavelength as well (\sim a few ion Larmor radii). TEM instabilities are thus in general strongly coupled to ITG instabilities in a tokamak [40]. This reflects the fact that ion dynamics plays an important role in the TEM instability mechanism as well.

Approximate TEM growth rates accounting for collisions are derived through a fluid model in Ref. [41]. In a regime of collisions satisfying $\nu_{ei} > \epsilon\omega_{ne}$, ν_{ei} being the electron-ion collision frequency, the growth rate of a TEM is estimated by the following expression:

$$\gamma_{TEM, \text{coll}} \simeq \eta_e \epsilon^{3/2} \omega_{ne}^2 \tau_e, \quad (2.54)$$

where τ_e is the electron collision time defined by Eq. (3.58). Note that the TEM growth rate at high collisionality ($\tau_e \omega_{ne} \ll 1$) does vanish. Eq. (2.54) may suggest a rough empirical modification in order to account for collisionality in the growth rate estimate, for a weakly collisional case:

$$\gamma_{TEM, \text{coll}} \simeq \frac{\gamma_{TEM, \text{no coll}}}{1 + 1/(\eta_e \epsilon^{3/2} \omega_{ne} \tau_e)}. \quad (2.55)$$

Predictions from Eq. (2.55) are compared against simulation results in Chapter 8 [Figure 8.15].

2.6 Transport in a tokamak

The concept of transport in a tokamak refers to the parallel or perpendicular fluxes of particles, momentum and energy, which affect the density, velocity and temperature profiles of the different species forming the tokamak plasma. Understanding the transport is of crucial interest for achieving fusion in a tokamak, since the temperature or the density in the core of the plasma, the key parameters regarding the fusion efficiency of a future reactor, are affected by the different fluxes. Transport in a tokamak is generated by two distinct mechanisms, collisions and turbulence, the latter being usually dominant.

2.6.1 Collisional transport: Classical and neoclassical treatment

The classical transport [42] is defined as the transport due to collisions in a plasma where the temperature and density variations are such that the mean free path λ_{mfp} between collisions is much smaller than the characteristic lengths of the gradients $L_n = n/|\nabla n|$ and $L_T = T/|\nabla T|$:

$$\lambda_{\text{mfp}}/L_n \sim \lambda_{\text{mfp}}/L_T \ll 1. \quad (2.56)$$

The equilibrium magnetic field has to be uniform in order for the classical treatment to be valid, or at least sufficiently uniform so that

$$\lambda_{\text{mfp}} \nabla B / B \ll 1. \quad (2.57)$$

The classical transport is described either by a fluid model or by the Fokker-Planck equation (3.3), developed and simplified according to the assumptions (2.56) and (2.57). The classical treatment leads to a classical diffusion coefficient $D_{\perp} \sim \rho_L^2 \nu \sim T\nu/B^2$ perpendicular to the magnetic field, where ν is the collision frequency. The perpendicular mean free path in the frame of the classical approach is the Larmor radius, $\lambda_{\text{mfp},\perp} \sim \rho_L$. In a tokamak, the classical assumption is thus satisfied in the perpendicular direction, since typically $\rho_L \nabla_{\perp} \ll 1$. However, the classical ordering does not hold in the parallel direction. The mean free path in the parallel direction is indeed given by $\lambda_{\text{mfp},\parallel} \sim v_{th}/\nu$. Considering the tokamak magnetic field of equilibrium, the classical ordering is thus not valid for standard tokamak parameters:

$$\frac{\lambda_{\text{mfp},\parallel} \nabla_{\parallel} B}{B} = \frac{v_{th} \nabla_{\parallel} B}{B\nu} \sim \frac{v_{th}}{R_0 \nu} \sim \frac{q_s \omega_t}{\nu} > 1, \quad (2.58)$$

where the transit frequency $\omega_t = v_{th}/R_0 q_s$ is in general larger than the collision frequency ν . The special regime where the tokamak plasma satisfies $\lambda_{\text{mfp},\parallel} \nabla_{\parallel} B / B \ll 1$ is called a collisional or Pfirsch-Schlüter regime. It is the only situation where a fluid model may be applied in order to study the collisional transport in a tokamak plasma. As soon as the classical assumption is not satisfied, i.e. considering a standard tokamak plasma, a careful kinetic treatment is required from the drift-kinetic equation, which retains the features of the magnetic field curvature in the collisional transport. This model is called *neoclassical* [43] [44], as an improvement to the classical approach specifically shaped for the tokamak geometry.

In the frame of the neoclassical theory, the banana width Δr_b is assumed to be much smaller than the characteristic length of the gradients L :

$$\frac{\Delta r_b}{L} \sim \frac{q_s}{\sqrt{\epsilon}} \frac{\rho_L}{L} \ll 1. \quad (2.59)$$

We furthermore assume that:

$$v_d \ll v_{\parallel}, \quad (2.60)$$

where $v_d = |\mathbf{v}_{\nabla B} + \mathbf{v}_c|$ is the magnetic drift velocity, which is main drive of neoclassical transport when combined with collisions. Moreover, a second ordering is introduced with respect to the collision frequency. The value of the ratio $\nu^* \simeq \nu_{\text{eff}}/\omega_b \sim q_s \nu_{\text{coll}} R_0 / \epsilon^{3/2} v_{th}$ [see Eqs. (3.57) and (3.58)], where $\nu_{\text{eff}} = \nu_{\text{coll}}/\epsilon$ is the effective detrapping collision frequency, is crucial for the behaviour of the neoclassical transport. The case $\nu^* < 1$ is called the banana regime, since the banana orbits of trapped particles are essentially preserved in case of a weak collisionality. The diffusion coefficient in banana regime is given by:

$$D_{\text{neo}} = \alpha_b \Delta r_b^2 \nu_{\text{eff}} \simeq \frac{q_s^2 \rho_L^2}{\epsilon^{3/2}} \nu, \quad (2.61)$$

where $\alpha_b \sim \sqrt{\epsilon}$ is the fraction of trapped electrons. The case $\nu^* > \epsilon^{-3/2}$ is called the collisional regime, where the collisionality is strong enough to destroy the banana orbits. The intermediate regime $1 < \nu^* < \epsilon^{-3/2}$, where the neoclassical diffusion coefficient D_{neo} is independent of the collisionality, is known as the plateau regime. Table NEO summarizes the scaling of D_{neo} with respect to collisionality.

Note that the electron neoclassical transport is much smaller than the ion neoclassical transport, according to Table NEO. Indeed, $\nu_e \sim \sqrt{m_i/m_e}\nu_i$ and $\rho_{Le} \sim \sqrt{m_e/m_i}\nu_i$ leading to $D_{\text{neo,e}}/D_{\text{neo,i}} \sim \sqrt{m_e/m_i} \ll 1$.

Table NEO. Collisionality dependence of the neoclassical diffusion coefficient D_{neo} .		
banana ($\nu^* < 1$)	plateau ($1 < \nu^* < \epsilon^{-3/2}$)	collisional ($\nu^* > \epsilon^{-3/2}$)
$D_{\text{neo}} = q_s^2 \rho_L^2 \nu / \epsilon^{3/2}$	$D_{\text{neo}} = q_s^2 \rho_L^2 \omega_b / \sqrt{\epsilon} = q_s^2 \rho_L^2 \omega_t$	$D_{\text{neo}} = q_s^2 \rho_L^2 \nu$

2.6.2 Transport due to microturbulence

The microinstabilities briefly described in Sec. 2.5 and the associated perturbed electric field generate a turbulent transport through the drift velocity $\mathbf{v}_{E \times B}$. Experimental measurements of perpendicular transport level in tokamaks show values much higher than those predicted by the purely collisional transport. Moreover, the classical scaling law $D \sim T/B^2$ appears not to be verified in magnetized plasmas, showing the importance of non-collisional processes involved in transport. According to experimental measurements while studying magnetic arcs which provided the dependence $D \sim B^{-1}$, Bohm has introduced in 1949 [45] the Bohm diffusion coefficient for magnetized plasmas $D_B \sim T/qB$.

An empirical approach for turbulent transport associated to given electrostatic or electromagnetic fields consists of retaining the mode perpendicular wavelength as the characteristic diffusion length, as well as the inverse of the mode linear growth rate as the characteristic diffusion time. This approach, called mixing length argument, leads to the following diffusion coefficient: $D_{ml} \simeq \gamma/k_\perp^2$. Considering the typical parameters of an ITG instability, $k_\perp \simeq \rho_{Li}^{-1}$ and $\gamma \simeq \omega_T$, and assuming $\nabla T \simeq T/a$, the following turbulent diffusion coefficient is obtained:

$$D_{ml} \simeq \frac{\gamma}{k_\perp^2} \simeq \frac{\nabla T}{qBk_\perp} \simeq \frac{\rho_{Li}}{a} \frac{T}{qB} \simeq \frac{\rho_{Li}}{a} D_B \ll D_B. \quad (2.62)$$

The new transport scaling provided by the mixing length argument in Eq. (2.62), i.e. the Bohm scaling corrected by the factor ρ_{Li}/a ($\ll 1$ in tokamak plasmas), is called the gyro-Bohm scaling $D_{GB} \simeq \rho_{Li}^2 v_{thi}/a$. Note that, if $T_e = T_i$ and $Z = 1$, ρ_{Li}/a is called the ρ^* parameter and defines basically the size of the plasma.

Note that turbulent transport according to gyro-Bohm scaling, although much smaller than Bohm transport, is usually larger than ion neoclassical transport (and thus than electron neoclassical transport) in a tokamak, operating mostly in banana or plateau regime. This conclusion is backed by comparing the gyro-Bohm diffusion coefficient with neoclassical diffusion coefficients given in Table NEO. Indeed, typically $\nu q_s^2 / \epsilon^{3/2} < v_{thi}/a$ for a weak collisionality, leading to dominant turbulent transport in banana regime. Moreover, $\omega_{thi} q_s^2 = v_{thi} q_s / R_0 < v_{thi}/a$, leading to dominant turbulent transport in plateau regime. This simple picture does not account

for the possible effects of collisionality on turbulence itself, like the mitigating effects of electron collisions on TEM turbulence described in Chapter 8.

The turbulent transport leads to relaxation of density and temperature gradients, i.e. the drive of the underlying microinstabilities. In the absence of external source of particles or heat, a stationary turbulence level cannot thus be established. Simulations aiming at understanding the features of turbulence in a tokamak plasma have thus to include heat or particle sources, as described in Sec. 3.4.

Chapter 3

The electrostatic ORB5 collisional model

3.1 The ORB5 code

The main tool of the present work is the global gyrokinetic δf Particle-In-Cell (PIC) ORB5 code, a tokamak turbulence simulation code developed since the last decade of the twentieth century by several scientists at the Centre de Recherches en Physique des Plasmas (CRPP) in Lausanne with major contributions from the Max-Planck Institut für Plasmaphysik in Garching. In fact, the original version of this code was developed by S. E. Parker [46] at Princeton Plasma Physics Laboratory (PPPL) and later by T. M. Tran [14] at CRPP, who can thus be considered as the 'fathers' of ORB5. Many important features have been added subsequently to the code, turning it into a state-of-the-art tool for gyrokinetic simulations. As examples, we mention the kinetic electron response implemented by A. Bottino and S. Jolliet [31], the canonical Maxwellian background by P. Angelino [47], the field-aligned-filter for the field solver by B. F. McMillan and S. Jolliet [48], the heat sources and the noise-control procedures by B. F. McMillan [49], as well as the linearized collision operators developed in the frame of this thesis work [16]. Numerous thesis [37] [50] [51] and papers are related to the code ORB5, presenting both numerical aspects of its development as well as the physics the code allows to address. So far, the electrostatic code ORB5 has been successfully used to study some crucial numerical problems, such as the noise control in a PIC code [49] [26], together with important physical issues. As examples, let us mention the zonal flow-turbulence coupling without and with ion collisions [52] [53] [54] [26], plasma current effects [55], the influence of plasma shaping on turbulence [56], the effects of heat sources [49] [57] and system size [58] on ITG turbulence, the entropy evolution [57], the neoclassical transport [16], the parallel velocity non-linearity [59], the trapped electron kinetic response [60] [61] [30] and the effects of background poloidal and toroidal flows [62]. The ORB5 code has proven to ensure an acceptable energy conservation, as shown in [51]. Recently, a 3D visualization module has been written by P. Angelino, which allows to obtain a representation of microturbulence within the full tokamak plasma using the visualization software VisIt. Examples of 3D electrostatic potential visualization are given in Figure 3.1, for a linear and a non-linear simulation respectively. Figure 3.1 (a) is generated

with MatLab, while Figure 3.1 (b) is obtained with VisIt.

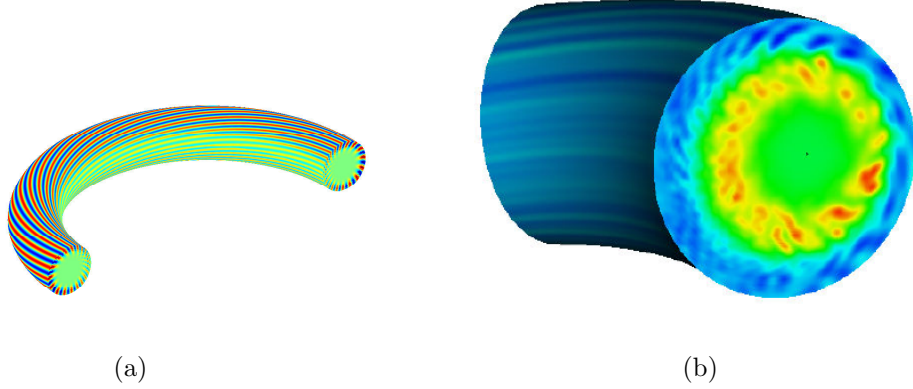


Figure 3.1: Examples of 3D electrostatic potential visualization: (a) Linear structure of a given toroidal mode ($n=16$). (b) Non-linear microinstability electrostatic potential (ITG regime).

The physical model considered by ORB5 is presented in this Chapter and the numerical basis on which the code relies [15], the so-called δf PIC algorithm, is presented in Chapter 4. The δf PIC method is an approach used for solving the gyrokinetic equation, along with a given set of Maxwell's equations in order to obtain self-consistently the electric and magnetic fields involved in the gyrokinetic equation. The ORB5 code was originally electrostatic, i.e. considering Poisson equation (or its further approximation, the quasi-neutrality equation) and not solving for Ampère's equation. The only perturbed field is in this case the electric field, and only the equilibrium magnetic field of the tokamak is considered. Recently, ORB5 has been upgraded in order to solve the Ampère's equation and to treat electromagnetic perturbations, where the magnetic field is perturbed as well, thanks to A. Bottino's work [31] [63]. The code has received the new name of NEMORB (New ElectroMagnetic ORB) after the upgrade. The present work deals with the electrostatic version of ORB5, studying the neoclassical axisymmetric physics as well as the electrostatic Ion-Temperature-Gradient (ITG) and Trapped-Electron-Mode (TEM) turbulence, with emphasis on effect of collisions which is the main contribution of this thesis. Before going into the details of numerical implementation, this Chapter briefly presents the key aspects of the gyrokinetic theory and the equations solved by the ORB5 code.

3.2 Statistical treatment

In principle, any species of charged particles in a plasma may be described by following the trajectory of all particles. The trajectory of a single particle is naturally governed by Newton's *lex secunda*:

$$m \frac{d\mathbf{v}}{dt} = q(\mathbf{E} + \mathbf{v} \times \mathbf{B}), \quad (3.1)$$

where \mathbf{v} is the particle velocity, m the particle mass and q the particle charge. In a tokamak, the fields \mathbf{E} and \mathbf{B} may be generated by the charged particles of the plasma or come from external

sources such as magnetic coils. The electrostatic potential ϕ and the magnetic potential \mathbf{A} are introduced, such that $\mathbf{E} = -\nabla\phi$ and $\mathbf{B} = \nabla \times \mathbf{A}$. A stationary magnetic field of equilibrium $\mathbf{A} = \mathbf{A}(\mathbf{x})$ is assumed here. The fully individual approach is however impractical due to the huge number N_{phys} ($\sim 10^{22}$) of particles in a tokamak plasma. The tools of statistical mechanics appear to be more appropriate for treating systems such as plasmas, leading to a description through a distribution function in phase space $f(\mathbf{x}, \mathbf{v}, t)$ for each species, \mathbf{x} being the configuration space variable and \mathbf{v} the velocity variable. $f(\mathbf{x}, \mathbf{v}, t)d^3x d^3v$ represents the number of particles statistically found, at time t , in a volume $d^3x d^3v$ centered around the position (\mathbf{x}, \mathbf{v}) in phase space. The evident necessity to find all the N_{phys} particles somewhere in phase space leads to the normalization condition:

$$\int f(\mathbf{x}, \mathbf{v}, t) d^3x d^3v = N_{\text{phys}}. \quad (3.2)$$

The equation governing the evolution of f at any position in phase space is the so-called Fokker-Planck equation, the master equation of kinetic theory:

$$\left. \frac{df}{dt} \right|_{\text{collisionless traj.}} = \frac{\partial f}{\partial t} + \mathbf{v} \cdot \frac{\partial f}{\partial \mathbf{x}} + \frac{q}{m} (\mathbf{E} + \mathbf{v} \times \mathbf{B}) \cdot \frac{\partial f}{\partial \mathbf{v}} = -C[f] + S[f], \quad (3.3)$$

where C is a general collision operator and S a general source term. $d/dt|_{\text{collisionless traj.}}$ represents the time derivative operator along collisionless trajectories. A thorough and systematic treatment of C in the frame of the code ORB5 is the main subject of this thesis, and is discussed in Chapter 5. In a non-driven collisionless system ($C = 0$, $S = 0$), the Fokker-Planck equation is called the Vlasov equation and reflects the conservation of the total distribution f along particle trajectories (note the analogy with Liouville's theorem):

$$\left. \frac{df}{dt} \right|_{\text{collisionless traj.}} = \frac{\partial f}{\partial t} + \mathbf{v} \cdot \frac{\partial f}{\partial \mathbf{x}} + \frac{q}{m} (\mathbf{E} + \mathbf{v} \times \mathbf{B}) \cdot \frac{\partial f}{\partial \mathbf{v}} = 0. \quad (3.4)$$

Neglecting collisions, i.e. considering the Vlasov equation (3.4) instead of the collisional Fokker-Planck equation (3.3), is an approximation frequently used and justified within certain limits in hot fusion plasmas. However, accounting for collisions in a fusion plasma may, as will be extensively discussed, significantly affect the behaviour of the system. Note that solving Eqs. (3.3) or (3.4) requires the self-consistent electromagnetic fields \mathbf{E} and \mathbf{B} .

If the distribution f is known at any time for any position in phase space, all the desired quantities related to the plasma may be computed, for instance the particle density n , the current density \mathbf{j} or the kinetic energy density e :

$$n(\mathbf{x}, t) = \int f(\mathbf{x}, \mathbf{v}, t) d^3v, \quad (3.5)$$

$$\mathbf{j}(\mathbf{x}, t) = q \int f(\mathbf{x}, \mathbf{v}, t) \mathbf{v} d^3v, \quad (3.6)$$

$$e(\mathbf{x}, t) = \int f(\mathbf{x}, \mathbf{v}, t) \frac{mv^2}{2} d^3v. \quad (3.7)$$

From the particle density n and the current density \mathbf{j} , the Maxwell equations are able to provide the self-consistent electromagnetic fields \mathbf{E} and \mathbf{B} at any time for any position in configuration space, forming a closed system with the Fokker-Planck equation. The statistical description for particles thus appears to be relevant and natural for a plasma, as it is for any gas of neutral particles. In principle, a simulation code could be implemented for solving the 6D Fokker-Planck (or Vlasov) equation for all species in a tokamak plasma. But in practice, this approach is not feasible, as explained in Sec. 3.3. This practical failure led to the development of the gyrokinetic theory.

3.3 The gyrokinetic equation

Today's computers are still not powerful enough in order to solve the full Fokker-Planck (or Vlasov) equation without further approximations. Dealing with the 6D particle phase space (\mathbf{x}, \mathbf{v}) in a complete tokamak system is extremely demanding in terms of computer resources, beyond the capabilities of current computing platforms, even the largest. Addressing the full 6D Fokker-Planck (or Vlasov) equation would indeed require a very small time step able to solve the gyromotion, as well as an additional grid along the gyroangle dimension. The gyrokinetic theory [64] [4] [65] is an approximation to the Vlasov equation and arises actually from the observation of the particle motion in a tokamak. Indeed, due to the presence of large equilibrium magnetic fields in a tokamak, the so-called Larmor motion, i.e. the motion of a charged particle around a field line at a frequency $\Omega = qB/m$, is much faster than any characteristic time scale relevant to microturbulence. The gyrokinetic approach makes use of this time scale separation and basically consists of averaging over the fast Larmor motion and reducing the dimensionality of the effective phase space from 6D to 5D, while conserving the important features of the Larmor motion. Consequently, the fast cyclotron time scale is absent in the resulting equations and thus does not need to be resolved, enabling significantly larger time steps.

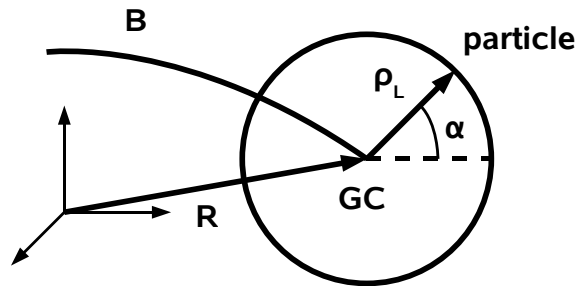


Figure 3.2: Guiding-center coordinates.

In the frame of the Lagrangian formalism, we introduce the Poincaré-Cartan form $\gamma_P = \mathbf{p} \cdot d\mathbf{x} - E_{\text{tot}} dt$, where E_{tot} is the total energy of a charged particle and $\mathbf{p} = \partial \mathcal{L} / \partial \mathbf{v}$ is the canonical momentum associated to the Lagrangian \mathcal{L} of a charged particle in the presence of

electromagnetic fields. The unperturbed Poincaré-Cartan form γ_{P0} , corresponding to a system with no perturbed electrostatic fields and only the equilibrium component of the magnetic field \mathbf{A} , is written in terms of particle variables (\mathbf{x}, \mathbf{v}) as follows:

$$\gamma_{P0} = [m\mathbf{v} + q\mathbf{A}(\mathbf{x})] \cdot d\mathbf{x} - \frac{1}{2}mv^2 dt. \quad (3.8)$$

The gyrokinetic formalism introduces a new set of variables, the guiding-center variables defined as $(\mathbf{R}, v_{\parallel}, \mu, \alpha)_{GC}$. \mathbf{R} is the guiding-center position, i.e. the position of the particle averaged over the Larmor motion. v_{\parallel} is the component of the particle velocity \mathbf{v} which is parallel to the magnetic field \mathbf{B} . The magnetic moment is written $\mu = mv_{\perp}^2/2B$, where v_{\perp} is the component of the particle velocity \mathbf{v} which is perpendicular to the magnetic field \mathbf{B} . α is the gyroangle, i.e. the phase of the gyromotion. The guiding-center variables are related to the particle variables as follows:

$$\mathbf{R} = \mathbf{x} - \boldsymbol{\rho}_L, \quad (3.9)$$

$$v_{\parallel} = \mathbf{v} \cdot \frac{\mathbf{B}}{B}, \quad (3.10)$$

$$\mu = \frac{m|\mathbf{B} \times \mathbf{v}|^2}{2B^3}, \quad (3.11)$$

$$\alpha = \arccos \left[\frac{(\mathbf{B} \times \mathbf{v}) \cdot \hat{\mathbf{e}}_R}{|\mathbf{B} \times \mathbf{v}|} \right], \quad (3.12)$$

where the Larmor vector is defined by $\boldsymbol{\rho}_L = (\mathbf{B} \times \mathbf{v})/\Omega B$. A small parameter $\delta = \rho_L/R$ is introduced, R standing here for a characteristic length of the plasma macro-scale (system size, temperature, density and magnetic field gradient length). In magnetic fusion plasmas, the ion Larmor radius is of the order of a few millimeters, while the electron Larmor radius is even smaller by the square root of the mass ratio. Typically $R \sim 1[m]$. The Poincaré-Cartan form for the charged particle (3.8) expressed in terms of the guiding-center variables $(\mathbf{R}, v_{\parallel}, \mu, \alpha)_{GC}$, keeping terms valid only up to order $\mathcal{O}(\delta)$, is given by [64]:

$$\gamma_{GC0} = \frac{m}{q}\mu d\alpha + \left[mv_{\parallel}\hat{b} + q\mathbf{A}(\mathbf{R}) \right] \cdot d\mathbf{R} - \left[\frac{1}{2}mv_{\parallel}^2 + \mu B(\mathbf{R}) \right] dt, \quad (3.13)$$

the unit vector along the magnetic field $\hat{b} = \mathbf{B}/B$ being defined. In the case of a uniform magnetic field, the guiding-center Poincaré-Cartan form (3.13) is actually valid at all orders in δ . Note that the gyroangle α is cyclic (in the absence of perturbed electrostatic potential ϕ). The associated conjugate momentum is the magnetic moment $\mu = \text{const}$. A perturbation is now added to the unperturbed Poincaré-Cartan form $\gamma_{GC} = \gamma_{GC0} + \gamma_1$, where γ_1 is given by:

$$\gamma_1 = -q\phi(\mathbf{x}, t)dt = -q\phi(\mathbf{R} + \boldsymbol{\rho}_L(\mu, \alpha), t)dt. \quad (3.14)$$

Note that the only explicit gyroangle dependence is in the perturbed part of the Poincaré-Cartan form (3.14), in the electrostatic potential ϕ . In the frame of microturbulence, it is assumed that the δ -ordering characterizes the perturbed electrostatic potential ϕ , its fluctuation frequency ω

as well as its parallel and perpendicular wavenumbers k_{\parallel} and k_{\perp} respectively:

$$\frac{\omega}{\Omega} \sim \frac{e\phi}{T} \sim \frac{k_{\parallel}}{k_{\perp}} \sim \mathcal{O}(\delta). \quad (3.15)$$

Note that the derivation of the gyrokinetic equations presented here is still valid if $e\phi/T \sim 1$, as long as the perpendicular wavelength of the considered mode is large enough to satisfy $k_{\perp}\rho_{Li}e\phi/T \sim v_{E \times B}/v_{thi} \sim \mathcal{O}(\delta)$, as shown in Ref. [66]. In order to ensure a cyclic gyroangle in presence of perturbations, a noncanonical Hamiltonian perturbation theory based on Lie transforms [67] is applied for transforming the guiding-center variables into a new set of variables, called gyrocenter variables, in which the gyroangle α remains cyclic even in the presence of perturbations:

$$(\mathbf{R}, v_{\parallel}, \mu, \alpha)_{GC} \leftrightarrow (\mathbf{R}, v_{\parallel}, \mu, \alpha)_{\text{gyro}}. \quad (3.16)$$

The Lie transform applied to the guiding-center variables leads to a new renormalized electrostatic potential, which to order $\mathcal{O}(\delta)$ is given by the gyro-averaged potential $\langle \phi \rangle$:

$$\langle \phi \rangle(\mathbf{R}, \mu, t) = \frac{1}{2\pi} \int_0^{2\pi} \phi(\mathbf{R} + \boldsymbol{\rho}_L(\mu, \alpha), t) d\alpha. \quad (3.17)$$

The total (unperturbed + perturbed) gyrocenter Poincaré-Cartan form reads:

$$\gamma_{\text{gyro}} = \underbrace{\frac{m}{q}\mu}_{\gamma_{\alpha}} d\alpha + \underbrace{\left[m v_{\parallel} \hat{b} + q \mathbf{A}(\mathbf{R}) \right]}_{\gamma_R} \cdot d\mathbf{R} - \underbrace{\left[\frac{1}{2} m v_{\parallel}^2 + \mu B(\mathbf{R}) + q \langle \phi \rangle(\mathbf{R}, \mu, t) \right]}_{\gamma_t} dt. \quad (3.18)$$

The Lie-transformed gyroangle is now clearly a cyclic variable of the total Poincaré-Cartan form γ_{gyro} . The associated constant of motion is the gyrocenter magnetic moment μ_{gyro} . Note that the subscript GC has been dropped for the guiding-center variables $(\mathbf{R}, v_{\parallel}, \mu, \alpha)_{GC}$ in Eqs. (3.13) and (3.14), as the subscript gyro has been dropped for the gyrocenter variables $(\mathbf{R}, v_{\parallel}, \mu, \alpha)_{\text{gyro}}$ in Eq. (3.18). As $\phi \rightarrow 0$, the Lie transform reduces to the identity transform. The Lie transform is thus called 'near identity' transform. The equations of motion for the other gyrocenter variables, \mathbf{R} and v_{\parallel} , are given by the Euler-Lagrange equations. Introducing the notation $\mathbf{z} = (\mathbf{R}, v_{\parallel}, \mu, \alpha)$ for representing the gyrocenter phase space variables, the Euler-Lagrange equations read:

$$\sum_j \left(\frac{\partial \gamma_j}{\partial z^i} - \frac{\partial \gamma_i}{\partial z^j} \right) \frac{dz^j}{dt} = \frac{\partial \gamma_i}{\partial t} - \frac{\partial \gamma_t}{\partial z^i} \quad \forall i. \quad (3.19)$$

Considering $z^i = \alpha$ provides $d\mu/dt = 0$, as expected. Considering $z^i = \mu$ gives the time evolution of the gyroangle:

$$\frac{d\alpha}{dt} = \Omega(\mathbf{R}) + \frac{q^2}{m} \frac{\partial \langle \phi \rangle}{\partial \mu}. \quad (3.20)$$

The case $z^i = \mathbf{R}$ in Eq. (3.19) provides the following equation of motion:

$$\begin{aligned} \frac{\partial \gamma_t}{\partial \mathbf{R}} - \frac{\partial \gamma_R}{\partial v_{\parallel}} \frac{dv_{\parallel}}{dt} - (\nabla \times \gamma_R) \times \frac{d\mathbf{R}}{dt} = \\ -\mu \nabla B - q \nabla \langle \phi \rangle - m \frac{dv_{\parallel}}{dt} \hat{b} + \frac{d\mathbf{R}}{dt} \times q \mathbf{B}^* = \mathbf{0}, \end{aligned} \quad (3.21)$$

where the modified magnetic field $\mathbf{B}^* = \mathbf{B} + mv_{\parallel}(\nabla \times \hat{b})/q = B_{\parallel}^* \hat{b} + mv_{\parallel} \hat{b} \times \hat{b} \cdot (\nabla \hat{b})/q$ is introduced. Applying the operator $\hat{b} \times (\dots)$ to both sides of Eq. (3.21) and using $v_{\parallel} = d\mathbf{R}/dt \cdot \hat{b}$ give the equation of motion for the gyrocenter position \mathbf{R} :

$$\frac{d\mathbf{R}}{dt} = \mathbf{v}_G = \frac{1}{\hat{b} \cdot \mathbf{B}^*} \left[v_{\parallel} \mathbf{B}^* + \frac{\mu \hat{b}}{q} \times \nabla B + \hat{b} \times \nabla \langle \phi \rangle \right] = \mathbf{v}_{\parallel} + \mathbf{v}_{\nabla B} + \mathbf{v}_c + \mathbf{v}_{E \times B}. \quad (3.22)$$

The gyrocenter velocity \mathbf{v}_G is thus composed of a parallel motion \mathbf{v}_{\parallel} , a ∇B drift velocity $\mathbf{v}_{\nabla B} = \mu \hat{b} \times \nabla B / q B_{\parallel}^*$, a curvature drift velocity $\mathbf{v}_c = mv_{\parallel}^2 \hat{b} \times \hat{b} \cdot (\nabla \hat{b}) / q B_{\parallel}^*$ and the gyroaveraged $\mathbf{E} \times \mathbf{B}$ drift velocity $\mathbf{v}_{E \times B} = \hat{b} \times \nabla \langle \phi \rangle / B_{\parallel}^*$. Applying the operator $\mathbf{B}^* \cdot (\dots)$ to both sides of Eq. (3.21) gives the equation of motion for the parallel velocity v_{\parallel} :

$$\frac{dv_{\parallel}}{dt} = -\frac{\mathbf{B}^*}{m(\hat{b} \cdot \mathbf{B}^*)} \cdot (\mu \nabla B + q \nabla \langle \phi \rangle) = -\frac{1}{mv_{\parallel}} \mathbf{v}_G \cdot (\mu \nabla B + q \nabla \langle \phi \rangle), \quad (3.23)$$

where the first term on the RHS is the mirroring term and the second term on the RHS is the parallel acceleration related to the electrostatic perturbation. Eqs. (3.22) and (3.23), along with $d\mu/dt = 0$, are used in order to build the gyrokinetic equation, providing the evolution of the gyroaveraged particle distribution expressed in the gyrocenter variables $\langle f(\mathbf{R}, v_{\parallel}, \mu, \alpha, t) \rangle$, which will be noted $f(\mathbf{R}, v_{\parallel}, \mu, t)$. Indeed, the Fokker-Planck equation (3.3) can be expressed in any variables, in particular in the gyrocenter variables $(\mathbf{R}, v_{\parallel}, \mu, \alpha)_{\text{gyro}}$:

$$\frac{\partial f}{\partial t} + \frac{d\mathbf{R}}{dt} \cdot \frac{\partial f}{\partial \mathbf{R}} + \frac{dv_{\parallel}}{dt} \frac{\partial f}{\partial v_{\parallel}} + \frac{d\alpha}{dt} \frac{\partial f}{\partial \alpha} = -C[f] + S[f]. \quad (3.24)$$

The cyclic nature of the gyroangle α provides the important following equality: $\langle d\alpha/dt \partial f / \partial \alpha \rangle = d\alpha/dt \langle \partial f / \partial \alpha \rangle = 0$. Moreover, $\langle d\mathbf{R}/dt \rangle = d\mathbf{R}/dt$ and $\langle dv_{\parallel}/dt \rangle = dv_{\parallel}/dt$. Applying the gyro-averaging operator over the cyclic variable α on Eq. (3.24) thus gives:

$$\frac{\partial \langle f \rangle}{\partial t} + \frac{d\mathbf{R}}{dt} \cdot \frac{\partial \langle f \rangle}{\partial \mathbf{R}} + \frac{dv_{\parallel}}{dt} \frac{\partial \langle f \rangle}{\partial v_{\parallel}} = -C[\langle f \rangle] + S[\langle f \rangle]. \quad (3.25)$$

Dropping the brackets, the gyrokinetic equation finally reads:

$$\frac{Df}{Dt} = -C[f] + S[f], \quad (3.26)$$

where D/Dt is the gyrokinetic advection operator:

$$\frac{D}{Dt} = \frac{\partial}{\partial t} + \frac{d\mathbf{R}}{dt} \cdot \frac{\partial}{\partial \mathbf{R}} + \frac{dv_{\parallel}}{dt} \frac{\partial}{\partial v_{\parallel}}, \quad (3.27)$$

where $d\mathbf{R}/dt$ and $dv_{||}/dt$ are given by Eqs. (3.22) and (3.23) respectively. The gyrokinetic equation (3.26) is non-linear, through the drift velocity $\mathbf{v}_{E \times B}$ in $d\mathbf{R}/dt$ and the parallel acceleration related to the electrostatic perturbation $\sim \mathbf{B}^* \cdot \nabla \langle \phi \rangle$ in $dv_{||}/dt$. Note that the collision operator in the gyrokinetic equation (3.26) is usually treated in a drift-kinetic approximation, i.e. by identifying the particle position \mathbf{x} to the gyrocenter position \mathbf{R} . There is thus in general no gyrokinetic corrections applied to the collision operator C in ORB5, as discussed in Chapter 5.

3.4 The δf method

In the δf method, the full distribution f is split into a background distribution f_0 and a perturbed part $\delta f = f - f_0$. This decomposition is useful for considering a linearized system of equations with respect to perturbations $e\phi/T \sim \delta f/f_0$ and, from a numerical point of view, to provide a low-noise Particle-In-Cell method (δf PIC, see Chapter 4). Two different background distributions may be chosen in ORB5. The first one is a local Maxwellian, $f_0 = f_{LM}$, written as follows:

$$f_{LM}(\Psi, \mathcal{E}) = \frac{n_0(\Psi)}{[2\pi T_0(\Psi)/m]^{3/2}} \exp \left[-\frac{\mathcal{E}}{T_0(\Psi)} \right], \quad (3.28)$$

where Ψ is the poloidal magnetic flux and $n_0(\Psi)$ and $T_0(\Psi)$ the background density and temperature profiles respectively. $\mathcal{E} = mv^2/2$ is the kinetic energy. The deviation of the total distribution from the local Maxwellian background f_{LM} is written $\delta f_{LM} = f - f_{LM}$. Note that f_{LM} is itself not an exact stationary state of the (collisionless) gyrokinetic equation as it is not a function of exact constants of motion: \mathcal{E} is a constant but not Ψ . A true stationary solution is given by the second possible choice for the background, the so-called canonical Maxwellian $f_0 = f_{CM}$, which reads [47]:

$$f_{CM}(\bar{\psi}, \mathcal{E}) = \frac{n_0(\bar{\psi})}{[2\pi T_0(\bar{\psi})/m]^{3/2}} \exp \left[-\frac{\mathcal{E}}{T_0(\bar{\psi})} \right], \quad (3.29)$$

$\bar{\psi}$ standing here for either the toroidal canonical momentum $\bar{\psi} = \Psi_0 = \Psi + mF(\Psi)v_{||}/qB$, where $F(\Psi) = RB_\varphi$, or for the corrected toroidal canonical momentum $\bar{\psi} = \hat{\Psi}$, where $\hat{\Psi}$ is defined by:

$$\hat{\Psi} = \Psi_0 + \text{corr} = \Psi_0 - \text{sign}(v_{||}) \frac{m}{q} R_0 \sqrt{\frac{2}{m} (\mathcal{E} - \mu B_{\max}(\Psi_0))} \mathcal{H}(\mathcal{E} - \mu B_{\max}(\Psi_0)), \quad (3.30)$$

with \mathcal{H} the Heaviside function and $B_{\max}(\Psi_0)$ the maximum magnetic field corresponding to the magnetic surface Ψ_0 . The correction in $\hat{\Psi}$ to the toroidal canonical momentum Ψ_0 is nearly zero for trapped particles and of opposite sign for forward and backward passing particles. $\hat{\Psi}$, being clearly a function of constants of motion of the unperturbed system, is itself a constant of motion of the unperturbed system and approximates the average of Ψ over the closed unperturbed guiding-center trajectory in a poloidal plane of the tokamak. f_{CM} is thus a function of the constants of the unperturbed motion, $(\hat{\Psi}, \mathcal{E}, \mu)$ or $(\Psi_0, \mathcal{E}, \mu)$, and is therefore solution of the

stationary, collisionless gyrokinetic equation in absence of perturbations [Eq. (3.26) with $\phi = 0$, $\partial/\partial t = 0$ and $C, S = 0$]. Since the constant of motion $\hat{\Psi}$ of a given particle provides a good estimate of the average $\langle \Psi \rangle_{\text{traj}}$ of the magnetic flux coordinate Ψ over the guiding-center trajectory, the profiles $n_0(\Psi)$ and $T_0(\Psi)$ are close to the effective density and temperature profiles of the background $f_{CM}(\hat{\Psi})$ when choosing $\bar{\psi} = \hat{\Psi}$ [47]. The difference between $n_0(\Psi)$, $T_0(\Psi)$ and the actual density and temperature profiles can however become significant, especially in smaller systems (large ρ^*) when choosing $\bar{\psi} = \Psi_0$. Moreover, note that choosing the background f_{CM} as a function of the corrected toroidal canonical momentum $\hat{\Psi}$ has the purpose of defining an equilibrium with essentially zero toroidal rotation [62]. The deviation of the total distribution from the canonical Maxwellian background f_{CM} is written $\delta f_{CM} = f - f_{CM}$.

The collision operator C , on the RHS of Eq. (3.26), is in all cases linearized with respect to local Maxwellian backgrounds:

$$C[f] \simeq C[f_{LM}, \delta f_{LM}] + C[\delta f_{LM}, f_{LM}] + \sum_{\alpha} (C_{\text{inter}}[f_{LM\alpha}, \delta f_{LM}] + C_{\text{inter}}[\delta f_{LM\alpha}, f_{LM}]), \quad (3.31)$$

where terms of the form $C[\delta f_{LM}, \delta f_{LM}]$ and $C_{\text{inter}}[\delta f_{LM\alpha}, \delta f_{LM}]$ are neglected as a result of the linearization process. In a system with strong flows, linearizing the collision operators with respect to properly chosen shifted Maxwellian distributions should reduce the ratio $|\delta f/f_0|$ and thus increase the relevance of the linearization. Indeed, in ORB5 the linearization of the collision operators is justified as long as δf_{LM} remains small compared to f_{LM} . This statement is verified in simulations presented in this work, and in particular for neoclassical results since the time scale we consider, typically a collision time, is small compared to the neoclassical confinement time. Indeed, an estimate for the deviation from the background distribution is given by $\delta f_{LM} \sim \Delta r \cdot \nabla f_{LM} \sim f_{LM} \Delta r / L_c$, where Δr is the typical radial excursion of the particle along its collisional trajectory and L_c the characteristic gradient length of equilibrium profiles. As $|\Delta r / L_c| \ll 1$ after a few collision times for the systems of interest, the scaling $|\delta f_{LM} / f_{LM}| \ll 1$ is indeed ensured. The terms $C[f_{LM}, \delta f_{LM}]$ and $C[\delta f_{LM}, f_{LM}]$ in Eq. (3.31) form the linearized self-collision operator and represent the collisions of δf_{LM} on the background f_{LM} and the background reaction respectively. The terms $C_{\text{inter}}[f_{LM\alpha}, \delta f_{LM}]$ and $C_{\text{inter}}[\delta f_{LM\alpha}, f_{LM}]$ represent the collisions of δf_{LM} on the background $f_{LM\alpha}$ of another species α , as well as collisions of f_{LM} on $\delta f_{LM\alpha}$, and form the linearized inter-species collision operator in ORB5. The details of the full linearized collision operator (3.31) are given in Chapter 5. The so-called test-particle operator $C_{TP}[\delta f_{LM}]$ is the total operator representing scattering of δf_{LM} :

$$C_{TP}[\delta f_{LM}] = C[f_{LM}, \delta f_{LM}] + \sum_{\alpha} C_{\text{inter}}[f_{LM\alpha}, \delta f_{LM}]. \quad (3.32)$$

The so-called background reaction operator $C_{BR}[f_{LM}]$ represents the collisions of the background f_{LM} on the perturbed parts of the different species:

$$C_{BR}[f_{LM}] = C[\delta f_{LM}, f_{LM}] + \sum_{\alpha} C_{\text{inter}}[\delta f_{LM\alpha}, f_{LM}]. \quad (3.33)$$

Note that the inter-species thermalization terms of the form $C_{\text{inter}}[f_{LM\alpha}, f_{LM}]$, which strictly speaking are non-zero if the temperatures are not equal, are neglected in all cases in ORB5 (more details in Chapter 5).

For the collisionless part of the gyrokinetic equation [Left-Hand-Side of Eq. (3.26)] one may either consider a decomposition of f with respect to a local Maxwellian background f_{LM} or a canonical Maxwellian background f_{CM} . Using the general notation f_0 for f_{LM} or f_{CM} and $\delta f = f - f_0$, the ORB5 gyrokinetic equation in the frame of the δf method reads:

$$\frac{D\delta f}{Dt} + C_{TP}[\delta f_{LM}] = -\frac{Df_0}{Dt} - C_{BR}[f_{LM}] + S_H[f_0, \delta f]. \quad (3.34)$$

Note that at this point, contrary to the collision operator, no approximation such as linearization has been considered for the gyrokinetic operator D/Dt . Let us detail here the actual heat source term S considered in ORB5:

$$S_H[f_0, \delta f] = -\gamma_H \left(\widetilde{\delta f}(\Psi, \mathcal{E}, t) - \widetilde{f_0}(\Psi, \mathcal{E}, t) \frac{\int d\mathcal{E} \widetilde{\delta f}(\Psi, \mathcal{E}, t)}{\int d\mathcal{E} \widetilde{f_0}(\Psi, \mathcal{E}, t)} \right), \quad (3.35)$$

where \sim stands for the operator which reconstructs the distribution in the (Ψ, \mathcal{E}) space. For any function A of the gyrocenter variables $(\Psi, \theta^*, \varphi, \mathcal{E}, \xi)$, where θ^* is the straight-field-line poloidal angle, φ the toroidal angle and $\xi = v_{||}/v$ the pitch angle, the operator \sim reads:

$$\widetilde{A}(\Psi, \mathcal{E}, t) = \frac{\int d\theta^* d\varphi d\xi J_{\Psi\theta^*\varphi} A(\Psi, \theta^*, \varphi, \mathcal{E}, \xi, t)}{\int d\theta^* d\varphi d\xi J_{\Psi\theta^*\varphi}}, \quad (3.36)$$

$J_{\Psi\theta^*\varphi}$ being the Jacobian for the magnetic coordinates $(\Psi, \theta^*, \varphi)$. The heating rate γ_H is chosen according to the physical system under consideration, essentially through the intensity of the heat fluxes. Note that the heat source term (3.35) is by construction particle conserving and is constant on a given flux surface.

ORB5 is able to consider two approximations related to the operator D/Dt applied to δf , i.e. to the Left-Hand-Side of the gyrokinetic equation (3.34). First, the code can run in *linear* regime, solving the following equation:

$$\left. \frac{D\delta f}{Dt} \right|_{\text{lin}} + C_{TP}[\delta f_{LM}] = -\frac{Df_0}{Dt} - C_{BR}[f_{LM}] + S_H[f_0, \delta f], \quad (3.37)$$

where

$$\left. \frac{D}{Dt} \right|_{\text{lin}} = \frac{\partial}{\partial t} + (\mathbf{v}_{||} + \mathbf{v}_{\nabla B} + \mathbf{v}_c) \cdot \frac{\partial}{\partial \mathbf{R}} - \frac{1}{mv_{||}} (\mathbf{v}_{||} + \mathbf{v}_{\nabla B} + \mathbf{v}_c) \cdot \mu \nabla B \frac{\partial}{\partial v_{||}}. \quad (3.38)$$

In the linear regime, having thus neglected the quadratic terms $\sim \delta f \cdot \phi$, the toroidal Fourier modes are decoupled in an axisymmetric system, which allows to study separately the growth rate and real frequency of modes of different toroidal mode numbers appearing in the turbulence

spectrum. Secondly, the local neoclassical limit gives the following equation:

$$\left. \frac{D\delta f_{LM}}{Dt} \right|_{\text{neo}} + C_{TP}[\delta f_{LM}] = -\frac{Df_{LM}}{Dt} - C_{BR}[f_{LM}] + S_H[f_{LM}, \delta f_{LM}], \quad (3.39)$$

where

$$\left. \frac{D}{Dt} \right|_{\text{neo}} = \frac{\partial}{\partial t} + \mathbf{v}_{\parallel} \cdot \frac{\partial}{\partial \mathbf{R}} - \frac{1}{m} \hat{\mathbf{b}} \cdot \mu \nabla B \frac{\partial}{\partial v_{\parallel}}. \quad (3.40)$$

$D/Dt|_{\text{neo}}$ is the drift-kinetic advection operator assuming small banana widths compared to the characteristic lengths of the system. This operator is considered for carrying out axisymmetric collisional transport calculations in the standard neoclassical ordering limit with no electric field. In this limit, the local Maxwellian background $f_0 = f_{LM}$ is considered (more details in Chapter 6).

The notation D'/Dt is introduced, which stands either for D/Dt , for $D/Dt|_{\text{lin}}$ or for $D/Dt|_{\text{neo}}$ such that in any case the equation for the distribution function solved by ORB5 reads:

$$\frac{D'\delta f}{Dt} + C_{TP}[\delta f_{LM}] = -\frac{Df_0}{Dt} - C_{BR}[f_{LM}] + S_H[f_0, \delta f]. \quad (3.41)$$

For later purposes, the time derivative operator \mathcal{D}/Dt is defined, combining the δf collisionless dynamics D'/Dt and the test-particle collision operator C_{TP} :

$$\frac{\mathcal{D}}{Dt} = \frac{D'}{Dt} + C_{TP}[\cdot]. \quad (3.42)$$

3.5 ORB5 models for ions

For microturbulence simulations, the time evolution of the ion distribution f_i in ORB5 is defined by the gyrokinetic equation (3.34) described in Sec. 3.4, retaining the effects of the finite Larmor radius for the collisionless dynamics, essential given that fluctuations related to microturbulence are such that $k_{\perp} \rho_{Li} \sim 1$. However, for neoclassical studies, for which the characteristic lengths L_c of all fields are such that $\rho_{Li}/L_c \ll 1$, the drift-kinetic approximation can be considered. In the drift-kinetic approximation, the gyrocenter is identified to the particle, which is equivalent to setting $\rho_{Li} = 0$. The gyrokinetic equation (3.34) within the latter approximation, i.e. considering $\langle \phi \rangle = \phi$ in Eqs. (3.22) and (3.23), is called the drift-kinetic equation. A canonical Maxwellian background $f_{i0} = f_{CMi}$ is usually considered for turbulent simulations, while a local Maxwellian background $f_{i0} = f_{LMi}$ is the standard choice for neoclassical simulations (some global neoclassical simulations with $f_0 = f_{CM}$ are presented as well in Chapter 6). For ion dynamics, only the self-collisions are considered, so that $C_{\text{inter}} = 0$. Neglecting the ion-electron collisions is justified since $\nu_{ie}/\nu_{ii} \sim \sqrt{m_e/m_i} \ll 1$, where ν_{ii} and ν_{ie} are the ion-ion and ion-electron collision frequencies respectively, but results in neglecting inter-species thermalization. The ion collision operator in ORB5 thus reads:

$$C[f_i] \simeq C_{ii}[f_{LMi}, \delta f_{LMi}] + C_{ii}[\delta f_{LMi}, f_{LMi}]. \quad (3.43)$$

An ion heat source defined by Eq. (3.35) may be used.

3.6 ORB5 models for electrons

Three different models exist in ORB5 for electrons:

- Fully adiabatic electrons. This is the first approximation for studying ITG turbulence, which does neither allow to address TEM nor ETG (electron-temperature-gradient) turbulence. The electrons are assumed sufficiently mobile (along \mathbf{B}) to be in an essentially thermodynamic equilibrium with respect to the fluctuation field ϕ , so that the electron density is given by the Gibbs distribution $n_e \simeq n_{e0} \exp(e\phi/T_e)$, which is further linearized to give the fluctuating electron density $\delta n_e \simeq n_{e0} e(\phi - \langle \phi \rangle_S)/T_e$, where $\langle \cdot \rangle_S$ stands for the flux-surface-average operator. Note the term $\langle \phi \rangle_S$ which ensures that the flux-surface-averaged electron density $\langle \delta n_e \rangle_S = 0$, essential for the dynamics of zonal flows [68]. For the adiabatic approximation to be justified, one must have $|\omega/k_{\parallel}| \ll v_{the}$, where ω is the frequency and k_{\parallel} is the parallel wavenumber of a typical mode. In this case, Eq. (3.34) is not solved for electrons.
- Hybrid model. This model, which works for studying ITG and TEM turbulence but does not for ETG turbulence, is developed in detail in [51]. The trapped electrons are considered drift-kinetic, i.e. the time evolution of the trapped electron distribution f_e^{trap} is given by Eq. (3.34) in the drift-kinetic limit, while the passing electrons are considered adiabatic, in the sense described above.
- Fully kinetic electrons. The time evolution of the full trapped and passing electron distribution f_e is given by Eq. (3.34) in the drift-kinetic limit ($\rho_{Le} \rightarrow 0$), i.e. considering no Finite-Larmor-Radius effects. The drift-kinetic approximation is justified since $\rho_{Le}/\rho_{Li} \sim \sqrt{m_e/m_i} \ll 1$.

A local Maxwellian background for electrons $f_{e0} = f_{LMe}$ is used in any case, since for electrons $\Psi \simeq \Psi_0$ due to $\rho_{Le}/\rho_{Li} \ll 1$. Electron self-collisions as well as electron-ion collisions are considered in Eq. (3.34) for electrons, as $\nu_{ee} \sim \nu_{ei}$. The electron collision operator in ORB5 thus reads:

$$C[f_e] \simeq C_{ee}[f_{LMe}, \delta f_{LMe}] + C_{ee}[\delta f_{LMe}, f_{LMe}] + C_{ei}[f_{LMi}, \delta f_{LMe}]. \quad (3.44)$$

Note that the term $C_{ei}[\delta f_{LMi}, f_{LMe}]$ is neglected (more details in Chapter 5). An electron heat source defined by Eq. (3.35) may be used.

3.7 The quasi-neutrality equation

In the electrostatic approximation, and considering ITG and TEM modes for which $k\lambda_D \ll 1$, the Maxwell system of equations reduces to the single quasi-neutrality equation expressed in

particles variables:

$$n_e(\mathbf{x}, t) = Zn_i(\mathbf{x}, t). \quad (3.45)$$

The ion and electron background densities are assumed to ensure local neutrality, $n_{e0} = Zn_{i0}$, such that the quasi-neutrality equation reads:

$$\delta n_e(\mathbf{x}, t) = Z\delta n_i(\mathbf{x}, t) = Z\overline{\delta n_i}(\mathbf{x}, t) + Z\delta n_{i,pol}(\mathbf{x}, t), \quad (3.46)$$

where Z is the ion charge. Note that the assumption $n_{e0} = Zn_{i0}$ is strictly valid only if $f_{i0} = f_{LMi}$. The latter assumption is approximately valid if $f_{i0} = f_{CMi}(\hat{\Psi})$ but is essentially irrelevant if $f_{i0} = f_{CMi}(\Psi_0)$. Note that the ion density δn_i is split into a gyrodensity term $\overline{\delta n_i}$ and a polarization drift term $\delta n_{i,pol}$ as detailed in Sec. 3.7.1.

3.7.1 Ion contribution

The gyrodensity $\overline{\delta n_i}$ is computed as follows:

$$\overline{\delta n_i}(\mathbf{x}, t) = \int \frac{B_{||}^*}{m} d^3R dv_{||} d\mu d\alpha \delta f_i(\mathbf{R}, v_{||}, \mu, t) \delta(\mathbf{R} + \boldsymbol{\rho}_{Li}(\mu, \alpha) - \mathbf{x}), \quad (3.47)$$

where $B_{||}^*/m = B/m + v_{||}(\nabla \times \hat{b}) \cdot \hat{b}/q$ is the Jacobian of the phase-space written in terms of variables $(\mathbf{R}, v_{||}, \mu, \alpha)$. The polarization drift term $\delta n_{i,pol}(\mathbf{x}, t)$ is given by the following integral operator:

$$\delta n_{i,pol}(\mathbf{x}, t) = \int \frac{B_{||}^*}{m} d^3R dv_{||} d\mu d\alpha \frac{q}{B} \frac{\partial f_0}{\partial \mu} [\phi(\mathbf{x}, t) - \langle \phi \rangle(\mathbf{R}, \mu, t)] \delta(\mathbf{R} + \boldsymbol{\rho}_{Li}(\mu, \alpha) - \mathbf{x}). \quad (3.48)$$

In ORB5 one furthermore considers the so-called long wavelength approximation, where $\delta n_{i,pol}$ is expanded to the second order in $k_{\perp}\rho_{Li}$, where k_{\perp} is the characteristic wavenumber perpendicular to \mathbf{B} , in order to take the following form:

$$\delta n_{i,pol}(\mathbf{x}, t) \simeq \nabla_{\perp} \cdot \left[\frac{n_{i0}}{B\Omega_i} \nabla_{\perp} \phi(\mathbf{x}, t) \right]. \quad (3.49)$$

This long wavelength approximation is currently a significant restriction to the applicability of the ORB5 model, especially in the TEM regime for which $k_{\perp}\rho_{Li} \gtrsim 1$ modes can be unstable. Implementing the integral form (3.48) valid to all orders in $k_{\perp}\rho_{Li}$, similar to Ref. [69], is thus a priority in the future development of the code.

3.7.2 Electron contribution and final form

3.7.2.1 Fully kinetic electrons

The electron density is computed in the drift-kinetic approximation:

$$\delta n_e(\mathbf{x}, t) = \int \frac{B_{\parallel}^*}{m} dv_{\parallel} d\mu d\alpha \delta f_e(\mathbf{x}, v_{\parallel}, \mu, t), \quad (3.50)$$

such that the quasi-neutrality equation reads:

$$-\nabla_{\perp} \cdot \left[\frac{n_{i0}}{B\Omega_i} \nabla_{\perp} \phi(\mathbf{x}, t) \right] = \overline{\delta n_i}(\mathbf{x}, t) - \frac{1}{Z} \delta n_e(\mathbf{x}, t). \quad (3.51)$$

3.7.2.2 Fully adiabatic electrons

The electron density is obtained from the assumed adiabatic electron response (linearized):

$$\delta n_e(\mathbf{x}, t) \simeq n_{e0} \frac{e[\phi(\mathbf{x}, t) - \langle \phi \rangle_S(\Psi, t)]}{T_{e0}(\Psi)} = Z n_{i0} \frac{e[\phi(\mathbf{x}, t) - \langle \phi \rangle_S(\Psi, t)]}{T_{e0}(\Psi)}, \quad (3.52)$$

where T_{e0} is the background temperature profile and $\langle \phi \rangle_S$ is the flux-surface-averaged electrostatic potential. The quasi-neutrality equation in this case becomes:

$$n_{i0} \frac{e[\phi(\mathbf{x}, t) - \langle \phi \rangle_S(\Psi, t)]}{T_{e0}(\Psi)} - \nabla_{\perp} \cdot \left[\frac{n_{i0}}{B\Omega_i} \nabla_{\perp} \phi(\mathbf{x}, t) \right] = \overline{\delta n_i}(\mathbf{x}, t). \quad (3.53)$$

3.7.2.3 Hybrid model

The trapped electron density is computed through the distribution function of trapped electrons, treated according to the drift-kinetic approximation:

$$\delta n_e^{\text{trapped}}(\mathbf{x}, t) = \int_{\text{trapped}} \frac{B_{\parallel}^*}{m} dv_{\parallel} d\mu d\alpha \delta f_e(\mathbf{x}, v_{\parallel}, \mu, t). \quad (3.54)$$

The passing particle contribution is assumed to be adiabatic, such that the quasi-neutrality equation of the hybrid model reads:

$$[1 - \langle \alpha_b \rangle_S] n_{i0} \frac{e[\phi(\mathbf{x}, t) - \langle \phi \rangle_S(\Psi, t)]}{T_{e0}(\Psi)} - \nabla_{\perp} \cdot \left[\frac{n_{i0}}{B\Omega_i} \nabla_{\perp} \phi(\mathbf{x}, t) \right] = \overline{\delta n_i}(\mathbf{x}, t) - \frac{1}{Z} \delta n_e^{\text{trapped}}(\mathbf{x}, t), \quad (3.55)$$

where $\langle \alpha_b \rangle_S = \langle \alpha_b \rangle_S(\Psi)$ is the flux-surface-averaged fraction of trapped electrons defined by Eq. (2.26).

3.8 Physical parameters

The size of the considered plasma is set by the ρ^* parameter, already briefly introduced in Chapter 2. Let us define the sound speed $c_s = \sqrt{ZT_e/m_i}$ and the sound Larmor radius $\rho_s =$

c_s/Ω_i , with T_e taken at the reference radial position and the cyclotron frequency $\Omega_i = ZeB/m_i$ evaluated using the magnetic field on axis. Note that, if $Z = 1$ and $T_e = T_i$, the sound speed is the ion thermal velocity $c_s = v_{thi}$ and the sound Larmor radius is the ion Larmor radius $\rho_s = \rho_{Li}$. The ρ^* parameter is defined in this work as follows:

$$\rho^* = \frac{\rho_s}{a}. \quad (3.56)$$

ρ^* ranges typically from $\sim 1/80$ for a small machine like the TCV tokamak up to $\sim 1/1000$ for ITER. The collisionality parameter ν^* is defined basically as the ratio between the detrapping collision frequency $\nu_{\text{detrapp}} = \nu/\theta_t^2 = \nu/\epsilon$, where $\theta_t \sim \sqrt{\epsilon}$ is the trapping angle, and the bounce frequency $\omega_b = \sqrt{\epsilon}v_{th}/q_s R_0$. It thus reads for ions:

$$\nu_i^* = \frac{R_0 q_s}{\tau_{ii} v_{thi} \epsilon^{3/2}}, \text{ with } \tau_{ii} = \frac{6\sqrt{\pi}}{\bar{\nu}_{ii}}, \quad (3.57)$$

and for electrons:

$$\nu_e^* = \frac{R_0 q_s}{\tau_e v_{the} \epsilon^{3/2}}, \text{ with } \tau_e = \frac{3\sqrt{2\pi}}{\bar{\nu}_{ei}}, \quad (3.58)$$

$\bar{\nu}_{ei}$ and $\bar{\nu}_{ii}$ being the thermal collision frequencies as given by Eqs. (5.57) and (5.38) in Chapter 5 respectively. The Coulomb logarithm $\ln \Lambda$, although weakly function of density and temperature ($\Lambda \sim n\lambda_D^3$), is assumed to be constant over the whole plasma and typically chosen $\ln \Lambda = 18$. Except for the Coulomb logarithm, the radial dependence of the collisionality, through the explicit dependence in density and temperature profiles, is accounted for. The notation ν^* , where the index has been dropped, refers to ν_i^* . Another notation ν_0^* is introduced and stands for the collisionality parameter at the reference magnetic surface.

Most of the simulations presented in this work are based on the so-called CYCLONE case, inspired by physical parameters underlying a shot of the DIII-D tokamak [70] (see Table CYCLONE).

Table CYCLONE. The CYCLONE case parameters.

$R_0[m]$	$a[m]$	$B_{\text{axis}}[T]$	$T_0^{i,e}[keV]$	$n_0^{i,e}[m^{-3}]$	q_{s0}	\hat{s}_0	ρ^*	R_0/L_{T_0}	R_0/L_{n_0}	ν_0^*
1.7	0.61	1.91	2	$4.5 \cdot 10^{19}$	1.4	0.8	1/180	6.9	2.2	0.045

3.9 Temperature and density profile initialization

In addition to the safety factor profile $\bar{q}(r) \simeq q_s(r)$ described in Chapter 2, several kinds of temperature and density profiles are available in ORB5. Note first that the temperature and density profiles, as well as the safety factor profile, may be read directly from reconstructed profiles based on a true MHD equilibrium, through the ORB5-CHEASE interface. Some analytical profiles are also available in the code, used in particular along with the *ad hoc* equilibrium described in Chapter 2. Let \mathcal{A} stand for either the temperature T or density n of a given species. The first kind of profile, referred to as type 1, is defined with respect to the poloidal

flux coordinate $s = \sqrt{\Psi/\Psi_{edge}}$:

$$\frac{d \ln \mathcal{A}}{ds^2} = -\frac{\kappa_{\mathcal{A}}}{(1 - \cosh^{-2}(s_0/\Delta_{\mathcal{A}}))} \left\{ \cosh^{-2}\left(\frac{s - s_0}{\Delta_{\mathcal{A}}}\right) - \cosh^{-2}\left(\frac{s_0}{\Delta_{\mathcal{A}}}\right) \right\}, \quad (3.59)$$

where the reference surface $s_0 = 0.5$ is chosen so that $d \ln \mathcal{A}/ds^2 = 0$ for $s = 0, 1$ and $d \ln \mathcal{A}/ds^2 = -\kappa_{\mathcal{A}}$ for $s = s_0$. Profiles referred to as type 2 are defined with respect to the geometrical radial coordinate r , with a similarly peaked shape as profiles of type 1:

$$\frac{d \ln \mathcal{A}}{d(r/a)} = -\kappa_{\mathcal{A}} \cosh^{-2}\left(\frac{r - \tilde{r}_0}{\Delta_{\mathcal{A}}}\right), \quad (3.60)$$

with $\tilde{r}_0 = 0.5a$. Note that contrary to type 1 profiles $d \ln \mathcal{A}/d(r/a)$ is not zero at $r/a = 0, 1$. Profiles referred to as type 3 are defined with respect to the same coordinate r , with a flat logarithmic gradient over a wide region of the torus:

$$\frac{d \ln \mathcal{A}}{d(r/a)} = -\frac{\kappa_{\mathcal{A}}}{2} \left[\tanh\left(\frac{r - (\tilde{r}_0 - \Delta_{\mathcal{A}})}{\Delta_r}\right) - \tanh\left(\frac{r - (\tilde{r}_0 + \Delta_{\mathcal{A}})}{\Delta_r}\right) \right], \quad (3.61)$$

where the typical values are $\tilde{r}_0 = 0.5a$ for the center of profile and $\Delta_r = 0.04a \ll \Delta_{\mathcal{A}}$ for the ramp up/down length. The width of the profile $\Delta_{\mathcal{A}}$ and the gradient value at the reference surface $\kappa_{\mathcal{A}} = (a/R_0)R_0/L_{\mathcal{A}_0}$, where $L_{\mathcal{A}_0}$ is the characteristic length of the gradient at $r = \tilde{r}_0$, are chosen relatively to the physical case under study. Note that the profiles of type 3 are systematically chosen for non-linear simulations in this work, except when a true MHD equilibrium, which requires profiles of type 1, is considered. Wide gradient profiles of type 3 are indeed appropriate for studying the development of turbulence over a wide radial region of the torus and capturing avalanche phenomena related to heat or particle transport. On the other hand, peaked gradient profiles of type 1 or 2 are particularly appropriate for linear simulations in associating the chosen toroidal Fourier mode n to a localized radial region \tilde{r} where the instability develops, providing a properly defined poloidal wavenumber $k_{\theta} \simeq nq_s/\tilde{r}$. Temperatures are normalized with respect to the electron temperature T_{e0} at the reference surface. Electron and ion density profiles are equal according to the local neutrality condition: $n_e = Zn_i := n$. Densities are normalized with respect to the density n_0 at the reference surface or the averaged plasma density written $\langle n \rangle$. In general $n_0 \simeq \langle n \rangle$. Figure 3.3 (a) shows the density profile of type 2 and the safety factor profile (2.11) corresponding to the global CYCLONE case. Figure 3.3 (b) presents the difference between the temperature gradient profiles of type 2 (with a peaked shape) and type 3 (with a flat logarithmic gradient over a wide region of the torus) respectively, for the CYCLONE case parameters. Note that the analytical profiles used along with *ad hoc* equilibria do not consider any significant gradients close to the plasma edge, according to the limited validity of gyrokinetic codes for describing microturbulence in this region of the plasma.

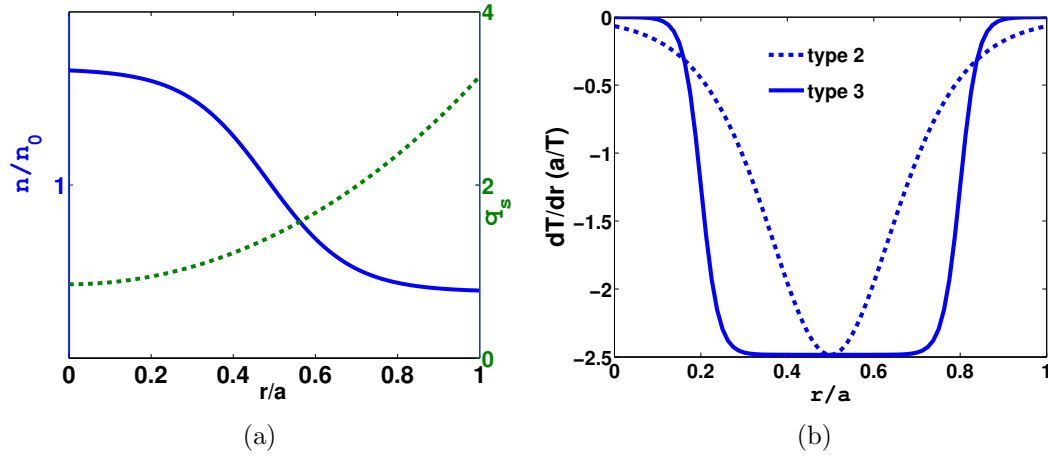


Figure 3.3: (a) Density profile of type 2 and safety factor profile corresponding to the global CYCLONE case. (b) Comparison of type 2 and 3 gradient profiles used in ORB5 along with the *adhoc* equilibrium.

3.10 Transport diagnostics

We define respectively the gyrocenter particle flux Γ , kinetic energy flux Q_{kin} , potential energy flux Q_{pot} and heat flux q_H as follows:

$$\Gamma = \left\langle \frac{\nabla \Psi}{|\nabla \Psi|} \cdot \int d^3v f \frac{d\mathbf{R}}{dt} \right\rangle_S = \left\langle \frac{1}{|\nabla \Psi|} \int d^3v f \frac{d\Psi}{dt} \right\rangle_S, \quad (3.62)$$

$$Q_{\text{kin}} = \left\langle \frac{1}{|\nabla \Psi|} \int d^3v \frac{m}{2} v^2 f \frac{d\Psi}{dt} \right\rangle_S, \quad (3.63)$$

$$Q_{\text{pot}} = \left\langle \frac{1}{|\nabla \Psi|} \int d^3v q \phi f \frac{d\Psi}{dt} \right\rangle_S, \quad (3.64)$$

$$q_H = \left\langle \frac{1}{|\nabla \Psi|} \int d^3v \left[\frac{m}{2} (v^2 - 5v_{th}^2) + q\phi \right] f \frac{d\Psi}{dt} \right\rangle_S, \quad (3.65)$$

where $d\Psi/dt = \nabla \Psi \cdot d\mathbf{R}/dt$ and $\langle \mathcal{A} \rangle_S = (1/S) \int_S \mathcal{A} d\sigma$ is defined as the poloidal flux-surface-average of a quantity \mathcal{A} , S being the surface value. In practice, to ensure sufficient statistical accuracy from the PIC approach, surface averages are replaced by volume averages using the relation $\langle \mathcal{A} \rangle_S = \langle |\nabla \Psi| \mathcal{A} \rangle_{\Delta V} / \langle |\nabla \Psi| \rangle_{\Delta V}$, where $\langle \mathcal{A} \rangle_{\Delta V} = \int_{\Delta V} \mathcal{A} d^3x / \Delta V$ stands for the volume average over the small volume ΔV enclosed between two neighboring magnetic surfaces Ψ and $\Psi + \Delta\Psi$. The heat flux q_H can be written as:

$$q_H = Q_{\text{kin}} + Q_{\text{pot}} - \frac{5}{2} T \Gamma. \quad (3.66)$$

Note that the presented simulations take into account the potential energy flux for a relevant computation of the effective heat diffusivity [71], defined as

$$\chi_H = \frac{q_H \langle |\nabla \Psi| \rangle_{\Delta V}}{n |dT/d\Psi| \langle |\nabla \Psi|^2 \rangle_{\Delta V}}. \quad (3.67)$$

In case of circular concentric magnetic surfaces as provided by the *ad hoc* equilibria, the heat diffusivity takes the simple form $\chi_H = q_H/(n|\nabla T|)$. Note that neglecting the potential energy flux leads in particular to unphysical neoclassical electron heat fluxes pointing outwards, as explained in Ref. [71]. The main contribution to the potential energy flux comes from a neoclassical term associated to the Maxwellian background, as discussed in Appendix A. Q_{pot} is thus only important for neoclassical computations related to Maxwellian background fluxes, as presented in Chapter 6. In turbulence simulations, the potential energy flux contribution to the total energy flux is small in general, as presented in Appendix A. In a collisionless simulation, or in a collisional simulation dropping the neoclassical drive $d\Psi/dt|_0$ in the weight equations as explained in Chapter 4, the potential energy flux does vanish and the total energy flux Q is the kinetic energy flux Q_{kin} .

In case of circular concentric magnetic equilibria, the particle diffusivity is defined as $D = \Gamma/|\nabla n|$ and the energy diffusivity is obtained by $\chi_E = Q/(n|\nabla T|)$. Note that the definitions of diffusivities used in this work are in fact approximate expressions which assume a local relation between fluxes and gradients (Fick's law) and neglect off-diagonal terms in transport matrix, for instance the thermodiffusive part of the particle flux driven by the temperature gradient. As a result, χ_H , D and χ_E are themselves functions of temperature and density gradients and in general would be integral operators over space and time [72]. Diffusivities are usually normalized with respect to the Gyro-Bohm (GB) units, briefly introduced in Sec. 2.6.2: $\chi_{GB} = c_s \rho_s^2/a$ or alternatively with respect to $\chi_{GB} a/L_n = c_s \rho_s^2/L_n$.

The contribution to the so-called bootstrap current \mathbf{j}_b [73] from a given species σ is given by:

$$\mathbf{j}_{b\sigma} = \int f_\sigma \mathbf{v}_\parallel B d^3v. \quad (3.68)$$

The neoclassical fluxes are obtained from the contributions $\delta f \cdot d\Psi/dt|_0$ and $f_0 \cdot d\Psi/dt|_{E \times B}$ in Eqs. (3.62)-(3.65), while the turbulent fluxes, the usual fluxes computed in collisionless gyrokinetic codes, are provided by the contribution $\delta f \cdot d\Psi/dt|_{E \times B}$ to $f \cdot d\Psi/dt$. Here one has introduced the $\mathbf{E} \times \mathbf{B}$ drift contribution to the radial velocity $d\Psi/dt|_{E \times B} = \nabla \Psi \cdot \mathbf{v}_{E \times B}$ and the magnetic drift contribution to the radial velocity $d\Psi/dt|_0 = \nabla \Psi \cdot (\mathbf{v}_{\nabla B} + \mathbf{v}_c)$.

Chapter 4

ORB5 numerical schemes: the δf Particle-In-Cell (PIC) approach

4.1 Introduction

ORB5 uses the low noise δf Particle-In-Cell (PIC) method [74], requiring the introduction of a set of N numerical markers in the gyrokinetic phase space $z = (\mathbf{R}, v_{\parallel}, \mu)$. As already mentioned, the distribution f is split into a background distribution f_0 and a perturbed part $\delta f = f - f_0$. The gyrokinetic equation is solved through a time splitting approach, considering successively and separately the time stepping of the collisionless dynamics, the collisional dynamics and the source term S_H . The markers are evolved along their collisionless and collisional trajectories in phase space. In addition, each marker r is described by two weights, $w_r(t)$ and $p_r(t)$, which are the time functions defined and described in Sec. 4.4. Collisionless and collisional dynamics both provide a contribution to the time evolution of the weights. The source terms modify the weights $w_r(t)$ as well. Finally, using a finite element method, the quasi-neutrality equation is solved at each time step, thus providing, after estimation of the perturbed density, the self-consistent electrostatic potential required in order to evolve the positions in phase space and the weights of the markers, i.e. the actual evolution of δf . This Chapter presents the numerical schemes on which the ORB5 code relies and provides the equations for marker trajectories in gyrocenter phase space, as well as the equations for the time evolution of the weights. The interpretation of marker weights in a collisional system is discussed. Some basic elements related to the field solver and the parallelization scheme are introduced. An algorithm for controlling the numerical noise, the coarse-graining procedure, is extensively described. Finally, the relevant choice of some crucial numerical parameters for ORB5 simulations is addressed.

4.2 Collisionless marker trajectories

The physical particle trajectories in gyrocenter phase space are given by Hahm's equations of motion [75], whose derivation is summarized in Chapter 3 and which are reminded here for the

sake of completeness:

$$\frac{d\mathbf{R}}{dt} = \mathbf{v}_G = \frac{1}{\hat{\mathbf{b}} \cdot \mathbf{B}^*} \left[v_{\parallel} \mathbf{B}^* + \frac{\mu}{q} \hat{\mathbf{b}} \times \nabla B + \hat{\mathbf{b}} \times \nabla \langle \phi \rangle \right] = \mathbf{v}_{\parallel} + \mathbf{v}_{\nabla B} + \mathbf{v}_c + \mathbf{v}_{E \times B}, \quad (4.1)$$

$$\frac{dv_{\parallel}}{dt} = -\frac{\mathbf{B}^*}{m(\hat{\mathbf{b}} \cdot \mathbf{B}^*)} \cdot (\mu \nabla B + q \nabla \langle \phi \rangle) = -\frac{1}{mv_{\parallel}} \mathbf{v}_G \cdot (\mu \nabla B + q \nabla \langle \phi \rangle), \quad (4.2)$$

$$\frac{d\mu}{dt} = 0. \quad (4.3)$$

As discussed in Sec. 4.4, considering the particular choice of the time evolution for marker distribution given by Eq. (4.11), the marker trajectories turn out to match exactly the physical particle trajectories, i.e. Eqs. (4.1)-(4.3) describe the actual marker trajectories in gyrocenter phase space. In the linear regime [see Eq. (3.37)], the electrostatic potential ϕ is switched off in the system (4.1)-(4.3) for evolving markers along their trajectories. In the standard neoclassical limit, only the parallel component of the velocity is retained in the marker motion ($\mathbf{v}_G = \mathbf{v}_{\parallel}$). In the configuration space, the equations of motion are solved in the magnetic coordinates (s, θ^*, φ) , the corresponding equations of motion being provided respectively by $ds/dt = d\mathbf{R}/dt \cdot \nabla s$, $d\theta^*/dt = d\mathbf{R}/dt \cdot \nabla \theta^*$ and $d\varphi/dt = d\mathbf{R}/dt \cdot \nabla \varphi$. The chosen time integrator is a 4th-order Runge-Kutta. The details of the equations integrated in magnetic coordinates are given in [51].

4.3 Collisional marker trajectories

The test-particle operator C_{TP} defined in Chapter 3 is accounted for through modifications of the marker trajectories in phase space. Considering drift-kinetic collision operators, i.e. neglecting the Finite-Larmor-Radius effects for the collisional dynamics, leads to modifications related to marker trajectories in velocity space only. Due to the diffusion part of the collision operators, the corresponding kicks in velocity space are implemented using random increments sampled from an appropriate probability distribution function (PDF). The numerical implementation of the different collision operators in ORB5 is described in detail in Chapter 5. The time integration of the C_{TP} dynamics through random kicks is a first-order scheme in the time step Δt , contrary to the collisionless trajectory integration which is a 4th-order scheme.

4.4 The two-weight δf -scheme

Here we summarize the two-weight δf -scheme, originally described in [21] and shown in [20] to be particularly useful when dealing with collisions. Considering a general phase space (z, t) , the marker distribution function $g(z, t)$ can be written in discretized form as follows:

$$g(z, t) \simeq \sum_{r=1}^N \delta[z - z_r(t)], \quad (4.4)$$

where r is an index labelling the N markers, and δ stands for the Dirac function. The physical perturbed distribution δf is linked to the marker distribution g by the so-called weight field

$W(z, t)$:

$$\delta f(z, t) = W(z, t)g(z, t), \quad (4.5)$$

which in discretized form, using (4.4), becomes:

$$\delta f(z, t) \simeq W(z, t) \sum_{r=1}^N \delta[z - z_r(t)] = \sum_{r=1}^N W[z_r(t), t] \delta[z - z_r(t)] = \sum_{r=1}^N w_r(t) \delta[z - z_r(t)], \quad (4.6)$$

having introduced the so-called marker weight $w_r(t)$ defined here as the value of the weight field at the marker position:

$$w_r(t) := W[z_r(t), t]. \quad (4.7)$$

The marker weight $w_r(t)$ represents the amplitude of δf carried by the marker r . In the same way, one may introduce the second weight field $P(z, t)$, linking the physical background distribution f_0 to g [21]:

$$f_0(z, t) = P(z, t)g(z, t), \quad (4.8)$$

which in discretized form, similar to (4.6), becomes:

$$f_0(z, t) \simeq \sum_{r=1}^N p_r(t) \delta[z - z_r(t)], \quad (4.9)$$

having introduced the second weight $p_r(t)$ of the marker, defined here as:

$$p_r(t) := P[z_r(t), t]. \quad (4.10)$$

At least formally, there is quite some freedom as to the choice of the evolution of the marker distribution g . However, for practical reasons, it is convenient to consider the following equation:

$$\frac{\mathcal{D}}{\mathcal{D}t} g = 0, \quad (4.11)$$

where $\mathcal{D}/\mathcal{D}t$ is defined by Eq. (3.42). Note that Eq. (4.11) is ensured by markers following trajectories in gyrocenter phase space given by the gyrocenter equations of motion (4.1)-(4.3), as well as through random kicks for markers in velocity space accounting for collisions, as briefly introduced in Sec. 4.3. More precisely, using the PIC representation (4.4), the evolution equation (4.11) for g is ensured by the marker trajectory equations. In the frame of the time splitting scheme, the time variation of the phase space position $z_r(t)$ of a given marker r can

be written:

$$\frac{\delta}{\delta t} z_r(t) = \frac{\delta}{\delta t} \Big|_{\text{no coll}} z_r(t) + \frac{\delta}{\delta t} \Big|_{\text{coll}} z_r(t), \quad (4.12)$$

where $\delta/\delta t|_{\text{no coll}} z_r(t)$ stands for the collisionless part of the trajectories, described in Sec. 4.2. The time variation $\delta/\delta t|_{\text{coll}} z_r(t)$ however stands for the collisional contribution accounting for the C_{TP} operator, described in detail in Chapter 5. The equation of motion (4.12) clearly involves stochastic trajectories resulting from random velocity kicks, which must be sampled from appropriate probability distribution functions (PDFs) for correctly representing C_{TP} . This type of stochastic equations of motion are called Langevin equations. To represent δf and f_0 with the numerical markers still requires, according to (4.6) and (4.9), an equation for the marker weights $w_r(t)$ and $p_r(t)$ respectively. For this purpose, one writes somewhat more explicitly the time derivative along trajectories (4.12) *acting as an operator on a phase space field*:

$$\frac{\delta}{\delta t} = \frac{D'}{Dt} + (\mathbf{\Gamma}_{TP} + \mathbf{a}_c) \cdot \frac{\partial}{\partial \mathbf{v}}, \quad (4.13)$$

where D'/Dt stands for the different forms of the collisionless gyrokinetic advection operator defined in Secs. 3.3 and 3.4, while $\mathbf{\Gamma}_{TP}$ is the drag and \mathbf{a}_c the random acceleration related to the diffusion part of the collision operator C_{TP} , which in general can be written as:

$$C_{TP}[\delta f_{LM}] = \frac{\partial}{\partial \mathbf{v}} \cdot \left[\mathbf{\Gamma}_{TP}(\mathbf{v}) \delta f_{LM} - \frac{\partial}{\partial \mathbf{v}} \cdot \underline{D}_{TP}(\mathbf{v}) \delta f_{LM} \right], \quad (4.14)$$

\underline{D}_{TP} being the diffusion tensor associated to the collision operator C_{TP} . The operator $\delta/\delta t$ is related to \mathcal{D}/Dt by the relation:

$$\frac{\delta}{\delta t} = \frac{\mathcal{D}}{Dt} - \left(\frac{\partial}{\partial \mathbf{v}} \cdot \mathbf{\Gamma}_{TP} \right) + \mathbf{a}_c \cdot \frac{\partial}{\partial \mathbf{v}} + \frac{\partial^2}{\partial \mathbf{v} \partial \mathbf{v}} : \underline{D}_{TP}. \quad (4.15)$$

4.4.1 Collisionless weight equations

4.4.1.1 Standard δf method

For the collisionless weight equations, the background distribution may be either a local Maxwellian $f_0 = f_{LM}$ or a canonical Maxwellian $f_0 = f_{CM}$ (see Sec. 3.4). Considering the collisionless part of the dynamics, we have, according to Eqs. (4.12) and (4.13):

$$\frac{\delta}{\delta t} \Big|_{\text{no coll}} = \frac{D'}{Dt}. \quad (4.16)$$

Within the collisionless stepping, the marker distribution thus follows the equation $D'g/Dt = 0$. To obtain the collisionless evolution equation for each weight $w_r(t)$, one takes its time derivative:

$$\left. \frac{d}{dt} \right|_{\text{no coll}} w_r(t) = \left. \frac{\delta}{\delta t} \right|_{\text{no coll}} W[z = z_r(t), t] = \left. \frac{\delta}{\delta t} \right|_{\text{no coll}} \left(\frac{\delta f}{g} \right) = \frac{1}{g} \frac{D'}{Dt} \delta f - \frac{\delta f}{g^2} \underbrace{\frac{D'}{Dt} g}_{=0}, \quad (4.17)$$

the last step having been carried out using the chain rule, which is justified as D'/Dt represents a first order differential operator. The collisionless gyrokinetic equation $D'\delta f/Dt = -Df_0/Dt$ provides thus the collisionless equation for the first weight w , making use of the p -weight definitions (4.8) and (4.10):

$$\left. \frac{d}{dt} \right|_{\text{no coll}} w_r(t) = -\frac{1}{g} \frac{D}{Dt} f_0 \Big|_{[z_r(t), t]} = -p_r(t) \frac{1}{f_0} \frac{D}{Dt} f_0 \Big|_{[z_r(t), t]}. \quad (4.18)$$

Let Υ stand either for Ψ , Ψ_0 or $\hat{\Psi}$ depending on the choice of background (local Maxwellian, canonical Maxwellian and corrected canonical Maxwellian respectively, see Sec. 3.4). The drive of the weight evolution (4.18) then reads:

$$\frac{D}{Dt} f_0 = \frac{\partial f_0}{\partial \Upsilon} \frac{d\Upsilon}{dt} - \frac{q}{T(\Upsilon)} f_0 \langle \mathbf{E} \rangle \cdot (\mathbf{v}_{\parallel} + \mathbf{v}_{\nabla B} + \mathbf{v}_c), \quad (4.19)$$

where $\langle \mathbf{E} \rangle$ is the gyroaveraged electric field, approximating in fact $\langle \mathbf{E} \rangle = \langle -\nabla \phi \rangle \simeq -\nabla \langle \phi \rangle$. When considering a local Maxwellian background, i.e. $\Upsilon = \Psi$, the term $\partial f_{LM}/\partial \Psi \cdot d\Psi/dt|_0 = \partial f_{LM}/\partial \Psi \cdot \nabla \Psi \cdot (\mathbf{v}_{\nabla B} + \mathbf{v}_c)$ is usually neglected for turbulence simulations. Note that keeping this term is however crucial in the frame of neoclassical simulations, since it provides the drive of collisional transport from density and temperature gradients:

$$\frac{\partial f_{LM}}{\partial \Psi} = \left[\frac{d \ln n}{d\Psi} + \frac{d \ln T}{d\Psi} \left(\frac{mv_{\parallel}^2/2 + \mu B}{T} - \frac{3}{2} \right) \right] f_{LM}. \quad (4.20)$$

Similarly, a collisionless equation for the second weight p is derived:

$$\left. \frac{d}{dt} \right|_{\text{no coll}} p_r(t) = \left. \frac{\delta}{\delta t} \right|_{\text{no coll}} P[z = z_r(t), t] = \left. \frac{\delta}{\delta t} \right|_{\text{no coll}} \left(\frac{f_0}{g} \right) = \frac{1}{g} \frac{D'}{Dt} f_0 - \frac{f_0}{g^2} \underbrace{\frac{D'}{Dt} g}_{=0}, \quad (4.21)$$

which gives directly:

$$\left. \frac{d}{dt} \right|_{\text{no coll}} p_r(t) = \frac{1}{g} \frac{D'}{Dt} f_0 \Big|_{[z_r(t), t]} = p_r(t) \frac{1}{f_0} \frac{D'}{Dt} f_0 \Big|_{[z_r(t), t]}. \quad (4.22)$$

Note that, in absence of collisions and if the full marker motion is retained ($D'/Dt = D/Dt$), the two weights are closely coupled by the relation $d/dt(p_r + w_r) = 0$, which in fact reflects the invariance of both the full distribution f and the marker distribution g along the collisionless trajectories. This relation also enables to express the p -weight in terms of the w -weight, thus illustrating how a single weight is sufficient for carrying out collisionless simulations.

4.4.1.2 Direct δf method

In case the full marker motion is retained ($D'/Dt = D/Dt$), instead of integrating numerically Eqs. (4.18) and (4.22) (standard δf method), one can handle the collisionless dynamics through the so-called direct- δf method [76] [77], taking advantage of the fact that the total distribution f is conserved along collisionless trajectories. In this case, the weight equations for collisionless dynamics can indeed be integrated analytically:

$$\frac{d}{dt}(w_r(t) + p_r(t)) = 0 \implies w_r + p_r = w_r(t_0) + p_r(t_0), \quad (4.23)$$

$$\frac{d}{dt} \ln \frac{p_r}{f_0|_{z_r}} = 0 \implies \frac{p_r}{f_0|_{z_r}} = \frac{p_r(t_0)}{f_0|_{z_r(t_0)}}. \quad (4.24)$$

Eq. (4.23) results from adding relations (4.18) and (4.22), while Eq. (4.24) is directly obtained by integrating Eq. (4.22). Let us consider a marker r going from position $z_r(t) = [\mathbf{R}_r(t), v_{||,r}(t), \mu_r(t)]$ to position $z_r(t + \Delta t) = [\mathbf{R}_r(t + \Delta t), v_{||,r}(t + \Delta t), \mu_r(t + \Delta t)]$ during a collisionless time step $t \rightarrow t + \Delta t$. Making use of Eqs. (4.23)-(4.24), the new weights are thus given by:

$$p_r(t + \Delta t) = p_r(t) \frac{f_0|_{z_r(t+\Delta t)}}{f_0|_{z_r(t)}}, \quad (4.25)$$

$$w_r(t + \Delta t) = w_r(t) + p_r(t) - p_r(t + \Delta t). \quad (4.26)$$

This scheme in particular allows to avoid explicitly evaluating unpractical terms such as $d\hat{\Psi}/dt$, appearing through Df_{CM}/Dt [Eq. (4.19)] in the case $\Upsilon = \hat{\Psi}$ for the time evolution of the weights. More precisely, the standard δf method considering $\Upsilon = \hat{\Psi}$ assumes $\partial\hat{\Psi}/\partial\mathcal{E} = 0$, which is wrong, in order to avoid singularities in the weight pushing. This latter assumption is not necessary in the frame of the direct δf method which allows to solve exactly the gyrokinetic equation with a corrected canonical Maxwellian background ($\Upsilon = \hat{\Psi}$).

4.4.2 Collisional weight equations

A local Maxwellian background $f_0 = f_{LM}$ is always chosen for handling the collisional dynamics, since the collision operators are linearized with respect to a local Maxwellian. The time derivative operator along collisional marker trajectories reads, according to Eq. (4.13):

$$\left. \frac{\delta}{\delta t} \right|_{\text{coll}} = (\mathbf{\Gamma}_{TP} + \mathbf{a}_c) \cdot \frac{\partial}{\partial \mathbf{v}}. \quad (4.27)$$

The actual collisional trajectory in phase space of a given marker is given by:

$$\left. \frac{\delta z_r(t)}{\delta t} \right|_{\text{coll}} = \mathbf{\Gamma}_{TP} + \mathbf{a}_c|_{z_r(t)}. \quad (4.28)$$

The operator (4.27) is expressed in terms of the drag $\mathbf{\Gamma}_{TP}$ and the diffusion tensor \underline{D}_{TP} as follows, according to Eqs. (3.42) and (4.15):

$$\left. \frac{\delta}{\delta t} \right|_{\text{coll}} = \frac{\partial}{\partial t} + C_{TP}[\cdot] - \left(\frac{\partial}{\partial \mathbf{v}} \cdot \mathbf{\Gamma}_{TP} \right) + \mathbf{a}_c \cdot \frac{\partial}{\partial \mathbf{v}} + \frac{\partial^2}{\partial \mathbf{v} \partial \mathbf{v}} : \underline{D}_{TP}. \quad (4.29)$$

In practice, one proceeds by making use of Eq. (4.29), but dropping the last two terms on the RHS of this relation [20]. One thus carries on by considering

$$\left. \frac{\delta}{\delta t} \right|_{\text{coll}} \stackrel{!}{=} \frac{\partial}{\partial t} + C_{TP}[\cdot] - \left(\frac{\partial}{\partial \mathbf{v}} \cdot \mathbf{\Gamma}_{TP} \right), \quad (4.30)$$

where the notation $\stackrel{!}{=}$ points out what may appear to be an ad hoc simplification. This issue is discussed in Sec. 4.4.3. Within the collisional stepping, one has $[\partial/\partial t + C_{TP}]g = 0$ as well as $[\partial/\partial t + C_{TP}]\delta f_{LM} = -C_{BR}[f_{LM}]$, which gives directly the collisional equation for the first weight w_{LM} :

$$\begin{aligned} \left. \frac{d}{dt} \right|_{\text{coll}} w_{LM,r}(t) &= \left. \frac{\delta}{\delta t} \right|_{\text{coll}} \left(\frac{\delta f_{LM}}{g} \right) = \frac{1}{g} \left. \frac{\delta}{\delta t} \right|_{\text{coll}} \delta f_{LM} - \frac{\delta f_{LM}}{g^2} \left. \frac{\delta}{\delta t} \right|_{\text{coll}} g \\ &\stackrel{!}{=} -p_{LM,r}(t) \frac{1}{f_{LM}} C_{BR}[f_{LM}] \Big|_{[z_r(t), t]}, \end{aligned} \quad (4.31)$$

noticing that the contribution from the compressibility of the drag term in (4.30), $\partial/\partial \mathbf{v} \cdot \mathbf{\Gamma}_{TP}$, cancels out. The details on evaluating C_{BR} for self-collisions are given in Sec. 5.10.2. Note that in the collisional dynamics, contrary to the situation of the collisionless dynamics, the value of the marker distribution $g(z, t)$ is not invariant along the marker trajectories $z_r(t)$. Making use of the second weight $p_{LM,r}(t)$ is thus required in order to avoid a practical problem at evaluating the factor $1/g[z_r(t), t]$, which can be identified to the phase space volume associated to the marker r . The two-weight scheme is thus mandatory in the frame of the collisional δf Particle-in-Cell scheme, while it is optional for a collisionless model. Since $C_{TP}[f_{LM}] = 0$, the collisional equation for the second weight p is trivial to derive:

$$\begin{aligned} \left. \frac{d}{dt} \right|_{\text{coll}} p_{LM,r}(t) &= \left. \frac{\delta}{\delta t} \right|_{\text{coll}} \left(\frac{f_{LM}}{g} \right) = \frac{1}{g} \left. \frac{\delta}{\delta t} \right|_{\text{coll}} f_{LM} - \frac{f_{LM}}{g^2} \left. \frac{\delta}{\delta t} \right|_{\text{coll}} g \\ &\stackrel{!}{=} p_{LM,r}(t) \frac{1}{f_{LM}} C_{TP}[f_{LM}] \Big|_{[z_r(t), t]} = 0. \end{aligned} \quad (4.32)$$

One notices that collisions have no effect on the p-weights for the considered local Maxwellian background f_{LM} .

4.4.3 Interpretation of marker weights

Dropping terms in the operator $\delta/\delta t$ going from (4.29) to (4.30) leads to the set of collisional weight equations (4.31) and (4.32) which are in fact exact when correctly reinterpreted. This was shown and discussed in detail in [78] and [20]. What needs to be reconsidered however are the original definitions of the weights $w_r(t)$ and $p_r(t)$ in terms of the weight fields $W(z, t)$ and

$P(z, t)$, given by Eqs. (4.7) and (4.10) respectively. Let us briefly review here the proof, given in the already mentioned papers, for validating the set of equations (4.6), (4.28), (4.31) and (4.32) as an exact representation (in the limit of large number of markers) of δf_{coll} , solution to the collisional dynamics of the gyrokinetic equation. For this purpose, one introduces the distribution $F(z, w, p, t)$ in the *extended* phase space (z, w, p) :

$$F(z, w, p, t) = \sum_{r=1}^N \delta[z - z_r(t)] \delta[w - w_r(t)] \delta[p - p_r(t)], \quad (4.33)$$

where the evolutions of $z_r(t)$, $w_r(t)$ and $p_r(t)$ are given by Eqs. (4.28), (4.31) and (4.32) respectively. The evolution equation for F within the frame of the collisional dynamics is given by:

$$\left(\frac{\partial}{\partial t} + C_{TP} \right) F + \frac{\partial}{\partial w} \left(\frac{dw}{dt} \Big|_{\text{coll}} F \right) + \frac{\partial}{\partial p} \left(\frac{dp}{dt} \Big|_{\text{coll}} F \right) = 0. \quad (4.34)$$

Taking different weight moments of the distribution (4.33), the three following fields are obtained:

$$\tilde{g}(z, t) = \int dw dp F(z, w, p, t) = \sum_{r=1}^N \delta[z - z_r(t)], \quad (4.35)$$

$$\widetilde{\delta f}(z, t) = \int dw dp w F(z, w, p, t) = \sum_{r=1}^N w_r(t) \delta[z - z_r(t)], \quad (4.36)$$

$$\widetilde{f_{LM}}(z, t) = \int dw dp p F(z, w, p, t) = \sum_{r=1}^N p_r(t) \delta[z - z_r(t)]. \quad (4.37)$$

While \tilde{g} corresponds obviously to the marker distribution g given by Eq. (4.4), it still has to be shown that $\widetilde{\delta f}(z, t)$ and $\widetilde{f_{LM}}(z, t)$, involving weights evolving according to Eqs. (4.31) and (4.32) respectively, may be actually identified to the physical distributions δf_{coll} and f_{LM} . By taking the corresponding moments of Eq. (4.34), one obtains the collisional evolution equations for $\widetilde{\delta f}$ and $\widetilde{f_{LM}}$ respectively:

$$\left(\frac{\partial}{\partial t} + C_{TP} \right) \widetilde{\delta f} = g \frac{dw}{dt} \Big|_{\text{coll}} = -C_{BR}[f_{LM}], \quad (4.38)$$

$$\left(\frac{\partial}{\partial t} + C_{TP} \right) \widetilde{f_{LM}} = g \frac{dp}{dt} \Big|_{\text{coll}} = 0 = C_{TP}[f_{LM}], \quad (4.39)$$

having used relations (4.31) and (4.32). Eqs. (4.38) and (4.39) are clearly the same collisional evolution equations verified by δf_{coll} and f_{LM} . Moreover, if the weights $w_r(t)$ and $p_r(t)$ are initialized according to their original definitions (4.7) and (4.10):

$$w_r(t=0) = \frac{\delta f_{\text{coll}}}{g} \Big|_{(z_r(0), t=0)}, \quad (4.40)$$

$$p_r(t=0) = \frac{f_{LM}}{g} \Big|_{(z_r(0), t=0)}, \quad (4.41)$$

the two sets of fields $(\widetilde{\delta f}, \widetilde{f_{LM}})$ and $(\delta f_{\text{coll}}, f_{LM})$ furthermore have the same initial conditions, which finally proves that they are identical at all times and that Eq. (4.36) in particular still holds as the marker representation of δf .

There is nonetheless an important effect from having dropped two terms in the operator $\delta/\delta t|_{\text{coll}}$, with significant practical consequences. As a result of the modifications leading to Eq. (4.30), once the system has evolved from its initial state and undergone collisional processes, two markers can meet at the same phase space point with different weights. In other words, a spreading of weights occurs over time at each phase space point z and at a rate which is proportional to the collision frequency. The original definitions of the weights (4.7) and (4.10) as the (single) value of the weight fields at the marker positions, used to initialize the weights at $t = 0$, are thus clearly violated at any time other than $t = 0$. It is in fact only the statistical average over all weights of markers in the vicinity of a phase space point which provides an estimate of the weight fields W and P , not the weights of a single marker. Contrary to a collisionless system, the weights w and p must thus be considered as additional effective dimensions of the numerical system, whose extensions grow on the collisional time scale. The practical price to pay for this weight spreading is increasing numerical noise as the simulation evolves. A solution to the numerical noise problem is presented in Sec. 4.8. The difference in the weight interpretation between a collisionless and a collisional case is presented in Figure 4.1

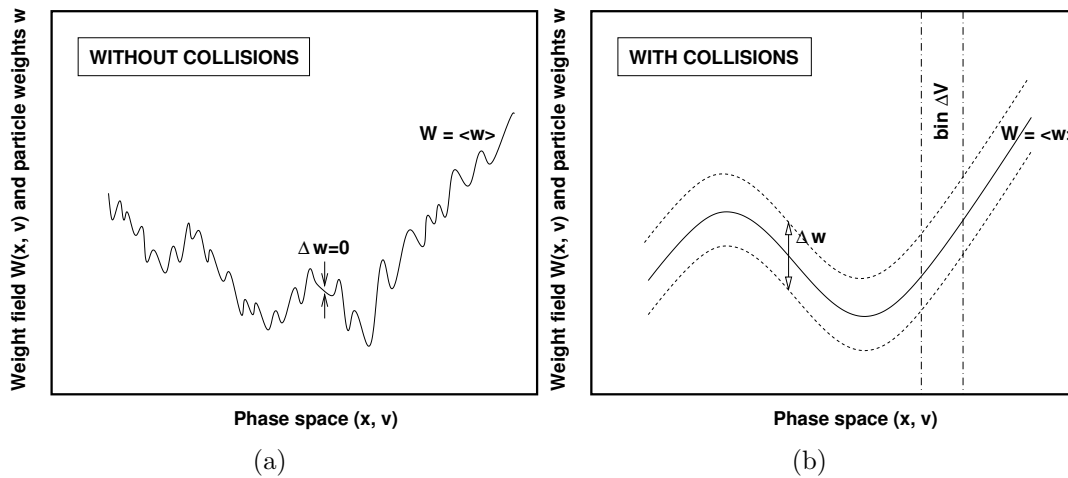


Figure 4.1: Schematic representation of marker particle weights in phase space for (a) a collisionless and (b) a collisional simulation. The local weight spreading Δw , which is nonzero in the collisional case, appears like a growing additional dimension to the numerical system. Figure courtesy of [20].

4.4.4 The background switching scheme

The background f_{CM} is a stationary state of the collisionless gyrokinetic equation. Making use of the two-weight approach, it is possible to take advantage of this collisionless equilibrium function even in collisional runs. This is achieved by switching, in the frame of the time splitting scheme, between a canonical Maxwellian background representation for carrying out the collisionless advection step and a local Maxwellian background representation for carrying out

the collisional step. This mixed background approach is schematized in Figure 4.2. Considering a local Maxwellian background for carrying out collisions is indeed a practical constraint, as the collision operators have been linearized with respect to such a distribution. Let us point out that this mixed background scheme is essentially used for ions, as $f_{LM} \simeq f_{CM}$ for electrons. For carrying out collisions, such a switching scheme requires transforming for each marker r between its two weights $(w_{CM,r}, p_{CM,r})$ in the canonical Maxwellian background f_{CM} representation and its two weights $(w_{LM,r}, p_{LM,r})$ in the local Maxwellian background f_{LM} representation. Two equations are necessary for defining this weight transformation. The first is obtained by requiring that at any time the same total distribution f must be obtained by the two representations:

$$f = f_{CM} + \delta f_{CM} = f_{LM} + \delta f_{LM}, \quad (4.42)$$

where δf_{CM} and δf_{LM} stand respectively for the deviations of the full distribution from the canonical and local Maxwellian backgrounds. In the frame of the δf PIC discretization, equation (4.42) implies for the weights of each marker r :

$$w_{CM,r} + p_{CM,r} = w_{LM,r} + p_{LM,r}. \quad (4.43)$$

The second equation is obtained by noticing that at any time and for any marker r one also has:

$$\frac{p_{CM,r}}{p_{LM,r}} = \frac{f_{CM}(z_r)}{f_{LM}(z_r)} = \sigma_r, \quad (4.44)$$

having introduced the notation σ_r for the ratio of the two backgrounds at the current marker position z_r in phase space. After the collisionless advection step, one can thus transform from canonical to local weights using Eqs. (4.43) and (4.44):

$$p_{LM,r} = \frac{p_{CM,r}}{\sigma_r}, \quad (4.45)$$

$$w_{LM,r} = w_{CM,r} + \left(1 - \frac{1}{\sigma_r}\right) p_{CM,r}, \quad (4.46)$$

and carry out the collisions in the frame of the local Maxwellian background representation, as described in Chapter 5. This will result for each marker in a new position z_r^* in phase space and a corresponding background ratio $\sigma_r^* = f_{CM}/f_{LM}|_{z_r^*}$, as well as a first weight increment Δw_{LM} from self-collisions. Let us recall that the second weight remains invariant, $\Delta p_{LM} = 0$, as a result of collisions. Transforming back to the canonical weights, one obtains the corresponding weight increments from the collisional step:

$$\Delta p_{CM,r} = \Delta \sigma_r p_{LM,r} = \left(\frac{\sigma_r^*}{\sigma_r} - 1\right) p_{CM,r}, \quad (4.47)$$

$$\Delta w_{CM,r} = \Delta w_{LM,r} - \Delta p_{CM,r} = \Delta w_{LM,r} - \left(\frac{\sigma_r^*}{\sigma_r} - 1\right) p_{CM,r}. \quad (4.48)$$

The new phase space positions z_r^* , as well as the weights $w_{CM,r}^* = w_{CM,r} + \Delta w_{CM,r}$ and $p_{CM,r}^* =$

$p_{CM,r} + \Delta p_{CM,r} = p_{CM,r} \sigma_r^* / \sigma_r$ of each marker may then be used for carrying out the next collisionless advection step, thus closing the time loop in Figure 4.2.

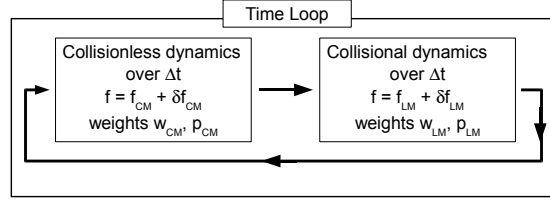


Figure 4.2: Mixed background collisional δf algorithm: Time loop for switching between a canonical Maxwellian background for stepping the collisionless dynamics and a local Maxwellian background for stepping the collisional dynamics.

4.5 Parallelization

The ORB5 code is designed in order to run making use of thousands of computer processors at the same time and is therefore parallelized using the standard Message Passing Interface (MPI). The ORB5 parallelization schemes are described in detail in Ref. [51]. Some basic features of the parallelization are recalled here for completeness. Considering a simulation running on $P = P_C \times N_D$ processors, the torus as a geometrical object is replicated P_C times, forming P_C clones of the torus, and each clone is decomposed into N_D domains. Each domain must handle at least one point of the toroidal grid for solving the quasi-neutrality equation, such that $N_D = P/P_C \leq N_\varphi$, N_φ being the number of grid points in the toroidal direction for the quasi-neutrality solver. Moreover, N_φ/N_D has to give an integer value, to ensure that all domains handle the same number of (equidistant) toroidal mesh intervals, essential for load balancing (same computational load for all processors). The markers are distributed over clones and domains according to Figure 4.3. The charge deposition on the toroidal 3D grid, essential for providing the self-consistent fields through the quasi-neutrality equation, is performed by summing the contributions of all the markers belonging to the different clones corresponding to a given toroidal domain.

4.6 The solver for the quasi-neutrality equation

Efficiently solving the quasi-neutrality equation (3.51), (3.53) or (3.55) in a toroidal geometry is a challenging problem. A lot of different studies have addressed the practical issue of solving numerically the quasi-neutrality equation in the frame of a δf PIC approach and improved the efficiency of the different algorithms. The remarkable features of the ORB5 solver, which is extensively described in Refs. [14], [51] and [48], are briefly summarized here. The general principle is to use a finite element method, similar to the simple solver for the Poisson equation in one dimension presented in Appendix B. However, the more complex tokamak configuration

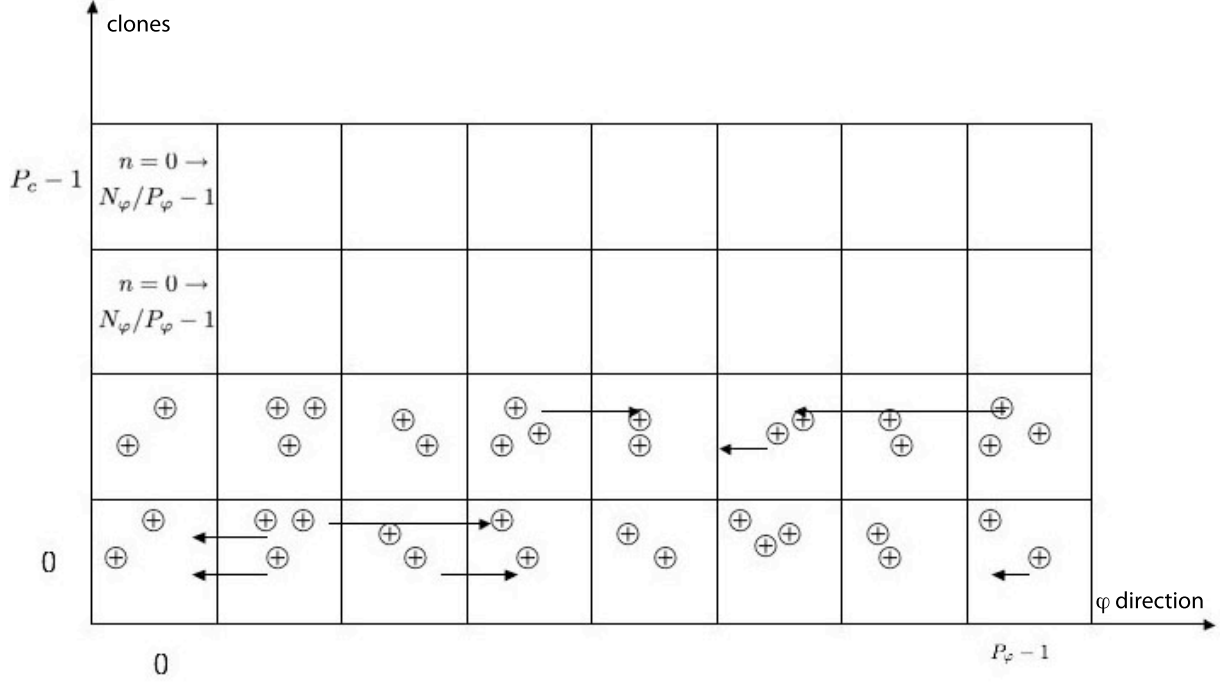


Figure 4.3: ORB5 domain cloning scheme, with markers distributed over the different clones and toroidal domains. Each block is handled by a processor. Figure courtesy of [51]. Here P_φ stands for N_φ .

leads to specific additional issues. The first step is to introduce a grid in the curvilinear straight-field-line coordinate system (s, θ^*, φ) for representing configuration space, considering $(N_s, N_{\theta^*}, N_\varphi)$ grid points respectively in each direction. The finite element method provides a representation of the electrostatic potential ϕ on the mentioned 3D grid as follows:

$$\phi(\mathbf{x}, t) = \sum_{\mu} \phi_{\mu}(t) \Lambda_{\mu}(\mathbf{x}), \quad (4.49)$$

where $\mu = i, j, k$ is a general 3D index corresponding to the three configuration space directions (s, θ^*, φ) respectively. $\{\Lambda_{\mu}(\mathbf{x})\}$ are tensor products of *B-splines* (piecewise continuous polynomials), usually chosen of order 3. In the finite element approach, the quasi-neutrality equation results in a linear system:

$$\sum_{\mu} M_{\nu\mu} \phi_{\mu} = b_{\nu}, \quad (4.50)$$

which results from inserting (4.49) in either one of the forms (3.51), (3.53) or (3.55) of the quasi-neutrality equation and projecting on a test function $\Lambda_{\nu}(\mathbf{x})$. While the matrix $M_{\nu\mu}$ is built once during the initialization phase of the simulation, the electric charge carried by the markers needs to be assigned at each time step to the different grid points in the vicinity of the current positions of the markers, in order to build the vector b_{ν} , the Right-Hand-Side of Eq. (4.50). This operation is called the charge assignment and is carried out naturally in the finite element approach through the projection procedure. Note that the charge density is summed over the clones for each toroidal grid point, as already mentioned. The charge density

is then Fourier-transformed in the toroidal and poloidal directions. A first filter is applied to the toroidal Fourier modes n , retaining one particular toroidal mode for linear simulations, a given range of toroidal modes for turbulence simulations, and only the axisymmetric toroidal mode $n = 0$ (or no mode at all) for pure neoclassical studies. As explained in Sec. 4.8 and with the purpose of reducing the numerical noise, a second filter is applied to the poloidal modes, retaining the modes m which are such that

$$|nq_s(\Psi) - m| \leq \Delta m \quad (4.51)$$

for each retained toroidal mode n . $q_s(\Psi)$ is here the safety factor profile and Δm is an input parameter, typically chosen as $\Delta m = 5$. The same toroidal and poloidal Fourier transforms are applied to the matrix $M_{\nu\mu}$, as well as the same filtering procedure, leading to a field solver in Fourier space for the poloidal and toroidal directions but remaining in direct space in the radial direction [48]. Note that, as a result of the linearization of the quasi-neutrality equation and the axisymmetry of the unperturbed system, different n modes are decoupled when solving for ϕ . Due to the toroidal dependence of the applied poloidal filter [see Eq. (4.51)], N_φ/N_D different transformed and filtered matrices are built in the beginning of the simulation. Solving the Fourier-transformed linear system gives the electrostatic potential in the toroidal-poloidal Fourier space. An inverse Fourier transform is then applied in order to get the solution ϕ_μ in the real configuration space. The boundary conditions are $\phi(s = 1) = 0$, as well as an imposed unicity on magnetic axis: $\phi(s = 0, \theta^*) = \phi(s = 0) \forall \theta^*$. Note that the toroidal-poloidal Fourier transform implies heavy data transpose according to the chosen parallelization scheme, which has an important cost in terms of the computer time required for one time loop. The Fourier transform in the toroidal direction indeed implies that a given processor needs to have access to the whole toroidal domain data set, which is naturally not the case if the data are not transposed, according to the parallelization scheme in the toroidal direction. The size of data which need to be transposed scales with $\sim \rho^{*-3}$ and can thus be responsible for a significant fraction of the simulation time for large plasmas. More importantly, the data transpose operations degrade the parallel scalability of the code, i.e. how well the computation performance scales with the number of processors allocated to a given simulation.

The main limitation of the ORB5 solver is the expansion of the polarization drift term in terms of $k_\perp \rho_{Li}$ (long wavelength approximation), as mentioned in Chapter 3. This expansion provides a solver which is valid only for $k_\perp \rho_{Li} < 1$.

The gyroaveraged electric field $\nabla \langle \phi \rangle$ involved in Hahm's equations (3.22) and (3.23) is computed as:

$$\nabla \langle \phi \rangle \simeq \langle \nabla \phi \rangle = \left\langle \sum_\mu \phi_\mu(t) \nabla \Lambda_\mu(\mathbf{x}) \right\rangle = \sum_\mu \phi_\mu(t) \langle \nabla \Lambda_\mu(\mathbf{x}) \rangle, \quad (4.52)$$

where the gyroaverage $\langle \rangle$ is taken over a Larmor ring discretized with a finite number of points, between 4 and 32. This gyroaveraging procedure in fact also appears in the charge assignment through the gyrodensity $\overline{\delta n}$. In ORB5, the Larmor motion is assumed to lie in the poloidal plane. Note that the approximation $\nabla \langle \phi \rangle \simeq \langle \nabla \phi \rangle$ actually drops a term $\sim \mathcal{O}(\rho_{Li}^2 \nabla B / aB) \ll 1$.

4.7 Initial conditions: Loading the markers and the weights

In ORB5 simulations, the initial distribution of each species is either chosen as the Maxwellian background, local or canonical, $[f(t=0) = f_M]$ or a perturbed Maxwellian $[f(t=0) = f_M + \delta f]$. The initial distribution of the N markers is always chosen uniform over configuration space and either uniform in the half-plane ($v_{\parallel}, v_{\perp} > 0$) with constraint $\sqrt{v_{\parallel}^2 + v_{\perp}^2} \leq k_v v_{th}(s)$:

$$g(s, \theta^*, \varphi, v_{\parallel}, v_{\perp}, t=0) = \frac{NB}{B_{\parallel}^* v_{\perp} [\pi k_v v_{th}(s)]^2 \int J_{s'\theta^*\varphi'} ds' d\theta^* d\varphi'}, \quad (4.53)$$

or uniform in a velocity sphere of radius $k_v v_{th}(s)$:

$$g(s, \theta^*, \varphi, v_{\parallel}, v_{\perp}, t=0) = \frac{NB}{B_{\parallel}^* [4\pi k_v^3 v_{th}^3(s)/3] \int J_{s'\theta^*\varphi'} ds' d\theta^* d\varphi'}, \quad (4.54)$$

where $k_v = 5$ is a constant introducing artificial borders in the velocity space for numerical purposes, $k_v = \infty$ being not feasible. Results are checked to be converged with $k_v = 5$, a mostly Maxwellian distribution satisfying $f_M(5v_{th}) \sim \exp(-(5v_{th})^2) \rightarrow 0$. The factor B/B_{\parallel}^* in Eqs. (4.53) and (4.54) comes from the gyrokinetic phase space Jacobian $d^6z = (B_{\parallel}^*/m) d^3R dv_{\parallel} d\mu d\alpha$. For a marker r initially at position z_{r0} in phase space, the weights are initialized as follows:

$$w_r(t=0) = \frac{[f(t=0) - f_0]_{z_{r0}}}{g(t=0)|_{z_{r0}}}, \quad (4.55)$$

$$p_r(t=0) = \frac{f_0|_{z_{r0}}}{g(t=0)|_{z_{r0}}}. \quad (4.56)$$

4.8 Controlling the numerical noise: Fourier-filtering, Krook operator and coarse-graining procedure

Due to the PIC representation considered in ORB5, a major impediment to obtaining physically relevant results is the problem of numerical noise. Noise is diagnosed in ORB5 by examining the charge density in non-resonant turbulent modes, which are very strongly Landau damped, and essentially arise due to sampling errors [51]. In order to define a signal-to-noise ratio, the following definitions are introduced: The signal is defined by the modes of the charge density inside a certain Fourier filter \mathcal{F} , while the noise is defined by the modes outside the Fourier filter:

$$\text{signal} = \frac{\int_0^a dr \sum_{(n,m) \in \mathcal{F}} |\delta n^{(n,m)}(r)|^2 / a}{\sum_{(n,m) \in \mathcal{F}}}, \quad \text{noise} = \frac{\int_0^a dr \sum_{(n,m) \notin \mathcal{F}} |\delta n^{(n,m)}(r)|^2 / a}{\sum_{(n,m) \notin \mathcal{F}}}. \quad (4.57)$$

Invoking the fact that microturbulence is essentially aligned along the magnetic field line, the filter \mathcal{F} retains Fourier modes (n, m) which, at a given radial position Ψ , satisfy the condition given by Eq. (4.51). Let us point out that the Fourier modes are computed using a straight-field-line poloidal angle. The Fourier components outside the filter \mathcal{F} are removed from the density fluctuations before computing the electrostatic field. This is the basic noise-control procedure.

If the noise becomes large compared to the physical signal, the simulations become irrelevant and are not further carried out. One must thus ensure that noise is kept as low as possible and under control. Noise control is especially crucial for simulations with collisions, which increase the noise due to the random kicks used for representing the diffusive part of the operators. Collisions indeed lead to weight spreading, in fact adding two additional dimensions w and p to the extended numerical phase space and thus requiring a new interpretation of the weights [78], as already discussed in Sec. 4.4.3. ORB5 was already equipped with a noise-reduction scheme which consists of an artificial decay of the weights through the so-called Krook operator $S_k = -\gamma_k \delta f + S_{\text{corr}}$, added to the Right-Hand-Side of Eq. (3.34). γ_k is the Krook decay rate, typically much smaller than the maximum linear growth rate of the considered instability. In ORB5, S_{corr} is designed in order for S_k to preserve the density, the energy, the parallel velocity and the zonal flows [49]. Unfortunately this method is not practical in a collisional simulation, since the required decay rate is at least of the same order as the typical collision frequency, thus masking the physical effects of collisions. ORB5 therefore also features a newly implemented noise-control scheme, appropriate for both collisionless and collisional simulations and based on the coarse-graining procedure proposed in Refs. [20] and [22]. The method involves a periodic binning of markers in phase space and a reassignment of each weight to the average weight value of all markers within the bin. This approach ensures a significant weight spreading reduction. The purpose of the coarse-graining is to reduce the numerical noise, by filtering the high- k modes both in configuration and velocity space in case of a collisionless run and/or by reducing the weight spreading in case of a collisional run [20]. The aim of this procedure is to enable to maintain the signal/noise ratio at a higher level than simulations without coarse-graining, while retaining the key physics from the simulation. At a given time step, the coarse graining procedure involves 1) the binning of the markers in the whole gyrokinetic phase space, i.e. a 5D binning, and 2) the smoothing of the marker weights within a same bin, achieved through the assignment of the marker weights to their average value.

4.8.1 Coarse-graining: 1) binning

Let us describe the critical choice of the bin sizes and number of marker particles. In every direction of phase space, coarse-graining in fact damps any fluctuation scale which is of the order or below the corresponding bin size. This damping, being unphysical, must therefore apply to scales which do not contribute significantly to turbulent transport. This constraint thus fixes an upper limit on the size of bins. A practical choice for an appropriate coordinate system and grid resolution for defining the bins is provided by the meshes used in Eulerian-based gyrokinetic codes [10]. However, for the coarse-graining to be effective, one must ensure that every marker meets sufficiently often at least one other marker in a same bin at the same

time step. This constraint in turn sets a lower limit on the number of required markers for a given number of bins. In other words, the binning must not be too large in order not to damp physically relevant scales and must not be too dense to be efficient. One must emphasize however that coarse-graining does not need to be applied to each marker at each time step. Such a constraint would naturally compromise any advantage of a PIC method versus a Eulerian approach. Practice has shown that, on average, markers need only to undergo an effective coarse-graining procedure (i.e. meet at least one other marker in the same bin) every n -th time step for this noise-control method to be efficient, where typically $n \sim 10$ for ITG simulations. As a result, the required ratio of marker number to bin number must be (at least) of order $1/n \sim 1/10$.

Let us define the normalized kinetic energy $E = v^2/2T(s)$ and the pitch angle $\xi = v_{||}/v$. Note that the energy dimension depends on the radial coordinate through the temperature profile $T(s)$. A uniform grid in θ^* is first built, leading to n_{θ^*} bins. Let us write $\theta_0^*(\theta^*)$ the function giving the position of the bin center θ_0^* corresponding to θ^* :

$$\theta_0^*(\theta^*) = \left[\text{FLOOR} \left(\frac{\theta^* + \pi}{\Delta\theta^*} \right) + \frac{1}{2} \right] \Delta\theta^* - \pi, \quad (4.58)$$

where $\theta^* \in [-\pi; \pi[$ and $\Delta\theta^* = 2\pi/n_{\theta^*}$ is the width of the bins along θ^* . $\text{FLOOR}(x)$ stands for the largest integer which is smaller or equal to x . We define a new field-aligned coordinate z :

$$z = \varphi - q_s(s)[\theta^* - \theta_0^*(\theta^*)]. \quad (4.59)$$

where q_s is the safety factor and $s = \sqrt{\Psi/\Psi_{\text{edge}}}$ the normalized radial coordinate. Note that this field-aligned coordinate enables to use the largest possible bins in the θ^* direction, which now parametrizes the position along the magnetic field line. Indeed in the coordinates (s, θ^*, z) the dependence with respect to θ^* of a field-aligned fluctuation quantity (such as resulting from microturbulence) represents the slowly varying envelope along the magnetic field line. The fast phase variation transverse to the magnetic field is represented by both s and z . The binning is then defined as a block-structured cartesian grid in the new set of variables (s, θ^*, z, E, ξ) . The number of bins in the θ^* direction is proportional to the radial coordinate s ($s\Delta\theta^* \sim \text{const.}$) in order to have bins of approximately the same volume, including near the magnetic axis, which is the center of the polar-like coordinates (s, θ^*) . Figure 4.4 shows how the binning follows the field lines in the (θ^*, φ) plane, as well as the bin structure in the (θ^*, z) plane and in the (θ^*, s) plane. Note that, unless otherwise specified, the grid resolution for the coarse-graining binning in velocity space is $n_E \times n_\xi = 64 \times 64$.

4.8.2 Coarse-graining: 2) smoothing

Let us write α the general index identifying a 5D bin. Considering the bin α , we define the averaged w -weight and p -weight for the markers with index r present in the bin α at a given

time t :

$$\bar{w}_\alpha(t) = \frac{1}{N_\alpha(t)} \sum_{r \in \alpha} w_r(t), \quad (4.60)$$

$$\bar{p}_\alpha(t) = \frac{1}{N_\alpha(t)} \sum_{r \in \alpha} p_r(t), \quad (4.61)$$

where $N_\alpha(t)$ is the number of markers in the bin α at time t . Let us consider a marker r in a bin α , with weights $w_r(t)$ and $p_r(t)$. Introducing the relaxation rates γ_w and γ_p , the modification brought to both weights of the marker r after a coarse-graining procedure is:

$$\Delta w_r = \mathcal{N} \Delta t \cdot \gamma_w \cdot (\bar{w}_\alpha - w_r), \quad (4.62)$$

$$\Delta p_r = \mathcal{N} \Delta t \cdot \gamma_p \cdot (\bar{p}_\alpha - p_r), \quad (4.63)$$

where \mathcal{N} is the number of time steps of length Δt between which each coarse-graining is performed. The typical parameters for the ITG simulations considering $\rho^* = 1/180$ and $\Delta t = 0.22[a/c_s]$ are $\mathcal{N} = 10$, $\gamma_w = 0.45[c_s/a]$ and $\gamma_p = 0.045[c_s/a]$, determined empirically. The latter parameters turn out to be inappropriate for TEM turbulence which requires the coarse-graining to be applied more frequently, at each time step actually, in order to control efficiently the numerical noise ($\mathcal{N} = 1$, $\gamma_w \Delta t = 1$). The coarse-graining on the p -weights appears not to be crucial regarding the simulation behaviour, $\gamma_p = 0$ is thus chosen for TEM turbulence simulations. Note that, as mentioned, the chosen values are specific to given physical quantities, like the growth rate of the instability or the collisionality, and are not universal. The only mandatory requirement is $\mathcal{N} \Delta t \cdot \gamma \leq 1$, where $\gamma = \max(\gamma_w, \gamma_p)$. A full relaxation of all weights in a bin to the averaged weight value corresponds to $\mathcal{N} \Delta t \cdot \gamma_w = \mathcal{N} \Delta t \cdot \gamma_p = 1$. The effects of the coarse-graining on ITG turbulence, as well as a proper choice of the bin size, are studied in Chapter 7 (Sec. 7.6). The issue of coarse-graining in TEM turbulence simulations is addressed in Chapter 8.

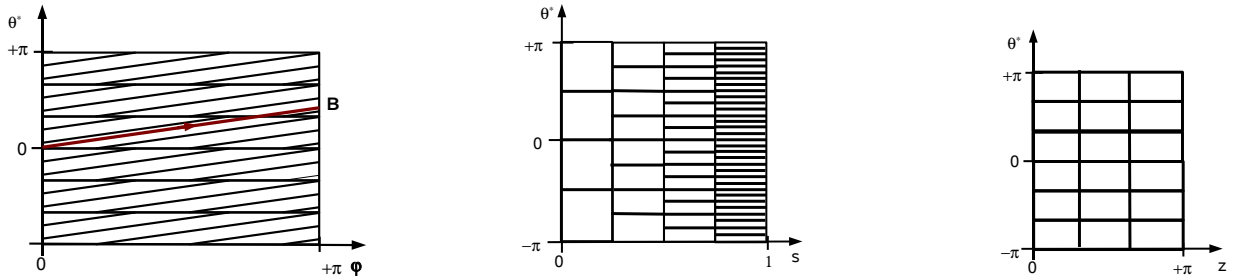


Figure 4.4: Field-aligned binning in configuration space represented respectively in the (θ^*, φ) plane, the (θ^*, s) plane and the (θ^*, z) plane.

4.9 Numerical parameters

This Section describes the important numerical parameters used in ORB5 in order to carry out relevant and converged simulations. Most of the crucial numerical parameters actually depend on the ρ^* value, i.e. the sound Larmor radius normalized to the considered plasma minor radius. Detailed ORB5 convergence tests, both in ITG and TEM regime, have already been performed in Refs. [51] and [37].

4.9.1 Number of markers

The number of markers, i.e. the accuracy of the distribution sampling, is crucial in order to obtain relevant results. The important quantity for estimating the relevance of microinstability simulations is the ratio between the number of markers N and the number of essential Fourier modes for representing the fluctuations (i.e. modes kept in filter \mathcal{F} in Eq. (4.57) [79]). For collisionless linear runs considering one single toroidal Fourier mode, $N \sim 10^6 - 2 \cdot 10^6$ for each species provides converged results for CYCLONE- ρ^* values. Non-linear runs addressing the issue of turbulence are naturally much more demanding and require $N \sim 100 \cdot 10^6 - 200 \cdot 10^6$ for each species in a collisionless case considering the CYCLONE- ρ^* values. The increased numerical noise due to the numerical treatment of collisions in the frame of a PIC code requires 2 or 3 times more markers for a collisional species. Finally, note that a global neoclassical simulation, even in absence of electric field, requires a substantial amount of markers, typically $N = 50 \cdot 10^6 - 100 \cdot 10^6$ for a standard $\rho^* = 1/150$, in order to provide converged and accurately resolved neoclassical fluxes. This is particularly true for quantities related to off-diagonal terms of transport matrix such as bootstrap current.

4.9.2 Time step

The chosen time step has to resolve the shortest characteristic time of the considered system: $\omega_{\max} \Delta t \ll 1$, where ω_{\max} is the largest characteristic frequency of the system which may be given by the mode frequency ω , the transit frequency ω_t , the parallel frequency $\omega_{\parallel} = k_{\parallel} v_{\parallel}$ or the perpendicular frequency $\omega_{\perp} = k_{\perp} v_{E \times B}$ of a given species. The bounce frequency ω_b of a given species may provide the shortest time as well, in the frame of a trapped kinetic response model such as the hybrid model for electrons in ORB5. For ITG simulations involving adiabatic electrons, the time step is typically $\omega_{ti} \Delta t_{\text{ITG}} \sim 0.03$. The suppression of the term $d\Psi/dt|_0 \partial f_{LM} / \partial \Psi$ in the gyrokinetic equation or the use of a canonical Maxwellian f_{CM} as the ion background distribution f_{i0} allows to increase the time step by a factor ~ 2 . Indeed, accounting for the term $d\Psi/dt|_0 \partial f_{LM} / \partial \Psi$ in a simulation starting from a local Maxwellian background drives spurious zonal flow oscillations in the initial phase of the simulation [80], thus providing a limiting factor for the time step through the $\mathbf{v}_{E \times B}$ drift velocity. Including fully kinetic electrons would bring a correction $\Delta t_{\text{TEM}} \simeq \sqrt{m_e/m_i} \Delta t_{\text{ITG}}$, while the hybrid model allows the time step to be larger, $\Delta t_{\text{TEM}} \simeq \sqrt{m_e/m_i} \Delta t_{\text{ITG}} / \sqrt{\epsilon}$, due to the ratio between the bounce frequency and the transit frequency $\omega_{be}/\omega_{te} \simeq \sqrt{\epsilon}$. In case of electrostatic simulations with fully kinetic electrons, the limiting factor regarding the time step is the frequency of

electrostatic shear Alfvén waves ω_H , given by:

$$\omega_H = \frac{k_{||}}{k_{\perp}} \sqrt{\frac{m_i}{m_e}} \Omega_i. \quad (4.64)$$

Namely, the time step Δt has to satisfy $\omega_H \Delta t \lesssim 1$ [81]. Another requirement related to the time step in collisional simulations is naturally $\nu \Delta t \ll 1$, where ν is the collision frequency. For reasonable collisionalities, i.e. not too far from the physical collisionality of the considered tokamak plasma, this latter requirement is always satisfied.

4.9.3 Configuration space grid

The resolution of the configuration space grid used for solving the field equations depends naturally on the shortest wavelengths which have to be represented. The shortest wavelength of the simulation system is actually determined by a maximum toroidal wavenumber $n_{\max} \sim k_{\perp, \max}$. Considering *B-splines* of order 3, it has been found that 3 points per wavelength are usually required for an accurate resolution (although the Nyquist limit would be 2 points only), such that [51]:

$$N_s \geq \frac{3}{2\pi} k_{\perp, \max} \rho_s \cdot \rho^{*-1}, \quad (4.65)$$

$$N_{\theta^*} \geq 3 k_{\perp, \max} \rho_s \cdot \rho^{*-1}, \quad (4.66)$$

$$N_{\varphi} \simeq N_{\theta^*} / q_s(r), \quad (4.67)$$

where q_s is the safety factor and Eq. (4.67) results from fluctuations being aligned along the magnetic field line. Note that the number of grid points scales with $\sim \rho^{*-3}$. The latter estimates combined with $k_{\perp, \max} \rho_{Li} \simeq 0.9$ (due to the long-wavelength approximation assumed by the solver) leads to $N_s \times N_{\theta^*} \times N_{\varphi} = 128 \times 512 \times 256$ for $\rho^* = 1/180$ and $N_s \times N_{\theta^*} \times N_{\varphi} = 64 \times 256 \times 128$ for $\rho^* = 1/80$. Note that a wedge option can be used in ORB5, allowing to retain only every n_{ft} -th Fourier modes in the filter and thus reducing the noise. But n_{ft} should not be too large, in order to preserve the non-linear coupling between the different toroidal modes. For typical CYCLONE- ρ^* values, $n_{ft} = 4$ is still acceptable.

Chapter 5

Linearized collision operators for a δf Particle-In-Cell code

5.1 Introduction

In the gyrokinetic model, different plasma species are coupled through the self-consistent electromagnetic mean fields related to collective phenomena, as well as through binary interactions (collisions). A general total collision operator for a given species a is composed of the sum of contributions related to collisional interactions with all other species b :

$$C[f_a] = \sum_b C_{ab}[f_b, f_a], \quad (5.1)$$

Each term C_{ab} is a non-linear operator with respect to $\{f_a, f_b\}$ as will be shown in Eq. (5.10). In fact $C_{ab}[f_b, f_a]$ is bi-linear with respect to $\{f_a, f_b\}$. Invoking bi-linearity, each term C_{ab} is decomposed as follows:

$$C_{ab}[f_b, f_a] = C_{ab}[f_{b,LM}, f_{a,LM}] + C_{ab}[f_{b,LM}, \delta f_a] + C_{ab}[\delta f_b, f_{a,LM}] + C_{ab}[\delta f_b, \delta f_a]. \quad (5.2)$$

In practice, a full non-linear collision operator is very demanding and complicated from a numerical point of view. The operators discretized in ORB5 are thus linearized, i.e. neglecting all the terms of the form $C_{ab}[\delta f_b, \delta f_a]$. Moreover, ORB5 was originally a code for a single ion species, and the collision operators have been developed and implemented accordingly. This Chapter presents the discretization of the linearized self-collision operator, used for ion-ion and electron-electron collisions, along with the treatment of the electron-ion collisions. Ion-electron collisions are neglected in ORB5, due to their small frequency $\nu_{ie}/\nu_{ii} \sim \sqrt{m_e/m_i} \ll 1 \ll \nu_{ei}/\nu_{ii} \sim \sqrt{m_i/m_e}$. Note that the finite Larmor-Radius-Effects (FLR) resulting from the change of variables from particle to gyrocenter variables, otherwise retained in the collisionless gyrokinetic turbulent dynamics, have been neglected in the standard ORB5 version for implementing the collision operators [82], [83]. Nonetheless, an attempt to estimate the effects of FLR corrections to collision operators in a PIC code, never used in practice, is presented in Sec. 5.12. The drift-kinetic approximation for collision operators is justified if the perpendicular wavelength of the electrostatic perturbation is larger than the

Larmor radius. This should be well satisfied for all species in the frame of neoclassical transport studies. This assumption should also hold for collisional damping of zonal flows as well as for collisional trapping/detrapping of electrons in the TEM turbulent regime.

5.2 Phenomenology of Coulomb collisions

Two charged particles are considered, with mass m_1 and m_2 and charge q_1 et q_2 respectively. \mathbf{r} stands for the relative position vector and $\mathbf{v} = d\mathbf{r}/dt$ is initially along the axis x (see Figure 5.1). The impact parameter b , the angle α and the deflection angle θ are defined in Figure 5.1. The reduced mass of the system $\mu = m_1 m_2 / (m_1 + m_2)$ is introduced. The relative equation of motion reads:

$$\mu \frac{d\mathbf{v}}{dt} = \frac{q_1 q_2}{4\pi\epsilon_0 r^3} \mathbf{r}. \quad (5.3)$$

The angular momentum conservation takes the following form:

$$vb = r^2 \dot{\alpha} \implies \frac{1}{r^2} = \frac{\dot{\alpha}}{vb}. \quad (5.4)$$

Using Eqs. (5.3) and (5.4), the relative velocity gain along the axis y can be written as:

$$\Delta v_y = \frac{q_1 q_2}{|q_1 q_2|} v \sin \theta = \int \frac{q_1 q_2}{\mu 4\pi\epsilon_0 r^2} \sin \alpha dt = \frac{q_1 q_2}{\mu 4\pi\epsilon_0 vb} \int_0^{\pi-\theta} \sin \alpha d\alpha = \frac{q_1 q_2}{\mu 4\pi\epsilon_0 vb} (1 + \cos \theta), \quad (5.5)$$

or equivalently:

$$\tan \frac{\theta}{2} = \frac{|q_1 q_2|}{4\pi\epsilon_0 \mu v^2 b} = \frac{b_0}{b}, \quad (5.6)$$

where $b_0 = |q_1 q_2| / 4\pi\epsilon_0 \mu v^2$ stands for the impact parameter producing a deflection with an angle of 90° . A relation is thus obtained between the impact parameter and the deflection angle. Note that the deflection angle is related to the center of mass frame. If the target is much heavier than the impact particle, then $\theta \simeq \theta_L$, where θ_L is the deflection angle in the laboratory frame.

5.3 Suitable expression for collision operators

The collisions of a species a on a species b are described in principle by the full Landau operator [84], which accounts for the binary interaction between the charged particles through the electrostatic Coulomb fields they generate. In a compact and symmetric form, the Landau operator reads:

$$C_{ab}[f_b, f_a] = -\frac{q_a^2 q_b^2 \ln \Lambda}{8\pi\epsilon_0^2 m_a} \frac{\partial}{\partial \mathbf{v}_a} \cdot \int \underline{U}(\mathbf{u}) \cdot \left(\frac{f_b}{m_a} \frac{\partial f_a}{\partial \mathbf{v}_a} - \frac{f_a}{m_b} \frac{\partial f_b}{\partial \mathbf{v}_b} \right) d^3 v_b, \quad (5.7)$$

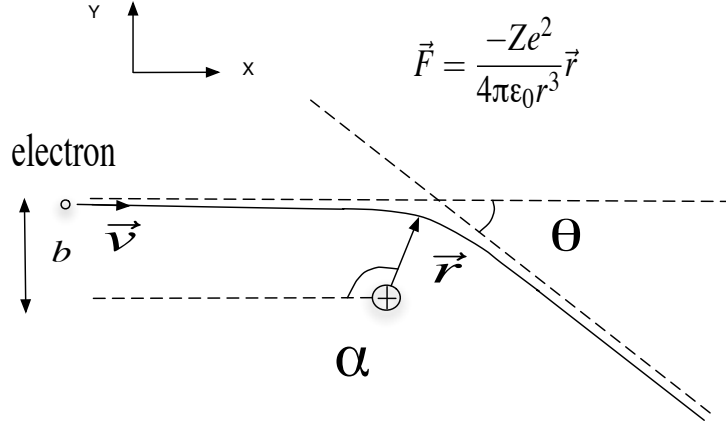


Figure 5.1: Example of a Coulomb collision, here an electron-ion collision.

where ϵ_0 is the permittivity of free space and $\ln \Lambda$ is the Coulomb logarithm, which is the integral over the inverse of the collision impact parameter b :

$$\ln \Lambda = \int_{b_0}^{\lambda_D} \frac{db}{b}. \quad (5.8)$$

$\mathbf{u} = \mathbf{v}_a - \mathbf{v}_b$ is the collision relative velocity and \underline{U} is a tensor defined as follows:

$$\underline{U}(\mathbf{u}) = \frac{1}{u}(\mathbb{I} - \hat{u}\hat{u}), \quad (5.9)$$

where $\hat{u} = \mathbf{u}/u$. The explicit drag and diffusion form of the Landau operator is:

$$\begin{aligned} C_{ab}[f_b, f_a] &= \frac{\partial}{\partial \mathbf{v}_a} \cdot \left[\mathbf{\Gamma}_{ab} f_a - \frac{\partial}{\partial \mathbf{v}_a} \cdot (\underline{D}_{ab} f_a) \right] \\ &= \frac{q_a^2 q_b^2 \ln \Lambda}{8\pi \epsilon_0^2 m_a} \left[\frac{\partial}{\partial \mathbf{v}_a} \cdot \frac{f_a}{\mu_{ab}} \int \underline{U}(\mathbf{u}) \cdot \frac{\partial f_b}{\partial \mathbf{v}_b} d^3 v_b - \frac{\partial}{\partial \mathbf{v}_a} \cdot \frac{f_a}{m_a} \int \underline{U}(\mathbf{u}) f_b d^3 v_b \right], \end{aligned} \quad (5.10)$$

where $\mu_{ab} = m_a m_b / (m_a + m_b)$ is the reduced mass. The drag vector $\mathbf{\Gamma}_{ab}$ and the diffusion tensor \underline{D}_{ab} are identified in Eq. (5.10):

$$\mathbf{\Gamma}_{ab} = \frac{q_a^2 q_b^2 \ln \Lambda}{8\pi \epsilon_0^2 m_a \mu_{ab}} \int \underline{U}(\mathbf{u}) \cdot \frac{\partial f_b}{\partial \mathbf{v}_b} d^3 v_b, \quad (5.11)$$

$$\underline{D}_{ab} = \frac{q_a^2 q_b^2 \ln \Lambda}{8\pi \epsilon_0^2 m_a^2} \int \underline{U}(\mathbf{u}) f_b d^3 v_b. \quad (5.12)$$

Noting that:

$$\frac{\partial}{\partial \mathbf{v}_b} \cdot \underline{U}(\mathbf{u}) = -\frac{\partial}{\partial \mathbf{u}} \cdot \underline{U}(\mathbf{u}) = 2 \frac{\mathbf{u}}{u^3}, \quad (5.13)$$

the drag vector can be further simplified by integrating by parts:

$$\begin{aligned}\Gamma_{ab} &= \frac{q_a^2 q_b^2 \ln \Lambda}{8\pi\epsilon_0^2 m_a \mu_{ab}} \int \underline{U}(\mathbf{u}) \cdot \frac{\partial f_b}{\partial \mathbf{v}_b} d^3 v_b = -\frac{q_a^2 q_b^2 \ln \Lambda}{8\pi\epsilon_0^2 m_a \mu_{ab}} \int f_b \frac{\partial \underline{U}}{\partial \mathbf{v}_b} d^3 v_b \\ &= -\frac{q_a^2 q_b^2 \ln \Lambda}{4\pi\epsilon_0^2 m_a \mu_{ab}} \int f_b \frac{\mathbf{u}}{u^3} d^3 v_b.\end{aligned}\quad (5.14)$$

The following Rosenbluth potentials are introduced:

$$h_b(\mathbf{v}_a) = \int f_b \frac{1}{u} d^3 v_b, \quad (5.15)$$

$$g_b(\mathbf{v}_a) = \int f_b u d^3 v_b. \quad (5.16)$$

Since $\partial h_b / \partial \mathbf{v}_a = \partial h_b / \partial \mathbf{u} = -\int (\mathbf{u} f_b / u^3) d^3 v_b$ and $\partial^2 g_b / \partial \mathbf{v}_a \partial \mathbf{v}_a = \int (\partial^2 u / \partial \mathbf{v}_a \partial \mathbf{v}_a) f_b d^3 v_b = \int (\partial^2 u / \partial \mathbf{u} \partial \mathbf{u}) f_b d^3 v_b = \int \underline{U}(\mathbf{u}) f_b d^3 v_b$, the drag vector and the diffusion tensor are rewritten using the Rosenbluth potentials:

$$\Gamma_{ab} = \frac{q_a^2 q_b^2 \ln \Lambda}{4\pi\epsilon_0^2 m_a \mu_{ab}} \frac{\partial h_b}{\partial \mathbf{v}_a}, \quad (5.17)$$

$$\underline{D}_{ab} = \frac{q_a^2 q_b^2 \ln \Lambda}{8\pi\epsilon_0^2 m_a^2} \frac{\partial^2 g_b}{\partial \mathbf{v}_a \partial \mathbf{v}_a}. \quad (5.18)$$

5.4 Collisions on a Maxwellian background and linearization

The case where f_b is a local Maxwellian $f_{b,LM}$ is considered first. The distribution f_a is decomposed into a Maxwellian background $f_{a,LM}$ and a perturbed part δf_a :

$$C_{ab,LM}[f_{b,LM}, f_a] = C_{ab,LM}[f_{b,LM}, f_{a,LM}] + C_{ab,LM}[f_{b,LM}, \delta f_a]. \quad (5.19)$$

The collisions of the Maxwellian $f_{a,LM}$ on the Maxwellian $f_{b,LM}$ are computed from Eq. (5.7):

$$C_{ab,LM}[f_{b,LM}, f_{a,LM}] = \frac{q_a^2 q_b^2 \ln \Lambda}{8\pi\epsilon_0^2 m_a} \frac{\partial}{\partial \mathbf{v}_a} \cdot f_{a,LM} \int \underline{U}(\mathbf{u}) \cdot \left(\frac{\mathbf{v}_a}{T_a} - \frac{\mathbf{v}_b}{T_b} \right) f_{b,LM} d^3 v_b. \quad (5.20)$$

It implies that $C_{ab,LM}[f_{b,LM}, f_{a,LM}] = 0$ if $T_a = T_b$, since $\underline{U}(\mathbf{u}) \cdot \mathbf{u} = \mathbf{0}$. The hypothesis $T_a = T_b$ is clearly satisfied for self-collisions. For electron-ion collisions, we assume $v_e \gg v_i$ (the so-called Lorentz approximation), which leads to $\underline{U}(\mathbf{u}) \cdot (\mathbf{v}_e / T_e - \mathbf{v}_i / T_i) \simeq \underline{U}(\mathbf{v}_e) \cdot \mathbf{v}_e / T_e = \mathbf{0}$, and as a consequence to $C_{ei}[f_{i,LM}, f_{e,LM}] \simeq 0$ according to Eq. (5.20), even if $T_e \neq T_i$. In other words, the thermalization process between electrons and ions is neglected in the Lorentz approximation.

The Rosenbluth potentials $h_{b,LM}$ and $g_{b,LM}$, associated to the Maxwellian distribution $f_{b,LM}$

and given respectively by Eqs. (5.15) and (5.16), may be computed analytically:

$$h_{b,LM}(\mathbf{v}_a) = \frac{n_b}{(2\pi)^{3/2}v_{thb}^3} \int \frac{e^{-v_b^2/2v_{thb}^2}}{|\mathbf{v}_a - \mathbf{v}_b|} d^3v_b = \frac{n_b}{v_a} \operatorname{erf}\left(\frac{v_a}{\sqrt{2}v_{thb}}\right), \quad (5.21)$$

$$\begin{aligned} g_{b,LM}(\mathbf{v}_a) &= \frac{n_b}{(2\pi)^{3/2}v_{thb}^3} \int |\mathbf{v}_a - \mathbf{v}_b| e^{-v_b^2/2v_{thb}^2} d^3v_b \\ &= \frac{n_b v_{thb}^2}{v_a} \left[\left(1 + \frac{v_a^2}{v_{thb}^2}\right) \operatorname{erf}\left(\frac{v_a}{\sqrt{2}v_{thb}}\right) + \sqrt{\frac{2}{\pi}} \frac{v_a}{v_{thb}} \exp\left(-\frac{v_a^2}{2v_{thb}^2}\right) \right], \end{aligned} \quad (5.22)$$

where $\operatorname{erf}(x) = (2/\sqrt{\pi}) \int_0^x \exp(-t^2) dt$ is the error function. Two dimensionless functions H_b and K_b are introduced [20]:

$$H_b(v_a) = \frac{v_{thb}^3}{v_a^3} \left[\operatorname{erf}(v_a/\sqrt{2}v_{thb}) - \sqrt{\frac{2}{\pi}} \frac{v_a}{v_{thb}} \exp(-v_a^2/2v_{thb}^2) \right], \quad (5.23)$$

$$K_b(v_a) = \frac{v_{thb}^3}{v_a^3} \left[\left(\frac{v_a^2}{v_{thb}^2} - 1\right) \operatorname{erf}(v_a/\sqrt{2}v_{thb}) + \sqrt{\frac{2}{\pi}} \frac{v_a}{v_{thb}} \exp(-v_a^2/2v_{thb}^2) \right]. \quad (5.24)$$

In the special case of collisions on a Maxwellian background, making use of the Maxwellian Rosenbluth potentials (5.21) and (5.22) in the expressions for the drag vector (5.17) and the diffusion tensor (5.18), respectively, leads to:

$$\mathbf{\Gamma}_{ab,LM} = -\frac{\bar{\nu}_{ab}v_{tha}^3}{2v_{thb}^3} \left(1 + \frac{m_a}{m_b}\right) H_b(v_a) \mathbf{v}_a, \quad (5.25)$$

$$\underline{D}_{ab,LM} = \frac{\bar{\nu}_{ab}v_{tha}^3}{4v_{thb}} \left(K_b(v_a) \left[\mathbb{I} - \frac{\mathbf{v}_a \mathbf{v}_a}{v_a^2} \right] + 2H_b(v_a) \frac{\mathbf{v}_a \mathbf{v}_a}{v_a^2} \right), \quad (5.26)$$

where the thermal collision frequency $\bar{\nu}_{ab}$ has been identified:

$$\bar{\nu}_{ab} = \frac{n_b q_a^2 q_b^2 \ln \Lambda}{2\pi \epsilon_0^2 m_a^2 v_{tha}^3}. \quad (5.27)$$

The collisions of a species a on the Maxwellian background of a species b are finally written as:

$$C_{ab,LM}[f_{b,LM}, \delta f_a] = \frac{\partial}{\partial \mathbf{v}_a} \cdot \left[\mathbf{\Gamma}_{ab,LM} \delta f_a - \frac{\partial}{\partial \mathbf{v}_a} \cdot \underline{D}_{ab,LM} \delta f_a \right], \quad (5.28)$$

where $\mathbf{\Gamma}_{ab,LM}$ and $\underline{D}_{ab,LM}$ are given by Eqs. (5.25) and (5.26) respectively. The spherical coordinates in velocity space (v, θ, α) are introduced. We note that:

$$\frac{\partial}{\partial \mathbf{v}} \cdot \left[\mathbb{I} - \frac{\mathbf{v} \mathbf{v}}{v^2} \right] \cdot \frac{\partial}{\partial \mathbf{v}} = \frac{1}{v^2} \left[\frac{1}{\sin \theta} \frac{\partial}{\partial \theta} \left(\sin \theta \frac{\partial}{\partial \theta} \right) + \frac{1}{\sin^2 \theta} \frac{\partial^2}{\partial \alpha^2} \right] := -\frac{1}{v^2} \hat{L}^2, \quad (5.29)$$

where the Lorentz operator \hat{L}^2 has been defined, which shows a clear similarity with respect to the angular momentum operator from quantum mechanics. In Eq. (5.29), θ is a pitch angle variable such that $\cos \theta = v_{\parallel}/v = \xi$. Note that the last term of the Lorentz operator defined by

Eq. (5.29) falls for gyroaveraged distributions. Using the drag vector (5.25) and the diffusion tensor (5.26), the collisions of the perturbed part δf_a on the Maxwellian background $f_{b,LM}$ may be expressed explicitly as the sum of a pitch angle scattering term and a thermalization term:

$$C_{ab,LM}[f_{b,LM}, \delta f_a] = \frac{\bar{\nu}_{ab} v_{tha}^3}{4 v_{thb}^3} \frac{K_b(v_a) v_{thb}^2}{v_a^2} \hat{L}^2 \delta f_a - \frac{\bar{\nu}_{ab} v_{tha}^3}{2 v_a^2 v_{thb}^3} \frac{\partial}{\partial v_a} \left[v_a^4 \frac{H_b(v_a) v_{thb}^2}{v_a^2} f_{a,LM} \frac{\partial}{\partial v_a} \left(\frac{\delta f_a}{f_{a,LM}} \right) \right]. \quad (5.30)$$

Considering now the collisions of $f_{a,LM}$ on a perturbed part δf_b related to the species b , $C_{a,LM,b}[\delta f_b, f_{a,LM}]$ is computed from Eq. (5.7), assuming again $T_a = T_b$:

$$C_{a,LM,b}[\delta f_b, f_{a,LM}] = \frac{q_a^2 q_b^2 \ln \Lambda}{8\pi \epsilon_0^2 m_a m_b} \frac{\partial}{\partial \mathbf{v}_a} \cdot f_{a,LM} \int \underline{U}(\mathbf{u}) \cdot \frac{\partial}{\partial \mathbf{v}_b} \left(\frac{\delta f_b}{f_{b,LM}} \right) f_{b,LM} d^3 v_b, \quad (5.31)$$

which is an integral operator on δf_b . Combining the collisions of the perturbed part δf_a on the background $f_{b,LM}$ [Eq. (5.30)] and the background reaction [Eq. (5.31)] gives the full linearized Landau operator:

$$C_{ab}^{\text{lin}}[f_b, f_a] = \frac{\bar{\nu}_{ab} v_{tha}^3}{4 v_{thb}^3} \frac{K_b(v_a) v_{thb}^2}{v_a^2} \hat{L}^2 \delta f_a - \frac{\bar{\nu}_{ab} v_{tha}^3}{2 v_a^2 v_{thb}^3} \frac{\partial}{\partial v_a} \left[v_a^4 \frac{H_b(v_a) v_{thb}^2}{v_a^2} f_{a,LM} \frac{\partial}{\partial v_a} \left(\frac{\delta f_a}{f_{a,LM}} \right) \right] + \frac{\bar{\nu}_{ab} v_{tha}^3}{4 n_b} \frac{m_a}{m_b} \frac{\partial}{\partial \mathbf{v}_a} \cdot f_{a,LM} \int \underline{U}(\mathbf{u}) \cdot \frac{\partial}{\partial \mathbf{v}_b} \left(\frac{\delta f_b}{f_{b,LM}} \right) f_{b,LM} d^3 v_b. \quad (5.32)$$

The first two terms of the linearized operator (5.32) correspond in fact to collisions of species a on species b in the test-particle operator $C_{TP}[\delta f_a]$, as defined by Eq. (3.32), while the last term of the linearized operator (5.32) is included in the background reaction operator $C_{BR}[f_{a,LM}]$ given by Eq. (3.33). Note that the term $C_{ab}[\delta f_b, \delta f_a]$ is neglected in the operator (5.32) as a result of the linearization process.

5.5 The self-collision operator

In ORB5, the linearized operator (5.32) is used for self-collisions, both for ions ($C_{ii}^{\text{lin}}[f_i, f_i]$) and electrons ($C_{ee}^{\text{lin}}[f_e, f_e]$), satisfying thus automatically the condition $T_a = T_b$. Dropping the index for the considered species (ions or electrons) and defining $\mathbf{v} = v/v_{th}$, the dimensionless functions H and K , following Eqs. (5.23) and (5.24), become:

$$H(\mathbf{v}) = \frac{1}{\sqrt{3}} \left[\text{erf}(\mathbf{v}/\sqrt{2}) - \sqrt{\frac{2}{\pi}} \mathbf{v} e^{-\mathbf{v}^2/2} \right], \quad (5.33)$$

$$K(\mathbf{v}) = \frac{1}{\sqrt{3}} \left[(\mathbf{v}^2 - 1) \text{erf}(\mathbf{v}/\sqrt{2}) + \sqrt{\frac{2}{\pi}} \mathbf{v} e^{-\mathbf{v}^2/2} \right], \quad (5.34)$$

$$G(\mathbf{v}) = (2\mathbf{v}^2 - 1) H(\mathbf{v}) - K(\mathbf{v}), \quad (5.35)$$

having defined the additional function $G(\mathbf{v})$. The drag vector $\mathbf{\Gamma}$ and the diffusion tensor \underline{D} for self-collisions are written as follows [20], according to Eqs. (5.25) and (5.26):

$$\mathbf{\Gamma} = -\bar{\nu}H(\mathbf{v})\mathbf{v}, \quad (5.36)$$

$$\underline{D} = \frac{\bar{\nu}}{4} \frac{v_{th}^2}{v^2} \left(K(\mathbf{v}) \left[\mathbb{I} - \frac{\mathbf{v}\mathbf{v}}{v^2} \right] + 2H(\mathbf{v}) \frac{\mathbf{v}\mathbf{v}}{v^2} \right), \quad (5.37)$$

with \mathbb{I} the identity tensor and

$$\bar{\nu} = \frac{nq^4 \ln \Lambda}{2\pi\epsilon_0^2 m^2 v_{th}^3} \quad (5.38)$$

being the thermal self-collision frequency for the species with mass m , charge q , thermal velocity $v_{th} = \sqrt{T/m}$ and background density n . The linearized self-collision operator \hat{C} thus reads, similarly to the operator (5.32):

$$\hat{C}(f) = C[f_{LM}, \delta f_{LM}] + C[\delta f_{LM}, f_{LM}], \quad (5.39)$$

where $C[f_{LM}, \delta f_{LM}]$ is included in the test-particle operator C_{TP} defined by Eq. (3.32) and $C[\delta f_{LM}, f_{LM}]$ is included in the background reaction operator C_{BR} defined by Eq. (3.33). The operator $C[f_{LM}, \delta f_{LM}]$ is explicitly decomposed into a pitch angle scattering term and a thermalization term:

$$C[f_{LM}, \delta f_{LM}] = \frac{\nu_D(v)}{2} \hat{L}^2 \delta f_{LM} - \frac{1}{v^2} \frac{\partial}{\partial v} \left[\frac{v^4}{2} \nu_{||}(v) f_{LM} \frac{\partial}{\partial v} \left(\frac{\delta f_{LM}}{f_{LM}} \right) \right]. \quad (5.40)$$

having defined $\nu_D(v) = \bar{\nu}K(\mathbf{v})/2v^2$ the pitch angle frequency and $\nu_{||}(v) = \bar{\nu}H(\mathbf{v})/v^2$ the thermalization frequency. Note that the thermalization term in (5.40) may be cast into the sum of a parallel drag term and an energy diffusion term:

$$\begin{aligned} C[f_{LM}, \delta f_{LM}] &= \underbrace{\frac{\nu_D(v)}{2} \hat{L}^2 \delta f_{LM}}_{\text{pitch angle scattering}} - \underbrace{\frac{\bar{\nu}v_{th}^2}{2} \frac{\partial}{\partial \mathbf{v}} \cdot \left[\left(\frac{2H(\mathbf{v})}{v_{th}^2} - \frac{K(\mathbf{v})}{v^2} \right) \delta f_{LM} \mathbf{v} \right]}_{\text{parallel drag}} \\ &\quad - \underbrace{\frac{\bar{\nu}v_{th}^2}{2} \frac{\partial^2}{\partial \mathbf{v} \partial \mathbf{v}} : \left[H(\mathbf{v}) \delta f_{LM} \frac{\mathbf{v}\mathbf{v}}{v^2} \right]}_{\text{energy diffusion}}. \end{aligned} \quad (5.41)$$

The term $C[\delta f_{LM}, f_{LM}]$ in Eq. (5.39) is the background reaction which ensures conservation of mass, momentum and kinetic energy of the linearized self-collision operator. For practical reasons, to avoid having to reconstruct δf_{LM} and taking its velocity derivative at each time step, operations strongly subject to numerical noise in a δf PIC code, one does not implement the exact form of this operator, as derived directly from the Landau operator and being the last term on the RHS of Eq. (5.32), but makes use of an approximate form $C[\delta f_{LM}, f_{LM}] \simeq f_{LM} \mathcal{B}(\delta f_{LM})$ [85], [20]:

$$\frac{C[\delta f_{LM}, f_{LM}]}{f_{LM}} \simeq \mathcal{B}(\delta f_{LM}) = \frac{1}{n(\mathbf{x})} \left\{ 6\sqrt{\pi} H(\mathbf{v}) \frac{\delta \mathcal{P}_{||} v_{||}}{v_{th}^2} + \sqrt{\pi} G(\mathbf{v}) \frac{\delta \mathcal{E}}{v_{th}^2} \right\}, \quad (5.42)$$

where $\delta\mathcal{P}_{||}$ and $\delta\mathcal{E}$ are respectively the changes in the parallel momentum and the kinetic energy of the perturbation distribution due to the operator defined in Eq. (5.40):

$$\delta\mathcal{P}_{||}(\delta f_{LM}, \mathbf{x}) = - \int C[f_{LM}, \delta f_{LM}] v_{||} d^3v, \quad (5.43)$$

$$\delta\mathcal{E}(\delta f_{LM}, \mathbf{x}) = - \int C[f_{LM}, \delta f_{LM}] v^2 d^3v. \quad (5.44)$$

Let us notice that, due to the invariance of the distribution function with respect to the gyroangle, we only need to consider the variation of the parallel component of the velocity in Eq. (5.43). The operator \mathcal{B} , although a physical simplification, nevertheless satisfies the local conservation properties. The functional form of Eq. (5.42) indeed ensures:

$$\int f_{LM} \mathcal{B}(\delta f_{LM}) d^3v = 0, \quad (5.45)$$

$$\int f_{LM} \mathcal{B}(\delta f_{LM}) v_{||} d^3v = \delta\mathcal{P}_{||}(\delta f_{LM}, \mathbf{x}), \quad (5.46)$$

$$\int f_{LM} \mathcal{B}(\delta f_{LM}) v^2 d^3v = \delta\mathcal{E}(\delta f_{LM}, \mathbf{x}). \quad (5.47)$$

The operators $C[f_{LM}, \delta f_{LM}]$ and $f_{LM} \mathcal{B}(\delta f_{LM})$ thus together conserve parallel momentum and kinetic energy and individually conserve mass. One can furthermore show [85], [20] that the operators (5.40) and (5.42) verify properties of self-adjointness and positivity, thus satisfying the H-theorem (increase of entropy through Coulomb collisions) and leading to the fact that a linearized shifted Maxwellian of the form:

$$\delta f_{LM} = f_{LM} \left(c_1 + c_2 \frac{v_{||}}{v_{th}} + c_3 \frac{v^2}{v_{th}^2} \right) \quad (5.48)$$

is annihilated by the total collision operator, i.e. $C[f_{LM}, \delta f_{LM}] + f_{LM} \mathcal{B}(\delta f_{LM}) = 0$, where c_1 , c_2 and c_3 are arbitrary constants.

5.6 The Lorentz approximation

The Lorentz approximation assumes $m_a \ll m_b$ and thus $v_a \gg v_{thb}$. Since:

$$\left(\frac{v_{thb}}{v_a} \right)^5 = \lim_{v_a \gg v_{thb}} \frac{H_b(v_a) v_{thb}^2}{v_a^2} \ll \lim_{v_a \gg v_{thb}} \frac{K_b(v_a) v_{thb}^2}{v_a^2} = \left(\frac{v_{thb}}{v_a} \right)^3, \quad (5.49)$$

the operator (5.30) takes the following simple form in the Lorentz approximation:

$$C_{ab,LM}^{\text{Lorentz}}[f_{b,LM}, \delta f_a] = \frac{\bar{v}_{ab}}{4} \left(\frac{v_{tha}}{v_a} \right)^3 \hat{L}^2 \delta f_a. \quad (5.50)$$

Within the Lorentz approximation, $\underline{U}(\mathbf{u}) = \underline{U}(\mathbf{v}_a)$ and the operator (5.31) becomes, writing here $T_a = T_b := T$:

$$\begin{aligned} C_{a,LM,b}^{\text{Lorentz}}[\delta f_b, f_{a,LM}] &= \frac{q_a^2 q_b^2 \ln \Lambda}{8\pi\epsilon_0^2 m_a T} \frac{\partial}{\partial \mathbf{v}_a} \cdot \underline{U}(\mathbf{v}_a) f_{a,LM} \cdot \underbrace{\int \delta f_b \mathbf{v}_b d^3 v_b}_{n_b \delta \langle \mathbf{v}_b \rangle} \\ &= -\frac{q_a^2 q_b^2 \ln \Lambda}{8\pi\epsilon_0^2 m_a T} 2 \frac{\mathbf{v}_a}{v_a^3} f_{a,LM} n_b \cdot \delta \langle \mathbf{v}_b \rangle. \end{aligned} \quad (5.51)$$

The full linearized operator in the Lorentz approximation is thus:

$$C_{ab}^{\text{Lorentz}}[f_b, f_a] = \frac{\bar{\nu}_{ab}}{4} \left[\left(\frac{v_{tha}}{v_a} \right)^3 \hat{L}^2 \delta f_a - 2 v_{tha} \frac{\mathbf{v}_a}{v_a^3} f_{a,LM} \cdot \delta \langle \mathbf{v}_b \rangle \right]. \quad (5.52)$$

The second term on the RHS of Eq. (5.52), which assumes $T_a = T_b$ contrary to the first term, is the momentum conserving term and may in general be neglected if there is no large flow in the considered system.

5.7 The electron-ion collision operator

The operator (5.52) neglecting the momentum conserving term is used in ORB5 for the collisions of electrons on ions. Invoking the low electron-ion mass ratio, $m_e/m_i \ll 1$, the electron-ion collisions are modeled by the Lorentz operator, assuming immobile ions in the lab frame:

$$C_{ei}[f_i, f_e] = \nu_{ei}(v) \hat{L}^2 f_e, \quad (5.53)$$

where:

$$\hat{L}^2 = - \left[\frac{\partial}{\partial \xi} (1 - \xi^2) \frac{\partial}{\partial \xi} + \frac{1}{1 - \xi^2} \frac{\partial^2}{\partial \alpha^2} \right], \quad (5.54)$$

having introduced the pitch angle variable $\xi = v_{||}/v$ and the gyroangle α . Considering the decomposition $f_e = f_{LM,e} + \delta f_{LM,e}$, one obtains:

$$C_{ei}[f_i, f_e] = C_{ei}[f_i, \delta f_{LM,e}] = \nu_{ei}(v) \hat{L}^2 \delta f_{LM,e}, \quad (5.55)$$

having noted that $C_{ei}[f_i, f_{LM,e}] = 0$, as the Lorentz operator annihilates any isotropic velocity distribution function. The electron-ion collision frequency $\nu_{ei}(v)$ is given by:

$$\nu_{ei}(v) = \frac{\bar{\nu}_{ei}}{4} \left(\frac{v_{the}}{v} \right)^3, \quad (5.56)$$

$$\bar{\nu}_{ei} = \frac{n_i Z^2 e^4 \ln \Lambda}{2\pi\epsilon_0^2 m_e^2 v_{the}^3}, \quad (5.57)$$

where m_e is the electron mass and $v_{the} = \sqrt{T_e/m_e}$ is the electron thermal velocity. It is assumed that the Coulomb logarithm $\ln \Lambda$ is constant over the whole plasma, and one approximates $n_i \simeq n_{i0}(\Psi)$ for computing the collision frequency, where $n_{i0}(\Psi)$ is the density of the ion local

Maxwellian background. The distribution being invariant with respect to α in the gyrokinetic description, the operator C_{ei} thus reduces to:

$$C_{ei}[f_i, \delta f_{LM,e}] = -\nu_{ei}(v) \frac{\partial}{\partial \xi} \left[(1 - \xi^2) \frac{\partial \delta f_{LM,e}}{\partial \xi} \right]. \quad (5.58)$$

5.8 The Langevin approach for solving the Fokker-Planck equation

In order to introduce the Langevin approach used for the practical implementation of the collision operators in ORB5, a general form for the Fokker-Planck equation is derived here by considering a general 1D phase space (x, t) and a collection of particles subjected to deterministic and stochastic motion. Let us introduce $P(x_1, x_2, t_1, t_2) \cdot (x_2 - x_1)$ the probability that a particle moves from a position x_1 to a position x_2 between the times t_1 and t_2 . $f(x, t)$ is the statistical particle distribution, which can be obtained from:

$$f(x, t) = \int f(x - \Delta x, t - \Delta t) P(x - \Delta x, x, t - \Delta t, t) d\Delta x. \quad (5.59)$$

Assuming small deflections Δx , Eq. (5.59) is Taylor-expanded with respect to Δx :

$$\begin{aligned} f(x, t) \simeq & f(x, t - \Delta t) \underbrace{\int P(x - \Delta x, x, t - \Delta t, t) d\Delta x}_1 \\ & - \frac{\partial}{\partial x} \left[f(x, t - \Delta t) \underbrace{\int \Delta x P(x - \Delta x, x, t - \Delta t, t) d\Delta x}_{\langle \Delta x \rangle} \right] \\ & + \frac{1}{2} \frac{\partial^2}{\partial x \partial x} \left[f(x, t - \Delta t) \underbrace{\int \Delta x \Delta x P(x - \Delta x, x, t - \Delta t, t) d\Delta x}_{\langle \Delta x \Delta x \rangle} \right]. \end{aligned} \quad (5.60)$$

Eq. (5.60) is divided by Δt to be written:

$$\frac{f(x, t) - f(x, t - \Delta t)}{\Delta t} + \frac{\partial}{\partial x} \left[\frac{\langle \Delta x \rangle}{\Delta t} f(x, t - \Delta t) \right] - \frac{\partial^2}{\partial x \partial x} \left[\frac{\langle \Delta x \Delta x \rangle}{2\Delta t} f(x, t - \Delta t) \right] = 0. \quad (5.61)$$

Taking the limit $\Delta t \rightarrow 0$ provides the Fokker-Planck equation:

$$\frac{\partial f}{\partial t} + \frac{\partial}{\partial x}(\Gamma f) - \frac{\partial^2}{\partial x \partial x}(Df) = 0, \quad (5.62)$$

where the drag coefficient Γ and the diffusion coefficient D are defined as follows:

$$\Gamma = \lim_{\Delta t \rightarrow 0} \frac{\langle \Delta x \rangle}{\Delta t}, \quad (5.63)$$

$$D = \lim_{\Delta t \rightarrow 0} \frac{\langle \Delta x \Delta x \rangle}{2\Delta t}. \quad (5.64)$$

Solving Eq. (5.62) through the Langevin approach requires the introduction of particles for modelling the distribution f . The time evolution of f is accounted for through individual particle motion. The position in phase space of the particle i at a given time t , $x_i(t)$, is computed from the position of the particle i at the previous time step $x_i(t - \Delta t)$ as follows:

$$x_i(t) = x_i(t - \Delta t) + \langle \Delta x \rangle + \mathcal{R}\sqrt{\langle \Delta x \Delta x \rangle} = x_i(t - \Delta t) + \Gamma \Delta t + \mathcal{R}\sqrt{2D\Delta t}, \quad (5.65)$$

where the introduction of the random number \mathcal{R} , sampled from a PDF of average 0 and variance 1, is required by the diffusive motion related to the second moment of the probability function P [the last term on the RHS of Eq. (5.60)]. The Langevin approach provides a sound basis for implementing collisions and the corresponding diffusive processes in a Particle-In-Cell code.

5.9 δf PIC implementation of the Lorentz e-i collision operator

The electron-ion collision operator defined by Eq. (5.55) contributes to the test particle operator C_{TP} [as defined by Eq. (3.32)], which, through random kicks, affects the marker trajectories in velocity space according to the Langevin approach briefly described in Sec. 5.8. Effectively, only the pitch angle direction ξ of the markers is modified. No background reaction operator C_{BR} appears in the electron-ion collisions, and the w-weight equation is thus unaffected by this type of collisions. Rewriting the e-i collision operator (5.58) as follows:

$$C_{ei}[f_i, \delta f_{LM,e}] = -\nu_{ei}(v) \left\{ \frac{\partial}{\partial \xi} (2\xi \delta f_{LM,e}) + \frac{\partial^2}{\partial \xi^2} [(1 - \xi^2) \delta f_{LM,e}] \right\}, \quad (5.66)$$

enables to conveniently identify the corresponding drag and diffusion in the ξ -direction. The random increment $\Delta \xi$ on the pitch angle variable resulting from e-i collision over an infinitesimally small time step Δt may thus be evaluated as:

$$\Delta \xi = -2\xi \nu_{ei}(v) \Delta t + \mathcal{R}\sqrt{2(1 - \xi^2)\nu_{ei}(v)\Delta t}, \quad (5.67)$$

where \mathcal{R} is a random number sampled from a PDF with average 0 and variance 1. In practice, making use of (5.67) for a finite time step may however result in $\xi_{out} = \xi + \Delta \xi$ falling outside of its correct interval $[-1, 1]$. For the purpose of conveniently treating e-i collisions, one thus temporarily expands the 2-dimensional gyrokinetic velocity space back to 3 dimensions as follows: at any configuration space point \mathbf{R} , one starts by defining \hat{e}_\perp as an arbitrary unitary vector perpendicular to \hat{b} . The incoming velocity, i.e. before the collisional kick, of a given particle at \mathbf{R} is defined as $\mathbf{v}_{in} = v_\parallel \hat{b} + v_\perp \hat{e}_\perp$, with $v_\perp = \sqrt{2B(\mathbf{R})\mu/m}$. As shown in Figure

5.2, one then expands the velocity space to 3-dimensions by introducing a first orthonormal coordinate system (x, y, z) with $\hat{e}_z := \hat{b}$ and $\hat{e}_y := \hat{e}_\perp$. A second orthonormal coordinate system (x', y', z') is then defined, such that $\hat{e}_{x'} := \hat{e}_x$ and $\hat{e}_{z'} := \mathbf{v}_{in}/v_{in}$. Let us introduce the spherical angles (θ, α) associated with the system (x', y', z') . In these variables, it is recalled that the e-i collision operator reads:

$$C_{ei}f = -\nu_{ei}(v) \left[\frac{1}{\sin \theta} \frac{\partial}{\partial \theta} \left(\sin \theta \frac{\partial f}{\partial \theta} \right) + \frac{1}{\sin^2 \theta} \frac{\partial^2 f}{\partial \alpha^2} \right]. \quad (5.68)$$

One clearly has $\theta_{in} = 0$. The angles $\theta_{out} = \Delta\theta$ and α_{out} for the outgoing velocity following the kick are obtained by taking two random angles: α_{out} from a uniform distribution between 0 and 2π , while $\Delta\theta = 2\mathcal{R}\sqrt{\nu_{ei}(v)\Delta t}$ is computed making use of \mathcal{R} sampled from a PDF of average 0 and variance 1 [86]. The new velocity reads:

$$\mathbf{v}_{out} = v_{in} [\sin(\Delta\theta) \cos(\alpha_{out}) \hat{e}_{x'} + \sin(\Delta\theta) \sin(\alpha_{out}) \hat{e}_{y'} + \cos(\Delta\theta) \hat{e}_{z'}]. \quad (5.69)$$

Note that the property $v_{in} = v_{out}$ is verified exactly, i.e. with no discretization error. Performing the reverse change of coordinates from (x', y', z') to (x, y, z) finally gives:

$$\begin{aligned} v_{||,out} &= \mathbf{v}_{out} \cdot \hat{e}_z = \mathbf{v}_{out} \cdot \left(-\sqrt{1 - \xi_{in}^2} \hat{e}_{y'} + \xi_{in} \hat{e}_{z'} \right) \\ &= v_{in} \left[-\sin(\Delta\theta) \sin(\alpha_{out}) \sqrt{1 - \xi_{in}^2} + \xi_{in} \cos(\Delta\theta) \right], \end{aligned} \quad (5.70)$$

$$v_{\perp,out}^2 = v_{in}^2 - v_{||,out}^2, \quad (5.71)$$

providing the outgoing gyrokinetic variables ($v_{||,out}, \mu_{out} = mv_{\perp,out}^2/2B$). The outgoing pitch angle variable $\xi_{out} = -\sin(\Delta\theta) \sin(\alpha_{out}) \sqrt{1 - \xi_{in}^2} + \xi_{in} \cos(\Delta\theta)$ resulting from (5.70) verifies $\xi_{out} \in [-1, 1]$ by construction even for finite values of $\Delta\theta$, which thus resolves the practical issue related to the scheme based on Eq. (5.67).

5.10 δf PIC implementation of the self-collision operator

5.10.1 Handling the test particle operator $C[f_{LM}, \delta f_{LM}]$

Similarly to the Lorentz operator, this part of the linearized self-collision operator is accounted for through appropriately defined random kicks to marker trajectories. Introducing again (x, y, z) and (x', y', z') , the orthogonal systems defined in Sec. 5.9, and making use of the Rosenbluth potentials defined by Eqs. (5.33) and (5.34), the velocity increments related to the Langevin method for like-species collisions can be written, according to Eqs. (5.36) and

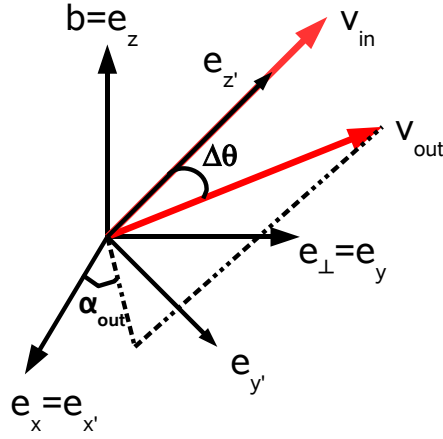


Figure 5.2: Extended 3-dimension velocity space for random kicks, with the different coordinate systems. The velocities before the kick \mathbf{v}_{in} and after the kick \mathbf{v}_{out} are shown.

(5.37) [20]:

$$\begin{aligned}\Delta v_{x'} &= v_{th} \sqrt{\frac{K(\mathbf{v}) \bar{\nu} \Delta t}{2}} R_1, \\ \Delta v_{y'} &= v_{th} \sqrt{\frac{K(\mathbf{v}) \bar{\nu} \Delta t}{2}} R_2, \\ \Delta v_{z'} &= -H(\mathbf{v}) v \bar{\nu} \Delta t + v_{th} \sqrt{H(\mathbf{v}) \bar{\nu} \Delta t} R_3,\end{aligned}\tag{5.72}$$

where R_1 , R_2 , and R_3 are three independent random numbers sampled from a PDF with average 0 and variance 1. Going back to gyrokinetic velocity variables provides the new values ($v_{||,out}, \mu_{out} = mv_{\perp,out}^2/2B$) with:

$$v_{||,out} = \frac{1}{v_{in}} [-\Delta v_{y'} v_{\perp,in} + (v_{in} + \Delta v_{z'}) v_{||,in}],\tag{5.73}$$

$$v_{\perp,out}^2 = \Delta v_{x'}^2 + \frac{1}{v_{in}^2} [\Delta v_{y'} v_{||,in} + (v_{in} + \Delta v_{z'}) v_{\perp,in}]^2.\tag{5.74}$$

Notice that by working temporarily in the expanded 3-dimensional velocity space avoids similar practical problems related to the bounded pitch angle variable space as for the e-i Lorentz collision operator.

5.10.2 Handling the background reaction operator $C[\delta f_{LM}, f_{LM}]$

The background reaction operator $C[\delta f_{LM}, f_{LM}]$ is handled in the w-weight equation according to Eq. (4.31) in Chapter 4, which is recalled here for the sake of completeness:

$$\left. \frac{dw_r}{dt} \right|_{\text{coll}} = -p_r \frac{1}{f_{LM}} C[\delta f_{LM}, f_{LM}] \Big|_{(z_r(t), t)}.\tag{5.75}$$

The functional form for $C[\delta f_{LM}, f_{LM}]$ is chosen as in Eq. (5.42). A straightforward estimation for the fields $\delta \mathcal{P}_{||}$ and $\delta \mathcal{E}$ would be given by [87] [85]:

$$\delta \mathcal{P}_{||}(\mathbf{x}) = \sum_r w_r \left. \frac{\Delta v_{||,r}}{\Delta t} \right|_{\text{coll}} \delta(\mathbf{x} - \mathbf{x}_r), \quad (5.76)$$

$$\delta \mathcal{E}(\mathbf{x}) = \sum_r w_r \left. \frac{\Delta(v_r^2)}{\Delta t} \right|_{\text{coll}} \delta(\mathbf{x} - \mathbf{x}_r). \quad (5.77)$$

where $\Delta/\Delta t|_{\text{coll}}$ stands for the variations due to self-collisions on the background. However, such an approach does not ensure exact conservation of mass, parallel momentum and energy, as it suffers from numerical errors related to the finite time stepping and to the statistical description with a finite number of markers. A modified scheme suggested by Satake *et al.* [88] has been implemented in ORB5 which ensures conservation of the three velocity moments within each configuration space bin α exactly, i.e. to numerical round-off. Let us briefly rederive here the underlying algorithm. In the time stepping algorithm, the integration of Eq. (5.75) follows the test particle scattering of markers off the background, which as described in Sec. 5.10.1 accounts for the contribution $C[f_{LM}, \delta f_{LM}]$ of the linearized self-collision operator. As a result of this scattering, each marker r , having an incoming velocity $\mathbf{v}_{in,r}$, is reassigned a new outgoing velocity $\mathbf{v}_{out,r} = \mathbf{v}_{in,r} + \Delta \mathbf{v}$. The integration of (5.75) can be written similarly as $w_{out,r} = w_{in,r} + \Delta w_r$. In view of computing Δw_r according to Eqs. (5.42) and (5.75), one considers the following functional form:

$$\Delta w_r = -\frac{p_r}{n_\alpha} \left[(1 - 3\sqrt{\pi}G(\mathbf{v}))\Delta N_\alpha + 6\sqrt{\pi}H(\mathbf{v})\frac{\Delta P_{||\alpha}v_{||out,r}}{v_{th\alpha}^2} + \sqrt{\pi}G(\mathbf{v})\frac{\Delta E_\alpha}{v_{th\alpha}^2} \right], \quad (5.78)$$

where the functions H and G given by Eqs. (5.33) and (5.35) are evaluated at the normalized outgoing velocity $\mathbf{v} = v_{out,r}/v_{th\alpha}$, n_α and $v_{th\alpha}$ being the background density and thermal velocity at the center of the bin α in which the marker is currently localized. The parameters ΔN_α , $\Delta P_{||\alpha}$ and ΔE_α , specific to each bin, are to be determined so as to ensure exact conservation of the velocity moments. In particular, note the additional term proportional to ΔN_α in Eq. (5.78) compared to (5.42), whose purpose is to ensure conservation of mass to round-off despite numerical discretization errors. Conservation of moments within the bin α of volume ΔV_α over the full discretized collision step reads:

$$\sum_{r \in \alpha} w_{in,r} = \sum_{r \in \alpha} w_{out,r} \implies \frac{1}{\Delta V_\alpha} \sum_{r \in \alpha} \Delta w_r = 0, \quad (5.79)$$

$$\sum_{r \in \alpha} w_{in,r} v_{||in,r} = \sum_{r \in \alpha} w_{out,r} v_{||out,r} \implies \frac{1}{\Delta V_\alpha} \sum_{r \in \alpha} \Delta w_r v_{||out,r} = -\Delta \mathcal{P}_{||\alpha}, \quad (5.80)$$

$$\sum_{r \in \alpha} w_{in,r} v_{in,r}^2 = \sum_{r \in \alpha} w_{out,r} v_{out,r}^2 \implies \frac{1}{\Delta V_\alpha} \sum_{r \in \alpha} \Delta w_r v_{out,r}^2 = -\Delta \mathcal{E}_{||\alpha}, \quad (5.81)$$

where $\Delta \mathcal{P}_{||\alpha} = \sum_r w_{in,r} \Delta v_{||,r} / \Delta V_\alpha$ and $\Delta \mathcal{E}_{||\alpha} = \sum_r w_{in,r} \Delta(v_r^2) / \Delta V_\alpha$, having defined $\Delta v_{||,r} = v_{||out,r} - v_{||in,r}$ and $\Delta(v_r^2) = v_{out,r}^2 - v_{in,r}^2$. Inserting (5.78) into (5.79), (5.80), (5.81) provides a linear system of three equations for the parameters $(\Delta N_\alpha, \Delta P_{||\alpha}, \Delta E_\alpha)$ which can be written as

follows:

$$\mathbf{M}_\alpha \begin{pmatrix} \Delta N_\alpha \\ \Delta P_\alpha \\ \Delta E_\alpha \end{pmatrix} = \begin{pmatrix} 0 \\ \Delta \mathcal{P}_{||\alpha} \\ \Delta \mathcal{E}_\alpha \end{pmatrix}, \quad (5.82)$$

with:

$$\mathbf{M}_\alpha = \frac{1}{\Delta V_\alpha} \sum_{r \in \alpha} \frac{p_r}{n_\alpha} \begin{bmatrix} 1 \\ v_{||out,r} \\ v_{out,r}^2 \end{bmatrix} \left([1 - 3\sqrt{\pi}G], 6\sqrt{\pi}H \frac{v_{||out,r}}{v_{th\alpha}^2}, \sqrt{\pi}G \frac{1}{v_{th\alpha}^2} \right). \quad (5.83)$$

The matrix \mathbf{M}_α and the RHS of system (5.82) must be computed separately for each bin α and at each collisional time step. The solution of (5.82) provides the coefficients $(\Delta N_\alpha, \Delta P_\alpha, \Delta E_\alpha)$, which are then inserted into Eq. (5.78), thus enabling to finally compute the weight increments Δw_r , and fully complete the self-collision stepping. The algorithm clearly ensures exact numerical conservation of the velocity moments by construction. In the limit of a large number of markers per bin, as well as $\Delta V_\alpha \rightarrow 0$, the scheme obviously converges to the original equation (5.42) for the background reaction. In particular, note that in this limit, the matrix \mathbf{M}_α reduces to:

$$\mathbf{M}_\alpha = \int d^3v \frac{f_{LM}}{n_0} \begin{pmatrix} 1 \\ v_{||} \\ v^2 \end{pmatrix} \left([1 - 3\sqrt{\pi}G], 6\sqrt{\pi}H \frac{v_{||}}{v_{th}^2}, \sqrt{\pi}G \frac{1}{v_{th}^2} \right) = \mathbb{I}, \quad (5.84)$$

so that, according to (5.82), $\Delta N_\alpha = 0$, $\Delta P_\alpha = \Delta \mathcal{P}_{||\alpha}$ and $\Delta E_\alpha = \Delta \mathcal{E}_\alpha$ as in Eq. (5.42).

5.10.3 Field-aligned binning for the background reaction

The numerical implementation of the background reaction procedure described in Sec. 5.10.2 requires a binning in the 3D configuration space. In ORB5, the background reaction binning, written by Ben McMillan, is field-aligned in order to take advantage of the microturbulence structure which develops mainly along the magnetic field lines. The size of the binning grid $(n_s, n_{\theta^*}, n_\varphi)$, different from the size of the field solver grid which is not field-aligned, is an input parameter. Note that the field-aligned binning for the background reaction term is similar but not strictly equivalent to the binning in configuration space for the coarse-graining procedure described in Sec. 4.8, the field-aligned coordinate being differently defined as explained in this Section and shown in Figure 5.3 (a). For axisymmetric runs, i.e. neoclassical runs or runs considering no electric field as presented in Chapter 6, a binning in the 2D poloidal plane (s, θ^*) (not field-aligned, with a single bin in the toroidal direction) is used, as presented in Figure 5.3 (b). However, the same binning as for coarse-graining in configuration space should in fact be used for the background reaction term of the self-collision operator as well. Note that the required number of bins related to collision operator background reaction is typically provided by the grid used by a field-aligned solver for the fluctuating fields.

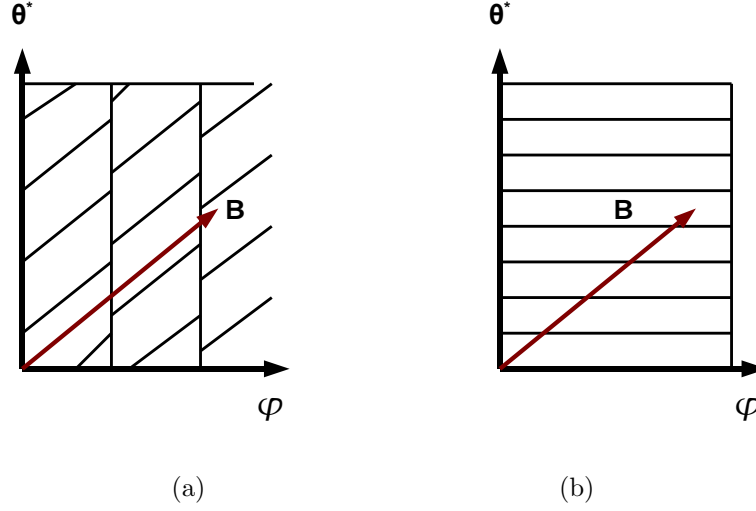


Figure 5.3: (a) Field-aligned binning for the background reaction term of the self-collision operator. (b) Binning used for neoclassical runs, with a single bin in the toroidal direction (not field-aligned).

5.10.3.1 Radial direction

The binning is uniform in $s = \sqrt{\Psi/\Psi_{edge}}$. Introducing the bin size $\Delta s = (s_{max} - s_{min})/n_s$, where s_{min} and s_{max} are the lower and upper radial boundary respectively ($s_{min} \leq s < s_{max}$), the related index is given by:

$$i_s = \text{INT} \left[\frac{s - s_{min}}{\Delta s} \right] + 1, \quad (5.85)$$

where $\text{INT}(x)$ is the function retaining only the integer part of x .

5.10.3.2 Toroidal direction, global treatment

Ignoring so far the parallelization issues, one first defines a global toroidal index, similarly to the radial index:

$$i_\varphi = \text{INT} \left[\frac{\varphi}{\Delta\varphi} \right] + 1, \quad (5.86)$$

where $\varphi \in [0; 2\pi[$ and $\Delta\varphi = 2\pi/n_\varphi$ is the width of the bins along φ .

5.10.3.3 Poloidal direction

The following field-aligned coordinate is introduced:

$$y = \theta_* - \frac{1}{q_s(s)}[\varphi - \varphi_0(\varphi)], \quad (5.87)$$

q_s being the safety factor and $\varphi_0(\varphi)$ being the function giving the position of the bin center φ_0 corresponding to φ , defined as:

$$\varphi_0(\varphi) = \left(i_\varphi - \frac{1}{2}\right) \Delta\varphi. \quad (5.88)$$

The number of grid points in the y -direction does vary with the radial coordinate:

$$n_y = \text{FLOOR} \left[\frac{s_{min} + i_s \Delta s}{s_{max}} n_{\theta^*} \right], \quad (5.89)$$

where the function FLOOR is defined in Sec. 4.8.1. The related index is computed as follows:

$$i_y = \text{FLOOR} \left[\frac{\text{Modulo}(y, 2\pi)}{2\pi} n_y \right] + 1, \quad (5.90)$$

The choice of the field-aligned coordinate y allows to take the largest possible bins in the toroidal direction φ , which now parametrizes the position along the field line.

5.10.3.4 Parallelization in the toroidal direction

The toroidal direction requires particular attention since part of the parallelization is based on domain decomposition, which is performed along the toroidal angle as explained in Sec. 4.5. The treatment of the n_φ toroidal bins thus depends on the number of domains N_D in this direction.

Case $N_D \geq n_\varphi$

It is the usual case. Here the final binning index $\alpha = (i_s, i_y, i_\varphi)$ does not depend on the toroidal direction since each field domain gets only one toroidal bin. It is computed as follows:

$$\alpha = (i_s - 1)n_{\theta^*} + i_y. \quad (5.91)$$

The different binned quantities have then to be summed over the clones, and over the field domains covered by each toroidal collision bin.

Case $N_D < n_\varphi$

This case is rare in practice. Here each field domain gets $n_{\varphi, \text{loc}}$ bins in the toroidal direction. We define a local toroidal index $i_{\varphi, \text{loc}}(i_\varphi)$ which locates the bin within the local field domain. The final binning index is given by:

$$\alpha = [(i_s - 1)n_{\theta^*} + (i_y - 1)]n_{\varphi, \text{loc}} + i_{\varphi, \text{loc}}. \quad (5.92)$$

Note that Eq. (5.92) is equivalent to Eq. (5.91) for $n_{\varphi, \text{loc}} = i_{\varphi, \text{loc}} = 1$, as expected. The different binned quantities have then to be summed over the clones.

As for the coarse-graining bins, the bins for collisions must be small compared to characteristic variations and as large as possible for statistics. This is ensured by the natural field-aligned coordinate system. Note that the practical implementation of the background reaction operator and the associated procedure to conserve exactly the different moments of the distribution

require at least $\sim 10 - 20$ markers per bin in configuration space. In turbulence simulations, where more than $100 \cdot 10^6$ markers are used, the size of the binning grid $(n_s, n_{\theta^*}, n_{\varphi})$ may easily be chosen similarly to the grid size of a field-aligned solver for the quasi-neutrality equation. A problem may nevertheless arise in case of linear simulations, where the number of markers is $\sim 10^6$. The number of bins for the background reaction has thus to be reduced accordingly, with *a priori* possible consequences on the linear physics of the mode. This issue is addressed in Chapter 8.

5.11 Basic tests

5.11.1 Lorentz operator for electron-ion collisions

In order to test the relevant behaviour of the discretized Lorentz operator, its analytical properties are studied. The Legendre polynomials $P_l(\xi)$ defined in Sec. B.2.1 of Appendix B, where $\xi = v_{\parallel}/v$ is the pitch angle variable, are eigenfunctions of the Lorentz operator, namely:

$$\hat{L}^2 P_l(\xi) = l(l+1)P_l(\xi), \quad (5.93)$$

where $l = 0, 1, 2, \dots$ is a positive integer. We consider the simple relaxation of a distribution δf in the pitch angle space according to the Lorentz operator scattering, described by the equation:

$$\frac{\partial \delta f}{\partial t} = -\nu \hat{L}^2 \delta f, \quad (5.94)$$

ν being the relaxation rate. The distribution is decomposed into Legendre polynomials:

$$\delta f(\xi, t) = \sum_l c_l(t) P_l(\xi). \quad (5.95)$$

Introducing Eq. (5.95) into Eq. (5.94) yields the time evolution of the coefficients c_l :

$$c_l(t) = c_l(t=0) \exp[-l(l+1)\nu t]. \quad (5.96)$$

In Figure 5.4 (a), the analytical damping given by Eq. (5.96) is compared successfully to the numerical damping predicted by the discretized form of the Lorentz operator for

$$\delta f(\xi, t=0) = P_2(\xi) = \frac{(3\xi^2 - 1)}{2}. \quad (5.97)$$

Note that the simulation corresponding to Figure 5.4 (a) has been performed with an initial marker distribution uniform in ξ -space, which is not affected by the Lorentz operator. A marker distribution which is initially Gaussian in ξ -space becomes uniform in ξ -space through the Lorentz operator scattering after several collision times, as checked in Figure 5.4 (b).

The diffusive nature of the electron detrapping through the Lorentz operator scattering can be emphasized. A simulation of pure collisional relaxation through pitch angle scattering is per-

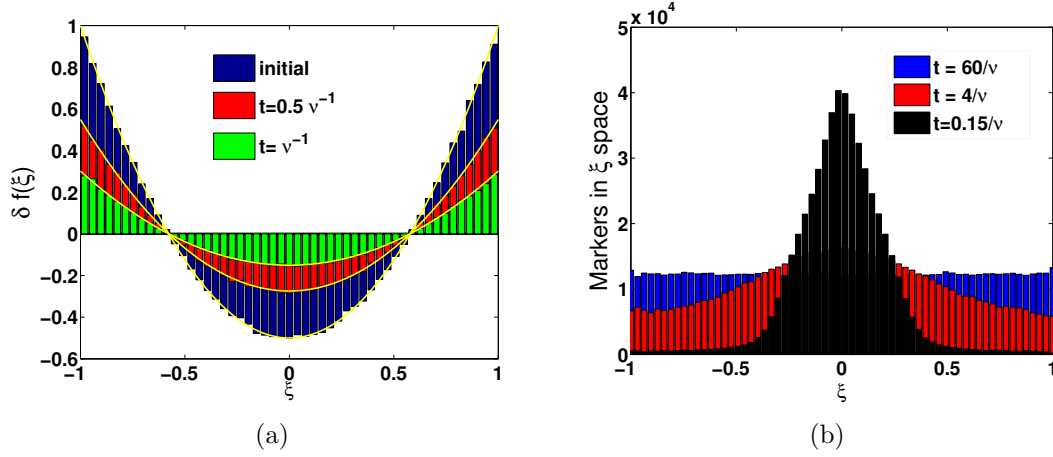


Figure 5.4: (a) The numerical damping of the Legendre polynomial $P_2(\xi)$ by the Lorentz operator is successfully compared to analytical predictions (yellow lines). Simulation results obtained with a marker distribution uniform in ξ -space. (b) In ξ -space, an initially Gaussian marker distribution is uniformized by the Lorentz operator scattering.

formed with ORB5, only trapped electrons being initially loaded at mid-radius of a CYCLONE-based tokamak, i.e. at $\epsilon \simeq 0.18$. A rough theoretical understanding of the process is obtained by a simple model where the finite pitch angle space ξ is replaced by the infinite space x for analytical convenience. The following initial 1D hat density $n(x, t = 0)$ is introduced:

$$n(x, t = 0) = \begin{cases} n_0 & \text{if } |x| < a, \\ 0 & \text{else.} \end{cases} \quad (5.98)$$

The situation describes initially trapped particles, which are supposed to be detrapped by a diffusion process. The evolution of the density n is thus governed by the diffusion equation, which takes the following form in Fourier space:

$$\frac{\partial}{\partial t} \hat{n}(k, t) = -Dk^2 \hat{n}(k, t) \implies \hat{n}(k, t) = \hat{n}(k, 0) e^{-Dk^2 t}, \quad (5.99)$$

where k is a given wavenumber and D the diffusion coefficient. The initial condition is computed:

$$\hat{n}(k, 0) = \frac{1}{2\pi} \int_{-a}^a n(x, 0) e^{-ikx} dx = \frac{n_0}{2\pi} \int_{-a}^a e^{-ikx} dx = \frac{n_0 a}{\pi} \frac{\sin ka}{ka}. \quad (5.100)$$

The particle number $N(t)$ in the initial hat area ($|x| < a$) is obtained by making use of Eqs. (5.99) and (5.100):

$$\begin{aligned} N(t) &= \int_{-a}^a n(x, t) dx = \int_{-a}^a \int_{-\infty}^{\infty} \hat{n}(k, t) e^{ikx} dk dx \\ &= \frac{n_0 a}{\pi} \int_{-a}^a \int_{-\infty}^{\infty} \frac{\sin ka}{ka} e^{-Dk^2 t} e^{ikx} dk dx = \frac{2n_0 a^2}{\pi} \int_0^{\infty} dk \left(\frac{\sin ka}{ka} \right)^2 e^{-Dk^2 t}. \end{aligned} \quad (5.101)$$

Defining the error function $\text{erf}(x) = (2/\sqrt{\pi}) \int_0^x e^{-y^2} dy$, the particle number is expressed as:

$$N(t) = 2n_0a \left[\text{erf} \left(\sqrt{\frac{a^2}{Dt}} \right) + \sqrt{\frac{Dt}{\pi a^2}} (e^{-a^2/Dt} - 1) \right]. \quad (5.102)$$

Considering small times $t \ll \frac{a^2}{D}$, the following limit is found:

$$N(t) \simeq 2n_0a \left(1 - \sqrt{\frac{Dt}{\pi a^2}} \right) = N(t=0) \left(1 - \sqrt{\frac{Dt}{\pi a^2}} \right). \quad (5.103)$$

The detrapping evolution, corresponding to the particles leaving the area $|x| < a$, exhibits the $\sim \sqrt{t}$ behaviour, typical of diffusion processes. The diffusion in pitch angle space being roughly similar to the above described process, the time behaviour of the detrapped electron fraction in ORB5 is expected to follow the law $\sim \sqrt{\nu_{ei}(v_{the})t}$ for $\nu_{ei}(v_{the})t \ll 1$. The latter analogy is clearly not fully accurate, due to the finiteness of the pitch angle space and the different collision frequency for each electron, depending on its velocity. Considering the collisionality $\nu_{ei}(v_{the}) = 0.05[c_s/a]$, Figure 5.5 shows the time evolution of the detrapped electron fraction, compared to the function $\sqrt{\nu_{ei}(v_{the})t/2}$. The diffusive nature of the electron detrapping in the early time of the simulation is confirmed. When the condition $\nu_{ei}(v_{the})t \ll 1$ is not satisfied anymore, both curves diverge significantly. In particular, after many collision times, the fraction of detrapped electrons eventually reaches a stationary value, roughly close to $1 - \sqrt{\epsilon} \sim 0.55$, through isotropization in ξ -space.

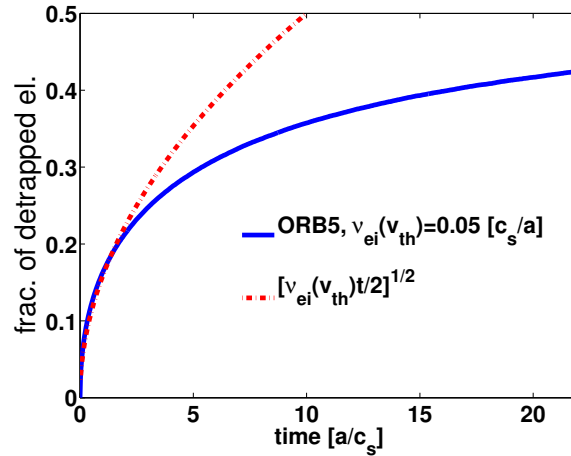


Figure 5.5: Time evolution of the detrapped electron fraction due to electron-ion collisions, illustrating the diffusive nature of the electron detrapping process through pitch angle scattering. At later times, the $\sim \sqrt{t}$ behaviour is broken due to the finiteness of the pitch angle space.

5.11.2 Self-collisions: conservation of moments

A linearized self-collision operator must conserve mass, momentum and kinetic energy. A shifted linearized Maxwellian, which is a stationary state of the linearized self-collision operator, is

loaded as initial perturbation in the code BIRDIE (a kinetic code describing a 1D unmagnetized and homogeneous plasma presented in Appendix B):

$$\delta f(x, v, \xi, t = 0) = c f_M(v) \left(\frac{v\xi}{v_{th}} + \frac{v^2}{v_{th}^2} \right), \quad (5.104)$$

where $c \ll 1$ is a numerical coefficient corresponding to the magnitude of the perturbation. The time evolution of the spatially averaged kinetic energy and momentum, due to simple relaxation, is shown in Figure 5.6, both for the full linearized operator and a simplified operator without background reaction. Considering the Langevin algorithm for the marker kicks without the background reaction term, by invoking the particle conservation and the fact that the operator $C[f_M, \delta f]$ relaxes any distribution to a Maxwellian, δf relaxes towards the Maxwellian distribution $3cf_M$ [the Maxwellian with the same density as the initial condition (5.104)]. As a consequence, the final parallel momentum is zero if no background reaction term is considered. The initial and final energies are computed by:

$$E_i = \int \frac{mv^2}{2L} \delta f dx d^3v = \frac{mc}{2v_{th}^2 L} \int v^4 f_M dx d^3v = \frac{15}{2} cnT, \quad (5.105)$$

$$E_f = \frac{3mc}{2L} \int v^2 f_M dx d^3v = \frac{9}{2} cnT, \quad (5.106)$$

L being the length of the 1D-system treated by BIRDIE (see Appendix B). The final energy is obviously lower than the initial one if no background reaction term is considered: $E_f/E_i = 0.6$. Figure 5.6 shows the relaxation towards the expected level of momentum and energy, as well as the exact conservation laws (to numerical round-off thanks to the scheme described in Sec. 5.10.2) when the background reaction is switched on, for $c = 0.05$ and $\nu\Delta t = 0.01$.

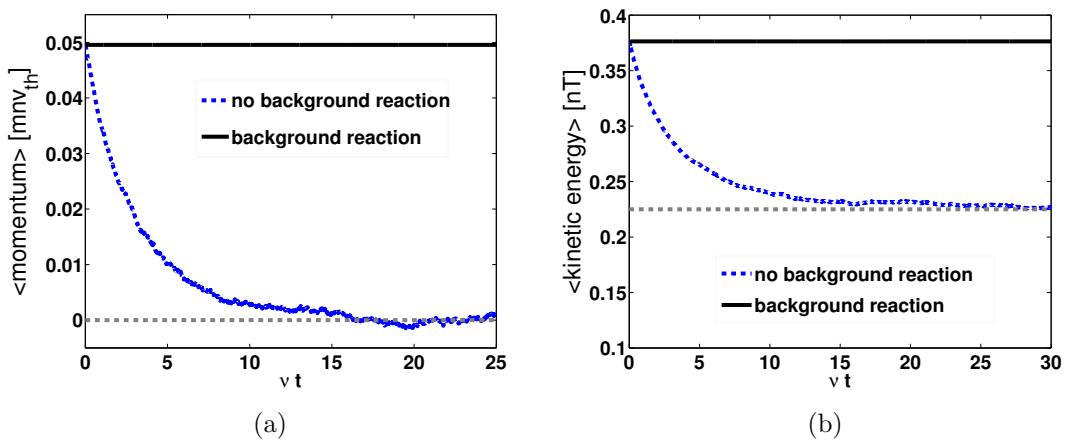


Figure 5.6: (a) Momentum and (b) energy conservation by the linearized self-collision operator, for $c = 0.05$ and $\nu\Delta t = 0.01$. As expected, the conservation laws are broken if no background reaction term is considered.

5.11.3 Electrical Spitzer conductivity

The Spitzer test consists in studying the balance between the collisional drag and a constant drive, e. g. a parallel constant electric field in the present case. The corresponding Spitzer problem [89] addresses the following equation:

$$\frac{\partial \delta f_e}{\partial t} - \frac{e}{m_e} \mathbf{E}_0 \cdot \frac{\partial f_{Me}}{\partial \mathbf{v}} = \frac{\partial \delta f_e}{\partial t} + \frac{e E_0 v_{||}}{m_e v_{the}^2} f_{Me} = -C[f_e]. \quad (5.107)$$

The parallel current is expected to reach a saturation level j_{sat} directly proportionnal to the external electric field E_0 . j_{sat} is computed by:

$$j_{\text{sat}} = -e \int \delta f_{\infty} v_{||} d^3 v, \quad (5.108)$$

where δf_{∞} is the stationary solution to Eq. (5.107). The theoretical Spitzer conductivity $\sigma_L = j_{\text{sat}}/E_0$ in the Lorentz model ($C[f_e] = \nu_{ei} \hat{L}^2 \delta f_e$) is given by:

$$\sigma_L = \frac{16}{\sqrt{2\pi}} \frac{e^2 n_e}{m_e \nu_{ei}(v_{the})}, \quad (5.109)$$

where $\nu_{ei}(v_{the})$ is the electron-ion collision frequency evaluated at the thermal velocity, according to Eqs. (5.56) and (5.57). An arbitrary electron-ion collision frequency ν_{ref} is chosen in order to build the frequency range $[1, 1.2, 1.4, 1.6, 1.8, 2] \times \nu_{\text{ref}}$. ORB5 simulations, solving Eq. (5.107), were performed and benchmarked against the theoretical Spitzer predictions. Figure 5.7 (a) shows how the conductivity computed by ORB5 decreases when the collisionality increases, consistently with Eq. (5.109). Figure 5.7 (b) presents results from ORB5 simulations performed with finite Z values (retaining both electron-ion and electron-electron collisions) for $\nu_{ei} = 1.6 \nu_{\text{ref}}$. The conductivity comes closer to the predicted Lorentz model value $\sigma_{L,\text{theo}}$ when the ion charge Z is increased, consistently with the Lorentz model assumption $Z \rightarrow \infty$ (electron-ion collisions only). Moreover, ORB5 results match well the Spitzer model predictions for finite values of Z (also numerical estimates), the difference between the two approaches being less than 10%.

5.12 Gyrokinetic corrections for collision operators

The ion collision operator used in ORB5 is based on the drift-kinetic approximation, while the collisionless ion dynamics is treated within the frame of a gyrokinetic model. It is therefore logical to attempt applying gyrokinetic corrections to the ion collision operator in order to make the ion model totally consistent. Such corrections are however not straightforward to handle in practice in a PIC code. Indeed, due to the velocity dependence of the Larmor radius ρ_L , a gyrokinetic operator leads to diffusion in gyrocenter configuration space as well, contrary to the diffusion in velocity space only associated to a drift-kinetic operator. The velocity derivatives appearing in a drift-kinetic operator involve a constant position for the particle, written $\partial/\partial \mathbf{v}|_{\mathbf{x}}$: The collision operator does not produce any diffusion in configuration space. In

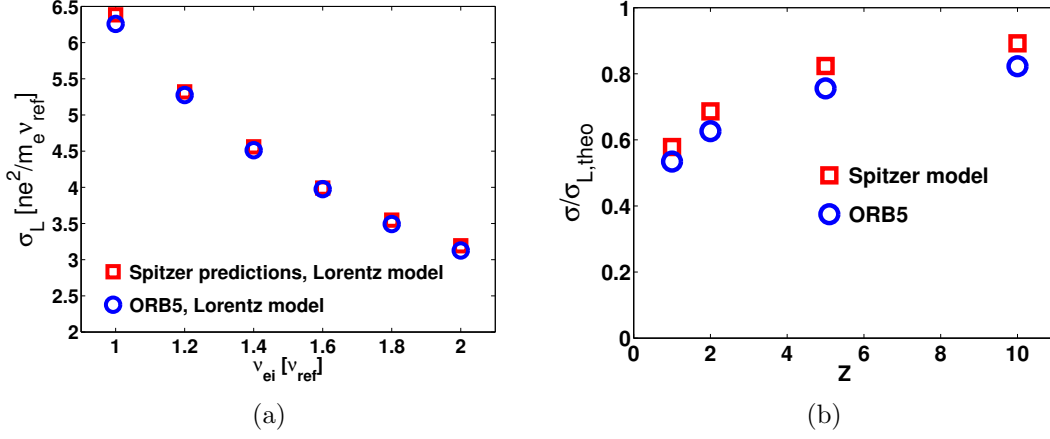


Figure 5.7: (a) Conductivity in the Lorentz model σ_L : comparison between Spitzer analytical predictions and ORB5 results. (b) Z-dependence of the conductivity σ for $\nu_{ei} = 1.6 \nu_{ref}$: ORB5 reproduces the Spitzer model predictions within a margin of error of 10%.

a gyrokinetic code, the gyrocenter positions are considered, and not the particle positions. The difference lies both in the FLR effects and the polarization drift. Only FLR effects are addressed here, related to transformation from particle to guiding center variables. As a consequence, a gyrokinetic correction should in principle be applied for collision operators in a gyrokinetic code. The development of gyrokinetic collision operators, as well as their discretization for implementation in a Eulerian code, are presented in Ref. [82] which neglects the polarization drift effects as well.

In order to derive formally the diffusion associated to gyrokinetic corrections, the following relations are introduced:

$$\left. \frac{\partial}{\partial v} \right|_{\mathbf{x}} = \left. \frac{\partial}{\partial v} \right|_{\mathbf{R}} + \frac{\partial \mathbf{R}}{\partial v} \cdot \frac{\partial}{\partial \mathbf{R}} = \left. \frac{\partial}{\partial v} \right|_{\mathbf{R}} - \frac{\partial \boldsymbol{\rho}_L}{\partial v} \cdot \frac{\partial}{\partial \mathbf{R}} = \left. \frac{\partial}{\partial v} \right|_{\mathbf{R}} - \frac{1}{v} \boldsymbol{\rho}_L \cdot \frac{\partial}{\partial \mathbf{R}}, \quad (5.110)$$

$$\left. \frac{\partial}{\partial \xi} \right|_{\mathbf{x}} = \left. \frac{\partial}{\partial \xi} \right|_{\mathbf{R}} + \frac{\partial \mathbf{R}}{\partial \xi} \cdot \frac{\partial}{\partial \mathbf{R}} = \left. \frac{\partial}{\partial \xi} \right|_{\mathbf{R}} - \frac{\partial \boldsymbol{\rho}_L}{\partial \xi} \cdot \frac{\partial}{\partial \mathbf{R}} = \left. \frac{\partial}{\partial \xi} \right|_{\mathbf{R}} + \frac{\xi}{1 - \xi^2} \boldsymbol{\rho}_L \cdot \frac{\partial}{\partial \mathbf{R}}, \quad (5.111)$$

$$\left. \frac{\partial}{\partial \alpha} \right|_{\mathbf{x}} = \left. \frac{\partial}{\partial \alpha} \right|_{\mathbf{R}} + \frac{\partial \mathbf{R}}{\partial \alpha} \cdot \frac{\partial}{\partial \mathbf{R}} = \left. \frac{\partial}{\partial \alpha} \right|_{\mathbf{R}} - \frac{\partial \boldsymbol{\rho}_L}{\partial \alpha} \cdot \frac{\partial}{\partial \mathbf{R}} = \left. \frac{\partial}{\partial \alpha} \right|_{\mathbf{R}} + \frac{\mathbf{v}_\perp}{\Omega} \cdot \frac{\partial}{\partial \mathbf{R}}, \quad (5.112)$$

where $\xi = v_{||}/v = \cos \theta$ is the cosine of the pitch angle θ , α is the gyroangle and $\partial/\partial|_{\mathbf{R}}$ stands for the derivative at constant gyrocenter position. The velocity derivative thus reads, using $\partial_\theta = -\sin \theta \partial_\xi = -\sqrt{1 - \xi^2} \partial_\xi$ and the gradient in spherical coordinates (v, θ, α) :

$$\left. \frac{\partial}{\partial \mathbf{v}} \right|_{\mathbf{x}} = \left. \frac{\partial}{\partial \mathbf{v}} \right|_{\mathbf{R}} - \frac{1}{v} \left[\boldsymbol{\rho}_L \cdot \frac{\partial}{\partial \mathbf{R}} \right] \hat{e}_v + \frac{1}{v_\perp} \left(-\xi \left[\boldsymbol{\rho}_L \cdot \frac{\partial}{\partial \mathbf{R}} \right] \hat{e}_\theta + \left[\frac{\mathbf{v}_\perp}{\Omega} \cdot \frac{\partial}{\partial \mathbf{R}} \right] \hat{e}_\alpha \right). \quad (5.113)$$

Note that, since the Larmor radius is perpendicular to the magnetic field, $\boldsymbol{\rho}_L \cdot \partial_{\mathbf{R}} = \boldsymbol{\rho}_L \cdot \partial_\perp$

here. Without loss of generality, the axis $\alpha = 0$ is aligned with $\boldsymbol{\partial}_\perp$, leading to:

$$\mathbf{v}_\perp \cdot \boldsymbol{\partial}_R = v_\perp \sin \alpha \partial_\perp, \quad (5.114)$$

$$\boldsymbol{\rho}_L \cdot \boldsymbol{\partial}_R = \rho_L \cos \alpha \partial_\perp. \quad (5.115)$$

The velocity derivative is then, making use of Eqs. (5.114) and (5.115) in Eq. (5.113):

$$\left. \frac{\partial}{\partial \mathbf{v}} \right|_{\mathbf{x}} = \left. \frac{\partial}{\partial \mathbf{v}} \right|_{\mathbf{R}} - \frac{1}{v} \rho_L \cos \alpha \partial_\perp \hat{e}_v - \frac{\xi \cos \alpha}{\Omega} \partial_\perp \hat{e}_\theta + \frac{\sin \alpha}{\Omega} \partial_\perp \hat{e}_\alpha. \quad (5.116)$$

In order to analyse the different gyroterms of the self-collision operator $C[f_{LM}, \delta f]$, we use the linearized form given by Eq. (5.41), valid for ion-ion collisions. Each term is treated separately.

5.12.1 Analytical expressions

The guiding center correction to the parallel drag term can be written, using Eqs. (5.41) and (5.110):

$$\Delta C_{GK, \text{drag}} = \frac{\bar{v} v_{th}^2}{2} \rho_L \cos \alpha \left(\frac{2H(\mathbf{v})}{v_{th}^2} - \frac{K(\mathbf{v})}{v^2} \right) \partial_\perp \delta f. \quad (5.117)$$

It appears immediately that there is no gyrokinetic correction coming from the drag term, since the gyrokinetic correction to the drag term $\Delta C_{GK, \text{drag}}$ given by Eq. (5.117) clearly vanishes once gyroaveraged. The gyrokinetic correction to the energy diffusion term is given again by Eqs. (5.41) and (5.110):

$$\Delta C_{GK, \text{energy}} = \frac{\bar{v} v_{th}^2 \rho_L^2}{2 v^2} \cos^2 \alpha H(\mathbf{v}) \partial_\perp^2 \delta f. \quad (5.118)$$

The associated gyrodifffusion coefficient is thus:

$$D_{GK, \text{energy}} = \left\langle \frac{\bar{v} v_{th}^2 \rho_L^2}{2 v^2} \cos^2 \alpha H(\mathbf{v}) \right\rangle_\alpha = \frac{\bar{v}}{4\Omega^2} v_{th}^2 H(\mathbf{v}) (1 - \xi^2), \quad (5.119)$$

where $\Omega = v_\perp / \rho_L$ is the cyclotron frequency. The gyrodifffusion coming from the Lorentz operator can be evaluated directly from Eqs. (5.111) and (5.112). Indeed, using Eq. (5.54):

$$\begin{aligned} \langle \Delta \hat{L}^2 \rangle_\alpha &= \left\langle \frac{\xi}{1 - \xi^2} \rho_L \cos \alpha \partial_\perp (1 - \xi^2) \frac{\xi}{1 - \xi^2} \rho_L \cos \alpha \partial_\perp \right\rangle_\alpha \\ &+ \left\langle \frac{1}{1 - \xi^2} \rho_L \sin \alpha \partial_\perp \rho_L \sin \alpha \partial_\perp \right\rangle_\alpha = \frac{v^2 \xi^2}{2\Omega^2} \partial_\perp^2 + \frac{v^2}{2\Omega^2} \partial_\perp^2, \end{aligned} \quad (5.120)$$

which gives the following diffusion coefficient, according to Eq. (5.41):

$$D_{GK, \text{pitch angle scattering}} = \frac{v_{th}^2}{8v^2} K(\mathbf{v}) \frac{\bar{v}}{\Omega^2} v^2 (1 + \xi^2) = \frac{v_{th}^2}{8} K(\mathbf{v}) \frac{\bar{v}}{\Omega^2} (1 + \xi^2). \quad (5.121)$$

Finally, the gyrodiffusion coefficient in gyrocenter configuration space is obtained by summing contributions from Eqs. (5.119) and (5.121):

$$D_{GK} = \frac{\rho_{L,th}^2 \bar{\nu}}{8} [2H(\mathbf{v})(1 - \xi^2) + K(\mathbf{v})(1 + \xi^2)], \quad (5.122)$$

which is proportional to $\rho_{L,th}^2 \bar{\nu} = v_{th}^2 \bar{\nu} / \Omega^2$ as expected, and definitely small compared to turbulent diffusion coefficients presented in Sec. 2.6.2 for reasonable collisionalities. The gyrodiffusion coefficient corresponds in fact to the classical transport coefficient and can be neglected for neo-classical studies in large aspect ratio tokamaks where the Larmor radius is much smaller than the banana width $\Delta r_b \simeq q_s \rho_L / \sqrt{\epsilon}$. In spherical tokamaks with small aspect ratio, the gyrodiffusion coefficient is however important for collisional transport studies as the Larmor radius is of the order of the banana width in a device where $\sqrt{\epsilon} \sim 1$.

5.12.2 In a PIC code with magnetic coordinates

In practice, the gyrokinetic corrections are implemented in the ORB5 ion-ion collision operator through random kicks $\Delta \mathbf{R}$ of marker positions in configuration space. The marker kick, as the Larmor radius, must lie in the poloidal plane. The variation of position is written as follows:

$$\Delta \mathbf{R} = A_1 \sqrt{2D_{GK}\Delta t} \left(\frac{\nabla s}{|\nabla s|} \cos(2\pi A_2) + \frac{\mathbf{B} \times \nabla s}{|\mathbf{B} \times \nabla s|} \sin(2\pi A_2) \right),$$

where A_1 is a random number sampled from a PDF with average 0 and variance 1, and A_2 is a random number taken from a uniform distribution between 0 and 1. D_{GK} is given by Eq. (5.122). In order to perform the kick, we use the pseudo-cartesian coordinates defined as follows:

$$\Xi = s \cos \theta^*, \quad (5.123)$$

$$\eta = s \sin \theta^*. \quad (5.124)$$

Introducing the notation

$$\Delta R = A_1 \sqrt{2D_{GK}\Delta t} = A_1 \frac{1}{2} \rho_L \sqrt{\bar{\nu} \Delta t [2H(\mathbf{v})(1 - \xi^2) + K(\mathbf{v})(1 + \xi^2)]}, \quad (5.125)$$

the kick in the variable Ξ is

$$\begin{aligned} \Delta \Xi &= \Delta \mathbf{R} \cdot \nabla \Xi \\ &= \Delta R \left[\left(|\nabla s| \cos \theta^* - \frac{\nabla s \cdot \nabla \theta^*}{|\nabla s|} s \sin \theta^* \right) \cos(2\pi A_2) \right. \\ &\quad \left. + \frac{F(\Psi)}{J_{s\theta^*} B |\nabla s|} s \sin \theta^* \sin(2\pi A_2) \right], \end{aligned} \quad (5.126)$$

while the kick in the variable η reads

$$\begin{aligned}\Delta\eta &= \Delta\mathbf{R} \cdot \nabla\eta \\ &= \Delta R \left[\left(|\nabla s| \sin\theta^* + \frac{\nabla s \cdot \nabla\theta^*}{|\nabla s|} s \cos\theta^* \right) \cos(2\pi A_2) \right. \\ &\quad \left. - \frac{F(\Psi)}{J_{s\theta^*\varphi} B |\nabla s|} s \cos\theta^* \sin(2\pi A_2) \right],\end{aligned}\tag{5.127}$$

where $J_{s\theta^*\varphi}$ is the Jacobian of the magnetic coordinate system (s, θ^*, φ) . The new magnetic coordinates are eventually built:

$$s + \Delta s = \sqrt{(\eta + \Delta\eta)^2 + (\Xi + \Delta\Xi)^2},\tag{5.128}$$

$$\theta^* + \Delta\theta^* = \text{Modulo}(2\pi, \text{ATAN2}(\eta + \Delta\eta, \Xi + \Delta\Xi)),\tag{5.129}$$

where ATAN2 is the standard variation of the arctangent function, related to computer languages, which produces results in the range $]-\pi, \pi]$. Unfortunately, the gyrokinetic corrections are not properly implemented for the ion-ion collision background reaction term $C[\delta f, f_{LM}]$, preventing the gyrokinetic collision operator in ORB5 from being relevant for analyzing collisional Finite-Larmor-Radius (FLR) effects. Accounting for FLR corrections in the background reaction term appears to be numerically tricky in a PIC code, especially within the frame of ORB5 algorithm which preserves to round-off precision the density, parallel momentum and kinetic energy. No practical solution has been found so far regarding FLR correction implementation in this part of the collision operator.

Chapter 6

Neoclassical studies using ORB5

6.1 Introduction

Collisional transport in a tokamak, so-called neoclassical transport briefly introduced in Sec. 2.6.1, relies on a well established theory [43] [44] providing estimates of transport coefficients based on certain approximations. Those estimates provide a mean of checking the validity of neoclassical simulations, which can further be applied to more complicated cases where an analytical solution is not available. Several studies of neoclassical transport have been performed in the past by codes designed specifically for carrying out computations within the neoclassical approximations [73], [90], [91], i.e. in particular $\Delta r_b/L_c \ll 1$, where Δr_b is the banana width and L_c the characteristic gradient length of the equilibrium profiles. However, going beyond neoclassical approximations is clearly of interest. This is achieved through the implementation of collision operators in global drift- or gyro-kinetic codes including full guiding-center trajectories, which opens many possibilities of investigating issues related to neoclassical transport beyond neoclassical approximations. Various studies of neoclassical transport and equilibria using global codes accounting for Finite-Banana-Width effects have thus already been performed, both considering Lagrangian [85], [92], [93], [94] and Eulerian [95], [96] methods. The corresponding axisymmetric electric field ensuring ambipolarity has also been investigated [92], [93], [94], showing its crucial effect on the neoclassical equilibrium. Such global neoclassical simulations including full ion and electron dynamics are studied in this Chapter.

Neoclassical transport benchmarks, both for ions and electrons, are first shown here in order to validate the implementation of the collision operators described in Chapter 5. Simulations are initialized with $\delta f_{LM}(t=0) = 0$. Invoking the axisymmetry of the neoclassical equilibrium which may be assumed in a tokamak, the binning for the background reaction operator described in Chapter 5 needs only to be performed in the poloidal plane (single bin in the toroidal direction). We use typically 64 bins in the radial direction and 128 bins in the poloidal direction. These values are determined essentially by profile gradient lengths. The typical number of markers used in the neoclassical simulations ranges from 100 millions for a typical global case ($\rho^* = 1/150$) with self-consistent electric field to 20 millions for local simulations assuming no electric field. The time step and the total simulation time are dictated by the transit time and the collision time respectively for the banana regime and inversely for the collisional regime.

6.2 Neoclassical ordering

In the frame of the neoclassical approach, the Finite-Larmor-Radius (FLR) effects are neglected in order to retain only the Finite-Orbit-Width (FOW) effects. The starting point for the neoclassical theory is thus the drift-kinetic equation, which reads in the guiding center variables $(\mathbf{R}, \mathcal{E}, \mu) = (\Psi, \theta, \varphi, \mathcal{E}, \mu)$, with $\mathcal{E} = mv^2/2$ the kinetic energy:

$$\frac{\partial f}{\partial t} + \left(v_{||} \hat{b} + \mathbf{v}_d \right) \cdot \nabla f = -C[f], \quad (6.1)$$

where $v_{||} = \sqrt{2[\mathcal{E} - \mu B(\Psi, \theta)]/m}$ and C is the non-linear Landau collision operator including intra- and inter-collisions in general. The distribution function is split into a main part f_0 and a perturbed part δf :

$$f = f_0 + \delta f, \quad (6.2)$$

where:

$$\frac{\delta f}{f_0} \sim \frac{v_d}{v_{||}} \sim \frac{\Delta r_b}{L_c} \sim \delta, \quad (6.3)$$

$v_d = |\mathbf{v}_{\nabla B} + \mathbf{v}_c|$ being the magnetic drift velocity, the main drive of neoclassical transport related to the magnetic field curvature. $\delta \ll 1$ is the small parameter of standard neoclassical ordering. Each order in the neoclassical equation (6.1) is treated separately. Note that no equilibrium electric field has been considered here.

6.2.1 Zeroth-Order equation

Invoking the axisymmetry of the neoclassical equilibrium, the parallel advection operator can be explicitated:

$$\mathbf{v}_{||} \cdot \nabla = v_{||} \frac{\mathbf{B} \cdot \nabla \theta}{B} \frac{\partial}{\partial \theta} = \frac{B_\theta v_{||}}{B r} \frac{\partial}{\partial \theta} \simeq \frac{v_{||}}{R q_s} \frac{\partial}{\partial \theta}, \quad (6.4)$$

where the last step is obtained within the circular large aspect ratio approximation. The stationary neoclassical equation at zeroth-order in δ thus reads:

$$-C[f_0] = v_{||} \hat{b} \cdot \nabla f_0 = \frac{v_{||}}{q_s R} \frac{\partial f_0}{\partial \theta}. \quad (6.5)$$

A non-shifted local Maxwellian $f_{LM}(\Psi, \mathcal{E})$ is obviously solution of Eq. (6.5). Indeed, on one hand a local Maxwellian is a stationary state to the Landau collision operator: $C[f_{LM}(\Psi, \mathcal{E})] = 0$. On the other hand $\partial f_{LM}(\Psi, \mathcal{E})/\partial \theta = 0$. Note that a shifted Maxwellian is not solution of Eq. (6.5), due to its θ -dependence through $v_{||} = \sqrt{2[\mathcal{E} - \mu B(\Psi, \theta)]/m}$.

6.2.2 First-Order equation

The explicit form of the solution at zeroth-order is used in order to compute the next order neoclassical equation. At first-order in δ , the stationary form of Eq. (6.1) becomes:

$$v_{||}\hat{b} \cdot \nabla \delta f + \mathbf{v}_d \cdot \nabla f_{LM} = \frac{v_{||}}{q_s R} \frac{\partial \delta f}{\partial \theta} + \mathbf{v}_d \cdot \nabla \Psi \frac{\partial f_{LM}}{\partial \Psi} = -\hat{C}[\delta f], \quad (6.6)$$

where \hat{C} is the linearized Landau collision operator. Since, for low pressure plasma (Eq. (3.24) in Ref. [43]):

$$\mathbf{v}_d = -v_{||} \left[\hat{b} \times \nabla \left(\frac{v_{||}}{\Omega} \right) \right], \quad (6.7)$$

the axisymmetry of a tokamak leads to:

$$\mathbf{v}_d \cdot \nabla \Psi = \mathbf{v}_{||} \cdot \nabla \left(\frac{F(\Psi)v_{||}}{\Omega} \right), \quad (6.8)$$

where $F(\Psi) = RB_\varphi$. The stationary form of the first-order neoclassical equation reads:

$$\mathbf{v}_{||} \cdot \nabla \left(\frac{F(\Psi)v_{||}}{\Omega} \frac{\partial f_{LM}}{\partial \Psi} + \delta f \right) = \frac{v_{||}}{q_s R} \frac{\partial}{\partial \theta} \left(\frac{F(\Psi)v_{||}}{\Omega} \frac{\partial f_{LM}}{\partial \Psi} + \delta f \right) = -\hat{C}[\delta f]. \quad (6.9)$$

6.2.2.1 Solution for zero collisionality

A solution to Eq. (6.6) depends on the form of the collision operator \hat{C} and in general is not possible to compute analytically without approximation. Here a solution $\delta f^{(0)}$ in the limit of no collisionality $\hat{C} = 0$ is derived. The general first-order neoclassical equation with $\hat{C} = 0$ is thus considered:

$$\frac{\partial \delta f^{(0)}}{\partial t} + \frac{v_{||}}{Rq_s} \frac{\partial}{\partial \theta} \left(\frac{F(\Psi)v_{||}}{\Omega} \frac{\partial f_{LM}}{\partial \Psi} + \delta f^{(0)} \right) = 0, \quad (6.10)$$

leading to:

$$\delta f^{(0)} = - \underbrace{\frac{F(\Psi)v_{||}}{\Omega} \frac{\partial f_{LM}}{\partial \Psi}}_{\delta f_s} + G(z, t), \quad (6.11)$$

where δf_s is a stationary solution to Eq. (6.10) and $G(z, t)$ is a function of time t and phase space variables z . The initial condition $\delta f^{(0)}(t=0) = 0$ is considered, such that $G(z, t=0) = -\delta f_s$. Furthermore, G satisfies the following equation:

$$\frac{\partial G}{\partial t} + \frac{v_{||}}{Rq_s} \frac{\partial G}{\partial \theta} = 0, \quad (6.12)$$

which can be solved by integrating along zeroth-order trajectories along magnetic field lines:

$$G(z, t) = G(z_0, 0) = -\delta f_s(z_0), \quad (6.13)$$

where z_0 is the origin of the trajectory at $t = 0$ which ends at z at time t . As a result of filamentation effect, the asymptotic behaviour (in time) of G is given by:

$$\lim_{t \rightarrow \infty} G(z, t) = -\langle \delta f_s \rangle_{\text{traj}} = \left\langle \frac{v_{\parallel}}{\Omega} \right\rangle_{\text{traj}} F(\Psi) \frac{\partial f_{LM}}{\partial \Psi}. \quad (6.14)$$

$\langle \cdot \rangle_{\text{traj}}$ stands for the average over the zeroth-order trajectory along the field lines, i.e. considering $\mathbf{v} = v_{\parallel} \hat{\mathbf{b}}$. It is in fact a time average defined by:

$$\langle \cdots \rangle_{\text{traj}} = \frac{1}{(t_2 - t_1)} \int_{t_1}^{t_2} \cdots dt = \frac{1}{(t_2 - t_1)} \int_{\theta(t_1)}^{\theta(t_2)} \cdots \frac{B d\theta}{v_{\parallel} \mathbf{B} \cdot \nabla \theta}, \quad (6.15)$$

where t_1 and t_2 are the starting time and the ending time of the particle trajectory respectively, with corresponding poloidal angles $\theta(t_1)$ and $\theta(t_2)$. The neoclassical equation, in the limit of no collisions, has thus the following stationary solution satisfying the considered initial condition $\delta f^{(0)}(t = 0) = 0$:

$$\delta f^{(0)}(t \rightarrow \infty) = F(\Psi) \frac{\partial f_{LM}}{\partial \Psi} \left[\left\langle \frac{v_{\parallel}}{\Omega} \right\rangle_{\text{traj}} - \frac{v_{\parallel}}{\Omega} \right]. \quad (6.16)$$

Note that $\langle v_{\parallel}/\Omega \rangle_{\text{traj}} = 0$ for trapped particles. It has to be pointed out that, contrary to the stationary solution to Eq. (6.10) [given by Eq. (6.16)], the stationary solution to the collisional neoclassical equation [Eq. (6.6) with $\hat{C} \neq 0$] is essentially independent of the initial conditions as a result of the dissipative nature of the collision operator. Indeed, considering different initial distributions with the same toroidal and poloidal flows leads to the same collisional equilibrium. Eq. (6.16) will be further considered in Sec. 6.4 for a large aspect ratio circular cross-section tokamak geometry.

6.3 Some features of neoclassical fluxes

Although the purpose of this work is not to provide analytical solutions to the general neoclassical equation (6.6), it is possible to derive some general consequences related to collisional transport even without specifying the form of the collision operator \hat{C} , following computations performed in Ref. [44]. It is important to note that the particle and kinetic energy fluxes associated to a local Maxwellian background through magnetic curvature and gradient drift velocities ($\sim f_{LM} d\Psi/dt|_0$) do vanish for the considered circular *ad hoc* equilibrium. The following general relation is derived:

$$(\mathbf{B} \times \nabla B) \cdot \nabla \Psi = F(\Psi) \frac{\partial B}{\partial \theta} (\nabla \varphi \times \nabla \theta) \cdot \nabla \Psi = \frac{F(\psi)}{J_{\Psi\theta\varphi}} \frac{\partial B}{\partial \theta}, \quad (6.17)$$

where $F(\Psi) = RB_\varphi$ and $J_{\Psi\theta\varphi}$ is the Jacobian of the magnetic coordinate system (Ψ, θ, φ) . The unperturbed particle flux associated to a local Maxwellian background is computed as follows:

$$\begin{aligned}
 & \left\langle \frac{1}{|\nabla\Psi|} \int d^3v f_{LM} \frac{d\Psi}{dt} \Big|_0 \right\rangle_S \\
 &= \frac{mn}{\sqrt{2\pi}qv_{th}^3} \left\langle \frac{\mathbf{B} \times \nabla B}{B^2} \cdot \frac{\nabla\Psi}{|\nabla\Psi|} \int_{-\infty}^{\infty} e^{-mv_{\parallel}^2/2T} v_{\parallel}^2 dv_{\parallel} \int_0^{\infty} e^{-\mu B/T} d\mu \right\rangle_S \\
 &+ \frac{mn}{\sqrt{2\pi}qv_{th}^3} \left\langle \frac{\mathbf{B} \times \nabla B}{B^2} \cdot \frac{\nabla\Psi}{|\nabla\Psi|} \int_{-\infty}^{\infty} e^{-mv_{\parallel}^2/2T} dv_{\parallel} \int_0^{\infty} e^{-\mu B/T} \mu B d\mu \right\rangle_S \\
 &= 2 \frac{nT}{q} \left\langle \frac{F(\Psi)}{J_{\Psi\theta\varphi} B^3 |\nabla\Psi|} \frac{\partial B}{\partial \theta} \right\rangle_S = - \frac{2\pi nT}{q} \frac{F(\Psi)}{S(\Psi)} \int_0^{2\pi} \frac{\partial}{\partial \theta} \frac{1}{B^2} d\theta = 0,
 \end{aligned} \tag{6.18}$$

where the next-to-last step has been performed by integrating by parts, and where $S(\Psi)$ is the flux surface defined by Eq. (A.3). The same conclusion is obtained for the kinetic energy flux. It is possible to show that the particle and kinetic energy fluxes associated to $f_{CM} d\Psi/dt|_0$ do vanish as well. However, as explained in Appendix A, the potential energy flux due to a local Maxwellian background does generally not vanish.

Considering certain forms of the collision operator, it is shown in this Section that the neo-classical particle and kinetic energy fluxes associated to the fluctuating part of the distribution δf do vanish as well. The pitch angle variable $\lambda = v_{\perp}^2/v^2 B = \mu/\mathcal{E}$ is first introduced. The infinitesimal volume element in velocity space d^3v takes the form:

$$d^3v = \sum_{\sigma} \frac{\pi B v^3 dv d\lambda}{|v_{\parallel}|} = \sum_{\sigma} \frac{2\pi B \mathcal{E} d\mathcal{E} d\lambda}{m^2 |v_{\parallel}|}, \tag{6.19}$$

where the sum is taken over σ , the sign of the parallel velocity. Let $S(\Psi)$ stand for the flux surface at a given radial coordinate Ψ . We define the flux-surface-averaged flux $\mathcal{F}(\Psi)$ of a general moment $\mathcal{M}(v, \lambda)$ as follows, using Eq. (6.8):

$$\begin{aligned}
 \mathcal{F}(\Psi) &= \left\langle \frac{1}{|\nabla\Psi|} \int d^3v \mathcal{M}(v, \lambda) \mathbf{v}_d \cdot \nabla\Psi \delta f \right\rangle_S \\
 &= \frac{2\pi}{S(\Psi)} \int_0^{2\pi} J_{\Psi\theta\varphi} d\theta \int d^3v \mathcal{M}(v, \lambda) \nabla_{\parallel} \left(\frac{F(\Psi) v_{\parallel}}{\Omega} \right) \delta f v_{\parallel}.
 \end{aligned} \tag{6.20}$$

Writing explicitly d^3v in terms of the (v, λ) variables using Eq. (6.19) gives:

$$\mathcal{F}(\Psi) = \frac{2\pi}{S(\Psi)} \int_0^{2\pi} J_{\Psi\theta\varphi} d\theta \sum_{\sigma} \pi B \int v^3 dv d\lambda \mathcal{M}(v, \lambda) \nabla_{\parallel} \left(\frac{F(\Psi) |v_{\parallel}|}{\Omega} \right) \delta f. \tag{6.21}$$

Invoking the following identity, valid for any functions $A(\Psi, \theta)$ et $C(\Psi, \theta)$:

$$\int_0^{2\pi} A(\nabla_{\parallel} C) B J_{\Psi\theta\varphi} d\theta = - \int_0^{2\pi} C(\nabla_{\parallel} A) B J_{\Psi\theta\varphi} d\theta, \tag{6.22}$$

the flux may be written from Eq. (6.21) as:

$$\mathcal{F}(\Psi) = -\frac{2\pi}{S(\Psi)} \int_0^{2\pi} J_{\Psi\theta\varphi} d\theta \int d^3v \mathcal{M}(v, \lambda) \frac{F(\Psi)v_{\parallel}}{\Omega} \nabla_{\parallel} \delta f. \quad (6.23)$$

Eq. (6.6) is arranged as follows:

$$v_{\parallel} \nabla_{\parallel} \delta f = -\mathbf{v}_d \cdot \nabla f_{LM} - \hat{C}[\delta f]. \quad (6.24)$$

Inserting (6.24) into (6.23) leads to:

$$\mathcal{F}(\Psi) = \frac{2\pi F(\Psi)}{S(\Psi)} \int_0^{2\pi} \frac{J_{\Psi\theta\varphi} d\theta}{\Omega} \int d^3v \mathcal{M}(v, \lambda) \left(\mathbf{v}_d \cdot \nabla f_{LM} + \hat{C}[\delta f] \right) v_{\parallel}.$$

For estimating the particle flux Γ [$\mathcal{M}(v, \lambda) = 1$] and energy flux Q [$\mathcal{M}(v, \lambda) = mv^2/2$], the contribution from the term $v_{\parallel} \mathbf{v}_d \cdot \nabla f_{LM}$ in the integral over velocity space does clearly vanish (odd function with respect to v_{\parallel}). Thus:

$$\Gamma(\Psi) = 2\pi \frac{F(\Psi)}{S(\Psi)} \int_0^{2\pi} \frac{J_{\Psi\theta\varphi} d\theta}{\Omega} \int d^3v \hat{C}[\delta f] v_{\parallel}. \quad (6.25)$$

$$Q(\Psi) = 2\pi \frac{F(\Psi)}{S(\Psi)} \int_0^{2\pi} \frac{J_{\Psi\theta\varphi} d\theta}{\Omega} \int d^3v \hat{C}[\delta f] \frac{mv^2 v_{\parallel}}{2}. \quad (6.26)$$

It appears clearly from Eq. (6.25) that a collision operator which is parallel momentum conserving, as for instance a self-collision operator, does not produce any particle flux Γ at the lowest order in the frame of the neoclassical theory. This latter property is verified by the ORB5 self-collision operator, as shown in Figure 6.1 presenting the time evolution of the neoclassical ion particle flux Γ at mid-radius $r/a = 0.5$, considering the CYCLONE case parameters and no electric field, for the collisionality $\nu^* = 3.8$. The self-collision operator nevertheless drives a neoclassical energy flux Q , as Eq. (6.26) in general does not vanish to zero. Another natural consequence of Eqs. (6.25) and (6.26) is the absence of neoclassical particle and energy fluxes in a collisionless system ($\hat{C} = 0$). Note that the flux derivation presented in this section is not valid for the parallel momentum flux since $mv_{\parallel} = \sqrt{2m\mathcal{E}}\sqrt{1 - \lambda B(\Psi, \theta)} \neq \mathcal{M}(v, \lambda)$. However, a collisionless system with no perturbed fields drives no transport, and in particular no parallel momentum transport. As a consequence, the establishment of stationary collisionless current profiles in ORB5 simulations is thus expected, as studied in the next Section.

6.4 Collisionless and collisional contributions to the parallel current

In this Section, an analytical model for predicting the collisionless unperturbed parallel current in a tokamak is derived [J. P. Graves, *Private Communications*]. The proposed drift-kinetic model assumes no electric field and describes an effective current similar to the diamagnetic current, however related to FOW effects instead of FLR effects. Note however that the FLR

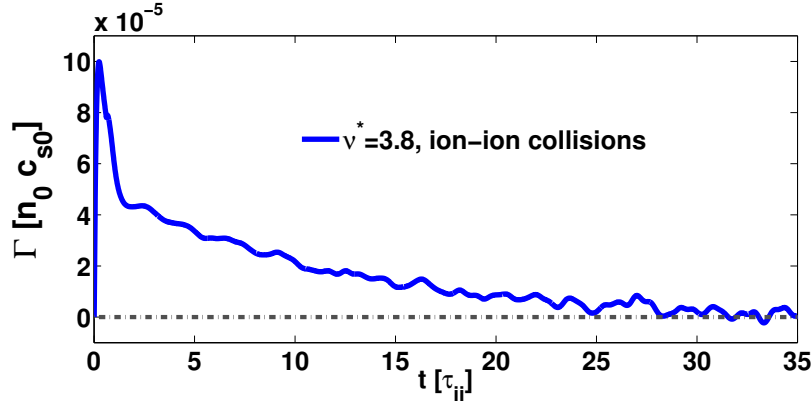


Figure 6.1: CYCLONE case parameters: Time evolution of the neoclassical ion particle flux Γ at mid-radius $r/a = 0.5$ with only ion-ion collisions and no electric field. After the initial transient and relaxation phase, the particle flux relaxes to zero, consistently with neoclassical theory.

diamagnetic current is not captured by the drift-kinetic model developed here. In the considered model, the current due to the stationary solution $\delta f^{(0)}$ of the collisionless drift-kinetic equation, given by Eq. (6.16), is computed.

6.4.1 Trapped particle contribution

The stationary solution $\delta f^{(0)}$ for trapped particle population reads, according to (6.16), as $\langle v_{||}/\Omega \rangle_{\text{traj}} = 0$ for trapped particles:

$$\delta f_{\text{trap}}^{(0)} = -\frac{\partial f_{LM}}{\partial \Psi} \frac{F(\Psi)v_{||}}{\Omega}. \quad (6.27)$$

The contribution to the poloidally averaged parallel velocity coming from the trapping region is computed as follows, making use of the pitch angle boundaries for a trapped particle $1/B_{\text{max}} < \lambda = \mu/\mathcal{E} < 1/B_{\text{min}}$:

$$\begin{aligned} \langle V_{||}^t \rangle_{\theta} &= \frac{1}{2\theta_b} \int_{-\theta_b}^{\theta_b} d\theta \int_t d^3v v_{||} \delta f_{\text{trap}}^{(0)} \\ &= \frac{\pi}{m^2\theta_b} \sum_{\sigma} \int_{-\theta_b}^{\theta_b} d\theta \int_0^{\infty} d\mathcal{E} \mathcal{E} \int_{1/B_{\text{max}}}^{1/B_{\text{min}}} d\lambda B \frac{v_{||}}{|v_{||}|} \delta f_{\text{trap}}^{(0)}, \end{aligned} \quad (6.28)$$

where Eq. (6.19) is used for writing the velocity space infinitesimal volume d^3v . Using the solution (6.27) in Eq. (6.28) leads to:

$$\langle V_{||}^t \rangle_{\theta} = -\frac{2\pi F(\Psi)}{mq\theta_b} \int_{-\theta_b}^{\theta_b} d\theta \int_0^{\infty} d\mathcal{E} \mathcal{E} \int_{1/B_{\text{max}}}^{1/B_{\text{min}}} d\lambda |v_{||}| \frac{\partial f_{LM}}{\partial \Psi}, \quad (6.29)$$

where the factor 2 comes from the sum over both signs of the parallel velocity. The parallel velocity can be written as follows:

$$|v_{||}| = \sqrt{2(\mathcal{E} - \mu B)/m} = \sqrt{2\mathcal{E}(1 - \lambda B)/m}. \quad (6.30)$$

Assuming circular concentric magnetic surfaces, at first order in ϵ the tokamak magnetic field takes the form $B = B_0(1 - \epsilon \cos \theta)$, leading to:

$$|v_{||}(\theta)| = 2\sqrt{\mu B_0 \epsilon (k^2 - \sin^2 \theta/2)/m} = 2\sqrt{\lambda \mathcal{E} B_0 \epsilon (k^2 - \sin^2 \theta/2)/m}, \quad (6.31)$$

where $\epsilon = r/R_0$ is the local inverse aspect ratio and having introduced a new pitch angle variable:

$$k^2 = \frac{1 + \lambda B_0 (\epsilon - 1)}{2\epsilon \lambda B_0}. \quad (6.32)$$

λ is rewritten as follows:

$$\lambda = [B_0(\epsilon(2k^2 - 1) + 1)]^{-1}. \quad (6.33)$$

Differentiating the definition (6.32) gives:

$$d\lambda = -2\epsilon B_0 \lambda^2 dk^2 = \frac{-2\epsilon}{B_0[\epsilon(2k^2 - 1) + 1]^2} dk^2. \quad (6.34)$$

Since the parallel velocity of a trapped particle does vanish at some point of its trajectory, the trapping condition becomes $0 \leq k^2 \leq 1$. A new rescaled poloidal variable X is introduced as well, such that:

$$k \sin X = \sin \theta/2. \quad (6.35)$$

The bounce limit angle corresponds to $X = \pi/2$, so that:

$$\frac{1}{\theta_b} \int_{-\theta_b}^{\theta_b} \sqrt{(k^2 - \sin^2 \theta/2)} d\theta = \frac{4}{\pi} \int_0^{\pi/2} \frac{k^2 \cos^2 X}{\sqrt{1 - k^2 \sin^2 X}} dX = \frac{4}{\pi} (\mathbf{E}(k^2) + (k^2 - 1)\mathbf{K}(k^2)), \quad (6.36)$$

where \mathbf{E} and \mathbf{K} are the elliptic integrals, respectively of the first and second kind:

$$\mathbf{K}(k^2) = \int_0^{\pi/2} \frac{dX}{\sqrt{1 - k^2 \sin^2 X}}, \quad (6.37)$$

$$\mathbf{E}(k^2) = \int_0^{\pi/2} \sqrt{1 - k^2 \sin^2 X} dX. \quad (6.38)$$

Using the parallel velocity (6.31) in Eq. (6.29) and performing the changes of variable $\theta \rightarrow X$ and $\lambda \rightarrow k^2$, an estimate of the trapped particle current is obtained:

$$\langle V_{||}^t \rangle_\theta = -\frac{32F(\Psi)}{m^{3/2}qB_0} \int_0^\infty \frac{\partial f_{LM}}{\partial \Psi} \mathcal{E}^{3/2} d\mathcal{E} \int_0^1 \frac{\epsilon^{3/2}}{[\epsilon(2k^2 - 1) + 1]^{5/2}} [\mathbf{E}(k^2) + (k^2 - 1)\mathbf{K}(k^2)] dk^2. \quad (6.39)$$

The integral over energy in Eq. (6.39) gives:

$$\int_0^\infty \frac{\partial f_{LM}}{\partial \Psi} \mathcal{E}^{3/2} d\mathcal{E} = \frac{3m^{3/2}}{8\sqrt{2}\pi} n(\Psi) T(\psi) \left[\frac{n'(\Psi)}{n(\Psi)} + \frac{T'(\Psi)}{T(\Psi)} \right] = \frac{3m^{3/2}}{8\sqrt{2}\pi} \frac{\partial P}{\partial \Psi}, \quad (6.40)$$

providing the pressure gradient dependence in the collisionless FOW current:

$$\langle V_{||}^t \rangle_\theta = -\frac{\partial P}{\partial \Psi} \frac{F(\Psi)}{qB_0} \int_0^1 \frac{3}{\pi} \frac{(2\epsilon)^{3/2}}{[\epsilon(2k^2 - 1) + 1]^{5/2}} [\mathbf{E}(k^2) + (k^2 - 1)\mathbf{K}(k^2)] dk^2. \quad (6.41)$$

The remaining integral in Eq. (6.41) has to be computed numerically and gives an estimate of the FOW related parallel current coming from trapped particles, for $F(\Psi) = R_0 B_0$ and retaining only the lowest order term in ϵ :

$$J_{||}^t = q \langle V_{||}^t \rangle_\theta \simeq -\frac{6}{5} \epsilon^{3/2} \frac{\partial P}{\partial \Psi} R_0, \quad (6.42)$$

which is valid in the limit $\epsilon \ll 1$.

6.4.2 Passing particle contribution

The stationary solution $\delta f^{(0)}$ for passing particle population reads:

$$\delta f_{\text{pass}}^{(0)} = \frac{\partial f_{LM}}{\partial \Psi} \left[\left\langle \frac{F(\Psi) v_{||}}{\Omega} \right\rangle_{\text{traj}} - \frac{F(\Psi) v_{||}}{\Omega} \right], \quad (6.43)$$

where the average over unperturbed trajectory is computed by, using Eq. (6.15):

$$\left\langle \frac{m F(\Psi) v_{||}}{qB} \right\rangle_{\text{traj}} = \frac{m}{q\tau_t} \int_0^{2\pi} \frac{BF(\Psi) v_{||}}{B(\mathbf{B} \cdot \nabla \theta) v_{||}} d\theta = \frac{m}{q\tau_t} \int_0^{2\pi} \frac{B_\varphi}{B_\theta} r R d\theta \simeq \frac{2\pi m}{q\tau_t} q_s R_0^2,$$

where the approximations $R \simeq R_0$ and $B_\varphi/B_\theta \simeq q_s R_0/r$ are used. The transit time τ_t is estimated as follows, using the new pitch angle variable $y^2 = 1/k^2$:

$$\begin{aligned} \tau_t &\simeq q_s R_0 \int_0^{2\pi} \frac{d\theta}{|v_{||}|} = \frac{q_s R_0}{\sqrt{2\mathcal{E}/m}} \int_0^{2\pi} \frac{d\theta}{\sqrt{1 - \lambda B}} = \frac{q_s R_0 |y|}{2\sqrt{\epsilon \lambda \mathcal{E} B_0/m}} \int_0^{2\pi} \frac{d\theta}{\sqrt{1 - y^2 \sin^2 \theta/2}} \\ &= \frac{2q_s R_0 |y|}{\sqrt{\epsilon \lambda \mathcal{E} B_0/m}} \mathbf{K}(y^2), \end{aligned} \quad (6.44)$$

where \mathbf{K} is the elliptic function defined by Eq. (6.37). The explicit form of the stationary solution (6.43) is thus:

$$\delta f_{\text{pass}}^{(0)} = \frac{\partial f_{LM}}{\partial \Psi} \frac{m}{q} \left[\underbrace{-\frac{F(\Psi) v_{||}}{B}}_{(1)} + \underbrace{\frac{\pi R_0 \sqrt{\epsilon \lambda \mathcal{E} B_0/m}}{|y| \mathbf{K}(y^2)}}_{(2)} \right]. \quad (6.45)$$

For a passing particle, $0 < \lambda = \mu/\mathcal{E} < 1/B_{\max}$. The contribution to the poloidally averaged parallel velocity coming from the passing region reads thus:

$$\begin{aligned}\langle V_{\parallel}^p \rangle_{\theta} &= \frac{1}{2\pi} \int_0^{2\pi} d\theta \int_p d^3v v_{\parallel} \delta f_{\text{pass}}^{(0)} \\ &= \frac{2}{m^2} \int_0^{2\pi} d\theta \int_0^{\infty} d\mathcal{E} \int_0^{1/B_{\max}} d\lambda B \frac{v_{\parallel}}{|v_{\parallel}|} \delta f_{\text{pass}}^{(0)},\end{aligned}\quad (6.46)$$

where the factor 2 comes from the sum over both signs of the parallel velocity. The contribution (1) of Eq. (6.45) is computed as follows from Eq. (6.46):

$$\langle V_{\parallel}^{p(1)} \rangle_{\theta} = -\frac{2F(\Psi)}{mq} \int_0^{2\pi} d\theta \int_0^{\infty} d\mathcal{E} \int_0^{1/B_{\max}} d\lambda |v_{\parallel}| \frac{\partial f_{LM}}{\partial \Psi}. \quad (6.47)$$

The change of variable $\lambda \rightarrow k^2$, as in Sec. 6.4.1, is then performed. Note that the passing condition is $k^2 > 1$. Using the expression (6.31) for the parallel velocity and integrating directly over the energy variable in order to get the result (6.40) yields:

$$\langle V_{\parallel}^{p(1)} \rangle_{\theta} = -\frac{\partial P}{\partial \Psi} \frac{F(\Psi)}{qB_0} \int_1^{\infty} \frac{3}{\sqrt{2\pi}} \frac{\epsilon^{3/2}}{[\epsilon(2k^2 - 1) + 1]^{5/2}} dk^2 \int_0^{2\pi} \sqrt{(k^2 - \sin^2 \theta/2)} d\theta. \quad (6.48)$$

Using the pitch angle variable $y^2 = 1/k^2$ gives an expression for the integral over θ in terms of the elliptic integral **E**:

$$\int_0^{2\pi} \sqrt{(k^2 - \sin^2 \theta/2)} d\theta = \frac{4}{|y|} \int_0^{\pi/2} \sqrt{(1 - y^2 \sin^2 X)} dX = \frac{4}{|y|} \mathbf{E}(y^2). \quad (6.49)$$

According to Eq. (6.49), writing Eq. (6.48) in terms of the variable y^2 leads to:

$$\langle V_{\parallel}^{p(1)} \rangle_{\theta} = -\frac{\partial P}{\partial \Psi} \frac{F(\Psi)}{qB_0} \int_0^1 \frac{3}{\pi} \frac{(2\epsilon)^{3/2}}{[\epsilon(2 - y^2) + y^2]^{5/2}} \mathbf{E}(y^2) dy^2. \quad (6.50)$$

The contribution (2) of Eq. (6.45) is computed from Eq. (6.46). Integrating directly over θ and performing the change of variable $\lambda \rightarrow y^2$ give:

$$\begin{aligned}\langle V_{\parallel}^{p(2)} \rangle_{\theta} &= \frac{2\pi R_0}{m^{3/2}q} \int_0^{2\pi} d\theta \int_0^{\infty} d\mathcal{E} \int_0^{1/B_{\max}} d\lambda \sqrt{\epsilon \lambda \mathcal{E} B_0} \frac{B}{|y| \mathbf{K}(y^2)} \frac{\partial f_{LM}}{\partial \Psi} \\ &= \frac{4\pi^2 R_0 (B_0)^{3/2}}{m^{3/2}q} \sqrt{\epsilon} \int_0^{\infty} \mathcal{E}^{3/2} \frac{\partial f_{LM}}{\partial \Psi} d\mathcal{E} \int_0^{1/B_{\max}} \frac{\sqrt{\lambda}}{|y| \mathbf{K}(y^2)} d\lambda \\ &= \frac{8\pi^2 R_0}{m^{3/2}q} \sqrt{\epsilon} \int_0^{\infty} \mathcal{E}^{3/2} \frac{\partial f_{LM}}{\partial \Psi} d\mathcal{E} \int_0^1 \frac{\epsilon}{[\epsilon(2 - y^2) + y^2]^{5/2} \mathbf{K}(y^2)} dy^2 \\ &= \frac{\partial P}{\partial \Psi} \frac{R_0}{q} \int_0^1 \frac{3\pi}{4} \frac{(2\epsilon)^{3/2}}{[\epsilon(2 - y^2) + y^2]^{5/2} \mathbf{K}(y^2)} dy^2.\end{aligned}\quad (6.51)$$

Gathering the contributions (6.50) and (6.51) gives the final current of passing particles, assuming $F(\Psi) = R_0 B_0$:

$$J_{\parallel}^p = q \langle V_{\parallel}^{p(1)} \rangle_{\theta} + q \langle V_{\parallel}^{p(2)} \rangle_{\theta} = -\frac{\partial P}{\partial \Psi} R_0 \int_0^1 \frac{(2\epsilon)^{3/2}}{[\epsilon(2-y^2) + y^2]^{5/2}} \left[\frac{3\mathbf{E}(y^2)}{\pi} - \frac{3\pi}{4\mathbf{K}(y^2)} \right] dy^2. \quad (6.52)$$

Performing numerically the integral in Eq. (6.52) provides the final contribution from passing particles to the FOW related parallel current, retaining only the lowest order term in ϵ :

$$J_{\parallel}^p \simeq -0.43\epsilon^{3/2} \frac{\partial P}{\partial \Psi} R_0, \quad (6.53)$$

which is again valid in the limit $\epsilon \ll 1$. Note that, in the frame of the considered collisionless model, the trapped particle contribution (6.42) is dominant compared to the passing particle contribution (6.53) for the large aspect ratio assumption underlying the presented derivation.

6.4.3 Numerical results

The CYCLONE case is considered ($R_0/L_{T_0} = 6.9$, $R_0/L_{n_0} = 2.2$), along with the profile shape of type 2 described in Chapter 3 and a width $\Delta_A = 0.2$. The electron distribution function is initialized to a local Maxwellian: $f_e(t=0) = f_{LM}(\Psi)$ and no electric field is considered. The collisionless analytical predictions derived in Secs. 6.4.1 and 6.4.2 are compared in Figure 6.2 to the ORB5 current profiles for trapped and passing electrons. Collisions are introduced through the Lorentz model described in Chapter 5, retaining only the collisions of electrons on ions. Note that the collisions do not affect the trapped particle current, as presented in Figure 6.2 (a) for $\nu_e^* = 0.5$, where the collisionless FOW current predicted by Eq. (6.42) is shown for reference. The situation is however different for passing particles. Figure 6.2 (b) shows the ORB5 collisionless current profile for passing electrons, compared to the current evaluated in Eq. (6.53). As expected, the trapped contribution is dominant compared to the passing contribution in a collisionless model. However, the passing contribution becomes dominant in a collisional case, due to the trapping-detraping process driven by the Lorentz operator. For $\nu_e^* = 0.5$, the current at mid-radius is $J_{\parallel}^{p,\text{coll}} \sim 0.05[e\langle n \rangle c_s] > J_{\parallel}^t$. The neoclassical current driven by collisions and Finite-Banana-Orbit effects is called the bootstrap current. At low collisionality, it is of the order J_{\parallel}^t/ϵ . It decreases when the collisionality increases [73] and is mainly carried by passing electrons, through the trapping-detraping process due to the electron collisions on ions. Note the difference with respect to the collisionless, FOW related current, which is the same for ions and electrons if $T_e = T_i$, according to Eqs. (6.42) and (6.53). Differences between the current coming from ORB5 simulations and from analytical predictions were expected, since the flux-surface-average performed in ORB5 takes into account the Jacobian of the magnetic coordinate system, while the analytical estimates developed in Secs. 6.4.1 and 6.4.2 neglect the poloidal dependence of the latter Jacobian. Moreover, only the dominant terms with respect to the ϵ ordering are retained in the analytical estimates obtained in Secs. 6.4.1 and 6.4.2. Furthermore, drifts are handled perturbatively in the presented derivations (according to the

neoclassical ordering), while ORB5 makes no approximation on FOW effects.

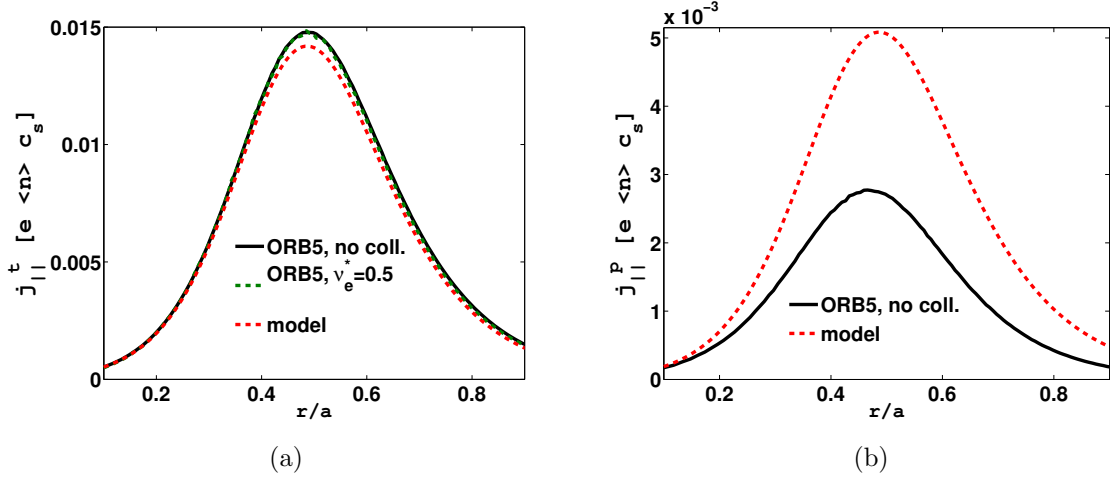


Figure 6.2: (a) Comparison between ORB5 simulations and analytical prediction (6.42) for the trapped particle contribution to the parallel current. Collisions do not affect the trapped particle current. (b) The collisionless ORB5 current coming from passing particles $J_{||}^p$ is compared to the analytical prediction (6.53). Collisional passing particle contribution at $r/a = 0.5$ is of order $J_{||}^{p, \text{coll}} \sim 0.05[e \langle n \rangle c_s]$ for $\nu_e^* = 0.5$ (not shown here).

6.5 Benchmarks for neoclassical transport, no electric field

6.5.1 Electron transport

The results of this sub-section, obtained with the parameters given in Table I and the *ad hoc* equilibrium described in Sec. 2.3, benchmark electron neoclassical transport computed with ORB5 against published numerical and analytical results. One considers the local neoclassical limit, i.e. solving Eq. (3.39) in Chapter 3 for the electron distribution and no electric field. The ion dynamics is not taken into account here as it is decoupled from the electron dynamics in the local limit. Simulations are carried out with either the full linearized electron collision operator, i.e. considering both e-e self-collisions and e-i pitch angle scattering, or the simplified Lorentz model, i.e. considering e-i collisions alone. Note that, in appropriately normalized units, the latter is equivalent to the former when setting the ion charge $Z \rightarrow \infty$.

The particle flux Γ produced by a density gradient alone, considering $\kappa_n = 5$ and $\kappa_T = 0$ according to Eq. (3.59), is shown in Figure 6.3, and the energy flux Q_{kin} produced by a temperature gradient alone, considering $\kappa_n = 0$ and $\kappa_T = 5$, is shown in Figure 6.4. These results are benchmarked against analytical fits to results from the Eulerian Fokker-Planck CQL3D code [90] and analytical results derived for the Lorentz model ($Z \rightarrow \infty$) in the review by Hinton and Hazeltine on neoclassical transport theory [43]. Figures 6.3 (a) and 6.4 (a) present the fluxes at the radial position $s=0.425$ as a function of the effective collisionality ν_e^* , ranging from the low collisionality (banana) regime for $\nu_e^* \ll 1$ up to the collisional regime for $\nu_e^* \gg 1$. Figures

6.3 (b) and 6.4 (b) present the neoclassical fluxes as a function of radius, accounting for the radial variations of density and temperature profiles both for computing the local gradients as well as for estimating collisionality. The collisionality at $s = s_0 = 0.5$ was fixed to $\nu_e^* = 0.18$ and $\nu_e^* = 0.68$ for Figures 6.3 (b) and 6.4 (b) respectively. The agreement between ORB5, CQL3D and the Hinton-Hazeltine results (H-H) may be considered satisfactory, in particular considering that the CQL3D curves are only obtained through approximate fits to the actual simulation results and the Hinton-Hazeltine curves are the result of approximate analytical derivations.

Table I. Run parameters for local neoclassical electron transport benchmarks.

profiles 1 [Eq. (3.59)]	$a/R_0 = 0.36$	$\Delta_T = 0.3$	$\Delta_n = 0.3$
-------------------------	----------------	------------------	------------------

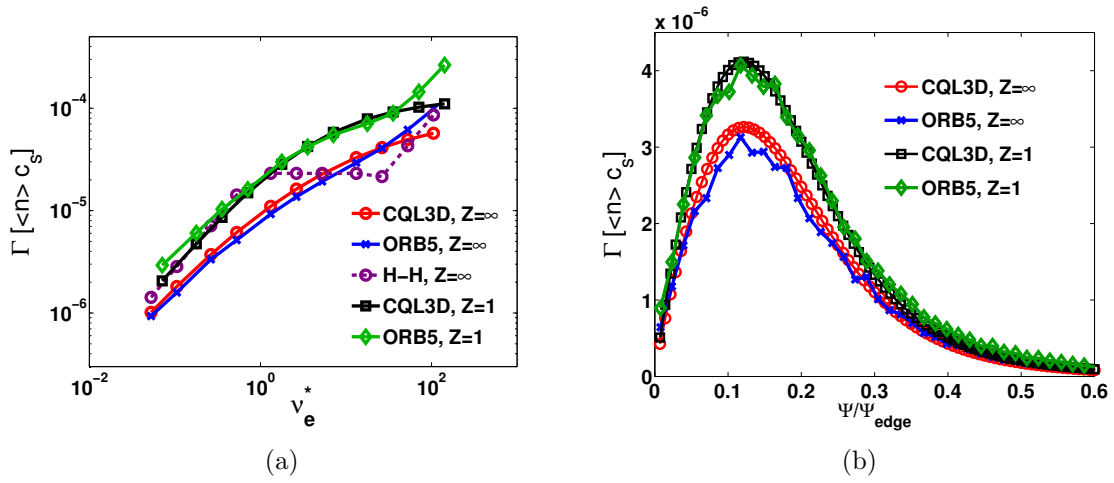


Figure 6.3: Neoclassical electron particle flux Γ for $\kappa_n = 5$, $\kappa_T = 0$, (a) as a function of the effective collisionality ν_e^* at the given radial position $s=0.425$ and (b) as a function of radius with a collisionality accounting for the density and temperature profiles, $\nu_e^*(s = s_0) = 0.18$. ORB5 results are shown for $Z = \infty$ (i.e. only e-i collisions) and $Z = 1$ and compared with analytical fits to CQL3D results for $Z = \infty$ and $Z = 1$ as well as analytical results for the Lorentz model given in the review by Hazeltine and Hinton (H-H).

6.5.2 Ion transport

The neoclassical transport of ions resulting from self-collisions, considering no electric field, is addressed here through a benchmark of ORB5 against the global version of the Eulerian GENE code [10]. Note that, contrary to what is assumed for the electron benchmarks presented in Sec. 6.5.1, the full marker motion, including the magnetic drift velocities (curvature and gradient drifts), is considered here. For the collisionality $\nu_0^* = 0.5$, Figure 6.5 shows the neoclassical ion energy flux profile $Q(r)$ and the ion contribution to the bootstrap current $j_{bi}(r)$ after two collision times τ_{ii} , considering the CYCLONE case parameters as defined in Sec. 3.8 with background profiles of type 2 considering $\Delta r/a = 0.2$ [see Eq. (3.60)]. Considering the different numerical implementations of the self-collision operator in both codes, the agreement obtained may be considered satisfactory.

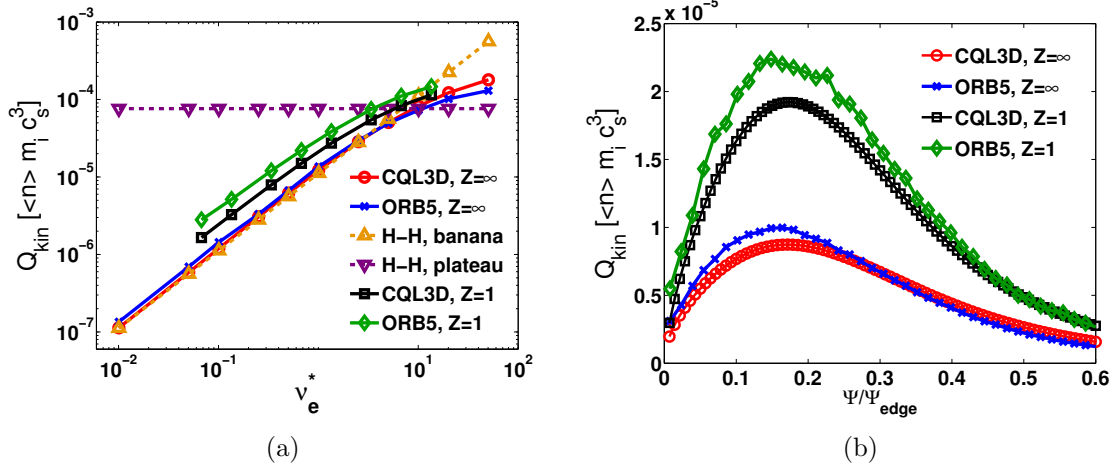


Figure 6.4: Neoclassical electron energy flux Q_{kin} for $\kappa_n = 0, \kappa_T = 5$, (a) as a function of the effective collisionality ν_e^* at the given radial position $s=0.425$ and (b) as a function of radius with a collisionality accounting for the density and temperature profiles, $\nu_e^*(s=s_0) = 0.68$. ORB5 results are shown for $Z = \infty$ and $Z = 1$ and compared with analytical fits to CQL3D results for $Z = \infty$ and $Z = 1$ as well as analytical results for the Lorentz model given in the review by Hazeltine and Hinton (H-H).

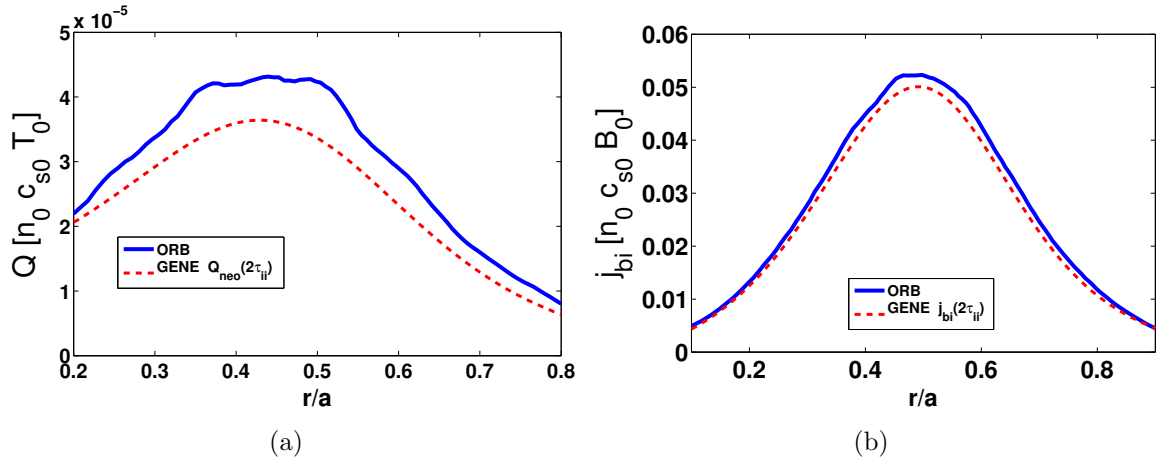


Figure 6.5: Neoclassical benchmark between ORB5 and GENE. (a) Neoclassical ion energy flux profile $Q(r)$ and (b) ion contribution to the bootstrap current $j_{bi}(r)$ for the collisionality $\nu_0^* = 0.5$ after two collision times $2\tau_{ii}$. CYCLONE case parameters, no self-consistent electric field. The agreement obtained between the two codes is satisfactory.

6.6 Global neoclassical ion transport with self-consistent electric field

The neoclassical theory predicts the establishment of a radial electric field leading to an axisymmetric equilibrium, which was first computed in a global simulation by Wang *et al.* using the FORTEC code [93]. In order to study a neoclassical equilibrium with self-consistent electric field, we solve the global drift-kinetic equation for ions. Indeed, as neoclassical simulations involve electric fields with long wavelengths, it is relevant to neglect FLR effects even in the

collisionless dynamics. The drift-kinetic form of Eq. (3.34) is thus solved, together with the quasi-neutrality equation (3.51) or (3.53), assuming axisymmetry, i.e. keeping only the toroidal Fourier mode $n = 0$ of δf_{LM} and ϕ . Note that no heat source is considered, according to the negligible neoclassical gradient relaxation over the collisional time scale which leads to approximately constant temperature profiles over the simulation time. Both adiabatic and kinetic electron dynamics will be considered in the following. The standard neoclassical approximation retains only the flux-surface-averaged potential and thus neglects the poloidal components of the field. The specific parameters of the simulations are given in Tables II (case 1) and III (case 2). If not mentioned otherwise, a standard run is carried out with full marker motion, i.e. in the global approach, and a purely radial electric field. The radial electric field E_r is obtained from the flux-surface-average $\langle \phi \rangle_S$ of the electrostatic potential ϕ , solution to the quasi-neutrality equation: $E_r = -\partial \langle \phi \rangle_S / \partial r$. The considered ion species is Deuterium. The electron and ion temperature profiles are identical. In global simulations, collision frequencies are estimated locally, i.e. consistent with background density and temperature variations.

Table II. Run parameters, ion transport benchmark, case 1.

profiles 2 [Eq. (3.60)]	$a/R_0 = 0.36$	$T_e/T_i = 1$	$\nu_i^*(r/a = 0.5) = 0.03$
$\kappa_T = 3.58$	$\kappa_n = 0.79$	$\Delta_{T_i}/a = \Delta_n/a = 0.3$	$1/\rho^* = 150$

Table III. Run parameters, ion transport benchmark, case 2.

profiles 2 [Eq. (3.60)]	$a/R_0 = 0.2$	$T_e/T_i = 1$	$0.012 < \nu_i^*(r/a = 0.5) < 12$
$\kappa_T = \kappa_n = 1.2$	$\Delta_{T_i}/a = 0.2$	$\Delta_n/a = 0.2$	$1/\rho^* = 150$

6.6.1 Zonal flow damping: Rosenbluth-Hinton test

The study of the self-consistent axisymmetric electrostatic fields in the frame of neoclassical transport is closely linked to the study of zonal poloidal flows, which play a crucial role in regulating ITG microturbulence [17], and Geodesic Acoustic Mode (GAM) oscillations [97]. We thus start by presenting here linear simulations [i.e. solving Eq. (3.37) for δf] of zonal flow damping, corresponding to the so-called Rosenbluth-Hinton (RH) test. In order to carry out RH tests, a local Maxwellian background $f_0 = f_{LM}$ is chosen for both the collisionless and collisional dynamics, and an initial distribution perturbation $\delta f_{LM} = (\delta n/n_0) \cos(\pi r/a) f_{LM}$ is loaded. The electrons are considered adiabatic and the full axisymmetric potential $\phi(r, \theta, t)_{n=0}$ is retained. The collisionless theory of zonal flow damping predicts an undamped residual value [98]. Collisions are expected to lead to a decaying residual zonal flow in a characteristic time of the order of the collision time [99]. Figure 6.6 shows the damping of the radial electric field E_r at the magnetic surface $s = 0.55$, for the geometrical parameters of case 2 but having set gradients to zero ($\kappa_n = \kappa_T = 0$), as usually done for carrying out the Rosenbluth-Hinton test. Oscillations, whose frequency is estimated by $\omega_G = (v_{thi}/R_0) \sqrt{11/2 + 43/(11q_s^2)}$ according to Ref. [100] in the drift-kinetic limit, are due to the initial excitation of GAMs, which involve poloidal Fourier components $m = \pm 1$ [97] and are Landau damped. Neglecting the Finite-Orbit-Width effects, which leads to a radially local derivation, an estimation of the damping rate is given by

$\gamma_G = (v_{thi}/R_0)\sqrt{2 + 1/q_s^2} \exp(-q_s^2 - 0.5)$, having made use of $\gamma_G = \omega_{G,\text{fluid}} \exp(-\omega_{G,\text{fluid}}^2/2k_{||}^2 v_{thi}^2)$ in the limit $\omega_{G,\text{fluid}} \gg |k_{||}|v_{thi}$, where $\omega_{G,\text{fluid}} = (v_{thi}/R_0)\sqrt{2 + 1/q_s^2}$ [101] and $|k_{||}| \simeq 1/(q_s R_0)$. Defining $\varpi = 1 + 1.6q_s^2/\sqrt{\epsilon}$, the time evolution of the radial electric field at a given radius r is written as follows [99]:

$$\frac{E_r(t)}{E_r(0)} = \left(1 - \frac{1}{\varpi}\right) \exp(-\gamma_G t) \cos(\omega_G t) + \frac{1}{\varpi} \exp\left(\frac{\beta^2 t}{\varpi^2}\right) \left[1 - \operatorname{erf}\left(\frac{\beta\sqrt{t}}{\varpi}\right)\right], \quad (6.54)$$

where erf is the error function defined in Chapter 5. The small long-time collisional response has been neglected here. Considering a finite collisionality $\bar{\nu}$ as defined by Eq. (5.38), the coefficient $\beta = 3\pi q_s^2 \sqrt{\bar{\nu}}/(\epsilon \ln^{3/2}[16\sqrt{\epsilon/\bar{\nu}t}])$ in Eq. (6.54) is introduced. Note that for $\beta \neq 0$, $E_r(t)/E_r(0)$ goes to zero over the collisional time scale $\bar{\nu}^{-1}$. In the collisionless limit, $\beta \rightarrow 0$ and Eq. (6.54) becomes [98]:

$$\frac{E_r(t)}{E_r(0)} = \left(1 - \frac{1}{\varpi}\right) \exp(-\gamma_G t) \cos(\omega_G t) + \frac{1}{\varpi}, \quad (6.55)$$

where the residual is given by $E_r(t \rightarrow \infty)/E_r(0) = 1/\varpi$. The predicted damping rates and residuals, shown by dash-dotted lines in Figure 6.6, match very well the time evolution of the radial electric field given by ORB5 at $s = 0.55$, where $\epsilon \simeq 0.15$ and $q_s \simeq 1.3$, for a collisionless and a collisional run respectively. This test is crucial in order to ensure correct levels of zonal flows in turbulent simulations.

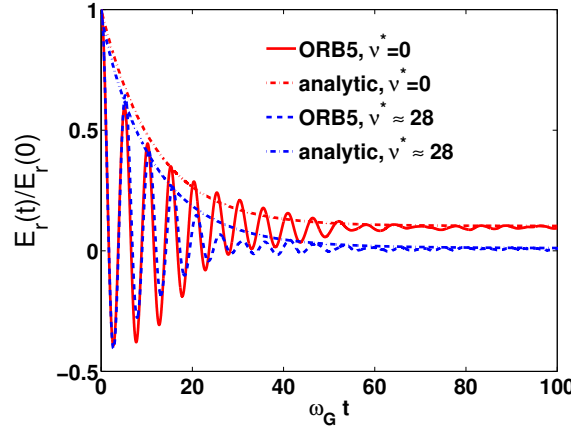


Figure 6.6: Rosenbluth-Hinton test at $s = 0.55$ considering an axisymmetric field, linear dynamics, without profile gradients. The time evolution of the radial electric field $E_r = -\partial\langle\phi\rangle_s/\partial r$ provided by ORB5 is compared to the theoretical estimate derived by Rosenbluth and Hinton, for both the collisionless and the collisional case. Time is normalized by the GAM frequency ω_G .

Finite temperature and density gradients may be considered for a Rosenbluth-Hinton test as well. In collisionless simulations, after relaxation of the GAM oscillations, the residual value of the radial electric field is proportional to the initial amplitude of the perturbation, as given by Eq. (6.55), independent of the profile gradients. In collisional simulations, the situation is fundamentally different: The zonal flows are damped as a result of collisions between passing and trapped ions [99] and the radial electric field always relaxes towards the neoclassical

equilibrium value, which is non-zero for finite background profile gradients, regardless of the initial electric field amplitude. As expected, the neoclassical equilibrium field does vanish if no gradients are considered, as already shown in Figure 6.6. Figure 6.7 illustrates these different scenarios by presenting the time evolution of the radial electric field $E_r(t)$ at $r/a = 0.5$, both for zero and non-zero CYCLONE case density and temperature gradients, considering density and temperature profiles of type 2 with $\Delta r/a = 0.2$. Note that the simulations considering collisions along with non-zero CYCLONE case density and temperature gradients need to include the neoclassical drive, i.e. the term $\partial f_{LM}/\partial \Psi \cdot d\Psi/dt|_0$ in the drift-kinetic equation, in order to establish neoclassical equilibrium fields as shown in Figure 6.7 (b).

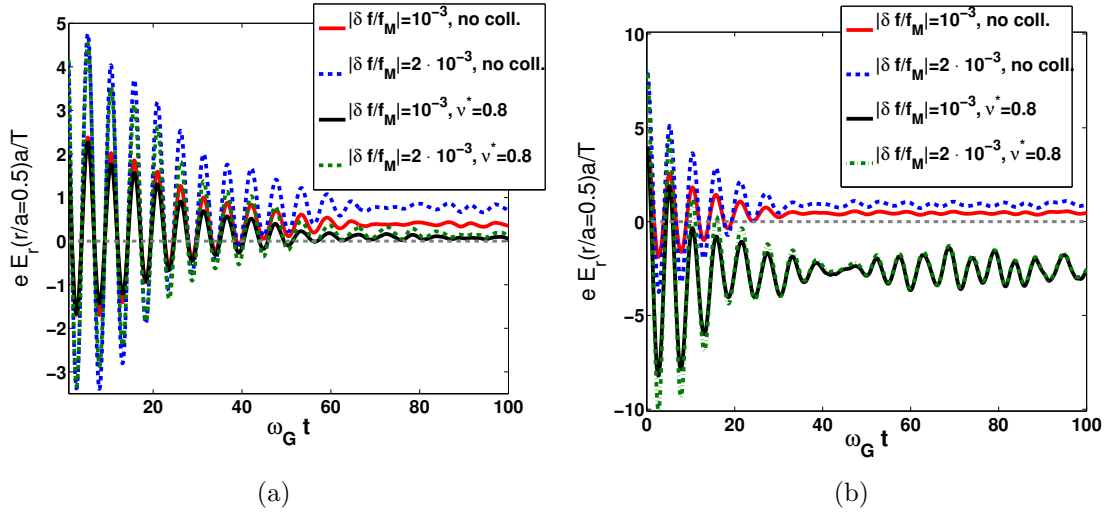


Figure 6.7: Rosenbluth-Hinton test where (a) no gradients and (b) the CYCLONE case gradients ($R_0/L_{n_0} = 2.2$, $R_0/L_{T_0} = 6.9$) are considered. Time evolution of the radial electric field E_r at mid-radius for both collisionless and collisional simulations. The collisionless residual is proportional to the initial amplitude of the perturbation $|\delta f/f_{LM}|$, while the collisional residual converges towards the neoclassical equilibrium value, regardless of the initial perturbation. Time is normalized by the GAM frequency ω_G .

6.6.2 Ion transport and neoclassical equilibrium with adiabatic electrons

In this Section, a benchmark is performed against previous global neoclassical numerical results obtained with both the Eulerian GT5D code and the PIC FORTEC-3D code [102], retaining only the flux-surface-averaged potential ($\phi = \langle \phi \rangle_s$). In ORB5 this is done by solving the standard quasi-neutrality equation and then assigning $\phi \leftarrow \langle \phi \rangle_s$. These results are also compared with neoclassical analytical results. All the ORB5 results are within the typical range of the small discrepancies between GT5D and FORTEC-3D and may thus be considered as consistent with these other codes. Figure 6.8 (a) presents the ion heat diffusivity χ_{Hi} as a function of radius in units of χ_{GBa}/L_n for case 1 parameters (Table II), which results exclusively from the $\delta f_{LM} \mathbf{v}_d \cdot \nabla \Psi$ contribution to the kinetic energy flux Q_{kin} given by Eq. (3.63), and matches well the analytical predictions from Chang and Hinton (C-H) [103] away from the magnetic axis,

where the standard neoclassical ordering is valid.

An important neoclassical relation is the ion force balance, which reflects the conservation of toroidal momentum:

$$\frac{j_{bi}}{n_i} \frac{d\Psi}{dr} = \frac{RB_\varphi T_i}{Ze} \left[(k-1) \frac{d}{dr} \ln T_i - \frac{d}{dr} \ln n_i + \frac{ZeE_r}{T_i} \right], \quad (6.56)$$

where E_r is the radial electric field, n_i is the ion density and j_{bi} is the ion contribution to the bootstrap current. This relation is derived by Hinton and Hazeltine in [43], Eq. (6.134), but where a ratio $B_\varphi/B_{\text{poloidal}}$ appears to be missing. The force balance coefficient k is shown around the mid-radius region for the same case 1 ($\nu_0^* = 0.03$) in Figure 6.8 (b) and compared with the analytical large aspect ratio predictions from Hinton and Hazeltine (H-H) [43], as well as with results from the moment equation approach derived by Hirshman and Sigmar (H-S) [104].

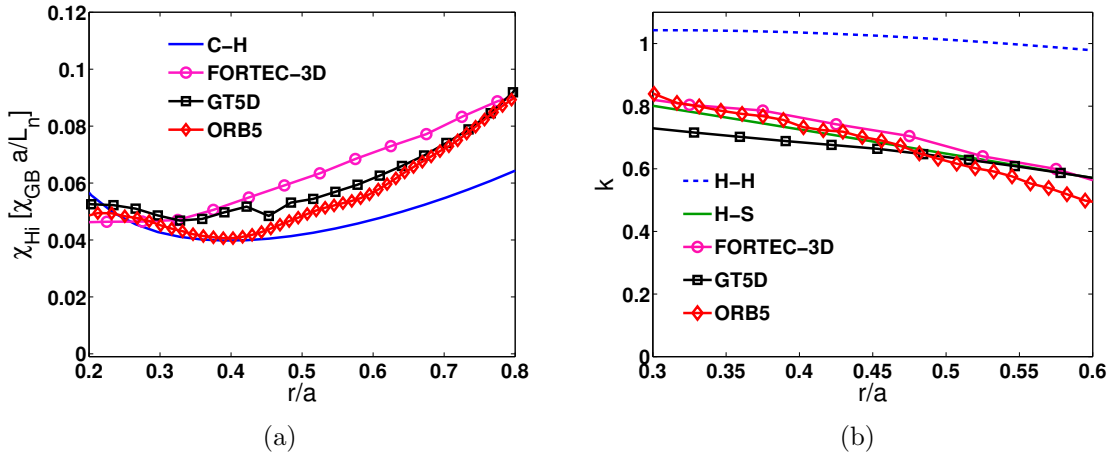


Figure 6.8: (a) Ion heat diffusivity χ_{Hi} and (b) neoclassical force balance coefficient k as a function of radius. Case 1 parameters ($\nu_0^* = 0.03$), adiabatic electrons, and retaining only $\langle \phi \rangle_S$ from the quasi-neutrality equation. Global ORB5 results at time $t = \tau_{ii}(r/a = 0.5)$ are compared to simulations from GT5D and FORTEC-3D, as well as to analytical results from Chang and Hinton (C-H), Hinton and Hazeltine (H-H), Hirshman and Sigmar (H-S).

Figure 6.9 shows a collisionality scan for the ion heat diffusivity χ_{Hi} and the neoclassical force balance coefficient k at $r = 0.5a$ for case 2 parameters (Table III). Predictions coming from the moment equation approach (H-S) [104] are shown in addition to results derived by Hinton and Hazeltine (H-H) in [43] for the coefficient k appearing in the force balance equation (6.56). In Figure 6.9 (a), note the larger discrepancy in the neoclassical diffusivity between the different code results at low collisionality $\nu^* = 0.01$, probably due to the very long time required by a simulation at low collisionality to fully converge. In Figure 6.10 (a), showing the time evolution of the gyrocenter flux at $r = 0.5a$ for the same case 2, the ambipolarity condition is verified, resulting in a vanishing ion flux for $t \rightarrow \infty$ since the electrons are assumed to respond adiabatically. The setting up of the neoclassical radial electric field at $r = 0.5a$ is shown in Figure 6.10 (b).

Possible effects from the poloidal Fourier modes $m \neq 0$, retained beyond the standard neoclas-

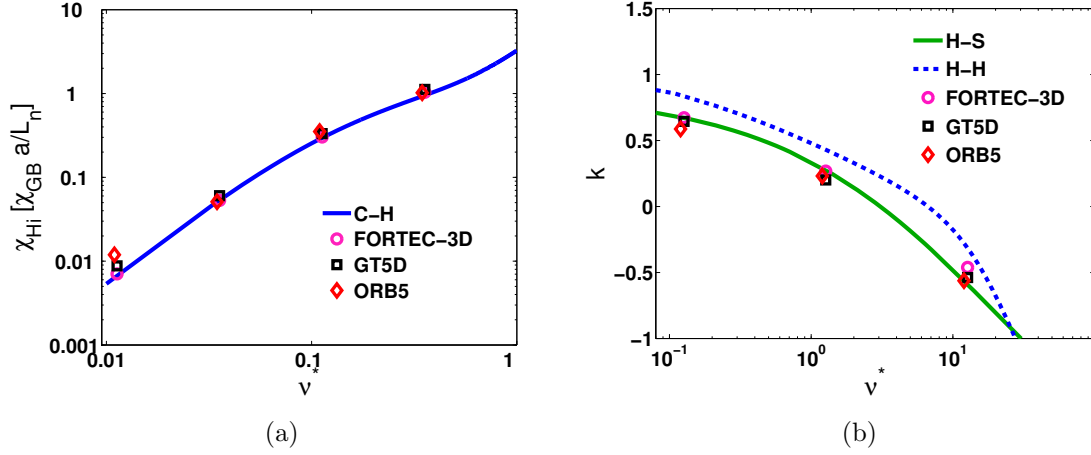


Figure 6.9: (a) Ion heat diffusivity χ_{Hi} and (b) neoclassical force balance coefficient k as a function of the effective collisionality ν^* . Considering parameters of case 2 and adiabatic electrons, global ORB5 results are shown for position $r/a = 0.5$ and at time $t \sim \tau_{ii}(r/a = 0.5)$. ORB5 results are compared to simulations from GT5D and FORTEC-3D, as well as analytical results from Chang and Hinton (C-H), Hinton and Hazeltine (H-H), Hirshman and Sigmar (H-S).

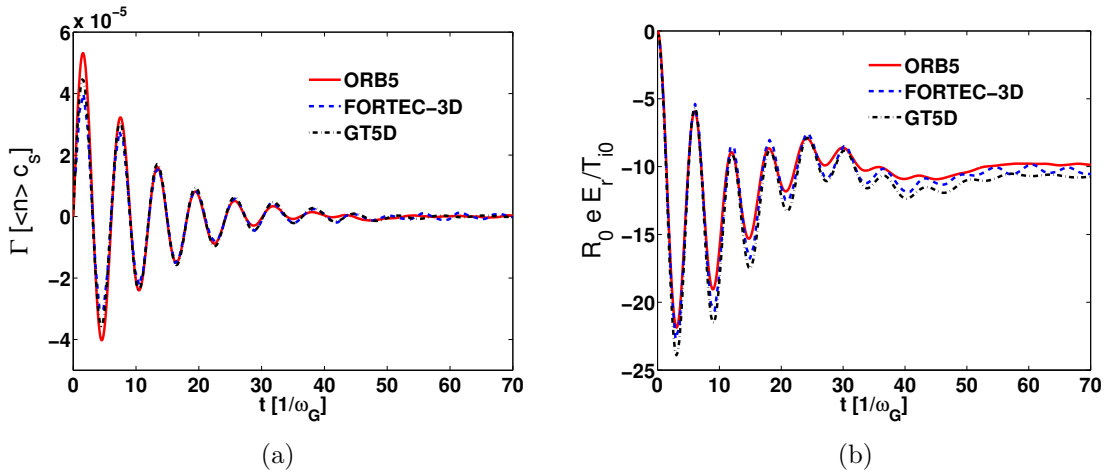


Figure 6.10: Time evolution of (a) gyrocenter flux Γ and (b) radial electric field $E_r = -\partial\langle\phi\rangle_S/\partial r$ at $r = 0.5a$ for case 2 parameters and $\nu^*(r/a = 0.5) = 0.12$. Comparison of global results from ORB5, GT5D and FORTEC-3D. The ambipolarity is satisfied and an equilibrium neoclassical electric field is established.

sical approximation, are studied in Figure 6.11, corresponding to case 1 parameters (Table II). In Figure 6.11 (a), the ORB5 results for $\phi = \langle\phi\rangle_S$ have been added for reference. Note that, if the full axisymmetric potential $\phi_{n=0} \neq \langle\phi\rangle_S$ is retained, there is a radial component to the $\mathbf{E} \times \mathbf{B}$ drifts leading to contributions to the fluxes from the local Maxwellian background f_{LM} (which compensate each other). Considering only the kinetic contribution to the heat flux, one thus could be misled into interpreting this kinetic energy flux as a contribution to the thermal transport. It is actually not, as pointed out in Ref. [71]. In fact, the potential energy flux from the background f_{LM} compensates the kinetic energy flux from the background f_{LM} , leading to essentially the same heat diffusivity level as in the standard neoclassical approximation (purely

radial electric field), as clearly shown in Figure 6.11 (a). The potential energy flux is crucial in order to treat the effects of the $m \neq 0$ poloidal modes in neoclassical transport, as discussed in Ref. [71]. Retaining the $m \neq 0$ poloidal modes still ensures a total vanishing gyrocenter flux, which is shown in Figure 6.11 (b): The full axisymmetric potential ϕ leads to an inward flux related to the drift velocity $\mathbf{v}_{E \times B}$ acting on f_{LM} , compensating the outward flux contribution from δf_{LM} related mainly to the magnetic drift velocity $\mathbf{v}_{\nabla B} + \mathbf{v}_c$. Ambipolarity is thus satisfied, as there is no electron transport, the electron response being assumed adiabatic in these simulations.

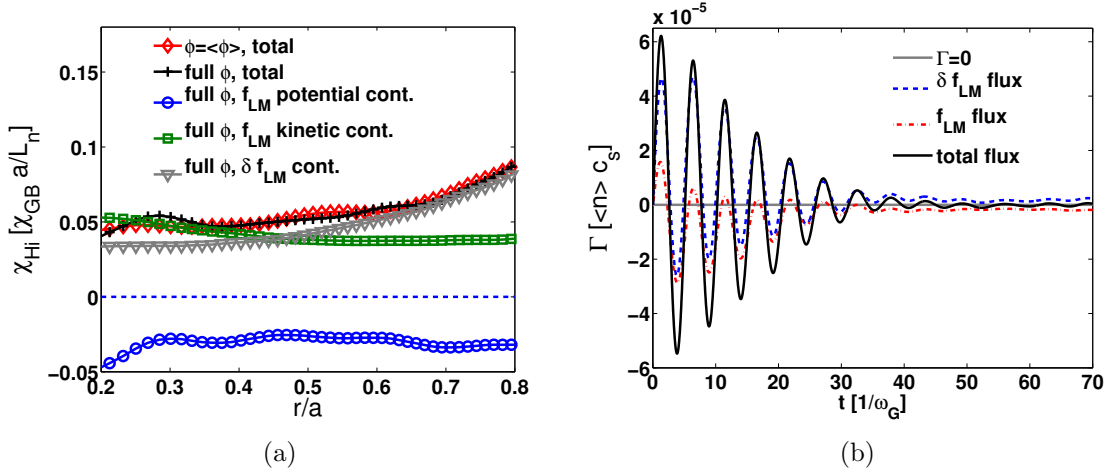


Figure 6.11: Retaining all poloidal Fourier modes of the axisymmetric potential and comparison to simulation results within the standard neoclassical approximation assuming a purely radial electric field (same as in Figure 6.8). (a) Case 1 parameters, adiabatic electrons, ion heat diffusivity at $t = 0.5\tau_{ii}$ ($r/a = 0.5$) as a function of radius. Retaining all poloidal Fourier modes does not change the heat transport level. (b) Case 2 parameters, time evolution of the gyrocenter flux at $r = 0.5a$ for $\nu^*(r/a = 0.5) = 0.085$. Ambipolarity is satisfied.

6.6.3 Adding collisional kinetic electrons

The case 1 simulations presented in Sec. 6.6.2 were repeated considering kinetic electrons with a non-physical ion-electron mass ratio $m_i/m_e = 200$ and experiencing both self-collisions as well as pitch angle scattering on ions. Thanks to the smaller mass ratio, the transit time scale separation between electrons and ions $\omega_{te}/\omega_{ti} \sim \sqrt{m_i/m_e}$ is reduced, which facilitates the multi-species kinetic simulations. The electron collisionality is chosen such that $\nu_{ee,th}/\nu_{ii,th} \sim 50$. We notice in Figure 6.12, obtained by enforcing $\phi = \langle \phi \rangle_S$, that the ratio between electron and ion heat transport is consistent with the neoclassical ordering of heat transport $\chi_e/\chi_i \sim m_e \nu_{ee,th}/m_i \nu_{ii,th} \sim 1/4$. Moreover, electrons and ions both show a similar outward particle flux, which ensures the ambipolarity condition. The small discrepancy between electron and ion particle diffusivities reflects the statistical numerical error, as well as the error of discretization when building the gradients from reconstructed profiles for computing the diffusivities.

The effect of kinetic electrons on the neoclassical equilibrium electric field is small, as clearly shown in Figure 6.13 (a). This results from the fact that the electric field ensuring the ambipolarity by shaping the particle orbits depends mainly on the ion dynamics, since the average

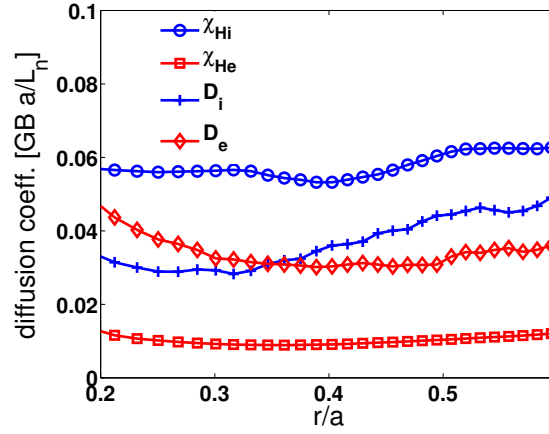


Figure 6.12: Case 1 parameters with collisional kinetic electrons. Particle and heat diffusivity of ions and electrons as a function of radius for $\phi = \langle \phi \rangle_S$ and time around $t \simeq \nu_{ii,th}^{-1} \simeq 50\nu_{ee,th}^{-1}$. Results in accordance with neoclassical transport scaling laws and ensuring ambipolarity.

ion orbit width is much larger (by a factor $\sqrt{m_i/m_e}$) than the electron orbit width. The orbit squeezing produced by the shear of the radial electric field is discussed in Ref. [105]. Figure 6.13 (b) shows that kinetic electrons lead to an important bootstrap current, mainly carried by passing electrons, while the ion contribution to this current does essentially vanish. Note that the observed vanishing ion current is related to the Lorentz model chosen for electron-ion collisions, which drops the momentum conserving term of the electron-ion collision operator as explained in Sec. 5.6.

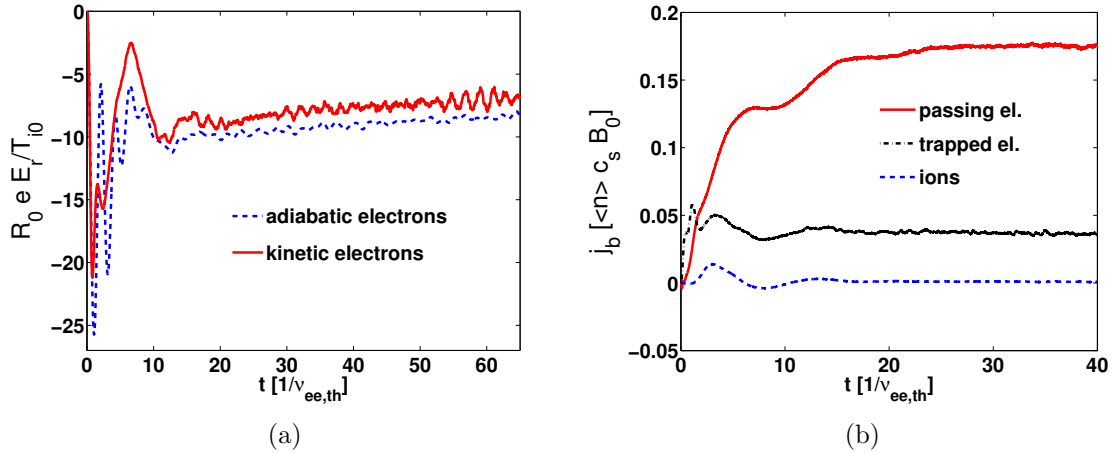


Figure 6.13: Case 1 parameters, $\phi = \langle \phi \rangle_S$. Kinetic electron contributions to (a) the neoclassical radial electric field E_r at $r = 0.5a$ and (b) the bootstrap current j_b at $r = 0.5a$. The electric field is weakly changed by considering kinetic electrons, while an important bootstrap current is produced and mainly carried by passing electrons.

6.6.4 Breakdown of the standard neoclassical approximation

The standard neoclassical approximation is valid under the assumption that the banana width is small compared to characteristic equilibrium lengths of the system. In order to illustrate the limitations of this approximation, one chooses a configuration without density gradient, considering the parameters of Table IV, i.e. with relatively low value of $1/\rho^*$. The computations are carried out without considering self-consistent electric fields. Let us point out that the usual neoclassical ordering breaks down near the magnetic axis, as the radial excursion of particles from a flux surface can become comparable to the minor radius. In particular, as stated explicitly in [106], in this region the ordering $|\mathbf{v}_d \cdot \nabla \delta f_{LM}| \sim |\mathbf{v}_d \cdot \nabla f_{LM}|$ applies instead of the standard neoclassical ordering $|\mathbf{v}_d \cdot \nabla \delta f_{LM}| \ll |\mathbf{v}_d \cdot \nabla f_{LM}|$, which in fact leads to transport being radially nonlocal. The temperature profile nonetheless does not relax significantly over the considered simulation times, making relevant the study of an effective diffusivity. It has to be emphasized that this nonlocal ordering does not alter the scaling $|\delta f_{LM}| \ll f_{LM}$. Indeed, it is the gradient and not δf_{LM} itself that becomes large. Considering the term $\mathbf{v}_d \cdot \nabla \delta f_{LM}$ along with a linearized collision operator thus brings a relevant correction to the local approximation, which breaks down near the axis. Note that this correction does not improve the accuracy of the calculation away from the magnetic axis, since in this case $\mathbf{v}_d \cdot \nabla \delta f_{LM}$ is of the same neoclassical order as the non-linear collisionality $C[\delta f_{LM}, \delta f_{LM}]$ we neglect. Comparing global and local ORB5 simulations in Figure 6.14, one notices that the neoclassical approximation is valid over the radial region $r/a \gtrsim 0.45$, while it breaks down near the magnetic axis. This result is mainly explained by the fact that near the magnetic axis, trapped particles follow potato orbits whose width is of order $\lambda_p \sim (q_s^2 \rho_L^2 R_0)^{1/3}$ [107], which may be significantly larger than the standard banana width $\Delta r_b \sim q_s \rho_L / \sqrt{\epsilon}$. These large orbit widths can thus become comparable to the local minor radius within a significant radial region around the magnetic axis for the large aspect ratio and large ρ^* tokamak considered here, which violates the standard neoclassical assumption. These results are consistent with previous ones: The reduction of the neoclassical transport near the axis (compared to the standard theory) has been predicted in a low collisionality regime by a Lagrangian transport theory [108], as well as by simulation results [107], [109].

Table IV. Run parameters for studying breakdown of neoclassical approximation.

profiles 2 [Eq. (3.60)]	a/R=0.28	$T_e/T_i = 1$	$\nu_i^*(r/a = 0.5) = 0.1$
$\kappa_n = 0$	$\kappa_T = 4$	$\Delta_{T_i} = 0.3$	$1/\rho^* = 80$

6.7 Towards gyrokinetic turbulent simulations

6.7.1 The coarse-graining procedure in neoclassical simulations

The beneficial effect of the coarse-graining procedure detailed in Sec. 4.8 on the noise level is illustrated here in the case of a neoclassical test based on the parameters given in Table

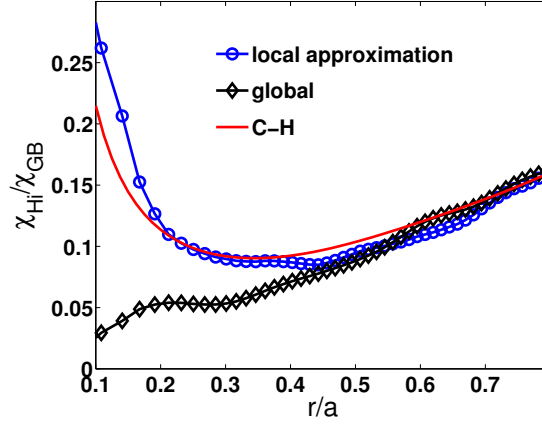


Figure 6.14: Neoclassical approximation breakdown. Reduction of the neoclassical transport predicted by ORB5 close to the magnetic axis, when considering the full marker motion. In the neoclassical limit, ORB5 results match well the analytical predictions by Chang and Hinton (C-H).

V, performed with adiabatic electrons and at low collisionality: $\nu^*(r = 0.5a) = 3.5 \cdot 10^{-2}$. Let us point out that, in view of preparing turbulent runs, these neoclassical simulations were performed by retaining poloidal modes $m \in [-5, 5]$ of the axisymmetric potential $\phi_{n=0}$ (see the field-aligned Fourier filter presented in Sec. 4.6). It is shown in Figure 6.15 (a) that the coarse-graining procedure stabilizes the weight spreading, which is reflected by the saturation of the total weight variance $\sigma = \sqrt{\langle w^2 \rangle - \langle w \rangle^2}$ once the system has reached collisional equilibrium at $t\nu_{ii} \gtrsim 1$. As a corollary, the numerical noise defined in Eq. (4.57) also stabilizes at the same time, as shown in Figure 6.15 (b). The neoclassical properties of the simulations are essentially unaffected by the coarse-graining procedure, as shown in Figure 6.16 presenting the heat diffusivity χ_{Hi} as a function of the radial position for the Table V parameters.

Table V. Run parameters, coarse-graining in neoclassical simulations.

profiles 3 [Eq. (3.61)]	$a/R_0 = 0.37$	$T_e/T_i = 1$	$\kappa_T = 2.63$	$\kappa_n = 0.81$	$1/\rho^* = 180$
-------------------------	----------------	---------------	-------------------	-------------------	------------------

6.7.2 Neoclassical tests of the local/canonical Maxwellian background switching scheme

In this Section, the background switching scheme described and explained in Sec. 4.4.4 is tested through global neoclassical simulations with self-consistent electric field and adiabatic electrons. To this end, we consider both the local Maxwellian background f_{LM} defined by Eq. (3.28) and the canonical Maxwellian background f_{CM} defined by Eq. (3.29) with $\bar{\psi} = \Psi_0$. The total distribution f is thus decomposed using either a local Maxwellian background $f = f_{LM} + \delta f_{LM}$ or a canonical Maxwellian background $f = f_{CM} + \delta f_{CM}$. In order to validate the background switching algorithm, a collisional simulation is carried out with this scheme, i.e. alternating between the LM and CM representation for the collisional and collisionless dynamics respectively, and compared to results obtained for the same physical conditions with the standard fixed local

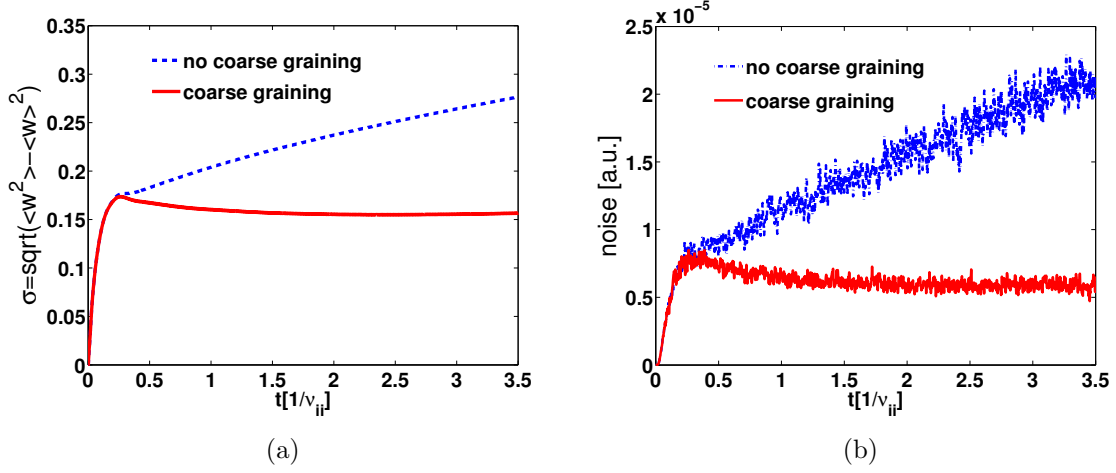


Figure 6.15: Effects of the coarse graining procedure. (a) Total weight variance and (b) numerical noise. Table V parameters with $\nu^*(r/a = 0.5) = 3.5 \cdot 10^{-2}$. The noise and the weight spreading are fully stabilized by the coarse-graining algorithm, for this low collisionality.

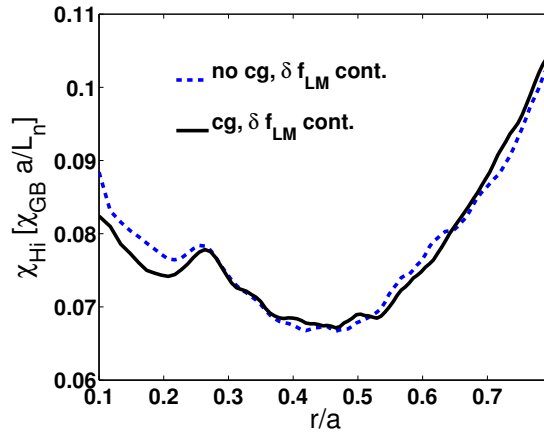


Figure 6.16: The coarse-graining (cg) procedure does not affect the fundamental neoclassical results such as the heat diffusivity χ_{Hi} . Comparing simulations, with and without coarse-graining, illustrates that the transport level may be conserved while controlling the noise. $\nu^*(r/a = 0.5) = 3.5 \cdot 10^{-2}$, $t = 0.5\tau_{ii}(r/a = 0.5)$.

Maxwellian background approach. It is recalled that the quasi-neutrality equation (3.53) for the self-consistent field ϕ is in fact linearized for fluctuations around a certain reference state. To be able to exactly compare results from the two algorithms, this reference state must be chosen the same in the two cases. This is achieved by introducing the density deviation $\overline{\delta n_0}$:

$$\overline{\delta n_0}(\mathbf{x}) = \int \frac{B_{||}^*}{m} d^3R dv_{||} d\mu d\alpha [f_i(\mathbf{R}, v_{||}, \mu, t=0) - f_{0,i}(\mathbf{R}, v_{||}, \mu)] \delta(\mathbf{R} + \boldsymbol{\rho} - \mathbf{x}), \quad (6.57)$$

where $f_{0,i}$ is the background (either f_{LM} or f_{CM}) considered when solving the quasi-neutrality equation. $\overline{\delta n_0}$ is then subtracted at each time step on the RHS of the quasi-neutrality equation

(3.53):

$$\frac{en_{i0}(\Psi)}{T_e(\Psi)}[\phi(\mathbf{x}, t) - \langle \phi \rangle(\Psi, t)] - \nabla_{\perp} \cdot \left(\frac{n_{i0}(\Psi)}{B\Omega_i} \nabla_{\perp} \phi \right) = \overline{\delta n_i}(\mathbf{x}, t) - \overline{\delta n_0}(\mathbf{x}). \quad (6.58)$$

Note that the RHS of Eq. (6.58) is actually:

$$\overline{\delta n_i} - \overline{\delta n_0} = \int \frac{B_{\parallel}^*}{m} d^3R dv_{\parallel} d\mu d\alpha [f_i(\mathbf{R}, v_{\parallel}, \mu, t) - f_i(\mathbf{R}, v_{\parallel}, \mu, t=0)] \delta(\mathbf{R} + \boldsymbol{\rho} - \mathbf{x}), \quad (6.59)$$

which reflects that the reference state for the distribution with respect to which the quasi-neutrality equation has been linearized is in fact the full initial distribution $f_i(t=0)$. Both algorithms make use of the coarse-graining procedure described in Sec. 4.8. The simulations solve the global neoclassical problem and consider the physical system described in Table V with $\nu^*(r=0.5a) = 3.5 \cdot 10^{-1}$. The two simulations must in particular represent identical initial conditions, chosen as the local Maxwellian for the total initial distribution, $f(t=0) = f_{LM}$. The standard algorithm is thus fully carried out with the local Maxwellian as a fixed background $f_0 = f_{LM}$ and $\delta f_{LM}(t=0) = 0$, while the new algorithm starts from the canonical Maxwellian background $f_0 = f_{CM}$ and $\delta f_{CM}(t=0) = f_{LM} - f_{CM}$, but then switches to the local Maxwellian background representation for carrying out collisions.

Having addressed the issues of identical initial states and linearizing the quasi-neutrality equation with respect to the same reference state, both simulations (with fixed and switching background) should provide the same evolution of the physical system in the limit of sufficient resolution. This is confirmed by the results shown in Figure 6.17 for the here considered test case problem. Figure 6.17 (a) plots the time evolution of the radial electric field E_r at $r/a = 0.5$ towards its equilibrium state over a typical collision time, while Figure 6.17 (b) presents the time traces for the ion kinetic energy flux Q_{kin} . Note that the curves related to the two numerical approaches are indeed essentially identical.

One of the advantages of using a canonical Maxwellian background for carrying out the collisionless dynamics is the fact that significantly larger time steps, typically by a factor of 2, may be taken, than when considering a local Maxwellian background, while still ensuring a stable and equivalently accurate simulation. This is obviously related to the fact that the Right-Hand-Side of the weight equations contains a term proportional to $d\Psi/dt|_0 \partial f_{LM}/\partial \Psi$ in the case of a local Maxwellian background, while the corresponding term $d\Psi_0/dt|_0 \partial f_{CM}/\partial \Psi_0$ in the case of a canonical Maxwellian is absent, as $d\Psi_0/dt|_0 = 0$. Here, $d/dt|_0$ stands for the time derivative along unperturbed trajectories, so that in particular:

$$\left. \frac{d\Psi}{dt} \right|_0 = \left. \frac{d\mathbf{R}}{dt} \right|_0 \cdot \nabla \Psi = (\mathbf{v}_{\nabla B} + \mathbf{v}_c) \cdot \nabla \Psi. \quad (6.60)$$

Considering the same basic parameters as for the simulation results of Figure 6.17, Figure 6.18 illustrates how the collisional algorithm based on background switching may be of an advantage when considering an appropriate initial distribution. Starting the run with $f(t=0) = f_{CM}$,

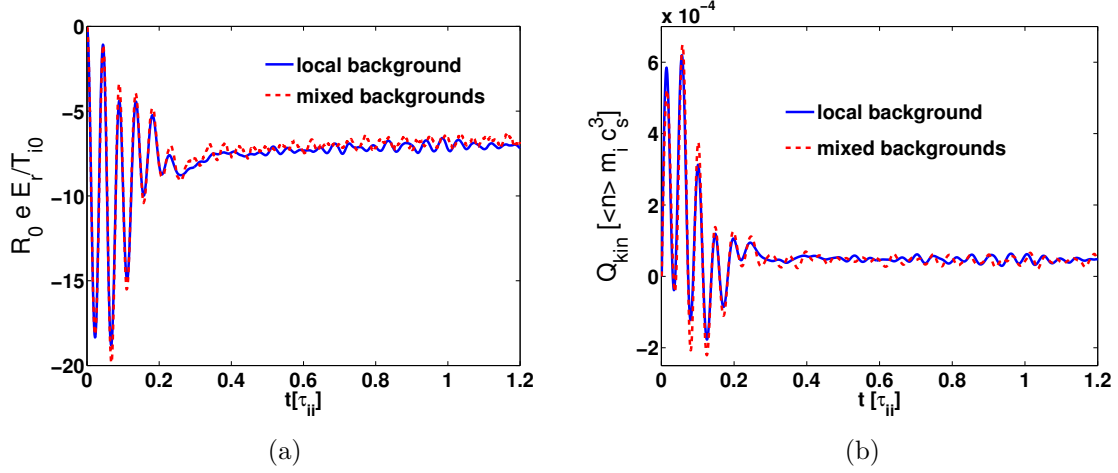


Figure 6.17: Comparing the fixed local Maxwellian background approach with the novel collisional algorithm switching between a canonical and local Maxwellian background. (a) Radial electric field E_r and (b) ion kinetic energy flux Q_{kin} as a function of time. $\nu^* = 0.35$.

the algorithm with background switching provides a better signal/noise ratio than the standard fixed local Maxwellian background scheme for the same initialization, as shown in Figure 6.18 (a), in addition to the increased time step already mentioned. The standard algorithm is however less noisy than the switching background scheme when considering a local Maxwellian f_{LM} as the total initial distribution: $f(t = 0) = f_{LM}$. Figure 6.18 (b) shows how different neoclassical radial electric fields are established for the different considered initial conditions. This is consistent with the fact that different toroidal flows are generated for the two types of initial distributions, which lead to different radial electric fields, in agreement with the force balance relation (6.56). In fact, the radial electric fields have opposite signs depending on whether the simulation starts from a canonical or local Maxwellian. Note in particular the absence of GAM oscillations in Figure 6.18 (b) for the initialization $f(t = 0) = f_{CM}$, the corresponding simulation therefore reaching more rapidly its stationary state. The ion particle and kinetic energy fluxes however appear not to be sensitive on the initial conditions, as shown in Figure 6.19.

6.8 Conclusions

Using the collision operators implemented in ORB5, neoclassical transport in a tokamak has been investigated in this Chapter. Simulations have been carried out both within the standard neoclassical approximation as well as beyond, corresponding to respectively neglecting or keeping drifts in the marker trajectories. Contrary to the former simulations, which are local to a magnetic surface, the latter, including the full particle trajectories, need to be carried out over the whole plasma volume and are therefore global. Global simulations have also been carried out accounting for the possible significant effects of self-consistent electrostatic fields. Collisionless and collisional currents predicted by ORB5 simulations have been compared to analytical models, providing a good agreement. The basic features of neoclassical fluxes have

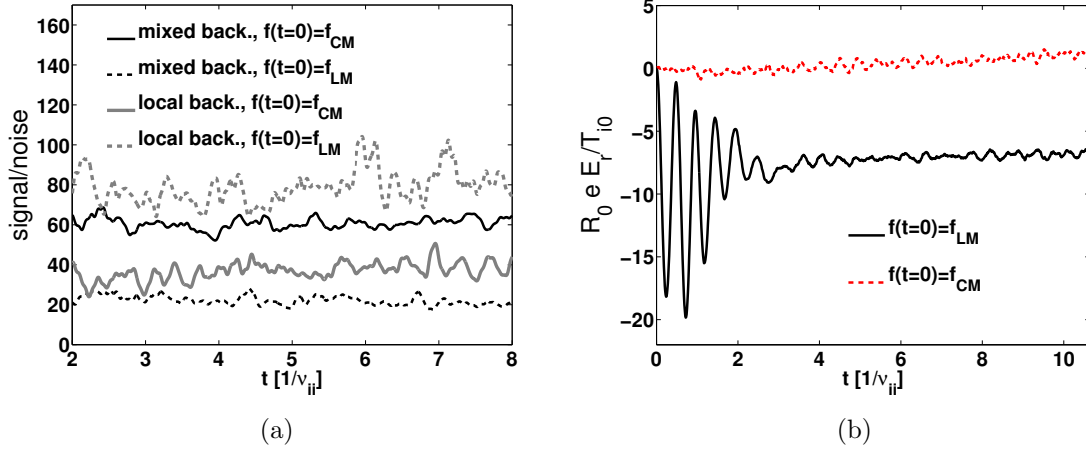


Figure 6.18: Results from global neoclassical simulations using the mixed background approach and the standard local background method, considering different initial conditions: either a local Maxwellian f_{LM} or a canonical Maxwellian f_{CM} . (a) Signal/noise ratio, $\nu^*(r/a = 0.5) = 3.5 \cdot 10^{-2}$ and (b) radial electric field E_r at mid-radius $r/a = 0.5$, $\nu^* = 3.5 \cdot 10^{-1}$.

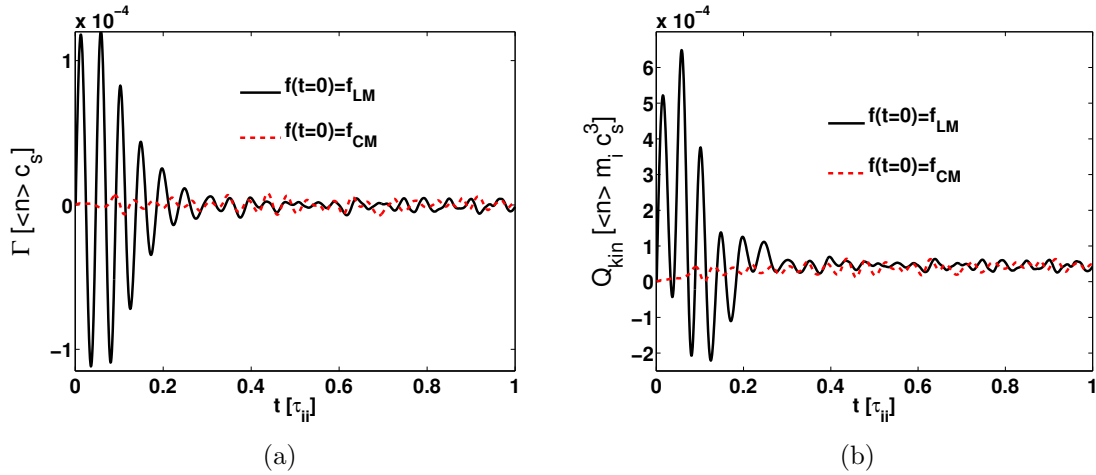


Figure 6.19: Results from global neoclassical simulations using the mixed background approach for different initial conditions. (a) Particle flux Γ and (b) kinetic energy flux Q_{kin} at mid-radius $r/a = 0.5$, $\nu^* = 3.5 \cdot 10^{-1}$.

been verified. Collisionless and collisional Rosenbluth-Hinton tests have validated the residual level of zonal flows provided by ORB5, both with and without collisions, and have thus demonstrated the feasibility of establishing a proper neoclassical equilibrium electric field in ORB5. Successful benchmarks of the collisional ORB5 code were carried out by comparing the simulations both with analytical results within the standard neoclassical approximation as well as with simulation results from other codes. Comparisons with the GENE, GT5D and FORTEC-3D codes were particularly valuable for validating the global simulations. In agreement with previous studies, limitations of the standard neoclassical approximations have been pointed out. This includes the breakdown of neoclassical ordering near the magnetic axis, leading to reduced fluxes in this region compared to those predicted by the standard theory. The

role played by the poloidally asymmetric modes of the electrostatic potential, usually neglected in neoclassical transport studies, has also been analyzed and has turned out to be effectively minor.

The coarse-graining procedure and the background switching scheme have been successfully tested within the frame of neoclassical simulations, opening interesting perspectives for the collisional simulations of turbulence discussed in the next chapters.

Chapter 7

Collisional Ion-Temperature-Gradient (ITG) turbulence and zonal flows

7.1 Introduction

The effect of the radial electric field related to axisymmetric modes and associated zonal flows on tokamak microturbulence has been widely studied in the frame of gyrokinetic simulations. In particular, the ITG turbulence saturation due to vortice shearing produced by zonal flows is a well established mechanism which reduces the turbulent transport in ITG-dominated regimes [17] [110] [25] [7]. Due to the high temperatures in the core of tokamak plasmas, collisionless gyrokinetic models have extensively been used for turbulent transport analysis. However, even though collisionality is not *a priori* a dominant effect for the core tokamak physics, it may nonetheless significantly affect the transport in at least three ways. First, collisions produce an intrinsic neoclassical transport, as studied in Chapter 6. Usually small compared to the turbulent transport, neoclassical transport may nevertheless reach a comparable level in conditions of marginal stability of microinstabilities. Secondly, collisions *damp* radial perturbations and associated zonal flows as predicted in Ref. [99]. Thirdly, collisions may in fact also *generate* a neoclassical radial electric field for ensuring ambipolarity in the presence of density and temperature gradients, leading to background $\mathbf{E} \times \mathbf{B}$ flows. This strong effect of collisions on radial electric field dynamics, appearing through a competition between generation and damping, affects in turn through zonal flow shearing the turbulent transport levels.

Studies of collisional ITG turbulence using gyrokinetic simulations have already been performed in the past, making use of Lagrangian (PIC) [23], Semi-Lagrangian [24] and Eulerian [95] methods. In [23], the damping of zonal flows by collisions was found to increase the turbulent heat diffusivity, at all values of the gradients considered. A Eulerian approach combined with a simplified Krook operator for ion-ion collisions provides the same trend, however somewhat less pronounced [111]. Turbulence studies in the frame of a Z-pinch configuration show as well a transport enhancement due to collisions [112]. This general conclusion is confirmed by ORB5 results. In this Chapter, we systematically analyze the mechanisms of neoclassical (purely collisional) and turbulent transport, as well as their possible interactions. To this end, in a first

phase of the simulation a neoclassical equilibrium is established by keeping only axisymmetric ($n = 0$) Fourier modes. In a second phase, turbulence is allowed to evolve freely by considering all toroidal Fourier modes ($n = 0$ & $n \neq 0$). Our simulations show that collisional effects are not simply additive to collisionless turbulent transport: Heat transport in the presence of both turbulence and collisions is larger than the sum of collisionless turbulent transport and neoclassical transport. The softening of the Dimits shift region (see Sec. 7.4.1) obtained in [23] is as well observed in ORB5 simulations [26] and is further characterized in this work. However, the bursting behaviour of the zonal flows in the Dimits shift region predicted in [23] is only clearly reproduced for narrow gradient profiles. For wider gradient profiles, a steadier regime is observed. Additional drive from increased turbulence levels in collisional simulations is found to essentially balance the zonal flow damping by collisions, leading to zonal flow amplitudes only slightly reduced in collisional simulations compared to the collisionless situation. Moreover, the zonal flow levels in collisional simulations turn out to be roughly independent of the finite collisionality considered. The analysis of ORB5 simulations show how the zonal flow saturation in fact results from a Kelvin-Helmoltz-like tertiary instability mechanism transferring energy from zonal modes back to turbulence [26], as originally demonstrated in Ref. [113]. Similarly to results obtained in the previously mentioned papers, the electrons are assumed adiabatic and therefore collisionless in this Chapter. Considering the dynamics of kinetic electrons along with the related electron collisionality may lead to different effects of collisions on turbulence in certain regimes [114], for instance related to the reduction of microinstability drive by electron collisions, as emphasized in Chapter 8. Note furthermore that all the collisional simulations of ITG turbulence presented in this Chapter are performed through the background switching scheme described in Sec. 4.4.4.

7.2 Linear studies and ion-ion collisions

The linear simulations for ITG instability studies are performed in this Section with narrow temperature and density profiles of type 2 [see Eq. 3.60] with width $\Delta_A/a = 0.2$. An *ad hoc* equilibrium is considered. Numerous comparisons between ORB5 and analytical predictions for the local collisionless ITG dispersion relations, derived in [34] and briefly recalled in Chapter 2, are given in [51]. As an example, the spectrum of the ITG linear growth rate for the CYCLONE case parameters is presented in Figure 7.1. The kinetic electron response, through the hybrid model described in Sec. 3.6, increases significantly the ITG growth rate of the most unstable modes, $k_\theta \rho_{Li} \simeq 0.3 - 0.4$, compared to simulations considering fully adiabatic electrons. More details about this mechanism are given in Sec. 7.7.

Ion-ion collisions have a negligible effect on the linear growth rates of ITG instabilities. Considering the CYCLONE case parameters defined in Sec. 3.8, Figure 7.2 shows a very weak increase of the growth rate with collisionality for a mode $k_\theta \rho_{Li} = 0.4$ ($\sim 5\%$ increase at $\nu^* = 0.45 \simeq 10 \nu_{\text{phys}}^*$), consistently with results obtained in [87] for slab-ITG instabilities. Note that, as mentioned in [87], the local parallel momentum conservation of the collision operator is crucial in order to obtain the mentioned increasing behaviour of the growth rate with respect to collisionality. The parallel momentum conservation is only obtained through a sufficiently

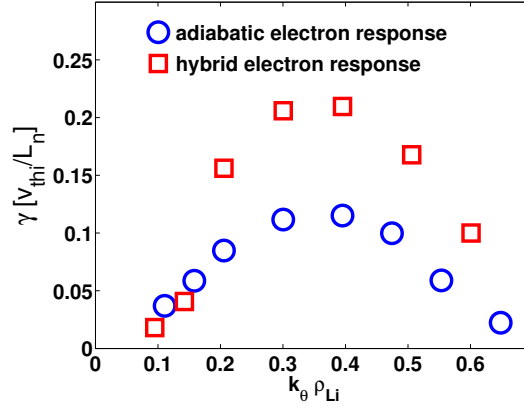


Figure 7.1: Linear growth rate spectrum for the CYCLONE case parameters, considering both adiabatic electrons and hybrid (kinetic trapped and adiabatic passing) electrons.

refined binning grid for the background reaction operator ($n_s \times n_{\theta^*} \times n_\varphi = 128 \times 256 \times 32$) and therefore requires a large number of markers ($80 \cdot 10^6$), much more than a collisionless linear simulation. In conclusion, the effect of ion-ion collisions on ITG linear growth rates appears to be negligible for physically relevant collisionalities.

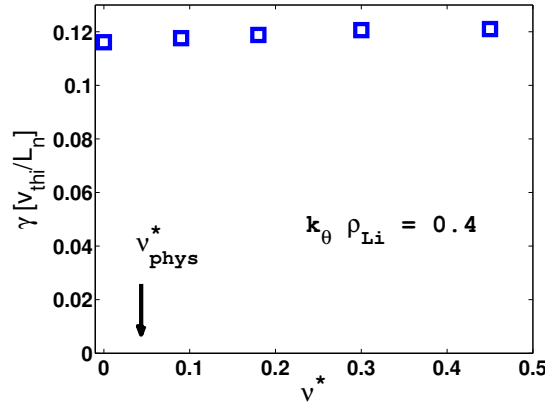


Figure 7.2: Very weak effect of ion-ion collisions on ITG linear growth rates. $k_\theta \rho_{Li} = 0.4$, CYCLONE case parameters.

7.3 Non-linear global ITG simulations with no heat sources

The CYCLONE base case [70] is chosen in order to study the effects of the ion-ion self-collisions on ITG microturbulence, considering adiabatic electrons and no heat source along with the wide gradient profiles given by Eq. (3.61). The total initial distribution is a canonical Maxwellian, $f(t=0) = f_{CM}$ with $\bar{\psi} = \Psi_0$, which is a stationary state of the collisionless gyrokinetic equation. Without collisions, simulations must start with a small perturbation to that equilib-

rium, in order for the turbulence to grow. With collisions, and at first enforcing axisymmetry by retaining only the toroidal Fourier mode $n = 0$, the full distribution will evolve towards a different distribution, i.e. a true neoclassical equilibrium together with the corresponding self-consistent axisymmetric electric field. After the neoclassical equilibrium has been reached, turbulence is switched on by letting the non-axisymmetric modes ($n \neq 0$) evolve freely. For the turbulent simulations presented in this Section, only every fourth toroidal Fourier mode is retained (namely $n = 0, 4, 8, \dots, 56$), as justified in Ref. [115] and corresponding in real space to a $1/4$ toroidal wedge. Note that $n_{\min} = 4$ corresponds to $k_{\theta, \min} \rho_{Li} \simeq 0.06$. 500 million markers are used along with the following grid in configuration space for solving the quasi-neutrality equation: $N_s = 128$ points in the radial direction, $N_{\theta^*} = 512$ points in the poloidal direction and $N_\varphi = 256 \simeq N_{\theta^*}/q_s$ points in the toroidal direction. These numerical parameters yield an average of ~ 30 markers per cell. However, since the perturbed density is filtered in the poloidal and toroidal Fourier spaces, the important ratio is the number of markers per Fourier mode and per radial grid point [51]. Invoking the alignment of microturbulence with the magnetic field lines, only the poloidal modes $m \in [nq_s - 5, nq_s + 5]$ are retained for each toroidal mode n . This filter leads to ~ 3 million markers per Fourier mode. It has been verified that even with collisions this resolution ensures converged results (for the considered radial resolution).

For the sake of clarity, the turbulent contribution to the kinetic energy flux Q_{turb} is defined in this Section as follows:

$$Q_{\text{turb}} = \left\langle \frac{\nabla r}{|\nabla r|} \cdot \int d^3v \frac{m_i v^2}{2} (f_0 + \delta f) \mathbf{v}_{E \times B} \right\rangle_S, \quad (7.1)$$

even though this term may contain a small neoclassical contribution through the axisymmetric but poloidally asymmetric modes ($n = 0, m \neq 0$). Note that the mentioned neoclassical contribution, related to the background f_0 , disappears if the potential energy flux is properly accounted for as in Sec. 7.4. $\langle \rangle_S$ is the flux surface average operator and m_i the ion mass. The neoclassical contribution to the kinetic energy flux Q_{neo} is defined as:

$$Q_{\text{neo}} = \left\langle \frac{\nabla r}{|\nabla r|} \cdot \int d^3v \frac{m_i v^2}{2} \delta f (\mathbf{v}_{\nabla B} + \mathbf{v}_c) \right\rangle_S, \quad (7.2)$$

where $\mathbf{v}_{\nabla B}$ is the ∇B drift and \mathbf{v}_c the curvature drift. The simulation system considered has no heat sources, so that the temperature profile is free to relax towards marginally stable gradients with respect to the instabilities underlying the microturbulence. Figure 7.3 (a) shows the initial and relaxed temperature profiles for both a collisionless case and $\nu^*(r/a = 0.5) = 0.18$, which corresponds to a collisionality about 4 times larger than the one derived from the actual DIII-D parameters underlying the CYCLONE case. Let us point out that, in the collisional case, the system never fully relaxes, since the neoclassical heat transport persists even after the turbulent transport has vanished. As shown below and as expected, this neoclassical transport is however small compared to the fully developed turbulent transport in the first phase of the simulation, so that it is therefore appropriate to define the system as having reached a quasi-equilibrium state once the turbulent transport falls to the level of the neoclassical one. Figure 7.3 (b) shows the evolution of the ion heat diffusivity χ_{Hi} with respect to the effective ion temperature

gradient R_0/L_{Ti} , averaged between $r = 0.3a$ and $r = 0.45a$. The critical gradient R_0/L_{Tcrit} is defined as the temperature gradient of this sourceless system once it has reached the quasi-equilibrium state as just defined. As clearly seen from Figure 7.3, the critical gradient of the collisional case is lower than the critical gradient of the collisionless case. Indeed, collisions yield a critical gradient close to the linear stability of the most unstable ITG modes, $R_0/L_{Ti} \simeq 5$. This is consistent with the fact that collisions damp the zonal flows and thus soften the so-called Dimits shift, defined as the difference between the critical gradient for linear stability and the critical gradient observed in nonlinear collisionless gyrokinetic turbulent simulations. The latter is larger due to the stabilizing effect of zonal flows. By damping the zonal flows, ion-ion collisions thus increase the level of ITG turbulent heat transport, as already observed and discussed in Ref. [23]. This effect will be studied in further detail in Sec. 7.4.

The time evolution of the kinetic energy flux at $r = 0.5a$ is plotted in Figure 7.4 (a), for the same cases. For the collisional simulation, the neoclassical phase (keeping only $n = 0$ modes) is carried out up to time $t = 2\tau_{ii}$, after which the turbulent phase is initiated (keeping modes $n \neq 0$ as well). The small discrepancy between the total flux and the $\mathbf{v}_{\nabla B} + \mathbf{v}_e$ contribution in the neoclassical phase is due to the small inward neoclassical $\mathbf{v}_{E \times B}$ contribution through the poloidally asymmetric modes, as explained above. The fully developed turbulent transport, corresponding to the bursty phase, is clearly much larger than the neoclassical transport. The neoclassical flux nevertheless becomes dominant once the temperature profile has relaxed. Figure 7.4 (b) presents the time evolution of the signal/noise ratio. The standard way of evaluating the noise in ORB5 has been described in Ref. [79] and briefly reminded in Sec. 4.8. The considered runs made use of the coarse-graining procedure [22] described in Chapter 4. Note that even in the late phase of the collisional simulation, the ratio remains above the statistically relevant threshold (considered to be of order ~ 10 , see Ref. [79]). As expected, the collisionless simulation remains significantly less noisy for the same numerical parameters.

7.4 Quasi-stationary collisional turbulence simulations started from a neoclassical equilibrium

Simulations based on the CYCLONE case parameters have been carried out for collisionalities in the range $\nu_0^* = 0.09 - 0.45$, i.e. 2 to 10 times larger than the physical one $\nu_{phys}^* = 0.045$. Note that for studying collisional effects, simulations must be carried out over multiple collision times while resolving the shorter time scale of the turbulent fluctuations. Low collisionality is thus numerically challenging due to the large number of time steps required in order to reach a sufficient simulation time, while high collisionality is challenging as well due to the large number of markers required for ensuring a sufficient signal/noise ratio. Collisional simulations are performed with $500 \cdot 10^6$ markers representing the ions and started from a canonical Maxwellian as the total initial distribution: $f(t = 0) = f_{CM}(\hat{\Psi})$. For collisional simulations and as previously done for simulations with no heat sources presented in Sec. 7.3, a first run with only axisymmetric modes ($n = 0$) is carried out over approximately two collision times τ_{ii} , in order to establish a neoclassical equilibrium with associated electric field and toroidal rotation profile. Note that the toroidal rotation profile of the neoclassical equilibrium is determined by the

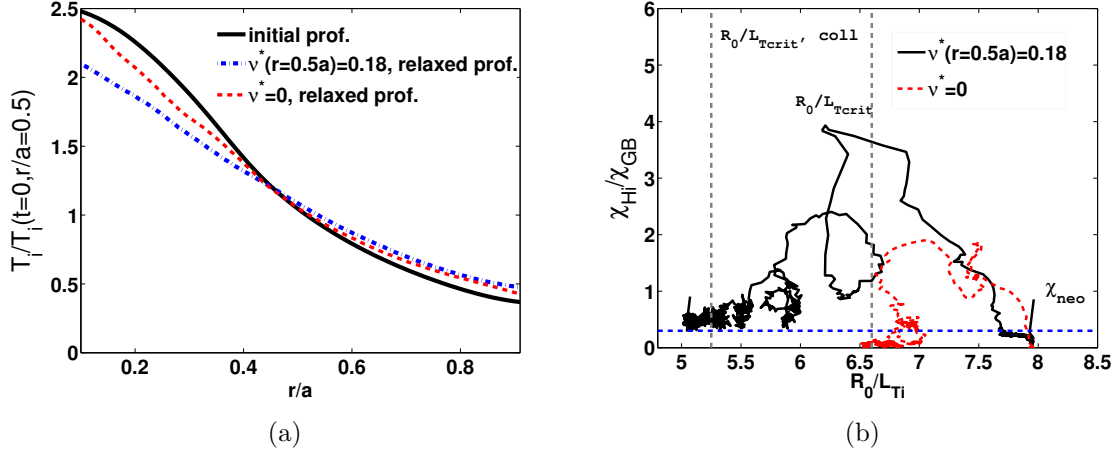


Figure 7.3: Collisionless and collisional turbulent CYCLONE case without heat sources: (a) Relaxation of the temperature profile towards the quasi-stationary state for both a collisionless and a collisional simulation with $\nu_0^* = 0.18$. (b) Evolution of the ion heat diffusivity $\chi_{Hi} = (Q_{neo} + Q_{turb})/(n_i |\nabla T_i|)$ in Gyro-Bohm units versus the temperature gradient. Collisions yield a lower nonlinear critical gradient. The quasi-stationary state is obtained when the heat diffusivity reaches the neoclassical level χ_{neo} .

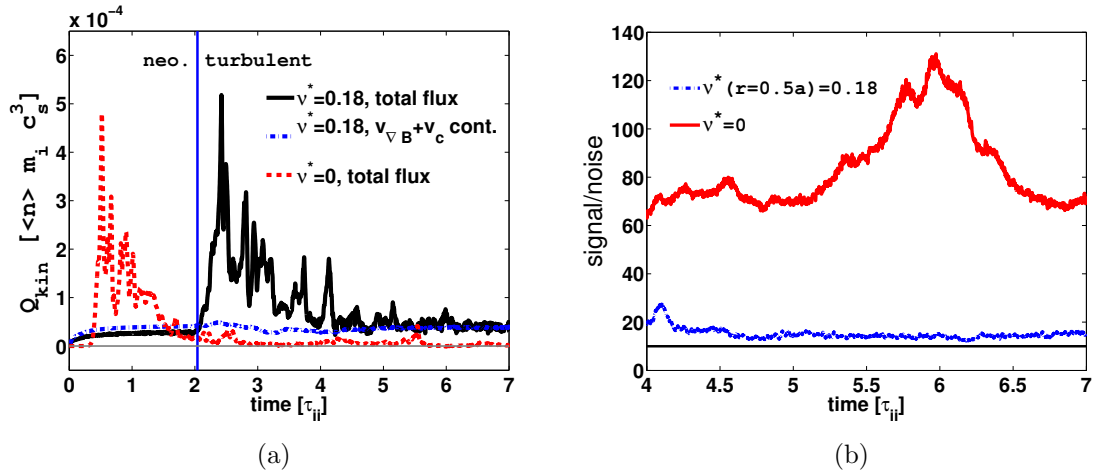


Figure 7.4: (a) Time evolution of the total kinetic energy flux $Q_{kin} = Q_{turb} + Q_{neo}$ at $r/a = 0.5$ for both a collisional (full black line) and a collisionless (dashed red) simulation. Also shown is the neoclassical contribution Q_{neo} for the collisional case (dash-dotted blue). An initial neoclassical phase is first carried out in order to set up a neoclassical equilibrium. In the bursty phase, the turbulent transport is much larger than the neoclassical transport. (b) Signal/noise ratio for simulations using 500 million markers and coarse-graining. The collisionless case is significantly less noisy, but the coarse-graining enables to keep the collisional simulation above the relevance threshold ~ 10 even at later simulation times.

initial ion distribution function and may in principle affect, through its shearing, the development of turbulence in the subsequent simulation. As mentioned in Chapter 3, the choice of the background $f_{CM}(\hat{\Psi})$ has the purpose of providing neoclassical equilibria with essentially zero toroidal rotation. For the typical collisional CYCLONE cases considered here, the maximum toroidal velocity is $v_{toro} \sim 0.02 - 0.03 v_{thi}$ and the associated toroidal shearing rate is much

smaller than the $\mathbf{E} \times \mathbf{B}$ shearing rate: $\omega_{\text{toro}} \sim dv_{\text{toro}}/dr \sim 0.1 \omega_{E \times B}$.

In a second phase, the simulation is resumed taking into account both the axisymmetric and the non-axisymmetric modes ($n = 0$ and $n \neq 0$), thus allowing turbulence to develop and enabling to study the resulting anomalous transport and in particular the interaction between turbulence, neoclassical background flows and turbulence-induced zonal flows. Only every second toroidal Fourier mode is retained, namely $n = 0, 2, 4, \dots, 56$, corresponding in real space to 1/2 toroidal wedge. The typical time evolution of the neoclassical and turbulent contributions to the kinetic energy flux Q_{kin} (as defined in Sec. 3.10 but removing the here irrelevant background contribution $\sim f_0 \cdot d\Psi/dt|_{E \times B}$), both in the neoclassical and turbulent phases of the simulation, is shown in Figure 7.5 for the temperature gradient $R_0/L_{T_0} = 6.9$ and collisionality $\nu_0^* = 4 \nu_{\text{phys}}^* = 0.18$. The use of the heat source described by Eq. (3.35) enables to reach a quasi-stationary level of transport by maintaining a constant temperature gradient, in a time-average sense. A remarkable observation is the fact that initiating the collisional turbulence simulations from a neoclassical equilibrium appears not to be equivalent to starting the turbulence simulations directly from a canonical Maxwellian as the total initial distribution. Figure 7.6 (a) shows the total heat diffusivity profile in both cases, in the quasi-stationary state of the simulation, for $\nu_0^* = 0.09$ and $R_0/L_{T_0} = 6.9$. The turbulent transport appears to be reduced by the preliminary neoclassical equilibrium. The structure of the radial electric field profile, for the same physical parameters, is affected as well by the initial conditions of the turbulence simulation, as presented in Figure 7.6 (b).

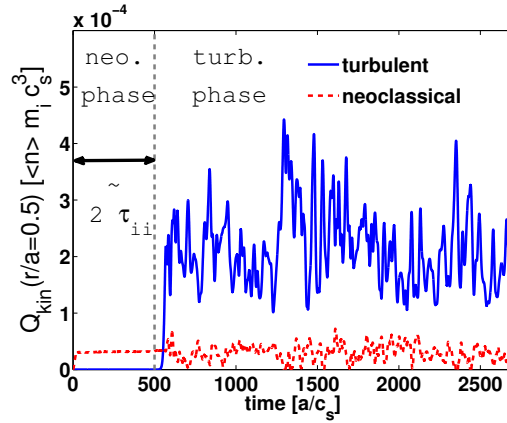


Figure 7.5: Time evolution of the neoclassical (red dashed line) and turbulent (blue plain line) contributions to the kinetic energy flux Q_{kin} at mid-radius, in the neoclassical phase ($t < 500[a/c_s] \sim 2\tau_{ii}$) and the turbulent phase ($t > 500[a/c_s]$) of the simulation, for $\nu_0^* = 0.18$. Once a neoclassical equilibrium is established, turbulence is switched on and turbulent transport becomes dominant compared to neoclassical transport, for the here considered CYCLONE case gradients ($R_0/L_{n_0} = 2.2$, $R_0/L_{T_0} = 6.9$). The neoclassical flux is perturbed by turbulence but remains constant in a time-average sense.

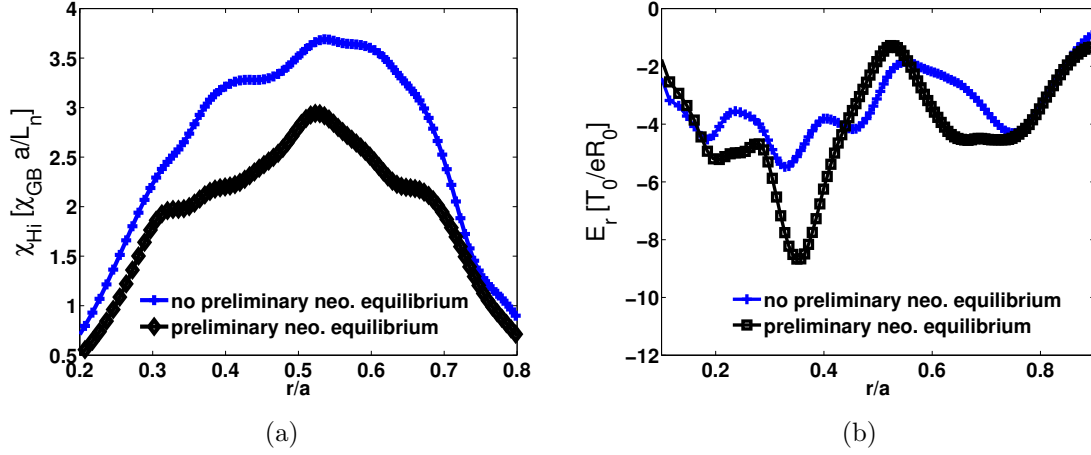


Figure 7.6: (a) Total heat diffusivity profile and (b) radial electric field profile in the quasi-stationary state of the simulation, for $\nu_0^* = 0.09$ and $R_0/L_{T_0} = 6.9$. Initiating the turbulence simulation from a neoclassical equilibrium modifies the turbulent transport as well as the radial electric field structure.

7.4.1 Temperature gradient and collisionality effects on heat diffusivity

In this Section, two temperature gradients are first considered, along with wide non-zero gradient profiles of type 3 ($\Delta_A = 0.3a$) for carrying out a collisionality scan. The first one, $R_0/L_{T_0} = 5.3$, is above the linear stability threshold $R_0/L_{T_0} \simeq 4.5$, but below the collisionless non-linear stability threshold $R_0/L_{T_0} \simeq 6.0$ of ITG turbulence in the considered physical system (CYCLONE), i.e. in the so-called Dimits shift region [70]. The second one, $R_0/L_{T_0} = 6.9$, is above the non-linear stability threshold and thus ensures a stronger drive for turbulence.

Figure 7.7 shows the neoclassical heat diffusivity χ_H^{neo} and the quasi-stationary total (neoclassical + turbulent) heat diffusivity $\chi_H^{\text{tot}} = \chi_H^{\text{neo}} + \chi_H^{\text{turb}}$ at mid-radius with respect to the collisionality. For the gradient below the non-linear stability threshold, $R_0/L_{T_0} = 5.3$, a non-vanishing turbulent transport illustrating a softening of the Dimits shift region is established through collisions. The turbulent diffusivity is relatively small in this latter case, i.e. of the order of the neoclassical diffusivity at each collisionality ($\chi_H^{\text{turb}} \sim \chi_H^{\text{neo}}$ such that $\chi_H^{\text{tot}} \sim 2 \chi_H^{\text{neo}}$). Note that, as expected, there is zero transport at $R_0/L_{T_0} = 5.3$ if the collisions are switched off [$\chi_H(\nu^* = 0, R_0/L_{T_0} = 5.3) = 0$]. For the higher temperature gradient $R_0/L_{T_0} = 6.9$, the increase of the total diffusivity due to collisions is significantly larger than for $R_0/L_{T_0} = 5.3$ [$\chi_H^{\text{turb}}(\nu^*) - \chi_H^{\text{turb}}(\nu^* = 0) > \chi_H^{\text{neo}}(\nu^*)$]. For all gradients above the linear stability threshold, one thus observes:

$$\chi_H^{\text{tot}}(\nu^*) > \chi_H^{\text{turb}}(\nu^* = 0) + \chi_H^{\text{neo}}(\nu^*). \quad (7.3)$$

In general, the heat transport in the presence of both turbulence and ion-ion collisions is thus larger than the sum of collisionless turbulent and neoclassical transport considered separately. This reflects the complex interplay between collisional effects, flows and turbulence.

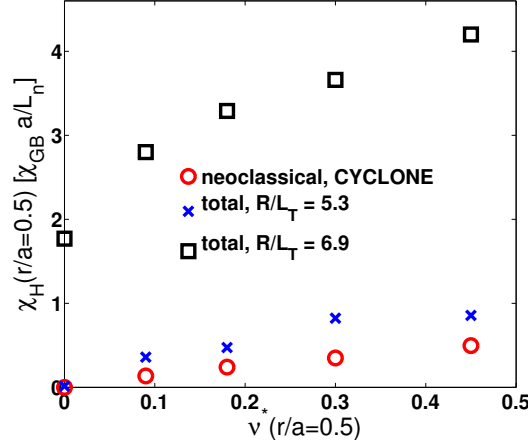


Figure 7.7: Heat diffusivity χ_H at mid-radius versus the ion collisionality parameter ν^* , for both temperature gradients $R_0/L_{T_0} = 5.3$ (blue crosses) and $R_0/L_{T_0} = 6.9$ (black squares). The contribution of the neoclassical diffusivity (red circles) to the total diffusivity is important for the weaker gradient $R_0/L_{T_0} = 5.3$, while it becomes relatively small for the larger gradient $R_0/L_{T_0} = 6.9$. The total diffusivity, increasing with collisions, is in all cases larger than the neoclassical diffusivity added to the collisionless turbulent diffusivity.

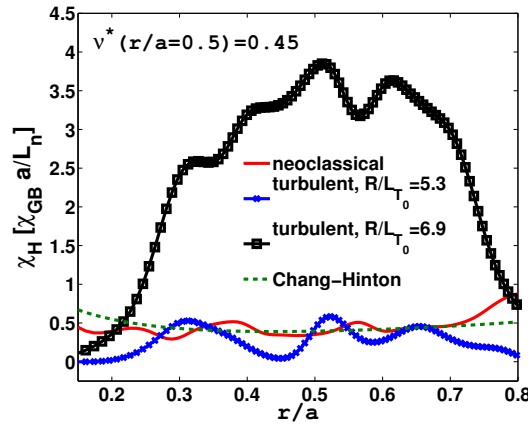


Figure 7.8: Heat diffusivity profile $\chi_H(r)$ in the quasi-stationary state of the simulation, for a collisionality $\nu_0^* = 0.45$ and both temperature gradients $R_0/L_{T_0} = 5.3$ and $R_0/L_{T_0} = 6.9$. For the weaker gradient $R_0/L_{T_0} = 5.3$, the turbulent contribution profile (blue crosses) is similar to the neoclassical contribution profile (red plain line), while the turbulent contribution profile in the case of the larger gradient $R_0/L_{T_0} = 6.9$ (black squares) is clearly dominant. The neoclassical contribution is successfully benchmarked against the Chang-Hinton predictions (green dashed line).

Figure 7.8 presents the radial profiles of the quasi-stationary diffusivity χ_H for the particular collisionality case $\nu_0^* = 10 \times \nu_{phys}^* = 0.45$. The neoclassical contribution computed during the turbulent phase is compared to an analytical prediction derived by Chang and Hinton [103], showing a good agreement. While the turbulent transport is of the order of the neoclassical transport in the case of the lower gradient $R_0/L_{T_0} = 5.3$, it becomes clearly dominant for $R_0/L_{T_0} = 6.9$.

The scan of considered temperature gradients is then extended at fixed collisionality, in order to

sketch the dependence of the collisional heat diffusivity on the ion temperature gradient. Similar to studies already done for the CYCLONE parameters in the frame of collisionless simulations [70], Figure 7.9 shows how the ion temperature gradient affects the ion heat diffusivity for ITG turbulence at mid-radius $r/a = 0.5$, for the chosen collisionality $\nu^* = 0.09 = 2 \nu_{\text{phys}}^*$ as well as for the collisionless situation for reference. The full blue line in Figure 7.9 is the fit to collisionless simulation results given in Ref. [70], provided by:

$$\chi_H \simeq 15.4 \left(1 - 6 \frac{L_{T_0}}{R_0} \right) \chi_{GB} \frac{a}{L_{n_0}}. \quad (7.4)$$

While the Dimits shift softening is again clearly illustrated by the difference between neoclassical diffusivity and total collisional diffusivity in the collisionless Dimits shift region ($4.5 \leq R_0/L_{T_0} < 6.0$), the collisional increase of the transport level is also emphasized in the region above the non-linear stability threshold ($R_0/L_{T_0} \geq 6.0$).

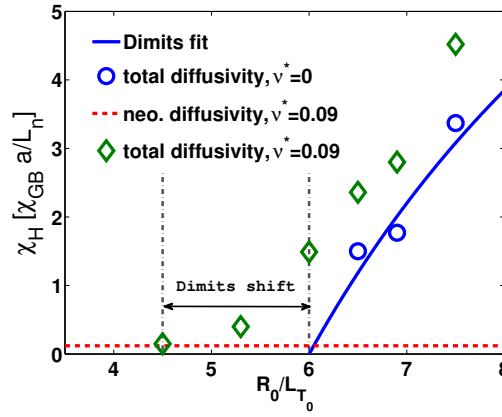


Figure 7.9: Heat diffusivity χ_H at mid-radius versus the temperature gradient R_0/L_{T_0} . The full blue line is the collisionless prediction resulting from a fit on gyrokinetic simulation results. For $\nu_0^* = 0.09$, the red dashed line shows the neoclassical diffusivity level and the green diamonds represent the total diffusivity for different temperature gradients. Collisions clearly increase the heat diffusivity and soften the so-called Dimits shift region separating the linear from the non-linear collisionless gradient threshold.

7.4.2 Zonal flows in collisional ITG turbulence simulations

As the ion-ion collisions have a marginal influence on the growth rate of the ITG modes in the linear phase of the simulation (a slight increase of the linear growth rate if the parallel momentum is correctly conserved by collisions [87], see Sec. 7.2), it is expected that the effect of collisions on the turbulent ITG transport happens mainly through their damping effect on the zonal flows. Just as for the collisionless case, the study of the zonal flows is thus essential in order to get insight into the collisional turbulent transport. The standard picture of the interaction between zonal flows and turbulence is the following [17] [25]: Above the linear ion temperature gradient threshold for the ITG instability, turbulence starts to develop and non-linearly drives zonal modes which in turn tend to quench the turbulence due to the $\mathbf{E} \times \mathbf{B}$

shearing rate $\omega_{E \times B}$, given by the following approximate form [116]:

$$\omega_{E \times B} = \frac{r}{q_s B_0} \frac{d}{dr} \left(\frac{q_s E_r}{r} \right). \quad (7.5)$$

The maximum saturation level of zonal flows appears to be determined by a tertiary, Kelvin-Helmoltz (KH)-type instability [113], providing a mechanism for transferring energy back from zonal flows to turbulence. The KH saturation mechanism is illustrated in Figure 7.10 (a), showing the time evolution of the radially averaged shearing rate $\langle |\omega_{E \times B}| \rangle_r$ for the CYCLONE base case with $R_0/L_{T_0} = 6.9$, having defined the radial average operator over the width $\Delta_{\mathcal{A}}$ of the gradient profiles:

$$\langle \cdots \rangle_r = \frac{1}{2\Delta_{\mathcal{A}}} \int_{r_0 - \Delta_{\mathcal{A}}}^{r_0 + \Delta_{\mathcal{A}}} \cdots dr. \quad (7.6)$$

In a first phase ($0 < tc_s/a < 130$), three collisionless simulations under the linear Rosenbluth-Hinton test conditions described in Sec. 6.6.1 are performed, for different amplitudes of the initial perturbation: $|\delta f_{LM}/f_{LM}|(t=0) = 0.01, 0.05, 0.1$. The zonal flow residual and associated shearing rate amplitudes established after a time $t \simeq 130[a/c_s]$ are proportional to the initial amplitude of the perturbation, as expected and observed in Figure 7.10 (a): $\langle |\omega_{E \times B}| \rangle_r \simeq 0.04, 0.21, 0.42[c_s/a]$ respectively. In a second phase ($130 < tc_s/a < 520$), the non-axisymmetric turbulent modes ($n \neq 0$) are enabled to evolve and interact with the axisymmetric zonal flows. The lowest initial amplitude case [$|\delta f_{LM}/f_{LM}|(t=0) = 0.01$] provides a residual zonal flow level clearly lower than the KH threshold level. Once the turbulence is switched on, it thus drives the zonal flows of the considered simulation to a higher level until the associated shearing rate reaches a saturation level of approximately $\langle |\omega_{E \times B}| \rangle_r \simeq 0.11[c_s/a]$, identified as the KH saturation level. For the higher amplitude cases [$|\delta f_{LM}/f_{LM}|(t=0) = 0.05, 0.1$], the shearing rate level of the residual zonal flow reached during the first phase of the simulation is clearly above the just mentioned KH saturation level. Once the non-axisymmetric modes ($n \neq 0$) are switched on, the axisymmetric modes transfer energy back to turbulence and the $\omega_{E \times B}$ shearing rate decays to the KH saturation level, $\langle |\omega_{E \times B}| \rangle_r \simeq 0.11[c_s/a]$, as observed in Figure 7.10 (a). These results are clear proof of the tertiary instability threshold limiting the $\omega_{E \times B}$ shearing rate amplitude.

In order to fully isolate the KH instability mechanism limiting the shearing rate of the self-induced zonal flows, the previous runs are repeated with zero density and temperature gradients. In this case, the growth of $n \neq 0$ modes can thus only result from the decay of the ZF's due to the tertiary instability, as the actual turbulent drive from the ITG instability has been removed. As shown in Figure 7.10 (a), for the initial amplitude case $|\delta f_{LM}/f_{LM}|(t=0) = 0.05$, the shearing rate again decays once the $n \neq 0$ modes are turned on and the KH instability is enabled to evolve, from $\langle |\omega_{E \times B}| \rangle_r \simeq 0.21[c_s/a]$ at $t = 130[a/c_s]$ to $\langle |\omega_{E \times B}| \rangle_r \simeq 0.11[c_s/a]$, i.e. to essentially the same KH threshold level observed in the presence of background gradients. For the initial amplitude case $|\delta f_{LM}/f_{LM}|(t=0) = 0.01$, the resulting shearing rate at $t = 130[a/c_s]$ again takes the value $\langle |\omega_{E \times B}| \rangle_r \simeq 0.04[c_s/a]$ as in the presence of gradients, i.e. lies below the KH threshold. As the turbulent drive of the zonal flows from the $n \neq 0$ modes is absent in

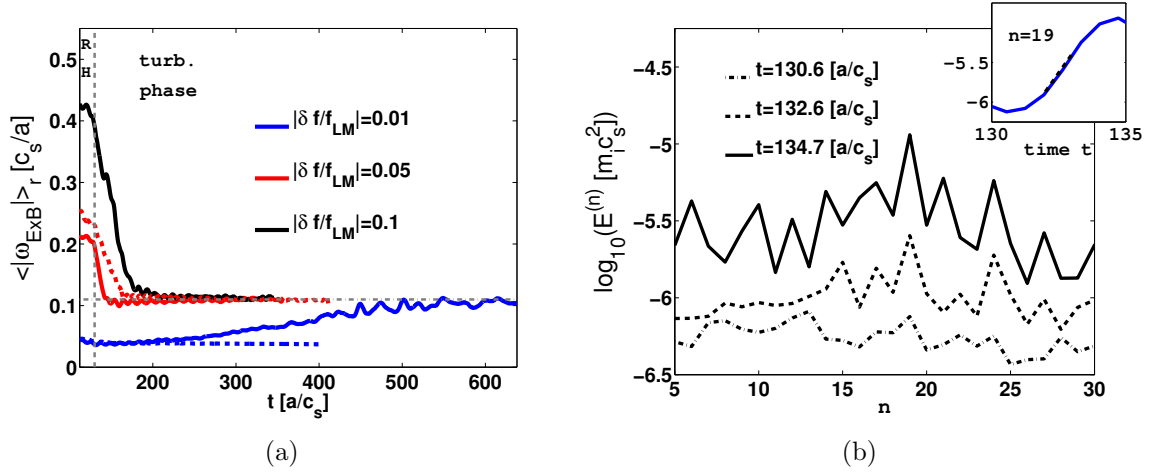


Figure 7.10: Illustration of the Kelvin-Helmoltz (KH) saturation mechanism. (a) Time evolution of the radially averaged zonal flow shearing rate $\langle |\omega_{E \times B}| \rangle_r$ in non-linear collisionless simulations, following an initial linear $n = 0$ phase (until $t \simeq 130[a/c_s]$) started at $t = 0$ from $|\delta f/f_{LM}| = 0.01, 0.05$ and 0.1 respectively. With external turbulence drive from density and temperature gradients (plain lines), all three cases establish, in the long time scale, a similar level of zonal flow shearing rate. With no external turbulence drive (dashed lines), transfer of energy is only possible from zonal flows to turbulence. Note that the KH saturation level with or without external turbulence drive remains the same. (b) Growth of the $n \neq 0$ modes through zonal flow decay, for $|\delta f/f_{LM}|(t = 0) = 0.1$ and no external turbulence drive. The most unstable mode is $n = 19$ and its exponential growth phase is detailed in the inset.

this case, this shearing rate remains stationary as expected. The exponential growths of the $n \neq 0$ modes during the initial phase of the tertiary instability mechanism have been estimated. Modes in the range $n = 17 - 20$ (corresponding to $k_{\theta} \rho_{Li} \simeq 0.26 - 0.31$) have been identified as the most unstable in this case. Evolution of the $n \neq 0$ modes during the KH instability are shown in Figure 7.10 (b) for the initial amplitude case $|\delta f_{LM}/f_{LM}|(t = 0) = 0.1$. A maximum growth rate $\gamma_{KH} = 0.55[c_s/a]$ for $n = 19$ was measured for this latter case, while essentially half this growth rate is measured for $|\delta f_{LM}/f_{LM}|(t = 0) = 0.05$, i.e. $\gamma_{KH} = 0.27[c_s/a]$ ($n = 17$), in very good agreement with theory [113] predicting that the KH growth rate is proportional to the amplitude of the zonal modes.

In a third phase, the simulation with gradients and the initial perturbation $|\delta f_{LM}/f_{LM}|(t = 0) = 0.05$ is then resumed from $t \simeq 330[a/c_s]$, considering two different collisionalities $\nu_0^* = 0.09$ and $\nu_0^* = 0.45$ as presented in Figure 7.11. The average zonal flow level $\langle |\omega_{E \times B}| \rangle_r$ is as expected damped by collisions, but nevertheless maintained close to the collisionless value through additional drive from increased turbulence in collisional simulations, as presented in Sec. 7.4.1. Moreover, one observes that both collisionalities considered lead to approximately the same collisional level of the zonal flow shearing rate $\omega_{E \times B}$, reduced by $\sim 30\%$ compared to the collisionless value, a fact which is interpreted as an example of self-organization. In the first phase of the collisional simulation, the zonal flows are more strongly damped for the largest collisionality $\nu_0^* = 0.45$, but then increase in a second phase through additional turbulence kicks in order to reach roughly the same level as obtained with the moderate collisionality $\nu_0^* = 0.09$. As a consequence of the stronger turbulence drive, the radially averaged turbulent

energy flux $\langle Q_{\text{turb}} \rangle_r$ for $\nu_0^* = 0.45$ is larger than for $\nu_0^* = 0.09$ [$\langle Q_{\text{turb}} \rangle_r(\nu_0^* = 0.45) / \langle Q_{\text{turb}} \rangle_r(\nu_0^* = 0.09) \simeq 1.8$], essentially in accordance with the collisional increase of the turbulent transport emphasized in Sec. 7.4.1 despite the different initial conditions.

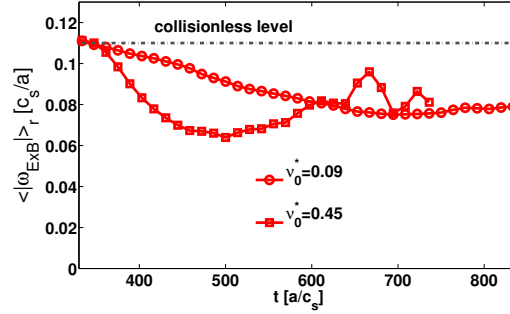


Figure 7.11: Non-linear simulations resumed at $t \simeq 330[a/c_s]$ from the simulation in Figure 7.10 started from $|\delta f/f_{LM}| = 0.05$ and with background gradients, turning on finite collisionalities $\nu_0^* = 0.09$ (circles) and $\nu_0^* = 0.45$ (squares) respectively. A moderate reduction of the average zonal flow shear level $\langle |\omega_{E \times B}| \rangle_r$ by collisions is observed, roughly independent of the considered collisionality at sufficiently long time scales.

In absence of collisions, if the zonal shearing rate $\omega_{E \times B}$ is strong enough below or at its KH saturation level in order to quench the turbulence, as is the case for the temperature gradient $R_0/L_{T_0} = 5.3$, no turbulent transport occurs. On the contrary, if the drive is strong enough, as is the case for the temperature gradient $R_0/L_{T_0} = 6.9$, turbulence is not totally quenched by the saturated zonal flow shearing and some turbulent transport develops. The existence of a tertiary instability threshold setting a saturation level on the zonal flows thus explains the end of the Dimits shift region starting from $R_0/L_{T_0} \simeq 6.0$, where the turbulence drive becomes too large compared to the saturated zonal flow level and is thus able to produce finite anomalous transport. The latter mechanism is emphasized in Figure 7.12, which compares the maximum linear growth rate γ_{\max} as well as the time average of the radially averaged shearing rate $\langle |\omega_{E \times B}| \rangle_{r,t}$ from non-linear simulations, for different values of the temperature gradient R_0/L_{T_0} . Both collisionless as well as finite collisionality $\nu_0^* = 0.09$ simulations have been considered for estimating $\langle |\omega_{E \times B}| \rangle_{r,t}$. Note that the collisionality $\nu_0^* = 0.09$ has a negligible effect on γ_{\max} . The end of the Dimits shift region, at approximately $R_0/L_{T_0} \simeq 6.0$, is characterized by a maximum linear growth rate γ_{\max} which becomes larger than the averaged zonal flow shear level $\langle |\omega_{E \times B}| \rangle_{r,t}$. Note that the difference between γ_{\max} and $\langle |\omega_{E \times B}| \rangle_{r,t}$ increases for temperature gradients $R_0/L_{T_0} > 6.0$, due to the mentioned tertiary instability mechanism which limits $\langle |\omega_{E \times B}| \rangle_{r,t}$ and thus allows a stronger turbulence to develop at higher temperature gradients.

Consistently with Figure 7.11, the averaged shearing rate for basically all gradients is only slightly reduced by collisions ($\sim 20\%$), although, as predicted in Ref. [99], the zonal flows driven by turbulence are shown to be damped by ion-ion collisions. This effect is detailed in Tables I & II, for both temperature gradients $R_0/L_{T_0} = 5.3$ and $R_0/L_{T_0} = 6.9$ respectively, where the averaged shearing rate amplitudes $\langle |\omega_{E \times B}| \rangle_{r,t}$ are presented, including statistical error estimates given by the variance of means for 4 overlapping time windows of width $200[a/c_s]$

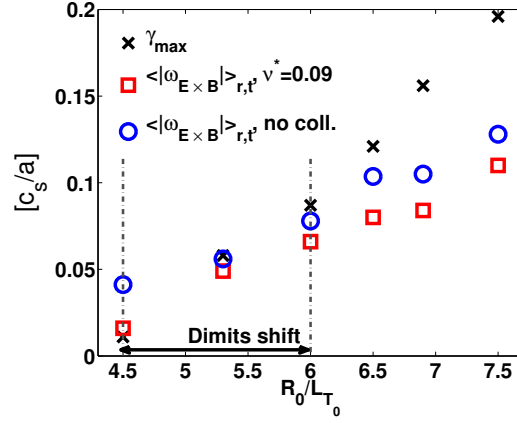


Figure 7.12: Maximum linear growth rate γ_{max} (black crosses) and averaged shearing rate $\langle |\omega_{E \times B}| \rangle_{r,t}$, considering both the finite collisionality $\nu_0^* = 0.09$ (red squares) and the collisionless case (blue circles), for different temperature gradients R_0/L_{T_0} . Note that the averaged shearing rate is in general slightly reduced by collisions. Beyond the Dimits shift region, $\gamma_{max} > \langle |\omega_{E \times B}| \rangle_{r,t}$. The important difference between γ_{max} and $\langle |\omega_{E \times B}| \rangle_{r,t}$ at large temperature gradients is due to a tertiary instability mechanism.

($\sim 2 \tau_{ii}$ for $\nu_0^* = 0.45$) in the quasi-stationary state of the simulation. These values are indeed only slightly reduced by finite collisionality over the whole considered range $\nu_0^* = 2-10 \nu_{phys}^*$ and thus remain of the order of the collisionless level. The additional drive for zonal flows, coming from the increased turbulence observed in collisional simulations, thus appears to essentially compensate the damping by ion-ion collisions. For collisional runs in the Dimits shift region (including $R_0/L_{T_0} = 5.3$), the averaged shearing rates can only be maintained at approximately the collisionless levels thanks to a finite turbulence level, leading to finite transport and to the so-called Dimits shift softening. A tight equilibrium between zonal flow damping by collisions and zonal flow drive by additional turbulence is thus apparently established. In the absence of collisions, no such tight balance between damping and drive is imposed on the zonal flows, which are thus free to exceed the minimum required level for quenching turbulence in the Dimits shift region. This probably explains the larger difference seen in Figure 7.12 between $\omega_{E \times B}$ for $\nu_0^* = 0$ and $\nu_0^* = 0.09$ at $R_0/L_{T_0} = 4.5$ than for other values of R_0/L_{T_0} .

Table I. Dependence on ν_0^* of averaged shearing rate $\langle |\omega_{E \times B}| \rangle_{r,t}$ for $R_0/L_{T_0} = 5.3$.

ν_0^*	0	0.09	0.18	0.3	0.45
$\langle \omega_{E \times B} \rangle_{r,t} [10^{-2} c_s/a]$	5.6 ± 0.09	4.9 ± 0.03	4.8 ± 0.03	5.2 ± 0.01	5.3 ± 0.03

Table II. Same as Table I but for $R_0/L_{T_0} = 6.9$.

ν_0^*	0	0.09	0.18	0.3	0.45
$\langle \omega_{E \times B} \rangle_{r,t} [10^{-2} c_s/a]$	10.5 ± 1.3	8.4 ± 0.4	9.5 ± 1.4	9.4 ± 0.5	9.5 ± 0.09

Figure 7.13 (a) shows the profiles of the absolute values of $\mathbf{E} \times \mathbf{B}$ shearing rate $|\omega_{E \times B}|(r)$, averaged over a time window of $200[a/c_s]$ in the quasi-stationary state of the turbulent simulation,

for different collisionalities and for the temperature gradient $R_0/L_{T_0} = 5.3$. For this case in the Dimits shift region, the averaged shearing rate $\langle |\omega_{E \times B}| \rangle_{r,t} \simeq 5.2 \cdot 10^{-2} [c_s/a]$ (average over all ν^*) is close to the linear growth rate of the most unstable mode $\gamma_{max} \simeq 5.8 \cdot 10^{-2} [c_s/a]$, consistently with Figure 7.12. Furthermore, as mentioned above, the averaged shearing rate $\langle |\omega_{E \times B}| \rangle_{r,t}$ is only slightly affected by collisions. This is remarkable, given that the radial shearing rate profile $|\omega_{E \times B}|(r)$ is significantly modified when going from zero to finite collisionality. Note however the almost identical shape of $|\omega_{E \times B}|(r)$ for the two considered finite collisionalities $\nu_0^* = 0.09$ and $\nu_0^* = 0.18$.

Figure 7.13 (b) is similar to Figure 7.13 (a) but considers the higher temperature gradient $R_0/L_{T_0} = 6.9$. For this case above the Dimits shift region, $\gamma_{max} \simeq 15.6 \cdot 10^{-2} [c_s/a]$ is significantly larger than the averaged shearing rate ($\langle |\omega_{E \times B}| \rangle_{r,t} \simeq 9.4 \cdot 10^{-2} [c_s/a]$, average over all ν^*), allowing the turbulence to survive and continuously drive anomalous transport, in accordance with Figures 7.9 and 7.12. As for $R_0/L_{T_0} = 5.3$, the amplitude of the collisional zonal flows appears to be only slightly reduced in the case $R_0/L_{T_0} = 6.9$ compared to the collisionless situation. The detailed shape of the profile $|\omega_{E \times B}|(r)$ is however affected by collisions and, unlike in the Dimits shift region, different collisionalities ($\nu_0^* = 0.09$ and $\nu_0^* = 0.18$) give different profiles $|\omega_{E \times B}|(r)$ for $R_0/L_{T_0} = 6.9$.

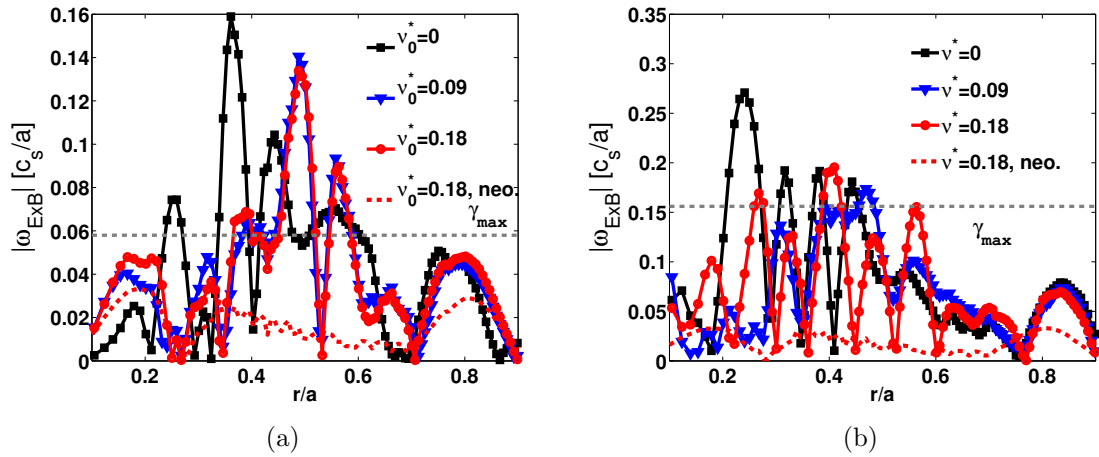


Figure 7.13: Profiles of the absolute value of $\mathbf{E} \times \mathbf{B}$ shearing rate $|\omega_{E \times B}|(r)$ for different collisionalities and a temperature gradient (a) $R_0/L_{T_0} = 5.3$ and (b) $R_0/L_{T_0} = 6.9$, the neoclassical contribution being emphasized for $\nu_0^* = 0.18$ (red dashed line). The averaged shearing rate level is of the order of the growth rate of the most unstable mode γ_{max} (grey dashed line) for $R_0/L_{T_0} = 5.3$, while the averaged shearing rate level is significantly lower than the growth rate of the most unstable mode γ_{max} for $R_0/L_{T_0} = 6.9$. The zonal flow damping by collisions appears to be balanced by an additional turbulence drive. For the considered collisionalities, the turbulence-driven zonal flows are dominant compared to the neoclassical flows.

Note that ion-ion collisions generate neoclassical background flows through the neoclassical equilibrium electric field. For the collisionalities considered in this Chapter (up to $10 \nu_{phys}^*$) and the temperature gradients $R_0/L_{T_0} = 5.3$ and $R_0/L_{T_0} = 6.9$, the turbulence-driven flows are dominant compared to the neoclassical background flows, as shown in Figure 7.13. At even larger collisionality, one may expect that the neoclassical shearing rate would become dominant, and thus that the turbulent transport would possibly be *reduced* due to collisions. However,

such a high collisionality range would be very far from the typical low collisionality regimes of fusion-relevant tokamak plasmas.

7.4.3 Details of the Dimits shift softening mechanism

In [23], the zonal flow damping by collisions was first identified as the cause for the non-vanishing collisional turbulent transport for $R_0/L_{T_0} = 5.3$, although the temperature gradient is in the Dimits shift region. A locally bursting behaviour of turbulence, associated zonal flow amplitude and turbulent transport was observed. The bursting behaviour results from the following mechanism: Turbulence driven by the (weak) temperature gradients in the Dimits shift region initially develops and drives zonal flows to sufficiently high levels such that the associated shearing rate $\omega_{E \times B}$ is able to quench the turbulence, as in the collisionless case. However, as a result of collisional damping, zonal flow amplitudes and related shearing then decrease, and turbulence is able to recover, thus completing a bursting cycle. The period of this bursting cycle therefore clearly scales with the collision time τ_{ii} . This result is confirmed by simulations performed with the collisional version of ORB5 based on the parameters of Sec. 7.4.1, but considering a *narrow* gradient profile of type 3, i.e. with $\Delta_A = 0.15a$. Figure 7.14 (a) shows the time evolution of the radial shearing rate profile $\omega_{E \times B}(r)$ for $\nu_0^* = 0.3$, considering a narrow gradient profile with $R_0/L_{T_0} = 5.3$. Note that the observation of a clear bursting behaviour, as in Figure 7.14 (a), requires narrow gradients. For comparison, Figure 7.14 (b) presents the time evolution of the radial shearing rate profile $\omega_{E \times B}(r)$ for the same collisionality $\nu_0^* = 0.3$ and considering a *wide* gradient profile of type 3, i.e. with $\Delta_A = 0.3a$, and still with $R_0/L_{T_0} = 5.3$. In this latter case, already discussed in Sec. 7.4.1, the bursting behaviour is much less obvious.

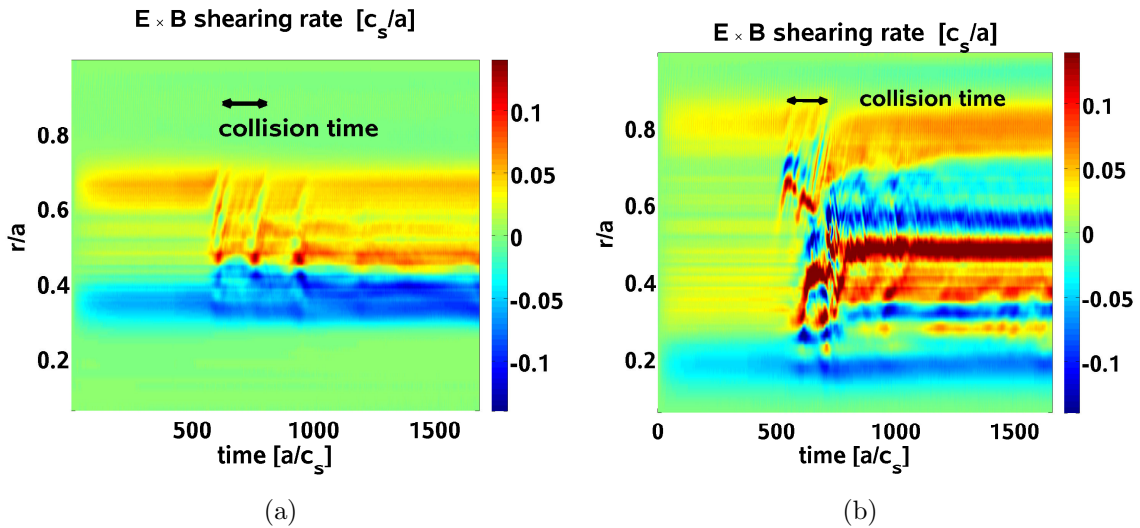


Figure 7.14: Time evolution of the $\mathbf{E} \times \mathbf{B}$ shearing rate profile, considering a collisionality $\nu_0^* = 0.3$ and a temperature gradient $R_0/L_{T_0} = 5.3$. The temperature and density gradients are non-zero from $r/a = 0.35$ to $r/a = 0.65$ (narrow-shaped profiles, $\Delta_A = 0.15a$) in (a) and non-zero from $r/a = 0.2$ to $r/a = 0.8$ (wide-shaped profiles, $\Delta_A = 0.3a$) in (b). The bursting evolution of the zonal flows is visible in (a), while much less obvious in (b).

The bursting behaviour due to collisions for profile width $\Delta_{\mathcal{A}} = 0.15a$ and gradient $R_0/L_{T_0} = 5.3$ is clearly illustrated in Figures 7.15 and 7.16. As expected, transport is totally absent in a collisionless case, as shown in Figure 7.15 for $\nu^* = 0$, since the temperature gradient $R_0/L_{T_0} = 5.3$ is in the Dimits shift region, where the collisionless zonal flows are strong enough to quench the turbulence. Considering again $R_0/L_{T_0} = 5.3$ and two different collisionalities $\nu^* \simeq 0.18$ and $\nu^* \simeq 0.3$ at the radial position $r/a = 0.45$, Figure 7.16 shows the time evolution of the turbulent ion energy flux Q_{turb} , normalized with respect to its corresponding neoclassical value Q_{neo} , as well as the time evolution of the $\mathbf{E} \times \mathbf{B}$ shearing rate $\omega_{E \times B}$, normalized with respect to the growth rate of the most unstable mode γ_{max} in the linear phase of the simulation. A non-vanishing turbulent transport is clearly established through collisions. The above mentioned bursting behaviour appears clearly in Figure 7.16: At an intermittance period which is proportional to the collision time τ_{ii} (indicated for reference in the plots), the $\mathbf{E} \times \mathbf{B}$ shearing rate is damped, which in turn leads to an increase of the turbulent ion energy flux. The presence of a non-vanishing turbulent transport implies that the Dimits shift region of ion temperature gradients is softened by collisions, as already discussed in Sec. 7.4.1 for the $\Delta_{\mathcal{A}} = 0.3a$ cases. As already mentioned, the observed bursting behaviour is however not as clearly identifiable if the gradient profiles are larger, maybe due to interaction of this bursting behaviour happening at different uncorrelated times at different radii, leading to a less coherent evolution of the overall system in particular resulting from collisionality varying with radius r . The basic underlying mechanisms of turbulence-driven zonal flow damping are however probably essentially the same, leading to an increase of the heat diffusivity with collisions for all gradient widths.

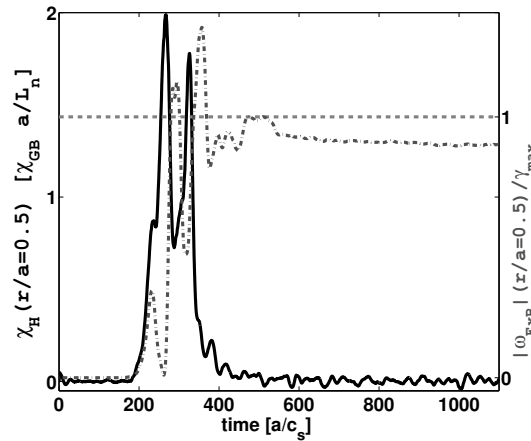


Figure 7.15: For a collisionless simulation and a narrow temperature gradient with $R_0/L_{T_0} = 5.3$, time evolution of both the heat diffusivity χ_H (black plain line) and the $\mathbf{E} \times \mathbf{B}$ shearing rate $|\omega_{E \times B}|$ (grey dash-dotted line) at mid-radius. $|\omega_{E \times B}|$ reaches a quasi-stationary value comparable to the linear growth rate of the most unstable mode γ_{max} (grey dashed line), fully quenching the turbulence and leading to a vanishing heat transport.

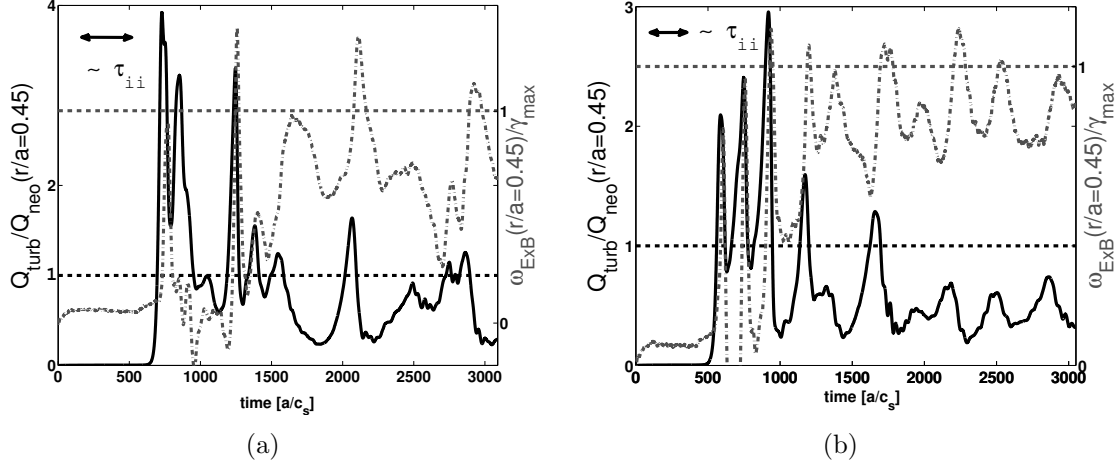


Figure 7.16: For (a) $\nu_0^* = 0.18$ and (b) $\nu_0^* = 0.3$, considering a narrow temperature gradient with $R_0/L_{T_0} = 5.3$, time evolution of both the kinetic energy flux driven by turbulence Q_{turb} (black plain line normalized with respect to the neoclassical contribution Q_{neo}) and the $\mathbf{E} \times \mathbf{B}$ shearing rate ω_{ExB} (grey dash-dotted line normalized with respect to the maximum linear growth rate γ_{max}) at $r/a = 0.45$. The periodic damping of zonal flows by collisions leads in turn to periodic bursts in the heat transport, at a rate proportional to the collision frequency.

7.5 Relevance of the pitch angle scattering approximation

Historically, collision operators have been implemented in gyrokinetic codes by making use of several approximations. Certain codes for instance only consider a pitch angle scattering operator for turbulence studies [11]. The linearized Landau operator implemented in ORB5 for self-collisions, described in detail in Chapter 5 and Ref. [16], accounts for pitch angle and energy diffusion, and thanks to its approximated background reaction term ensures all the essential conservation and symmetry properties. In this respect it is clearly more realistic than the simpler pitch angle scattering operator (Lorentz approximation). A pitch angle scattering operator for electron-ion collisions, acting only through random kicks on the markers' pitch angle variable, is also implemented in ORB5 and described in full detail in Chapter 5 and Ref. [16]. Such an operator is clearly relevant for simulating the collisions of electrons on ions, due to the large mass ratio m_i/m_e between the two species. Such a mass ratio argument clearly does not apply for ion-ion collisions, which are thus different from electron-ion collisions, and the use of a pitch angle scattering operator for ion-ion collisions may be questioned. Using a Lorentz operator in order to account for self-collisions is equivalent to considering the linearized Landau self-collision operator without the background reaction term $C[\delta f_{LM}, f_{LM}]$ and without the energy diffusion term, such that the simplified self-collision operator reads [see Eq. (5.41)]:

$$\hat{C}(\delta f_{LM}) = \frac{\nu_D(v)}{2} \hat{L}^2 \delta f_{LM} = \frac{\nu_{ii} K(\mathbf{v})}{4v^2} \hat{L}^2 \delta f_{LM}, \quad (7.7)$$

where $\mathbf{v} = v/v_{th}$, $\hat{L}^2 = -\partial/\partial\xi(1 - \xi^2)\partial/\partial\xi$ and $K(\mathbf{v})$ is given by Eq. (5.34).

Considering the standard CYCLONE case with $R_0/L_{T_0} = 5.3$, a turbulent run started from a neoclassical equilibrium at very high collisionality $\nu_0^* \simeq 0.71$ is first studied. As expected, the neoclassical equilibrium to which the system settles with the Lorentz operator (7.7) is different from the equilibrium obtained with the full self-collision operator (5.39). The neoclassical kinetic energy flux Q_{neo} predicted by the Lorentz operator is for instance larger, by a factor ~ 2 , than the neoclassical kinetic energy flux predicted by the Landau self-collision operator, as shown in Figure 7.17 (a). Note that the neoclassical electric field is in some sense inconsistent in the case of the Lorentz operator, since the Lorentz operator does not conserve parallel momentum and thus leads to a neoclassical ion particle flux which is unphysical for self-collisions [44]. The neoclassical electric field, which must ensure a vanishing ion particle flux in order to satisfy the quasi-neutrality equation with adiabatic electrons, is thus distorted by the unphysical particle flux driven by the Lorentz operator. However, the use of the Lorentz operator in the frame of turbulence studies seems to be roughly justified. Despite evident neoclassical discrepancies, the time-averaged turbulent kinetic energy flux at mid-radius $r/a = 0.5$ remains comparable between the operators: $\langle Q_{\text{turb, Lorentz}} \rangle_{\text{time}} / \langle Q_{\text{turb, self-coll}} \rangle_{\text{time}} = 1.14$. Considering the statistical uncertainty of 15 % [49], this deviation is probably not significant. Figure 7.17 (b) shows the evolution in time of the turbulent kinetic energy flux at mid-radius $r/a = 0.5$ for both operators.

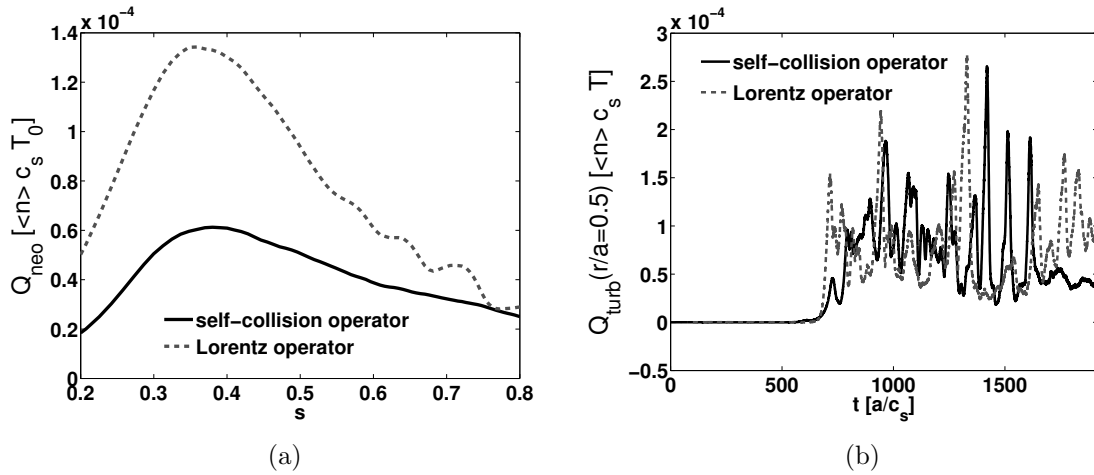


Figure 7.17: For $\nu_0^* \simeq 0.71$ ($\tau_{ii} \simeq 70[a/c_s]$) and $R_0/L_{T_0} = 5.3$, (a) neoclassical kinetic energy flux profile due to ion-ion collisions $Q_{\text{neo}}(s)$ and (b) time evolution of the turbulent kinetic energy flux Q_{turb} at mid-radius, predicted by both the Lorentz operator (grey dashed line) and the Landau self-collision operator (black plain line). The Lorentz approximation is not accurate enough in order to describe correctly the neoclassical transport due to self-collisions, while the time-averaged level of turbulent transport is essentially identical using both collision operators.

In order to reduce the importance of the neoclassical transport compared to the turbulent transport, the gradient $R_0/L_{T_0} = 6.9$ is then chosen, along with a weaker collisionality $\nu_0^* = 0.14$. The simulation is carried out in this latter case without any neoclassical initialization phase. Figure 7.18 shows the evolution in time of the turbulent heat diffusivity $\chi_{\text{turb}} = Q_{\text{turb}}/n|\nabla T|$, averaged between $r/a = 0.4$ and $r/a = 0.6$, for both operators. The difference is obviously small, at least in a time-average sense: $\langle \chi_{\text{turb, Lorentz}} \rangle_{\text{time}} / \langle \chi_{\text{turb, self-coll}} \rangle_{\text{time}} = 1.05$. The discrepancy is

probably again insignificant relative to the statistical error. The Lorentz approximation for ion-ion collisions thus appears to make sense in the frame of collisional ITG turbulence simulations, at least for a moderate collisionality. Note that this conclusion is strongly related to the similar damping of zonal flows provided by both the unphysical Lorentz operator for ion-ion collisions and the proper ion self-collision operator, the pitch angle scattering process contained in both operators being essentially responsible for zonal flow damping. The importance of collisional zonal flow damping for ITG turbulence is thus once again emphasized. However, the Lorentz approximation is obviously inappropriate for handling neoclassical transport of ions.

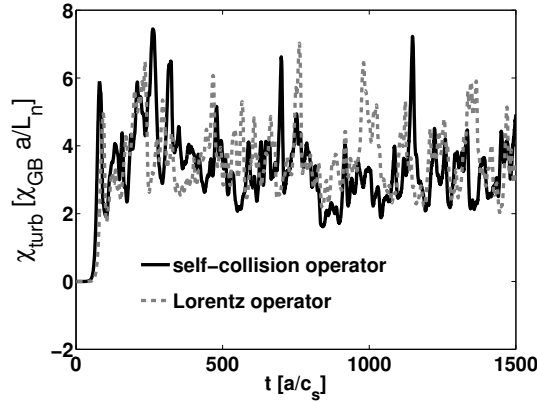


Figure 7.18: For $\nu_0^* \simeq 0.14$ ($\tau_{ii} \simeq 350[a/c_s]$) and $R_0/L_{T_0} = 6.9$, time evolution of the turbulent heat diffusivity χ_{turb} averaged between $r/a = 0.4$ and $r/a = 0.6$, predicted by both the Lorentz operator (grey dashed line) and the Landau self-collision operator (black plain line). The time-averaged turbulent transport levels using the different collision operators essentially agree.

7.6 Effects of the coarse-graining procedure on ITG turbulence

The simulations presented in this Chapter use the coarse-graining procedure, described in Sec. 4.8, in order to control the numerical noise. As already mentioned, the size of the bins needs to be chosen so as to be smaller than any length scale relevant to a correct estimation of the turbulent transport levels. Considering the CYCLONE base case with $R_0/L_{T_0} = 6.9$ and taking $n_s \times n_{\theta^*} \times n_z \times n_E \times n_\xi = 128 \times 32 \times 128 \times 40 \times 40$ as the binning grid for half of the torus (corresponding to a total of $\sim 840 \cdot 10^6$ bins), we first consider a non-heated collisionless plasma discretized with $100 \cdot 10^6$ markers. On average, each marker is thus expected to undergo an effective coarse-graining procedure every 10 time steps, 10 corresponding roughly to the ratio between the here considered number of bins and number of markers. Figure 7.19 (a) shows that the coarse-graining procedure has no significant effect on the growth and non-linear saturation of different ITG modes, $n = 10$ and $n = 44$ corresponding respectively to $k_\theta \rho_{Li} \simeq 0.15$ and $k_\theta \rho_{Li} \simeq 0.68$. This result is in agreement with the purpose of the coarse-graining procedure, i.e. to reduce numerical noise while not affecting scales relevant to turbulent transport. The size of the binning is, as expected, very important: If the bins are too large, significant length

scales of the turbulence are affected through the numerical damping of corresponding modes, as illustrated in Figure 7.19 (a) for a number of bins reduced by a factor two in each direction. Let us emphasize again that this noise-control method is fully compatible with the physics of collisions as explained in Sec. 4.8 and Ref. [16]. As the self-induced zonal flows play an essential role in the saturation of ITG turbulence, it is important to verify that their dynamics remains unaffected by the coarse-graining procedure as well. As these flows involve large scales, they are not expected to be directly affected by the potential damping of the binning process. They may however be indirectly affected by the flow drive, coming from the shorter scale fluctuation modes. This point is addressed in Figure 7.19 (b) for the same conditions as in Figure 7.19 (a), showing how the radially averaged $\mathbf{E} \times \mathbf{B}$ shearing rate $\langle |\omega_{E \times B}| \rangle_r$, defined by Eqs. (7.5) and (7.6), is clearly unaffected in a time-average sense by the coarse-graining procedure.

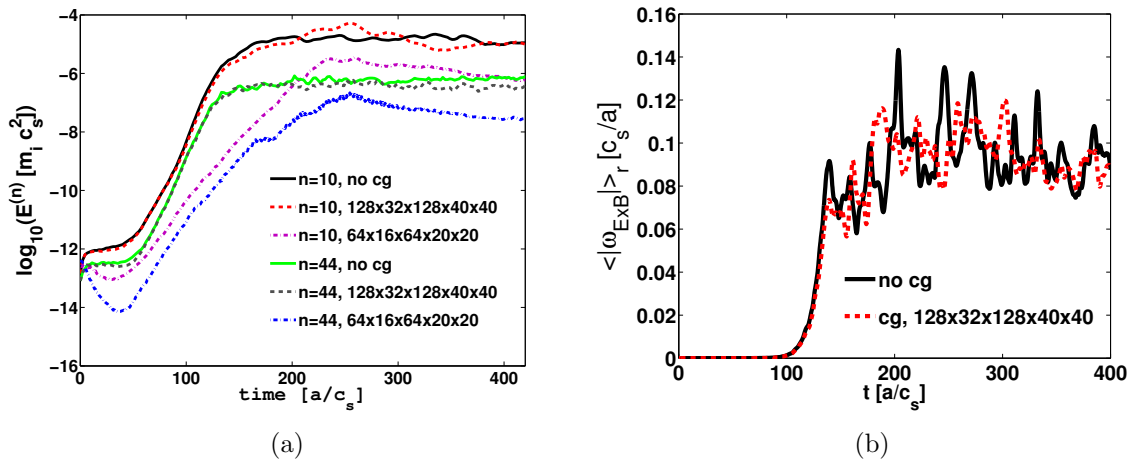


Figure 7.19: (a) Evolution in time of the energy $E^{(n)}$ of two toroidal Fourier modes ($n = 10$ and $n = 44$), for different coarse-graining parameters, in the linear phase and the early non-linear phase of the simulation. An appropriate choice of the binning parameters for coarse-graining allows to preserve the linear growth rate of the modes, while too large bins lead to an important non-physical energy dissipation. (b) Time evolution of the radially averaged $\mathbf{E} \times \mathbf{B}$ shearing rate $\langle |\omega_{E \times B}| \rangle_r$ without (plain line) and with (dashed line) coarse-graining: The coarse-graining procedure does not affect the time-averaged $\mathbf{E} \times \mathbf{B}$ flow shearing rate, as desired.

Considering the appropriate binning mentioned above, the positive effect of the coarse-graining is clearly illustrated in Figure 7.20, showing the signal/noise ratio for runs with either $90 \cdot 10^6$ or $180 \cdot 10^6$ markers, the heating operator being switched on. It has to be noticed from Figure 7.20 that the coarse-graining procedure is able to stabilize the signal/noise ratio. The simulations for which the noise is not controlled by the coarse-graining method indeed present a decaying signal/noise ratio in the time evolution, ultimately reaching a level below the threshold of simulation relevance (~ 10). The described coarse-graining procedure thus allows to carry out relevant studies of turbulence in the frame of the collisional δf PIC method over multiple collision times.

Finally, note that the field-aligned coordinates are compatible with the gyrokinetic ordering (small $k_{\parallel} \rho_{Li}$) and are thus the natural choice for representing microturbulence. Considering bins aligned along these coordinates enables to take the largest possible bins, essential for

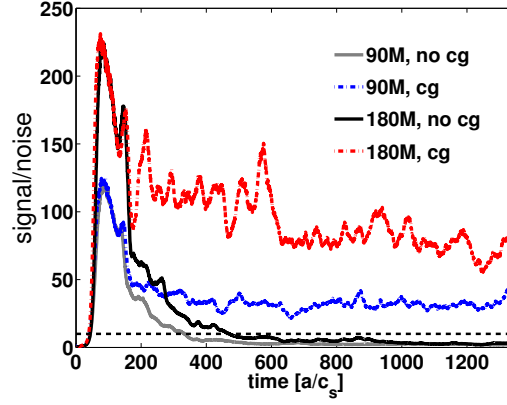


Figure 7.20: Time evolution of the signal-to-noise ratio considering the coarse-graining procedure either switched off (plain lines) or on (dash-dotted lines), both for $90 \cdot 10^6$ and $180 \cdot 10^6$ markers. The coarse-graining method is crucial in order to carry out simulations above the SNR threshold of relevance (~ 10 , dashed line).

ensuring that every marker meets sufficiently often at least one other marker in a same bin at the same time step, while avoiding the coarse-graining procedure to smooth out essential physical length scales. This is illustrated by the number of bins considered in configuration space ($128 \times 32 \times 128$ for half of the torus) versus the number of grid points considered in straight-field-line coordinates for the field solver ($128 \times 512 \times 128$ for half of the torus).

7.7 Effects of trapped electron kinetic response on ITG turbulence

The main results of this Chapter were obtained, as already emphasized, considering an adiabatic electron response. While this latter assumption is in general well justified for passing electrons which can move freely along the magnetic field lines, it is not appropriate for trapped electron dynamics. Actually, the proper kinetic treatment of trapped electrons provides different linear ITG growth rates, as already shown in Figure 7.1. It turns out that in the ITG regime, the trapped electrons essentially do not respond to the related microinstabilities. An improved reduced electron model for ITG turbulence would thus simply consist of only retaining the adiabatic response of passing electrons and neglecting the response of trapped electrons. This is achieved by weighting the adiabatic response of electrons by the passing fraction α_p and is equivalent to increasing the temperature ratio ZT_e/T_i , which is known to have a destabilizing effect on ITG modes as clearly reflected by Figure 7.1. Considering the CYCLONE case with $R_0/L_{T_0} = 6.9$ and wide non-zero gradient profiles of type 3 ($\Delta_A = 0.3a$), a non-linear simulation within the frame of the hybrid electron model exhibits a level of ion heat transport which is much higher (by a factor ~ 4) than the one obtained with a fully adiabatic electron response, as shown in Figure 7.21 (a). This latter result is consistent with Ref. [63]. A modification of the radial electric field profile $E_r(r/a)$ presented in Figure 7.21 (b) is also observed. As expected in the ITG regime and confirmed in Figure 7.21 (a), the heat diffusivity related to trapped

electrons χ_{He} is much smaller than the ion heat diffusivity χ_{Hi} . The trapped electrons are thus in effect not fully non-responsive in the ITG regime. Note that the coarse-graining procedure is applied to all electron markers as well, considering the same numerical parameters as for the ion coarse-graining.

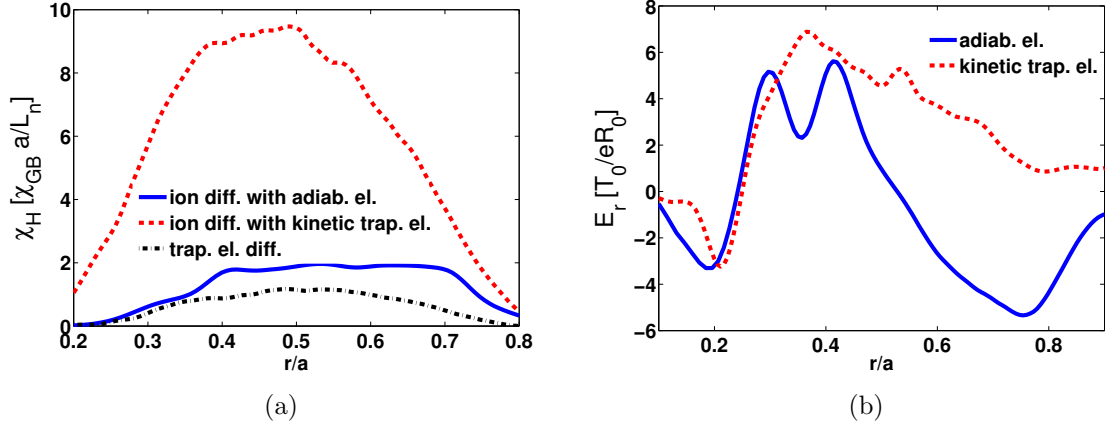


Figure 7.21: Effects of kinetic trapped electrons on ITG turbulence, for the CYCLONE case parameters, in the quasi-stationary state of the simulation. (a) The ion heat diffusivity χ_{Hi} is increased by the kinetic response of trapped electrons. (b) Modifications of the radial electric field profile $E_r(r/a)$ by kinetic trapped electron dynamics, leading to a weaker zonal flow shearing rate in a wide radial region of the torus.

7.8 A simple predator-prey model for studying zonal flow-turbulence interactions

In this Section, a simple non-linear local model is proposed, inspired by [117] and which analyzes the interaction between turbulence (A) and zonal flows (Z), following a predator-prey approach:

$$\frac{dZ}{dt} = -\nu Z + AZ - H(Z - Z_c) \cdot (Z - Z_c)/2, \quad (7.8)$$

$$\frac{dA}{dt} = \gamma A - AZ^2 - [AZ - H(Z - Z_c) \cdot (Z - Z_c)/2], \quad (7.9)$$

where H is the Heaviside function and $Z_c = 0.5$ is a critical zonal flow level, set for instance by a Kelvin-Helmoltz-type instability as described in Sec. 7.4.2. All the coefficients are normalized to 1. γ is the instability growth rate and ν is the collisionality damping the zonal flows. In the RHS of (7.8), the first term is the collisional damping, the second non-linear term is the zonal flow drive from turbulence and the third term is the KH instability effect. In the RHS of (7.9), the first term is the turbulence drive (from temperature gradient and magnetic curvature and gradient) and the second term describes the zonal flow shearing effect, whose Z^2 quadratic dependence comes from semi-empirical observations of imposed sheared $\mathbf{E} \times \mathbf{B}$ flow effects [118]. The third and fourth terms reflect the total energy conservation in the energy exchange between turbulence and zonal flows. This model is relevant in the sense that it can

reproduce the standard picture of zonal flow-turbulence interaction.

Choosing an important drive for turbulence ($\gamma = 1$), which would represent a temperature gradient beyond the Dimits shift region, we note in Figure 7.22 (a) that going from a collisionless to a collisional simulation (from $\nu = 0$ to $\nu = 1$) leads to a moderately reduced zonal flow level and a significantly increased turbulence within the frame of the proposed model. Increasing the collisionality (from $\nu = 1$ to $\nu = 2$) increases again significantly the turbulence but does not affect the stationary zonal flow level.

Considering a weak turbulence drive ($\gamma = 0.2$) in order to approach the Dimits shift region conditions leads to vanishing turbulence in a collisionless case, as expected. In the collisional case however, a bursting behaviour of turbulence and zonal flows through collision effects appears, as seen in Figure 7.22 (b). This bursting behaviour is well reproduced in ORB5 if the temperature gradient profiles are sufficiently narrow, i.e. sufficiently close to a local system situation, as shown in Sec. 7.4.3. Additionally, the bursting frequency is also increased by a larger collisionality. The general conclusion obtained for $\gamma = 1$ are still valid: Going from a collisionless to a collisional simulation (from $\nu = 0$ to $\nu = 0.2$) leads to a reduced averaged zonal flow level and a significantly increased turbulence. Increasing the collisionality (from $\nu = 0.2$ to $\nu = 0.4$) increases again significantly the turbulence but does not affect the averaged zonal flow level. The general conclusions presented in this Chapter relative to the effect of ion collisions on ITG microturbulence can thus qualitatively be represented with a simple predator-prey model.

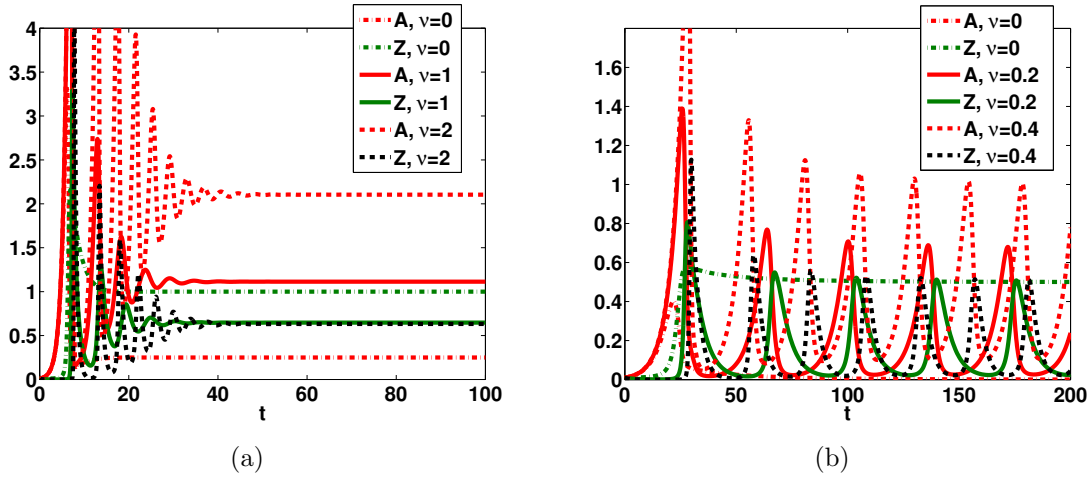


Figure 7.22: Non-linear evolution of turbulence and zonal flows according to a simple predator-prey approach modelling their mutual interactions, for (a) a strong turbulence drive ($\gamma = 1$) and (b) a weak turbulence drive ($\gamma = 0.2$). The conclusions of ORB5 gyrokinetic simulations are qualitatively reproduced.

7.9 ITG simulations considering MHD equilibria

The previously presented results in this Chapter were obtained considering the *ad hoc* equilibrium described in Chapter 2. In this section, a true MHD equilibrium inspired by the DIII-D tokamak and computed by the code CHEASE [32] is accounted for. The considered equilibrium

is shaped, with a non-zero Shafranov shift, elongation and triangularity, and corresponds to the equilibrium II described in Ref. [119]. Two different plasma sizes are studied, $\rho^* = 1/90$ and $\rho^* = 1/180$. The temperature and density profiles of type 1 are defined with respect to the s coordinate, as described by Eq. (3.59) in Chapter 3, with $s_0 = 0.6$ and $\Delta = 0.3$. Electrons are treated adiabatically and the gradient values for both species are roughly based on the CYCLONE case ($T_e = T_i$, $\kappa_n = 0.8$, $\kappa_T = 2.5$). The simulations start from a local Maxwellian f_{LM} for the ion distribution function. The spectrum of linear growth rates of the ITG-type microinstabilities is computed. The corresponding results presented in Figure 7.23 (a) show values similar to growth rates provided by the *ad hoc* equilibrium (see Figure 7.1). For the range of wavelengths treated properly by the ORB5 solver, i.e. for $k_\theta \rho_{Li} \lesssim 0.6$, there is no significant difference between $\rho^* = 1/90$ and $\rho^* = 1/180$ regarding the growth rate spectrum, except that both spectra do not peak at the same poloidal wavenumber. Figure 7.23 (b) shows the poloidal cross-section of the considered equilibrium for $\rho^* = 1/90$, as well as the perturbed electrostatic potential $e\phi/T_e$ of the linear eigenmode $n = 16$.

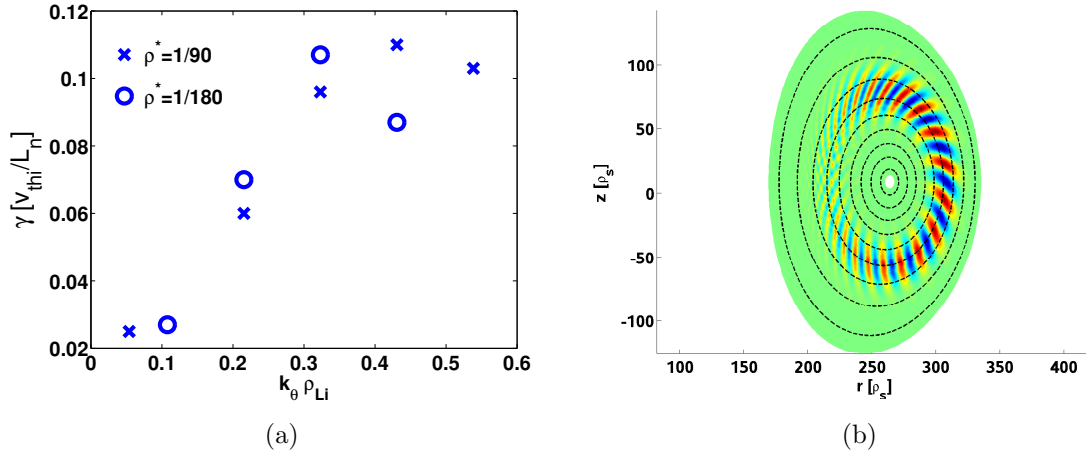


Figure 7.23: (a) Growth rate spectrum for the CYCLONE case gradients, considering adiabatic electrons and a proper DIII-D MHD equilibrium solution of the Grad-Shafranov equation, with non-zero elongation and triangularity. (b) Poloidal cross-section of the considered realistic DIII-D MHD equilibrium and eigenmode structure of the electrostatic toroidal mode $n = 16$ ($\rho^* = 1/90$).

Non-linear simulations are performed, considering the equilibrium II used for the linear analysis as well as the equilibria III, IV and V detailed in Ref. [119], along with the previously described profiles of type 1 for density and temperature. The considered equilibria are briefly characterized as follows: Equil. III is both Shafranov-shifted and elongated but with zero triangularity, Equil. IV is circular and Shafranov-shifted, and Equil. V is circular with a zero Shafranov shift, being thus close to the *ad hoc* model used for most simulations presented in this thesis. Figure 7.24 shows the ion energy flux profile $Q_i(s)$, averaged between $t = 950[a/c_s]$ and $t = 1050[a/c_s]$, for the two plasma sizes $\rho^* = 1/90$ and $\rho^* = 1/180$, considering the four mentioned equilibria. The elongation parameter, which is non-zero for Equil. II and III, appears to have a clear stabilizing effect on ITG turbulence as predicted by Ref. [56], while the Shafranov shift, non-zero for the circular equil. IV but zero for the circular equil. V, does not lead to significant modifications of the ion energy flux. Note that both ρ^* values provide similar ion energy fluxes for elongated

equilibria, while ion energy fluxes in case of circular equilibria show a strong ρ^* dependence (the circular plasmas with $\rho^* = 1/90$ exhibiting a larger ion energy flux in the considered units).

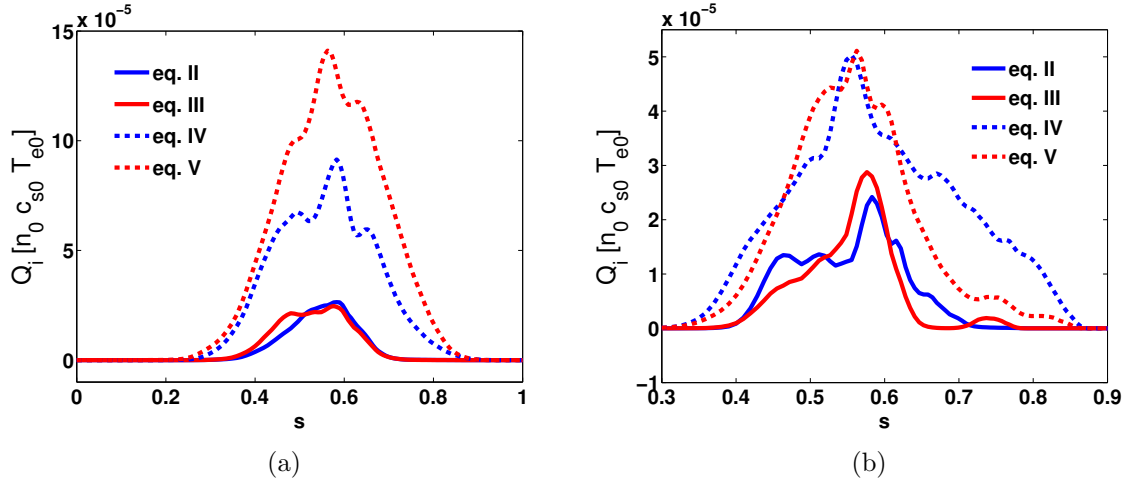


Figure 7.24: Ion energy flux profile $Q_i(s)$, averaged between $t = 950[a/c_s]$ and $t = 1050[a/c_s]$, for the plasma size (a) $\rho^* = 1/90$ and (b) $\rho^* = 1/180$. The different equilibria lead to significant differences in the turbulent transport level.

7.10 Conclusions

The issue of ion-ion collision effects on electrostatic ITG turbulent transport has been studied thanks to robust collision algorithms implemented in the global gyrokinetic code ORB5. Our turbulence simulations with collisions have been systematically started from a neoclassical equilibrium. The so-obtained neoclassical transport level thus provides a reference for evaluating the relative effects of collisions on turbulent transport. Through ORB5 simulations, the issue of the possible interaction between neoclassical and turbulent transport physics has been addressed: Strong collisional damping of turbulence-driven zonal $\mathbf{E} \times \mathbf{B}$ flows is observed, while the shearing effect from neoclassical background $\mathbf{E} \times \mathbf{B}$ flows remains weak for the smooth density and temperature background profiles considered. As a result, a general increase in ion heat transport due to collisions is observed in agreement with previous studies within the frame of the adiabatic electron model [23]. The mechanisms leading to the mentioned increased transport (neoclassical contributions and amplified turbulent contributions via interactions with collisionally damped zonal flows) have been emphasized and studied for different ion temperature gradients R_0/L_{T_i} .

Conditions similar to Ref. [23] have been revisited in this Chapter. A more extensive scan in ion collisionality ν^* and ion temperature gradient R_0/L_{T_i} in particular enabled to provide a more detailed characterization of the Dimits shift softening by collisions. The width of the temperature gradient profile was varied as well in this Chapter. In most respects, results of Ref. [23] are confirmed: (i) Above the Dimits shift region, the synergetic effect of collisions on turbulence leads to an increased collisional turbulent transport with respect to the collisionless situation [$\chi_H^{\text{tot}}(\nu^*) > \chi_H^{\text{turb}}(\nu^* = 0) + \chi_H^{\text{neo}}(\nu^*)$]. (ii) Within the Dimits shift region, finite

turbulent transport is established through collisions (Dimits shift softening). (iii) The bursting behaviour described in [23] for ion temperature gradients in the Dimits shift region is reproduced in the case of *narrow* temperature gradient profiles, enabling a coherent regime. However, for *wider* gradient profiles a steadier regime is observed, which we have interpreted as resulting from interactions between different radial regions of the basic bursting mechanism, happening at different phases at different radii.

Both within and above the Dimits shift region for wide gradient profiles, a relatively steady state of zonal flows and associated shearing rate $\omega_{E \times B}$ is thus observed. Noteworthy is the fact that the shearing rate level at finite collisionality ($\nu^* > 0$) is only slightly reduced compared to the collisionless situation ($\nu^* = 0$). Moreover, this collisional shearing rate level appears to be only weakly dependent on the finite collisionality considered. Above the Dimits shift region, a detailed study has shown that the shearing rate level is limited by Kelvin-Helmoltz-type tertiary instabilities affecting the zonal flows. It has also been shown that the instability threshold level is only weakly dependent on the collisionality. At finite ν^* , the collisional damping of zonal flows however requires increased drive from turbulence to reach this threshold, resulting in increased turbulent transport levels. Within the Dimits shift region, zonal flow shearing rates below the tertiary instability threshold are sufficiently strong to fully quench the turbulence (less strongly driven than for gradients above the Dimits shift region) in the collisionless regime. With finite collisionality, the averaged shearing rates are maintained close to the collisionless levels thanks to a finite turbulence drive counter-acting the collisional damping, thus leading to finite transport. When increasing collisionality, a balance is thus apparently maintained between strengthened zonal flow damping and additional zonal flow drive from amplified turbulence levels. This general conclusion has been confirmed by a simple predator-prey model for representing the interactions between zonal flows and turbulence.

Both for neoclassical and turbulence simulations, the Lorentz approximation for self-collisions was tested against the linearized Landau self-collision operator in ORB5, which accounts for thermalization and ensures the local conservation of density, parallel momentum and kinetic energy. While a physically accurate self-collision operator is required in order to correctly estimate the neoclassical transport, the Lorentz approximation is sufficient for capturing the essential features of the collisional turbulent transport in the ITG regime. However, the Lorentz approximation is inappropriate for handling properly the ion neoclassical transport and thus leads to inaccurate estimates of the total transport.

Numerical aspects have been addressed as well, such as the successful use of the background switching scheme or the relevance of the coarse-graining approach for controlling the noise in collisional ITG turbulence simulations. The kinetic treatment of trapped electrons has been shown to enhance the ITG turbulence level through an increase of the effective ratio T_e/T_i . Finally, the ORB5 interface with the code CHEASE has been tested through linear and non-linear simulations accounting for realistic MHD equilibria. A few insights into the effects of plasma shaping on turbulence level have thus been given, in particular the stabilizing effect of elongation.

Chapter 8

Global gyrokinetic studies of collisionless and collisional Trapped-Electron-Modes (TEMs)

8.1 Introduction

The adiabatic electron model considered in Chapter 7, although very efficient from the practical point of view of computer resources, is not always applicable since the adiabatic assumption does not hold for trapped electrons nor for passing electrons located at low order mode rational flux surfaces (i.e. where the safety factor is rational: $q_s = m/n$, m and n being integers) [120] [121] [122]. In particular, the adiabatic electron model does not allow to address the electrostatic Trapped Electron Modes (TEMs) nor the electromagnetic instabilities. The hybrid electron model, briefly explained in Chapter 3 and designed for studying electrostatic TEM instabilities by providing a kinetic trapped electron response, was implemented quite early in the development of the ORB5 code, but only a few collisionless results have been published before this thesis work [60] [61] [51]. Note that the hybrid model has the main advantage of allowing larger time steps for TEM simulations compared to fully kinetic electron simulations, by a factor corresponding roughly to the ratio between the electron transit frequency ω_{te} and the electron bounce frequency ω_{be} : $\omega_{te}/\omega_{be} = 1/\sqrt{\epsilon}$, where $\epsilon = r/R_0$ is the local inverse aspect ratio. Moreover, the hybrid model prevents electrostatic shear Alfvén waves [81] from appearing and thus relaxes the corresponding constraint on the time step (see Sec. 4.9.2). Note that thorough and reliable TEM studies with a global gyrokinetic code, requiring the evolution of both kinetic ions and electrons, are very challenging computationally due to the multiple time and length scales involved in such multi-species simulations. As a consequence, very few global results have been published so far, those related to ORB5 being found in Refs. [60] [37] [61] [51] [30]. One of the major questions regarding the physics of TEM microturbulence is the importance of zonal flows in turbulence saturation mechanism. The answer to this question remains complex and not fully understood. Non-linear global simulations of collisionless electrostatic TEM turbulence at $\eta_e = \nabla \ln T_e / \nabla \ln n_e \simeq 3.1$ obtained by using ORB5 are described in Ref. [51], emphasizing a moderate role of zonal flows in the saturation mechanism of non-linear temperature-

gradient-driven TEM instabilities, in agreement with flux-tube (local results) obtained using the GENE code, see Ref. [27]. This latter result has recently been confirmed by other local simulations, stating that zonal flows only have an important saturation effect at $\eta_e \lesssim 1$ [29]. Recent global simulations tend to show that zonal flows may constitute an important saturation mechanism in the case $T_e = T_i$ [123]. The importance of the parameter range in determining the efficiency of turbulence saturation by the zonal flow shearing has been pointed out in Ref. [124] as well. For $\eta_e \gtrsim 1$, an alternative TEM saturation mechanism through perpendicular particle diffusion is proposed in Ref. [28]. Note that a nondiffusive component in the electron heat flux due to TEM turbulence is obtained in Ref. [125].

In this Chapter, we at first address some important numerical issues related to the δf PIC algorithm applied to global collisional gyrokinetic TEM simulations. In particular, the relevance of the different noise-control procedures available for a PIC code, both in collisionless and collisional configurations, is discussed. Different physical cases are considered, featuring either a pure TEM spectrum or a TEM-dominated spectrum. From a physical point of view, the role of zonal flows in TEM simulations is studied, as well as collisional effects and finite- ρ^* -effects on TEM turbulence.

8.2 ORB5 simulations of TEM instabilities: model and physical cases

The standard CYCLONE case features dominant ITG modes at low $k_\theta \rho_{Li} \lesssim 1$ and dominant TEM modes at higher $k_\theta \rho_{Li} \gtrsim 1$. This physical situation is a major impediment to CYCLONE TEM studies with ORB5, since the quasi-neutrality solver assumes $k_\theta \rho_{Li} \ll 1$ (long wavelength approximation, see Sec. 3.7.1). In order to study a typical temperature-driven Trapped-Electron-Mode instability, we define a so-called TEM CYCLONE case, which is essentially the CYCLONE case except for a weaker ion temperature gradient: $R_0/L_{Ti} = R_0/L_n = 2.2$, $R_0/L_{Te} = 6.9$. Here, L_n and L_T are the characteristic lengths of the density and temperature gradients respectively. A smaller case, called the TEM TCV case, is inspired by the parameters of the *tokamak à configuration variable* (TCV) [126]. The TEM TCV case considers the same temperature, density and safety factor profiles as the TEM CYCLONE case and keeps the same normalized gradients $a/L_n = a/L_{Ti} \simeq 0.789$ and $a/L_{Te} \simeq 2.484$ from the TEM CYCLONE case, while $R_0 = 0.88[m]$, $a = 0.25[m]$, $B_0 = 1.43[T]$ and $\rho^* = 1/80$. Deuterium is chosen as the ion species for both cases. Choosing the parameters of either the TEM CYCLONE case or the TEM TCV case leads to dominant TEM instabilities even at low $k_\theta \rho_{Li}$. Considering some TCV-relevant temperature and density values ($n \sim 10^{19} - 2 \cdot 10^{19}[m^{-3}]$ and $T_e \sim 1 - 2.5[keV]$) provides a range of physical collisionality $\nu_{ei,phys} \sim 5 \cdot 10^{-3} - 5 \cdot 10^{-2}[v_{thi}/a]$. The same range of physical collisionality is obtained for the TEM CYCLONE case, considering relevant DIII-D parameters ($n \sim 2 \cdot 10^{19} - 3 \cdot 10^{19}[m^{-3}]$ and $T_e \sim 2 - 5[keV]$). For both cases, the conditions $T_i = T_e$ (the standard temperature ratio considered unless otherwise specified) as well as $T_i < T_e$ are studied. The linear simulations for TEM instability studies are performed with peaked temperature and density gradient profiles of type 2 (with $\Delta_A = 0.2$ or 0.3), while non-linear simulations usually consider wide temperature and density gradient profiles of type

3 (see Sec. 3.9). An *ad hoc* equilibrium is considered. For linear simulations with electron collisions, $8 \cdot 10^5$ and $3 \cdot 10^6$ markers are typically used for ions and electrons respectively. In all the non-linear simulations in the TEM regime, heat sources applied both to electron and ion distribution functions maintain the turbulence drive and thus provide quasi-stationary states of temperature-gradient-driven TEM turbulence.

Note that both TEM TCV and TEM CYCLONE cases do not exhibit a purely temperature-gradient-driven TEM spectrum. Indeed, Electron-Temperature-Gradient (ETG) modes are present at smaller poloidal wavelengths, $k_\theta \rho_{Li} \gg 1$, which are not resolved both due to the assumption $k_\theta \rho_{Li} < 1$ of the ORB5 solver and the fact that passing electrons are forced to respond adiabatically in the hybrid electron model used in ORB5, while ETG modes require a kinetic representation for this group of particles. A physical case corresponding to a purely temperature-gradient-driven TEM spectrum was found through a linear analysis carried out with the GENE code, which shows that geometrical parameters of the CYCLONE case with $T_i = 0.3 T_e$, $R_0/L_n = 1.0$, $R_0/L_{Te} = 4.75$, and $R_0/L_{Ti} = 3.0$ lead to the so-called pure temperature-gradient-driven TEM case, i.e. a case with no ETG modes and very weak ITG modes.

Table TEM CASES. Different cases considered for TEM simulations.						
Case	a/R_0	ρ^*	a/L_n	a/L_{Ti}	a/L_{Te}	T_i/T_e
TEM CYCLONE	0.36	1/180	0.789	0.789	2.484	≤ 1
small TEM CYCLONE	0.36	1/60	0.789	0.789	2.484	≤ 1
TEM TCV	0.28	1/80	0.789	0.789	2.484	≤ 1
pure TEM	0.36	1/180	0.36	1.08	1.71	0.3

In ORB5, the electrons may be treated in the frame of a fully drift-kinetic model, the electron FLR effects being neglected according to the scaling $\rho_{Le}/\rho_{Li} \sim \sqrt{m_e/m_i}$. With the aim of simulating electrostatic TEMs, a hybrid model detailed in Ref. [51] and briefly reminded in Chapter 3 has been developed, considering the passing electrons as adiabatic and the trapped electrons as drift-kinetic. As already mentioned, the hybrid model allows a larger time step compared to the fully drift-kinetic electron model, since the bounce motion of trapped electrons is slower, by a factor $\sqrt{\epsilon}$, than the transit motion of passing electrons. Except for the results of Sec. 8.6 where fully kinetic electrons are used, all other results discussed in this Chapter are obtained within the frame of the hybrid electron model.

In order to further facilitate the numerical simulations of TEM instabilities, which are very demanding regarding the required computer resources, artificially heavy electrons are considered, $m_e = m_p/100$ instead of the physical mass ratio $m_e = m_p/1836$, where m_p is the proton mass. Considering Deuterium as the ion species leads to $m_i/m_e = 200$. Heavy electrons are slower than real electrons and thus allow a larger time step. Note that using heavy electrons should be relevant as long as $|\omega/\omega_{be}| \ll 1$, where ω is a characteristic TEM frequency of the considered system and $\omega_{be} = \sqrt{\epsilon T_e/m_e}/q_s R_0$ is an averaged electron bounce frequency. The relevance of heavy electrons for TEM studies is in fact related to the essentially ion time scale of TEM instabilities ($\omega \sim v_{thi}/a$). A bounce-averaged model for electrons is thus appropriate in this context and turns out to be electron mass independent if the FOW effects are neglected (see Sec. 2.5.2).

The time step chosen for TEM simulations performed using the hybrid model is typically $\Delta t \sim 2 \cdot 10^{-2} [a/c_s]$. In the frame of the hybrid model, a mass ratio $m_i/m_e = 200$ is sufficiently large in order to provide nearly converged values for the linear frequencies and growth rates. Figure 8.1 shows the collisional linear growth rate γ of the mode $k_\theta \rho_{Li} = 0.35$ as a function of m_i/m_e , considering the TEM TCV case parameters, for both cases where the collision frequency ν_{ei} [Eq. (5.56)] is fixed or the ν_e^* parameter [Eq. (3.58)] is fixed. The electron-ion and electron-electron collisions are taken into account. The electron mass, if chosen reasonably small compared to the ion mass ($m_i/m_e \gtrsim 200$), has little effect on the growth rate if the collisionality ν_{ei} is fixed (here at $\nu_{ei} a/v_{thi} = 6.5 \cdot 10^{-3}$). Note that this result is consistent with collisionless TEM results presented in Refs. [27] and [37]. Imposing a fixed ν_e^* parameter leads however to an actual collision frequency ν_{ei} which varies with the electron mass, providing variations of the linear growth rate with m_i/m_e as shown in Figure 8.1. As a consequence, using heavy electrons does not allow to study *neoclassical* and *turbulent* transport at the same time. Considering indeed a fixed physical collision frequency, as required in order to estimate correctly the level of turbulence, and varying the electron mass lead automatically to the variation of the ν_e^* parameter, through the mass dependence of the electron bounce frequency $\omega_{be} \sim 1/\sqrt{m_e}$. The level of neoclassical transport thus depends on the electron mass through the ν_e^* parameter, leading to unphysical neoclassical fluxes from heavy electrons if the physical electron collision frequency is considered.

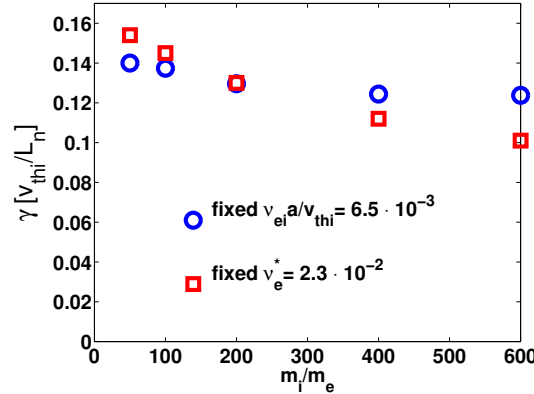


Figure 8.1: TEM instability, TEM TCV parameters. Effect of the artificial electron mass m_e on the linear growth rate of the mode $k_\theta \rho_{Li} = 0.35$, for both cases where $\nu_{ei} a/v_{thi} = 6.5 \cdot 10^{-3}$ is fixed and $\nu_e^* = 2.3 \cdot 10^{-2}$ is fixed.

Note that the hybrid model should provide similar growth rates as the fully kinetic electron model for TEM instabilities if the physical electron mass is considered, as checked in Figure 8.2, which shows the electron mass dependence of a typical TEM growth rate ($k_\theta \rho_{Li} \simeq 0.6$), for both the fully kinetic electron model and the hybrid model. The physical parameters corresponding to Figure 8.2 are $\rho^* = 1/60$, $a/L_{Ti} = 0$ and $a/L_{Te} = 2.5$ (the complete set of physical and numerical parameters can be found in Ref. [37], Sec. 4.1.1). Note that using heavy electrons appears to be physically valid for studying TEM microturbulence only within the frame of the hybrid model. A fully kinetic electron simulation apparently needs a physical electron/ion mass ratio in order to provide accurate results, at least for the considered case (small plasma).

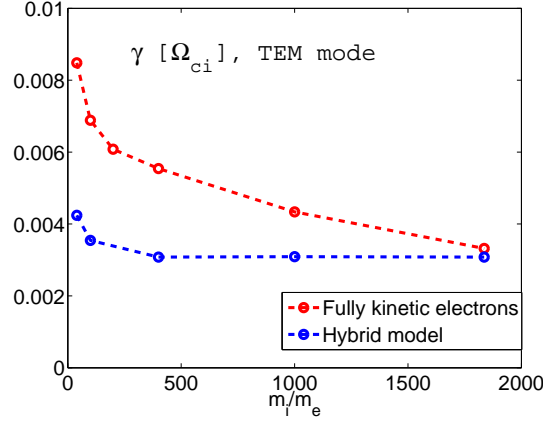


Figure 8.2: Electron mass dependence of a typical linear TEM growth rate ($k_\theta \rho_{Li} \simeq 0.6$, $\rho^* = 1/60$, $a/L_{Ti} = 0$, $a/L_{Te} = 2.5$). Using the hybrid model with heavy electrons allows to obtain physically relevant results regarding the TEM regime.

As a consequence of the use of heavy electrons, contrary to the ITG simulations presented in Chapter 7, the TEM turbulence simulations do not take into account neoclassical transport and therefore do not start from a neoclassical equilibrium. The backgrounds f_0 are chosen as local Maxwellian distributions for both species, and the term which drives the neoclassical transport in the kinetic equation, $(\mathbf{v}_{\nabla B} + \mathbf{v}_c) \cdot \nabla f_{LM}$, is artificially suppressed for both species. For the practical purpose of reducing the number of markers, the ions are considered collisionless in the frame of the TEM turbulence simulations. Collisionless ions in TEM simulations appear to make sense since $\nu_i/\nu_e \sim \sqrt{m_e/m_i}$. Both species start the simulation from a local Maxwellian distribution, slightly perturbed for ions ($f_e(t=0) = f_{LM,e}$, $f_i(t=0) = f_{LM,i} + \delta f_i$).

8.3 Importance of background reaction term $C_{ee}[\delta f_{LM,e}, f_{LM,e}]$ and associated binning

In addition to electron-ion collisions, accounting for electron-electron collisions requires a background reaction operator $C_{ee}[\delta f_{LM,e}, f_{LM,e}]$, as explained in Chapter 5. The practical implementation of the background reaction operator involves a binning in configuration space, described in Sec. 5.10.3. In principle, the size of the field-aligned binning grid should resolve the characteristic length scales of the fluctuating fields along the different spatial directions, in order to avoid the numerical damping of any length scale of interest. In practice however, the size of the binning grid for the background reaction term of the electron-electron collision operator appears to have a marginal influence on the linear growth rate of TEM instabilities. Considering indeed a TEM TCV case with $k_\theta \rho_{Li} = 0.42$ and $\nu_{ei}a/v_{thi} = 5 \cdot 10^{-3}$ (electron-ion + electron-electron collisions), the linear growth rate of the TEM γ does not vary significantly with the binning grid size, as shown in Table BINS. This latter quasi-invariance reflects the fact that the linear growth rate of a TEM instability depends mainly on the electron detrapping process driven by the electron-ion collisions and the pitch angle scattering part of the electron-electron collisions, not on the background reaction part which is the only term involving the binning procedure. It

reflects the fact that the background reaction term of the collision operator $C_{ee}[\delta f_{LM,e}, f_{LM,e}]$ is probably not strongly significant regarding collisional TEM turbulence simulations.

Table BINS. TEM TCV case, linear growth rate, $k_\theta \rho_{Li} = 0.42$, $\nu_{ei}a/v_{thi} = 5 \cdot 10^{-3}$.

$n_s \times n_{\theta^*} \times n_\varphi$	$8 \times 32 \times 4$	$16 \times 64 \times 8$	$32 \times 128 \times 8$	$64 \times 256 \times 32$
$\gamma[v_{thi}/L_n]$	0.156	0.154	0.154	0.155

8.4 Linear simulations: Convergence with the number of markers

According to the conclusion reached in Sec. 8.3 and considering the same physical case, a coarse binning grid $n_s \times n_{\theta^*} \times n_\varphi = 16 \times 64 \times 8$ is chosen in order to vary the number of electron markers down to 10^5 in linear simulations, a level which still fullfills the requirement of $\sim 10-20$ markers per bin in configuration space. Figure 8.3 shows how the linear growth rate is well converged already for 10^6 electron markers. Note that non-linear simulations require many more markers as explained in Sec. 4.9.1.

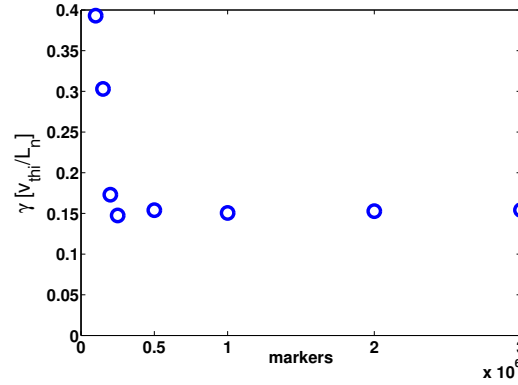


Figure 8.3: TEM TCV case, linear growth rate of the mode $k_\theta \rho_{Li} = 0.42$. Convergence with the number of electron markers, $\nu_{ei}a/v_{thi} = 5 \cdot 10^{-3}$.

8.5 Different contributions to the TEM instabilities

The contributions from the different dynamics of the different species to the growth of a microinstability are identified through the dot product between the current carried by a given species $\mathbf{j}_{\text{species}}$ and the electric field \mathbf{E} , related as follows to the growth rate associated to a given species γ_{species} :

$$\gamma_{\text{species}} = \frac{-\int \mathbf{j}_{\text{species}} \cdot \mathbf{E} \, d^3x}{2E_{\text{field}}}, \quad (8.1)$$

where E_{field} is the field energy. Considering a collisionless TEM CYCLONE case with $k_\theta \rho_{Li} = 0.4$, Figure 8.4 shows both the ion and electron contributions to the associated linear

TEM instability growth rate. The ions do not provide any significant contribution, since the stabilizing ion parallel dynamics balances the destabilizing ion drift motion, consistent with the TEM nature of the instability. In the frame of the electron hybrid model used for this study, the trapped electron parallel dynamics does not bring any contribution either, trapped electrons changing periodically the sign of their parallel velocity, while the adiabatic passing electrons do not provide any contribution to the current. The main contribution to the growth of the mode thus comes from the electron ∇B drift and curvature drift. Note that the ∇B drift $\sim v_\perp^2$ is dominant compared to the curvature drift $\sim v_\parallel^2$, consistent with the typical velocity ratio $v_\perp/v_\parallel \gg 1$ of trapped particles.

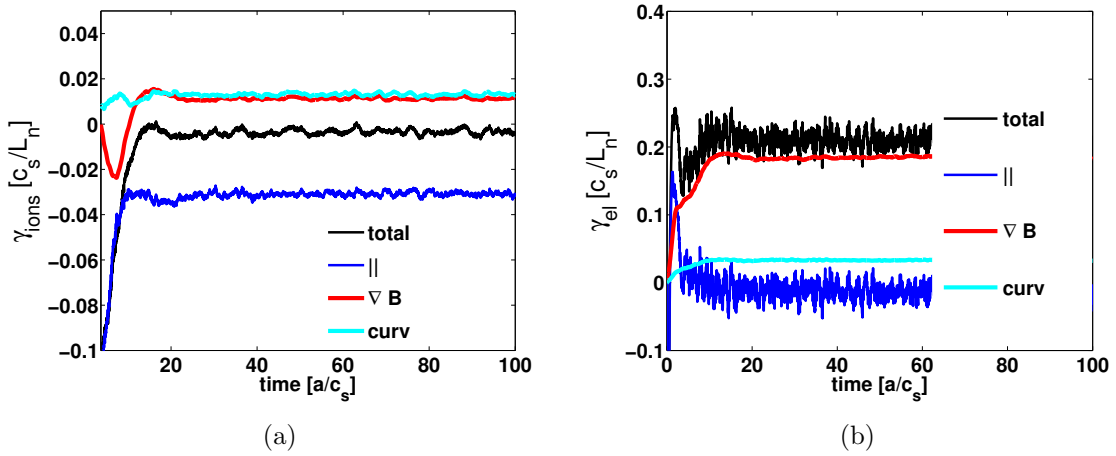


Figure 8.4: Contributions from different ion and electron dynamics to the linear growth rate of a TEM instability. TEM CYCLONE parameters, $k_\theta \rho_{Li} = 0.4$. (a) The ions do not provide any significant contribution to the growth of a Trapped-Electron-Mode. (b) The electron ∇B and curvature drifts combined to trapped electron dynamics in the presence of pressure gradients are the main driving mechanisms for a Trapped-Electron-Mode instability.

8.6 ORB5-GENE linear TEM benchmark

Considering the TEM CYCLONE case with $T_i = T_e$ and the peaked gradient profiles of type 2 for density and temperature, as described by Eq. (3.60) with $\Delta_A = 0.3a$, a global collisionless linear benchmark in the TEM regime is performed against the global version of the Eulerian-based gyrokinetic code GENE [10]. Contrary to the other results and simulations presented in this Chapter, fully kinetic electrons of mass $m_i/m_e = 400$ are considered in this Section. In the electrostatic approximation, fully kinetic electrons may destabilize electrostatic shear Alfvén modes and thus require small time steps for proper TEM simulations with particles, as explained in Ref. [81]. The required time step scales with $\Delta t \sim k_\theta$ according to Eq. (4.64) and thus needs to be even smaller for simulations considering long poloidal wavelengths. ORB5 uses time steps in the range $\Delta t \sim 5 \cdot 10^{-4} - 5 \cdot 10^{-3} [a/c_s]$ for the considered TEM CYCLONE case with fully kinetic electrons. Due to the above-mentioned numerical challenges, the simulation for the lowest considered value $k_\theta \rho_s = 0.125$ has in fact been performed in the case of ORB5 within the frame of the hybrid model. Figure 8.5 shows the benchmark results for both the

growth rate spectrum and the real frequency spectrum. Note the very good agreement at long wavelengths ($k_\theta \rho_s \lesssim 0.5$) between both codes. Discrepancies at larger $k_\theta \rho_s \gtrsim 0.5$ can probably be attributed to the long wavelength approximation assumed by the ORB5 field solver. In addition, local (flux-tube) results obtained with GENE are shown in Figure 8.5. Only a very small difference is observed in the linear growth rates and real frequencies between local and global simulations. The weakness of finite- ρ^* -effects in linear temperature-gradient-driven TEM simulations is confirmed by ORB5 simulations presented in Sec. 8.8.

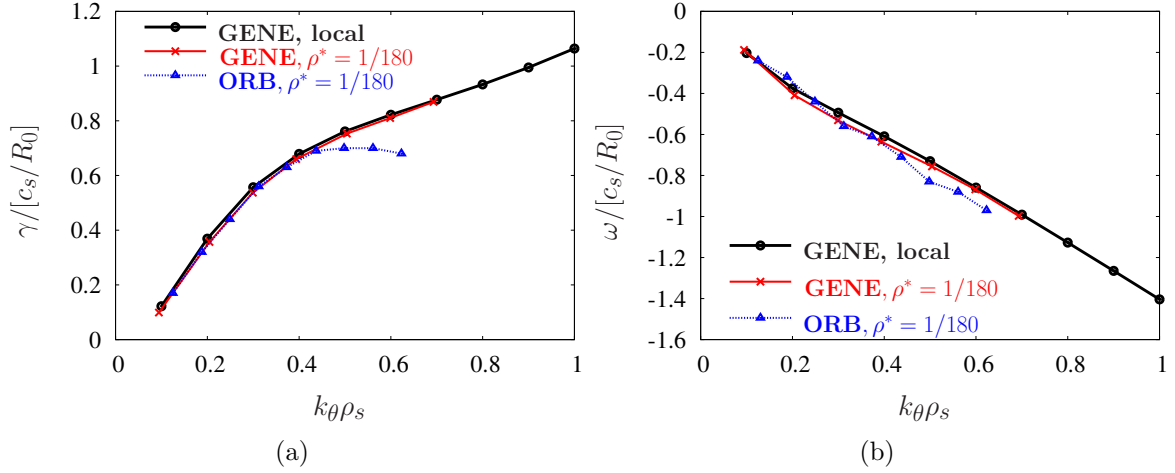


Figure 8.5: TEM CYCLONE case, $T_e = T_i$. Global simulations for $\rho^* = 1/180$ and fully kinetic electrons (except $k_\theta \rho_s = 0.125$ for ORB5 where hybrid electrons are considered). Linear benchmark in TEM regime between ORB5 and GENE, providing a good agreement regarding (a) the linear growth rate spectrum and (b) the real frequency spectrum for $k_\theta \rho_s \lesssim 0.5$. Discrepancies at larger $k_\theta \rho_s \gtrsim 0.5$ come from the long wavelength approximation assumed by the ORB5 field solver. For comparison, local (flux-tube) simulations obtained with GENE are also shown.

8.7 Comparison of noise-control methods

In view of carrying out collisional, non-linear simulations it is essential to address the issue of numerical noise. In this Section, a comparison of collisionless TEM simulations using different noise-control methods for electrons, either the Krook operator or the coarse-graining as explained in Chapter 4, is performed within the frame of the hybrid model. The choice of the coefficient γ_K for the Krook operator, which needs to be smaller than the maximum linear growth rate of the spectrum corresponding to the considered physical system, is naturally important, as well as the coarse-graining parameters. Note that, for a so far unknown reason, TEM simulations require a coarse-graining procedure applied to electrons at each time step in order to maintain a stationary transport level (while applying the coarse-graining every 10th time step is sufficient for ITG turbulence with adiabatic electrons [26]). At each time step, the electron w -weight is thus set to the average bin value, while the p -weight is unaffected. Moreover, a higher grid resolution in configuration space appears to be required for the coarse-graining binning in TEM simulations. As a consequence, a small plasma is easier to handle for the comparison between the Krook operator and the coarse-graining, due to the

fact that a higher grid resolution in configuration space can be afforded. A reduced TEM CYCLONE case is thus chosen, considering $T_i = T_e/3$ and $\rho^* = 1/60$. Non-linear simulations are performed, using either the Krook operator or the coarse-graining procedure, for different numerical parameters as presented in Figure 8.6 (a) showing the electron energy diffusivity χ_{el}^E averaged between $r/a = 0.2$ and $r/a = 0.8$. Within the statistical uncertainty range inherent to non-linear simulations, a good agreement related to turbulent transport is obtained between the two noise-control methods. However, as shown in Figure 8.6 (b) presenting the energy spectrum, the turbulent modes are more damped by the coarse-graining procedure in the range of shorter wavelengths ($n \sim 20$ corresponding to $k_\theta \rho_s \sim 1$). Due to the limited role of short wavelength modes in the turbulent transport, the electron diffusivity is only marginally affected by the choice of the noise-control method, as already emphasized. Note however that, as already mentioned, the Krook operator is inappropriate for collisional simulations.

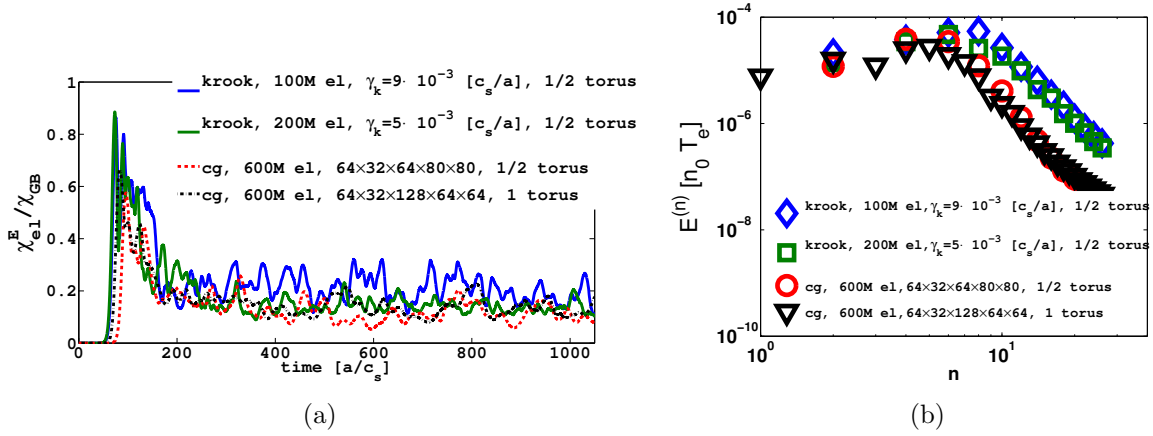


Figure 8.6: Small TEM CYCLONE case, $T_i = T_e/3$, $\rho^* = 1/60$. (a) Electron energy diffusivity χ_{el}^E averaged between $r/a = 0.2$ and $r/a = 0.8$ compared for different noise-control methods, both Krook operator and coarse-graining (cg), and different numerical parameters. (b) Toroidal mode energy spectrum $E^{(n)}$ averaged between $t = 800[a/c_s]$ and $t = 1050[a/c_s]$. Differences at short wavelengths are observed between the coarse-graining procedure and the Krook operator.

8.8 Linear and non-linear ρ^* effects in TEM regime

The plasma finite-size-effects on the turbulence level, appearing through the $\rho^* = \rho_s/a$ parameter in global simulations, turn out to be important both in linear and non-linear ITG regimes, as discussed e.g. in Refs. [127], [128], [10] and [58]. Global simulations are found to provide lower linear growth rates and turbulent diffusivities than simulations performed in the local flux-tube limit ($\rho^* \rightarrow 0$). As an illustration, let us quote results from the standard ITG-dominated CYCLONE case ($\rho^* = 1/180$, $T_i = T_e$, $R/L_{T_i} = R/L_{T_e} = 6.9$, $R/L_n = 2.2$). ORB5 CYCLONE simulations with adiabatic electrons provide a maximum linear growth rate $\gamma_{max}(\rho^* = 1/180) \simeq 0.12[v_{thi}/L_n]$, while the same simulations considering $\rho^* = 1/60$ give a significantly reduced maximum linear growth rate $\gamma_{max}(\rho^* = 1/60) \simeq 0.07[v_{thi}/L_n] \simeq 0.58\gamma_{max}(\rho^* = 1/180)$. The situation in the TEM regime is however different. Figure 8.7 (a) shows the k_θ -spectrum

of the collisionless TEM growth rate γ , for the TEM CYCLONE case ($\rho^* = 1/180$), the TEM TCV case ($\rho^* = 1/80$) and a small TEM CYCLONE case ($\rho^* = 1/60$), considering $T_e = T_i$ and the hybrid model for electrons. Peaked gradient profiles of type 2 described by Eq. (3.60) with $\Delta_A = 0.2a$ are used here. Although the plasma size is different for each case, the linear growth rates appear to be only slightly reduced in a smaller plasma. This observation can be explained by the radial extension scaling of linear TEM modes. While the radial extension of ITG modes Δr_{ITG} scales as $\Delta r_{ITG}/\rho_s \sim 1/\sqrt{\rho^*}$ or $\Delta r_{ITG}/a \sim \sqrt{\rho^*}$ [129] [130] [7], we observe that the radial extension of TEM modes Δr_{TEM} scales as $\Delta r_{TEM}/\rho_s \sim 1/\rho^*$ or $\Delta r_{TEM}/a \sim \text{constant}$. For the mode $k_\theta \rho_s = 0.3$ corresponding to the TEM CYCLONE case, the radial extension $\Delta r_{TEM}/a \simeq 0.2$ is found for all the ρ^* values considered. The TEM modes are thus more radially localized in a small plasma, as illustrated in Figure 8.8, leading to weaker profile shearing effects [131] due to finite plasma size and hence to a weaker reduction of growth rates compared to the ITG case. In addition, results of collisional linear simulations, accounting for both electron-ion and electron-electron collisions with collisionality $\nu_{ei}a/v_{thi} = 5 \cdot 10^{-3}$, are shown in Figure 8.7 (b) and provide the same trend as the collisionless case regarding the plasma finite-size-effects, i.e. weak ρ^* effects. Consistently with results obtained in Sec. 8.11, the linear growth rates are reduced by collisions through the electron detrapping process, regardless of the considered wavelength or plasma size. Note that, as mentioned in Sec. 8.2, different temperature and density profile shapes are used for linear and non-linear simulations, which could provide different sensitivities to finite- ρ^* -effects. In order to address this issue and further pursue the study of finite- ρ^* -effects in linear TEM simulations, the TEM CYCLONE case is again considered, this time with $T_i = T_e/3$ and using the wide gradient temperature and density profiles of type 3 as given by Eq. (3.61), the same profiles as for non-linear simulations. The growth rate of the mode $k_\theta \rho_s = 0.5$ is found to be $\gamma(\rho^* = 1/180) \simeq 0.27[c_s/L_n]$. The same simulation is repeated for $\rho^* = 1/60$, i.e. corresponding to a small TEM CYCLONE case. The obtained growth rate, $\gamma(\rho^* = 1/60) \simeq 0.24[c_s/L_n]$, is only marginally reduced ($\sim 10\%$) with respect to the TEM CYCLONE growth rate, which confirms the weak ρ^* effects in linear temperature-gradient-driven TEM simulations.

Considering again the TEM CYCLONE case, the TEM TCV case and a small TEM CYCLONE case ($\rho^* = 1/60$), non-linear collisionless simulations of turbulence using the hybrid electron model are performed for $T_i = T_e/2$ (the chosen temperature ratio aiming at stabilizing the ETG modes), and using the Krook operator in order to control the numerical noise ($\gamma_k \sim 0.03[c_s/a]$). The turbulence energy spectra, averaged between $t = 1000[a/c_s]$ and $t = 1100[a/c_s]$, are similarly shaped but exhibit a turbulence level depending on the plasma size, as shown in Figure 8.9 (a). The electron energy diffusivity χ_{el}^E in gyro-Bohm units, averaged between $t = 800[a/c_s]$ and $t = 950[a/c_s]$, is much larger for the largest plasma case, i.e. the TEM CYCLONE case, as presented in Figure 8.9 (b). The TEM-related turbulent electron transport reduction through finite- ρ^* -effects is thus of the same order as observed for ion transport in the ITG regime, i.e. a reduction of corresponding diffusivities by a factor ~ 4 when going from $\rho^* = 1/180$ to $\rho^* = 1/80$ (see also Figure 1 of Ref. [58]). As shown in Figure 8.9 (b), going from $\rho^* = 1/180$ to $\rho^* = 1/60$ reduces the electron energy diffusivity of the TEM CYCLONE case by a factor ~ 10 in Gyro-Bohm units. Contrary to the linear ρ^* effects, the non-linear ρ^*

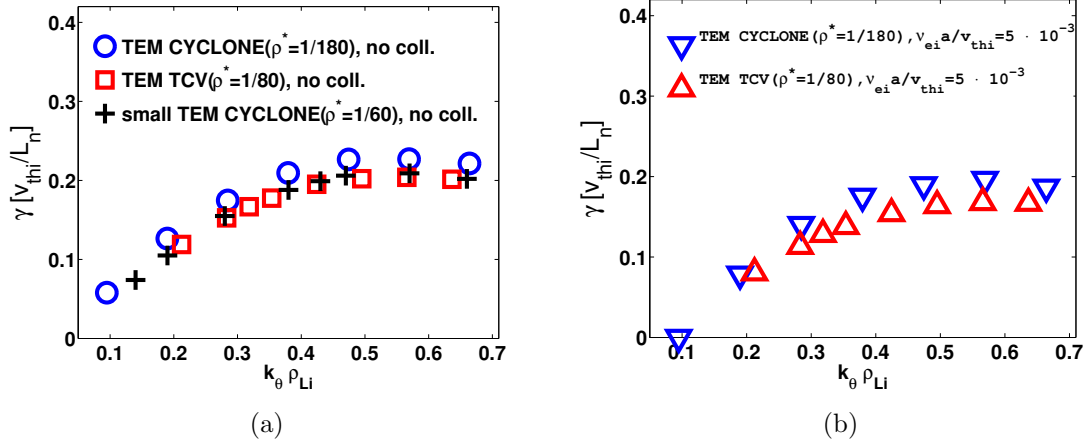


Figure 8.7: k_θ -spectrum of the linear growth rate γ , for the TEM CYCLONE case ($\rho^* = 1/180$) and the TEM TCV case ($\rho^* = 1/80$) with $T_e = T_i$, considering (a) a collisionless case and (b) a collisional case. Additional collisionless results related to a small TEM CYCLONE case ($\rho^* = 1/60$, $T_e = T_i$) are shown as well. The influence of plasma size (through ρ^* effects) on TEM linear growth rates turns out to be small, both for the collisionless and the collisional situations. As expected, electron collisions tend to reduce the linear growth rate at each value of $k_\theta \rho_{Li}$.

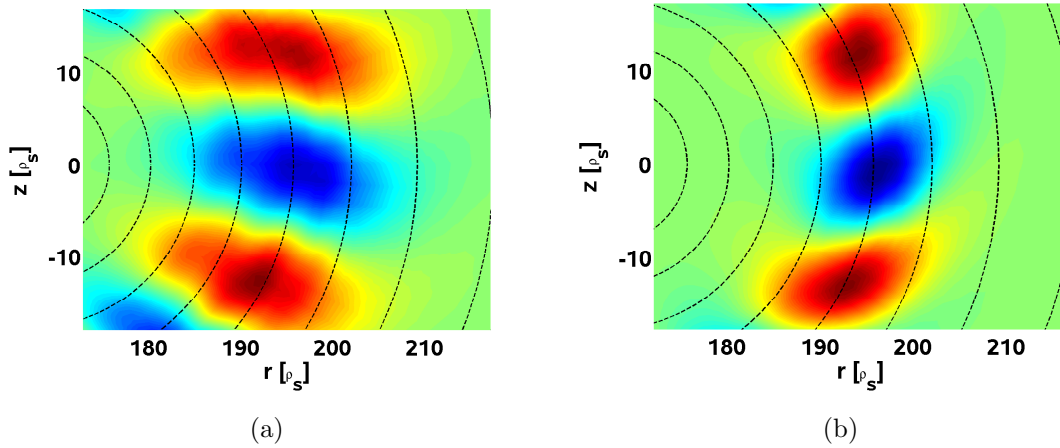


Figure 8.8: Linear structure of the mode $k_\theta \rho_s = 0.3$, in the poloidal plane, for (a) an ITG-dominated regime and (b) a TEM-dominated regime in a small plasma ($\rho^* = 1/60$) considering $T_e = T_i$. TEM instabilities are more radially localized than ITG instabilities.

effects thus appear to be important in the TEM regime, in agreement with Ref. [125].

8.9 Effects of axisymmetric modes on temperature-gradient-driven TEM turbulence

The axisymmetric electric fields, corresponding to the toroidal Fourier mode $n = 0$, and associated zonal flows are a well-established mechanism for ITG turbulence saturation [17] [26]. In the TEM regime, the effects of zonal flows on the saturation mechanism turn out to be

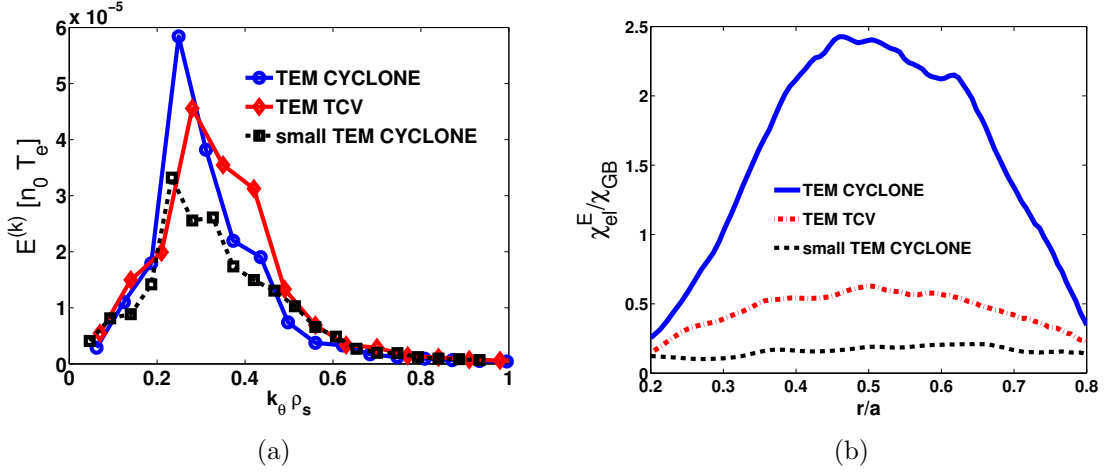


Figure 8.9: (a) Turbulence energy spectra averaged between $t = 1000[a/c_s]$ and $t = 1100[a/c_s]$ and (b) electron energy diffusivity profile $\chi_{el}^E(r)$ averaged between $t = 800[a/c_s]$ and $t = 950[a/c_s]$, for the TEM CYCLONE case ($\rho^* = 1/180$), the TEM TCV case ($\rho^* = 1/80$) and a small TEM CYCLONE case ($\rho^* = 1/60$), considering $T_i = T_e/2$. Important non-linear finite- ρ^* -effects regarding the electron energy transport are observed, the diffusivity in Gyro-Bohm units being significantly reduced in smaller plasmas (similarly to the ITG regime behaviour).

less obvious. Refs. [27] and [29] claim that zonal flows do not contribute significantly to the TEM saturation mechanism for $\eta_e = \nabla \ln T_e / \nabla \ln n_e > 1$, i.e. for mainly temperature-gradient-driven TEM turbulence. This assertion is confirmed in Ref. [51], where only a limited role of zonal flows in TEM turbulence simulations is observed for the TEM CYCLONE case with both $T_i = T_e$ and $T_i = T_e/3$. Here, additional confirmation regarding the latter conclusions is provided through new collisionless simulations (within the frame of the hybrid model) of the pure temperature-gradient-driven TEM turbulence case described in Sec. 8.2, for which $\eta_e = 4.75$. Figure 8.10 shows the electron energy diffusivity profile $\chi_{el}^E(r)$ averaged between $t = 1000[a/c_s]$ and $t = 1800[a/c_s]$, for both cases where the toroidal Fourier mode $n = 0$ is retained or not in the simulation. The transport level is clearly only marginally affected by the presence of zonal flows, contrary to the transport level in ITG regime which is largely reduced in the presence of zonal flows. The Krook operator is used both for ions and electrons, with $\gamma_k \sim 0.02[c_s/a]$ significantly smaller than the maximum linear growth rate $\gamma_{max} \sim 0.07[c_s/a]$ of the most unstable TEM.

8.10 Varying the electron temperature gradient in TEM regime

In this Section, a comparison between linear and non-linear electron temperature gradient scans is performed, considering the collisionless TEM CYCLONE case with $T_i = T_e/2$ along with the wide gradient density and temperature profiles of type 3 [Eq. (3.61)]. The Krook operator is used for controlling the numerical noise, both for electrons and ions. Note that the relaxation rate γ_k does vary according to the maximum linear growth rate γ_{max} of the considered system,

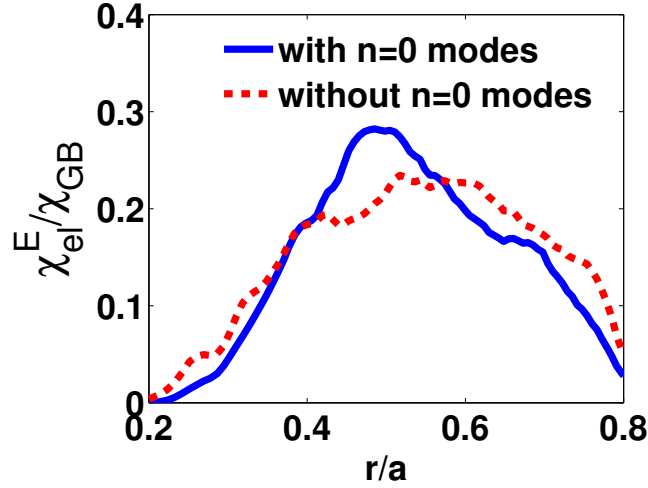


Figure 8.10: Effects of axisymmetric Fourier modes ($n = 0, m$) on electron transport level in temperature-gradient-driven TEM regime (pure TEM case described in Sec. 8.2). Electron energy diffusivity profile $\chi_{el}^E(r)$ averaged between $t = 1000[a/c_s]$ and $t = 1800[a/c_s]$. Regarding the averaged turbulent transport level, no clear effect of zonal flows is visible in the temperature-gradient-driven TEM regime.

i.e. according to the electron temperature gradient.

In the ITG regime, there is a well-established difference between the collisionless linear and non-linear critical ion temperature gradients, the so-called Dimits shift [70]: Due to the shearing effects of zonal flows, a temperature gradient which provides a linear unstable ITG mode might be unable to sustain a non-vanishing turbulent transport if the corresponding maximum linear growth rate γ_{max} is of the order of the averaged $\mathbf{E} \times \mathbf{B}$ shearing rate $\langle |\omega_{E \times B}| \rangle_r$. For a finite turbulence level to persist, the ion temperature gradient should provide a maximum growth rate γ_{max} which is clearly larger than the maximum possible zonal flow shearing rate, limited by Kelvin-Helmoltz-like instabilities: $\gamma_{max} > \langle |\omega_{E \times B}| \rangle_r$ [110] [26].

The situation in the temperature-gradient-driven TEM regime turns out to be different, as shown in Figure 8.11 obtained with the TEM CYCLONE case parameters. Considering low electron temperature gradients ($a/L_{Te} \lesssim 1.5$), which provide marginally unstable linear TEM instabilities, a non-vanishing turbulent transport level is obtained in non-linear simulations. Both the linear growth rates γ_{max} and the non-linear turbulent diffusivities χ_{el}^E appear to scale linearly with the electron temperature gradient (the drive of turbulence) and to have approximately the same critical gradient ($a/L_{Te} \simeq 1$), contrary to the ITG regime where ion temperature gradients in the so-called Dimits shift region give rise to linear instabilities but cannot maintain a finite turbulent transport as a result of the shearing of turbulence by zonal flows [17]. Note that a finite level of electron energy transport is found even for electron temperature gradients at which $\gamma_{max} \simeq \langle |\omega_{E \times B}| \rangle_r$, contrary to the ITG regime situation (see Figure 7.12). This illustrates the limited effects of zonal flows on temperature-gradient-driven TEM turbulence, as already discussed in Sec. 8.9.

A convergence check is performed for a particular case addressed in this section, i.e. considering the electron temperature gradient $a/L_{Te} = 2.484$. Increasing the electron marker number by a

factor 2, i.e. considering $200 \cdot 10^6$ electron markers, and reducing the relaxation rate by a factor 2, i.e. considering $\gamma_k \simeq 0.015[c_s/a]$, provide an electron energy diffusivity of $\chi_{el}^E/\chi_{GB} \simeq 2.1$, averaged between $r/a = 0.4$ and $r/a = 0.6$. The latter value is within the typical uncertainty range of 15% [49] regarding the diffusivity $\chi_{el}^E/\chi_{GB} \simeq 2.35$, obtained with $100 \cdot 10^6$ electron markers and $\gamma_k \simeq 0.03[c_s/a]$ and shown in Figure 8.11 (b). Note that the signal/noise ratio, i.e. the energy of the nearly field-aligned Fourier modes divided by the energy of the unphysical, non-field-aligned Fourier modes, is satisfactory for both simulations (above 50). The latter result thus provides confidence as to the convergence of the presented TEM non-linear results.

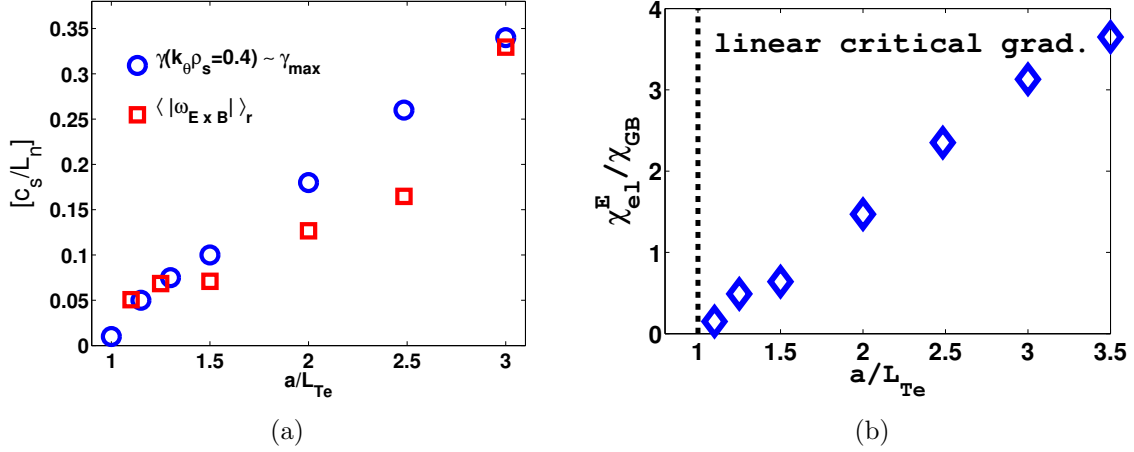


Figure 8.11: Electron temperature gradient a/L_{Te} dependence of (a) the maximum TEM linear growth rate γ_{\max} and the radial average of the absolute value of the $\mathbf{E} \times \mathbf{B}$ shearing rate $\langle |\omega_{\mathbf{E} \times \mathbf{B}}| \rangle_r$ (averaged between $r/a = 0.4$ and $r/a = 0.6$), and (b) the electron energy diffusivity χ_{el}^E , averaged between $r/a = 0.4$ and $r/a = 0.6$ and over a time window of $\Delta t \sim 300[a/c_s]$, in the quasi-stationary state of the simulation ($t \sim 1000[a/c_s]$). Linear and non-linear critical temperature gradients are obviously essentially identical ($a/L_{Te} \simeq 1$).

8.11 Linear and non-linear collisional effects in TEM regime

While ion collisions tend to non-linearly increase the ITG turbulence through zonal flow damping as developed in Chapter 7, electron collisions have a strong and mostly linear effect on temperature-gradient-driven TEM instabilities, actually reducing the TEM drive through the electron detrapping process they generate. The most obvious collisional effect is thus the reduction of TEM linear growth rates with increasing collisionality. The TEM TCV case is chosen for illustrating this latter fact, considering the following modified gradients: $a/L_{Ti} = 0$, $a/L_{Te} = 1.70$, $a/L_n = 0.85$ which provide an essentially pure TEM regime. Figure 8.12 (a) shows the dependence on electron collisionality ν_{ei} of the linear growth rate γ corresponding to the mode $k_{\theta}\rho_{Li} = 0.4$, for different temperature ratios T_e/T_i and collision operators. As expected, neglecting electron-electron collisions (Lorentz model) leads to a weaker collisional growth rate reduction. Note that the collisional reduction of the growth rates is in accordance

with numerical results obtained in Ref. [132] using the flux-tube version of the gyrokinetic code GEM. The collisionality ν_{ei} is normalized with respect to the real frequency of the mode at zero collisionality $\omega(\nu_{ei} = 0)$, i.e. $\omega(\nu_{ei} = 0) \simeq 0.54[v_{thi}/a]$ for $T_i = T_e/3$ and $\omega(\nu_{ei} = 0) \simeq 0.38[v_{thi}/a]$ for $T_i = T_e/2$. Note that ω remains essentially unaffected by electron collisions.

A small TEM CYCLONE case, i.e. the TEM CYCLONE case described in Sec. 8.2 with $\rho^* = 1/60$, is chosen in order to address the difference between linear and non-linear collisional effects on temperature-gradient-driven TEM instabilities. The temperature ratio $T_i = T_e/3$ is considered. The collisional reduction of the maximum linear growth rate γ_{max} (corresponding to the mode $k_{\theta}\rho_{Li} = 0.3$) with increasing electron-ion collision frequency ν_{ei} is shown in Figure 8.12 (b) and compared to the collisional damping of the quasi-stationary electron turbulent energy flux Q_{el} , averaged between $r/a = 0.4$ and $r/a = 0.6$. The reduction of non-linear turbulent transport (compared to a collisionless case) turns out to be stronger than the reduction of the linear growth rate and can thus not be explained by a simple mixing length argument $\chi \sim \gamma_{max}/\langle k_{\perp}^2 \rangle$. Note that the real frequency of the mode $k_{\theta}\rho_{Li} = 0.3$, $\omega \simeq 0.48[c_s/L_n]$, remains essentially unaffected by collisions, and that both electron-ion and electron-electron collisions are accounted for. The non-linear runs for simulating collisional TEM turbulence presented in Figure 8.12 (b) are actually very challenging due to the large number of markers which is required ($\sim 600 \cdot 10^6$ electrons and $\sim 200 \cdot 10^6$ ions) combined with the small time step related to electron dynamics, leading to $\sim 500'000$ CPU hours consumed for each simulation.

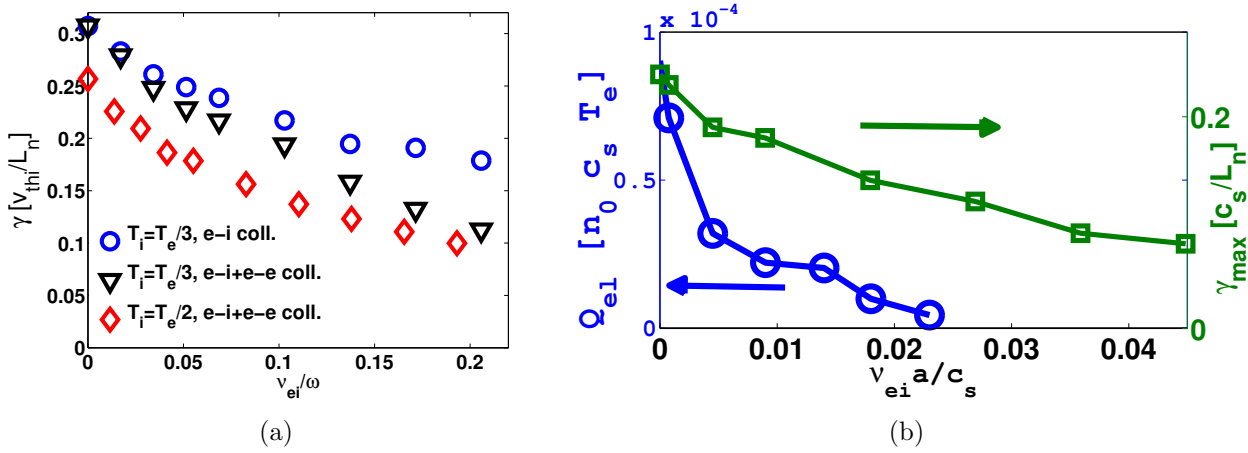


Figure 8.12: (a) Collisional damping of linear growth rates in TEM regime. TEM TCV case with $a/L_{Ti} = 0$, $a/L_{Te} = 1.70$, $a/L_n = 0.85$, mode $k_{\theta}\rho_{Li} = 0.4$. The electron-ion collision frequency ν_{ei} is normalized with respect to ω , the collisionless real frequency of the considered mode $k_{\theta}\rho_{Li} = 0.4$. (b) Small TEM CYCLONE case, $T_i = T_e/3$. Electron collisionality scan, both for the quasi-stationary electron turbulent energy flux Q_{el} , averaged between $r/a = 0.4$ and $r/a = 0.6$, and for the maximum linear growth rate γ_{max} . Electron collisions have a damping effect on TEM instabilities both in linear and non-linear simulations, the damping of non-linear turbulent transport (compared to a collisionless case) being however stronger than the damping of linear growth rates.

Considering again the small TEM CYCLONE case with $T_i = T_e/3$, Figure 8.13 shows the turbulent component (in the poloidal plane) of the electrostatic potential, $e(\phi - \langle \phi \rangle_S)/T_{e0}$, at $t = 1000[a/c_s]$ for the two collisionalities $\nu_{ei}a/c_s(r/a = 0.5) = 7.5 \cdot 10^{-4}$ and $\nu_{ei}a/c_s(r/a = 0.5) = 4.5 \cdot 10^{-3}$. As expected, the averaged turbulence level is weaker for a stronger collisionality.

Note that the collisionality dependence on density and temperature profiles is accounted for in ORB5 simulations, leading in fact to stronger collisionality close to the plasma edge and weaker collisionality close to the magnetic axis. The collisionality increase towards the edge is explained by a weaker reduction of collisionality due to lower density ($\sim n$) than the increase of collisionality due to lower temperature ($\sim T_e^{-3/2}$), as shown in Figure 8.14 which presents the electron collision frequency profile $\nu_{ei}(r/a)$ corresponding to the TEM CYCLONE case. Compared to the weakly collisional situation, the TEM turbulence in the case of stronger collisionality is thus more reduced and even quenched when going towards the plasma edge as illustrated in Figure 8.13.

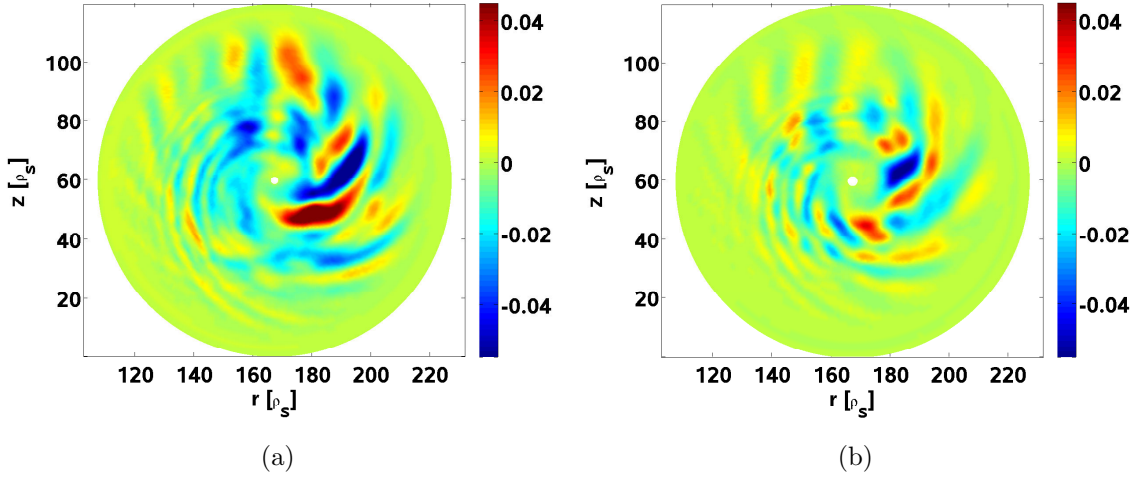


Figure 8.13: Small TEM CYCLONE case, $T_i = T_e/3$. Poloidal cross-section of the non-zonal component of the electrostatic potential $e(\phi - \langle \phi \rangle_S)/T_{e0}$ at $t = 1000[a/c_s]$ for the two collisionalities (a) $\nu_{ei}a/c_s(r/a = 0.5) = 7.5 \cdot 10^{-4}$ and (b) $\nu_{ei}a/c_s(r/a = 0.5) = 4.5 \cdot 10^{-3}$. The turbulence reduction through electron collisions is clearly visible.

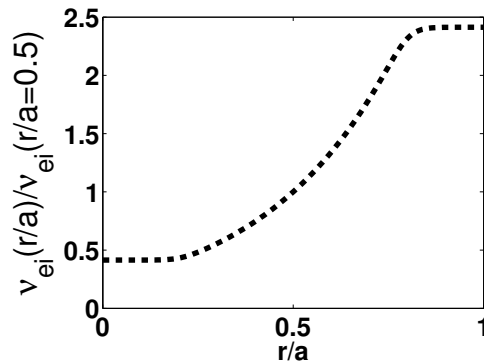


Figure 8.14: TEM CYCLONE case, electron-ion collision frequency $\nu_{ei} \sim n/T_e^{3/2}$ as a function of radius r/a , normalized with respect to collision frequency at mid-radius $r/a = 0.5$. Collisionality is significantly stronger close to the plasma edge than close to the magnetic axis.

In order to further study the effects of electron collisions on linear TEM instabilities and possibly compare them with analytical estimates, additional results are shown in Figure 8.15 (a) which

presents the growth rates of the TEM CYCLONE case for $k_\theta \rho_{Li} = 0.3$ and clearly demonstrates the stabilizing effect of collisions, both for the Lorentz model (electron-ion collisions only) and for the full linearized collision operator for electrons (electron-ion and electron-electron collisions). Note that the growth rate reduction through electron collisions is qualitatively consistent with Figure 8.12 (a), obtained for the TEM TCV case and different temperature and density gradients. The analytical estimates in Figure 8.15 (a) are provided by a numerical solution to the analytical collisionless dispersion relation derived in [34] (also based on a hybrid model), along with the re-scaling described in Eq. (2.55) for low collisionality. The fully kinetic electron model provides growth rates which are higher than those predicted by the hybrid model. Consistently, a higher collisionality is required in order to stabilize the mode if trapped and passing kinetic electrons are considered. The difference between the hybrid model and the fully kinetic model arises partly because of the choice of heavy electrons ($m_i/m_e = 200$) for carrying out the simulations both in the fully kinetic model and the hybrid model, the results of the fully kinetic model being not fully converged with respect to the electron mass. According to Figures 8.12 (a) and 8.15 (a), one may conclude that a TEM instability can be significantly stabilized by electron collisions for TCV and DIII-D plasmas of order $\nu_{ei} \sim 10^{-2} v_{thi}/a$. Note that electron collisionality affects only marginally the real frequency of a Trapped-Electron-Mode, as shown in Figure 8.15 (b) which presents for both collisionless and collisional situations the time evolution of the TEM electrostatic potential ϕ at position $(r/a = 0.5, \theta = 0, \varphi = 0)$, the growing part $e^{\gamma t}$ being subtracted. The considered mode is here $k_\theta \rho_{Li} = 0.4$ and the associated real frequency read from Figure 8.15 (b), $\omega \simeq 0.8 \omega_{ne}$, is as expected close to the diamagnetic density drift frequency ω_{ne} .

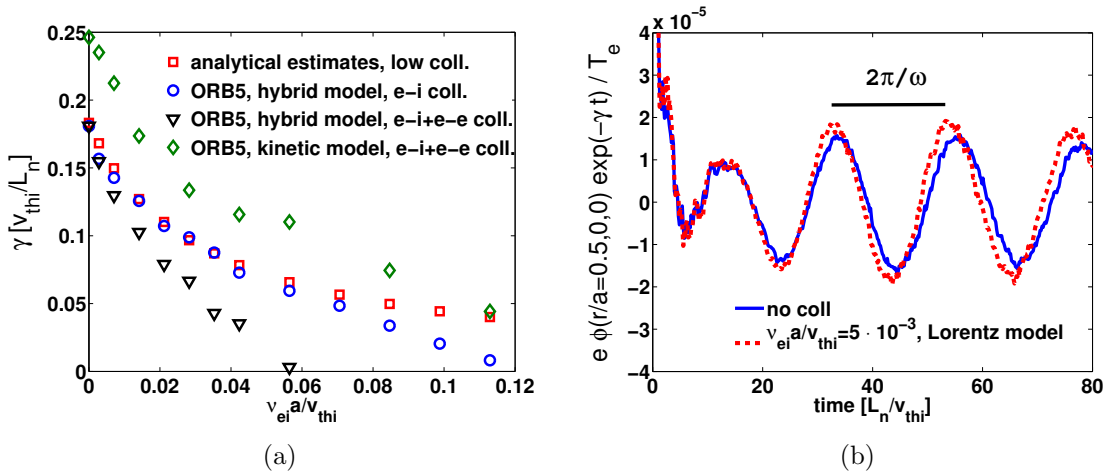


Figure 8.15: TEM CYCLONE case, $T_i = T_e$. (a) Electron collisions have an important effect on the growth rate of TEM instabilities. Analytical estimates are compared to ORB5 results, both for the Lorentz model and the full linearized collision operator, $k_\theta \rho_{Li} = 0.3$. (b) Marginal influence of collisionality (Lorentz model) on the real frequency $\omega \simeq 0.8 \omega_{ne}$ of a Trapped-Electron-Mode, $k_\theta \rho_{Li} = 0.4$.

Finally, the linear dependence of the TEM growth rates on the electron temperature gradient, as established in Sec. 8.10 for a collisionless case, is shown to persist in the presence of electron collisions. For a collisionless TEM CYCLONE case, the critical gradient for $k_\theta \rho_{Li} = 0.3$

is $R_0/L_{Te}|_{\text{crit}} \simeq 3$, as shown in Figure 8.16. In other words, the considered TEM instability is suppressed if $\eta_e = L_n/L_{Te}$ falls below $\simeq 1.4$, the density gradient being kept constant ($R_0/L_n = 2.2$). For the collisionality $\nu_{ei}a/v_{thi} = 1.4 \cdot 10^{-2}$, the critical instability threshold of the temperature gradient is raised up to $R_0/L_{Te}|_{\text{crit}} \simeq 5$, clearly reflecting the stabilizing effect of electron collisions on the TEMs, while the growth rate still increases linearly with the electron temperature gradient (Figure 8.16).

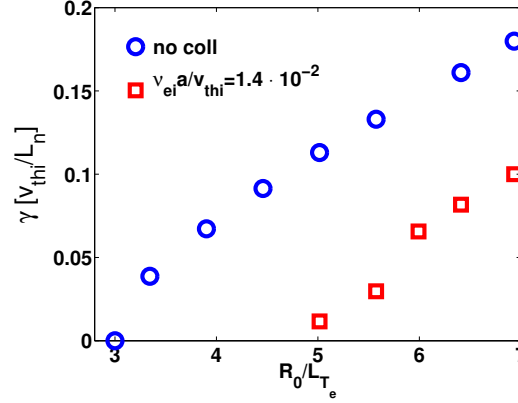


Figure 8.16: Electron collisions (electron-ion + electron-electron) raised the critical linear instability threshold of the electron temperature gradient R_0/L_{Te} . In a collisionless model, stabilization occurs at $R_0/L_{Te}|_{\text{crit}} \simeq 3$ for the TEM CYCLONE case parameters and $k_\theta \rho_{Li} = 0.3$, while at $\nu_{ei}a/v_{thi} = 1.4 \cdot 10^{-2}$ and for the same mode $k_\theta \rho_{Li} = 0.3$, $R_0/L_{Te}|_{\text{crit}} \simeq 5$.

8.12 Effects of electron collisions on zonal flows

As studied in Chapter 6 and demonstrated in [99], ion-ion collisions have a damping effect on zonal flows. Here we numerically address the issue of electron collisional effects on zonal flows (ion-ion collisions being neglected), considering the CYCLONE case geometrical parameters with zero density and temperature gradients. The so-called Rosenbluth-Hinton test defined in Sec. 6.6.1 is performed by initializing the simulation with a perturbed ion distribution function of the form $\delta f_{LM,i} = 10^{-3} \cos(\pi r/a) f_{LM,i}$. Figure 8.17 (a) shows that the residual of the radial electric field $E_r(t)$, averaged between $r/a = 0.4$ and $r/a = 0.6$, is essentially unmodified by the fully kinetic and collisional electron response (compared to the adiabatic electron model results). Figure 8.17 (b) reaches the same conclusion in the frame of the hybrid model with electron collisions, i.e. the zonal flow levels appear to be unaffected by electron collisions.

8.13 Realistic simulation of microturbulence related to the TCV shot # 45353

This Section presents collisionless simulation results obtained by considering the realistic magnetic equilibrium corresponding to the TCV shot # 45353 at 0.3 [s], just before the electron

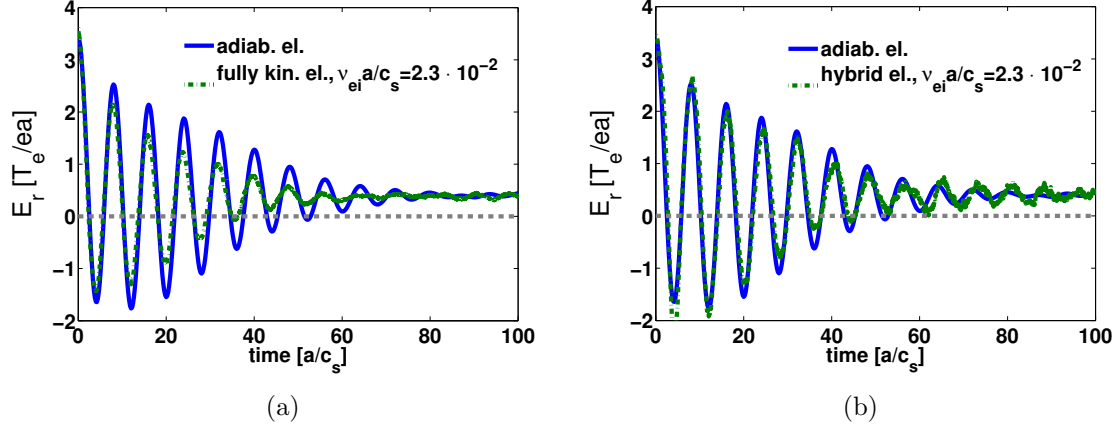


Figure 8.17: RH test considering collisional electrons, CYCLONE case geometrical parameters, no gradients. Time evolution of the radial electric field $E_r(t)$ in the presence of electron collisions, averaged between $r/a = 0.4$ and $r/a = 0.6$, for (a) the fully kinetic electron model and (b) the hybrid electron model. Both cases are compared with the adiabatic (collisionless) electron model results. Electron collisions are found to have no influence on zonal flow levels, both for the fully kinetic electron model and the hybrid electron model.

cyclotron resonance heating by the gyrotrons. The related experimental density and temperature profiles, measured and/or reconstructed from different TCV diagnostics, are accounted for as shown in Figure 8.18. The associated microturbulence being clearly TEM-dominated, the hybrid model is chosen for describing the electron dynamics, in order to capture the TEM instabilities. Note the corresponding $\rho^* = 1/81$ at the reference surface $s_0 = 0.6$. Heat sources and particle sources aim at maintaining the temperature and density gradients approximately constant in a time-average sense, in order to obtain a quasi-stationary state of turbulence providing reliable levels of heat and particle transport. The particle diffusivity profiles $D(s)$, both for ions and electrons, are shown in Figure 8.19 (a), while the energy diffusivity profiles $\chi^E(s)$, again both for ions and electrons, are shown in Figure 8.19 (b). All the diffusivity profiles are averaged between $t = 800[a/c_s]$ and $t = 1100[a/c_s]$. Figure 8.19 (a) shows the same particle diffusivity profiles both for ions and electrons, reflecting the ambipolarity of the particle flux. Figure 8.19 (b) shows a dominant electron energy diffusivity compared to the ion energy diffusivity (by a factor ~ 2), consistent with the TEM-dominated nature of the turbulence regime related to the mentioned TCV shot.

The poloidal cross-section of the perturbed, non-zonal electrostatic potential $e(\phi - \langle \phi \rangle_s)/T_{e0}$ (corresponding to the TCV shot # 45353) is presented in Figure 8.20, both in the linear phase of the simulation ($t \simeq 40[a/c_s]$) and in the early non-linear phase of the simulation ($t \simeq 100[a/c_s]$). The typical ballooning structure of microinstabilities is clearly visible on the low-field-side of the torus in Figure 8.20 (a), while the typical microturbulence chaotic structure is presented in Figure 8.20 (b).

Figure 8.21 (a) shows the time evolution of the $\mathbf{E} \times \mathbf{B}$ shearing rate profile $\omega_{E \times B}(s)a/c_s$ [as defined by Eq. (7.5)], which exhibits GAM oscillations close to plasma edge with clear outward propagation. Figure 8.21 (b) presents the $\mathbf{E} \times \mathbf{B}$ drift velocity profile $v_{E \times B}(s)$ in the sound speed unit, averaged between $t = 800[a/c_s]$ and $t = 1100[a/c_s]$. As expected, the drift velocity

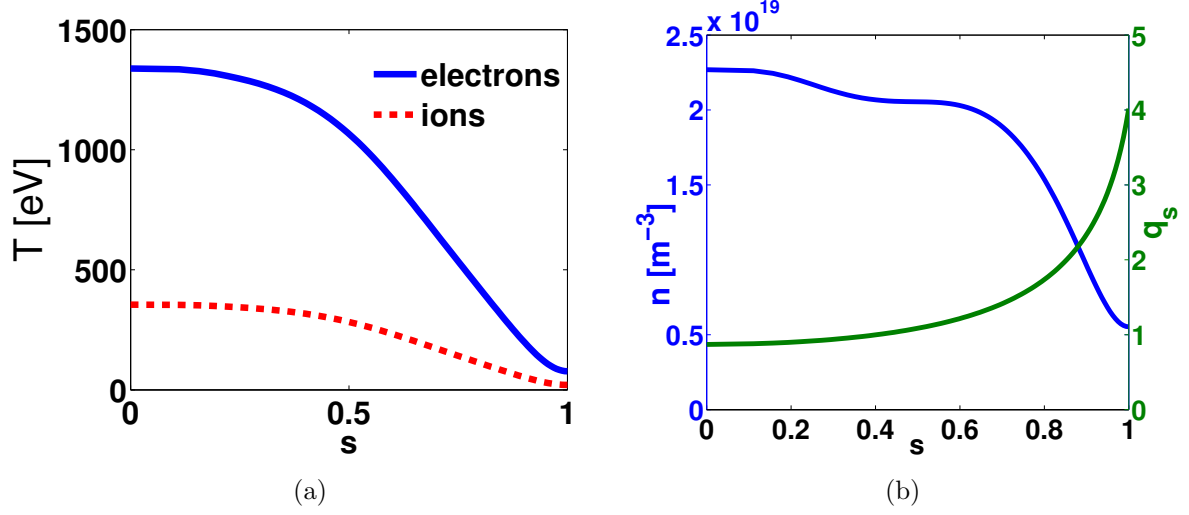


Figure 8.18: TCV shot # 45353 at 0.3[s]. (a) Electron temperature profile $T_e(s)$ measured by the Thomson scattering diagnostics and estimated ion temperature profile $T_i(s)$. (b) Density profile $n(s)$ measured by the Thomson scattering diagnostics and safety factor profile $q_s(s)$ reconstructed from magnetic measurements.

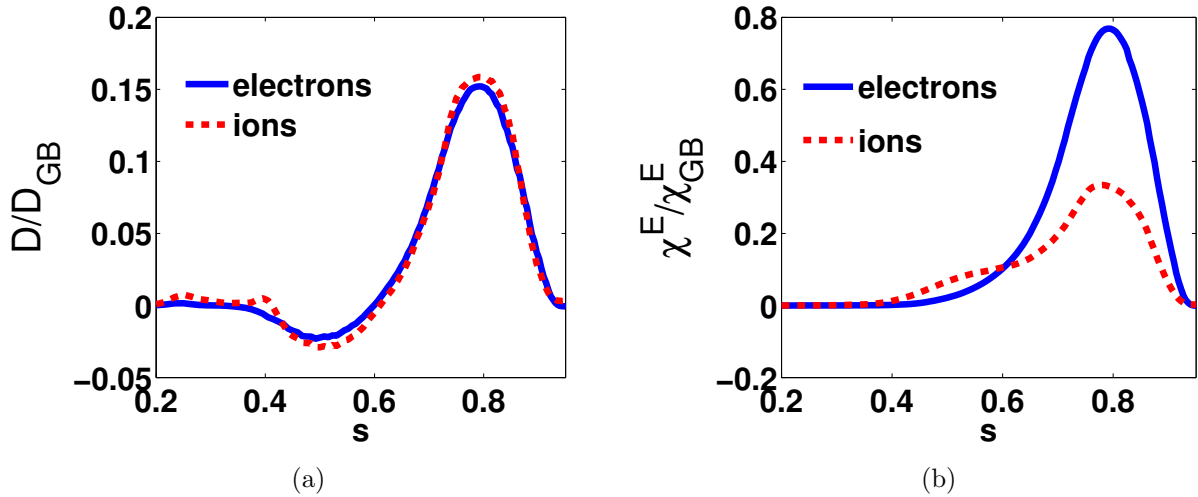


Figure 8.19: Simulation of the TCV shot # 45353 (equilibrium at 0.3[s]). Both for ions and electrons and averaged between $t = 800[a/c_s]$ and $t = 1100[a/c_s]$, (a) particle diffusivity profiles $D(s)$ and (b) energy diffusivity profiles $\chi^E(s)$. Ambipolarity is satisfied, while electron energy transport is larger than ion energy transport, as expected in a TEM-dominated regime.

$v_{E \times B}$ is larger in the radial region where the temperature and density gradients are maximum, i.e. close to $s \simeq 0.8$ (see Figure 8.18). Note that a good agreement with GAM experimental measurements is obtained [133].

8.14 Conclusions

In this Chapter, results from global gyrokinetic simulations of temperature-gradient-driven TEM turbulence performed with the code ORB5 are discussed. In order to validate the pre-

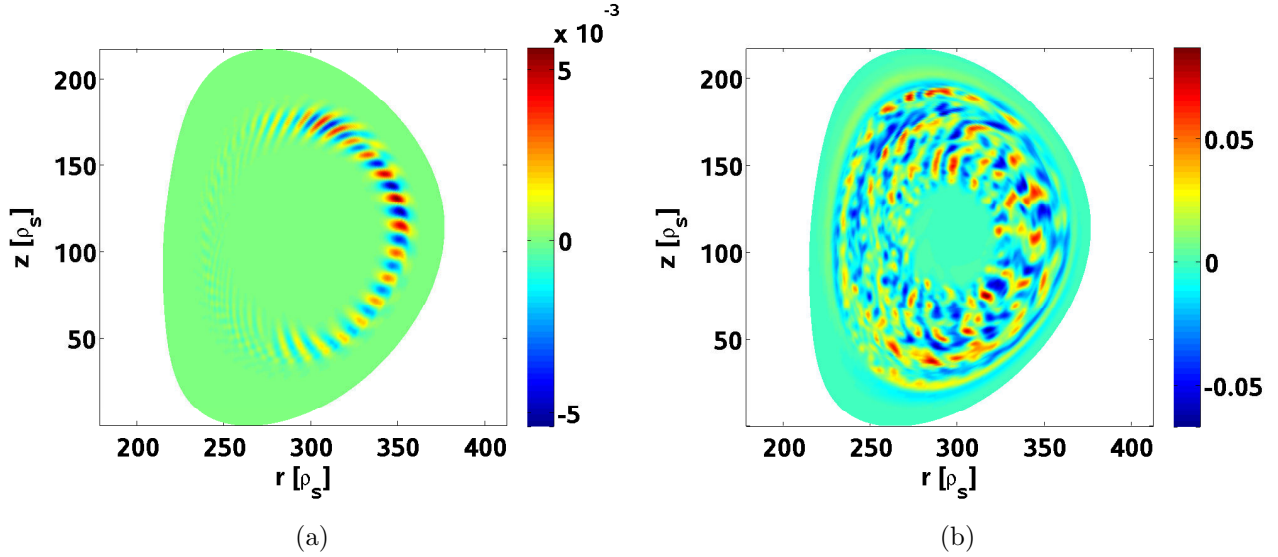


Figure 8.20: Simulation of the TCV shot # 45353 (equilibrium at 0.3[s]). Poloidal cross-section of the perturbed, non-zonal electrostatic potential $e(\phi - \langle \phi \rangle_S)/T_{e0}$, both (a) in the linear phase of the simulation ($t \simeq 40[a/c_s]$) and (b) in the early non-linear phase of the simulation ($t \simeq 100[a/c_s]$).

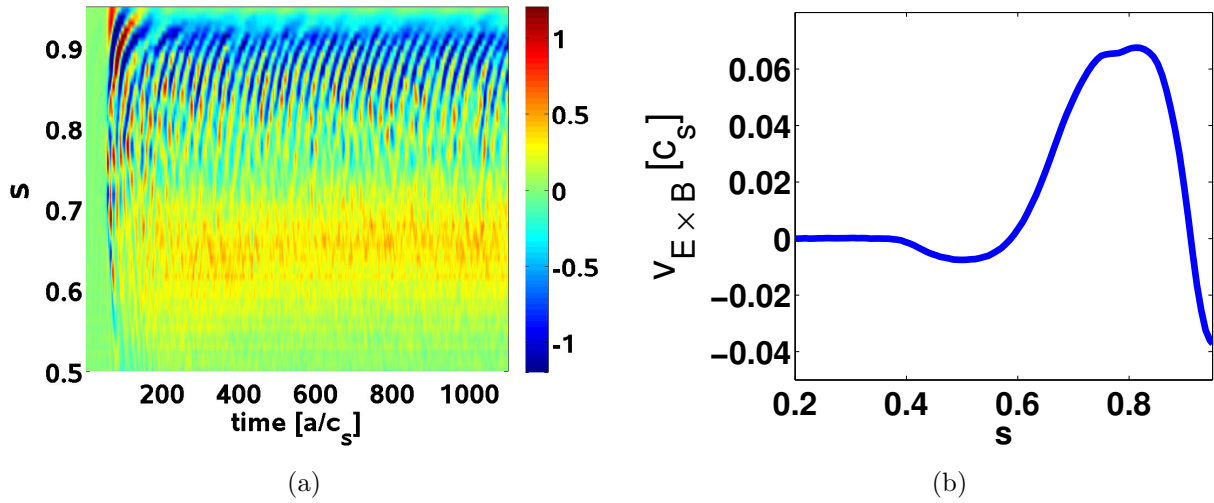


Figure 8.21: Simulation of the TCV shot # 45353 (equilibrium at 0.3[s]). (a) Time evolution of the $\mathbf{E} \times \mathbf{B}$ shearing rate profile $\omega_{E \times B}(s)a/c_s$ with GAM oscillations. (b) $\mathbf{E} \times \mathbf{B}$ drift velocity profile $v_{E \times B}(s)/c_s$, averaged between $t = 800[a/c_s]$ and $t = 1100[a/c_s]$.

sented results, convergence tests were first carried out. Two different methods for controlling the numerical noise (inherent to the PIC approach) were successfully evaluated and compared in TEM simulations. A linear benchmark in the TEM regime against the Eulerian gyrokinetic code GENE is presented (accounting for a fully kinetic electron response), which shows a good agreement between both codes at long wavelengths ($k_\theta \rho_s \lesssim 0.5$). At shorter wavelengths ($k_\theta \rho_s \sim 1$), a discrepancy between both codes arises, essentially due to the long wavelength approximation in the quasi-neutrality equation solved by ORB5.

While there is almost no effect of finite plasma size in the TEM linear regime, the effects of finite plasma size on TEM instabilities turn out to be important in the TEM non-linear regime. Note the difference compared to ITG-dominated cases, where the effects of finite plasma size are important both in linear and non-linear regimes.

In the temperature-gradient-driven TEM regime, the zonal flows are shown to play no role in turbulence saturation, at least in considered parameter range ($T_i < T_e$, $\eta_e > 1$), confirming previous studies [27] [29]. Accordingly, no Dimits shift region is observed in this regime, unlike in the ITG regime which features a Dimits shift region as a consequence of the importance of zonal flow shearing on associated turbulence saturation.

Electron collisions are found to reduce both the linear growth rates and the transport levels related to TEM instabilities, through the collisional electron detrapping process. Note that, oppositely, the ion collision effects on ITG turbulence are almost fully non-linear and lead to a general increase in ITG turbulence level through zonal flow damping [23] [26].

Finally, a realistic global gyrokinetic simulation of a TCV tokamak shot, accounting for the actual experimental profiles and magnetic equilibrium and considering a trapped electron kinetic response, has successfully been carried out and thus demonstrates the ability of the ORB5 code to provide relevant predictions regarding the physics of real tokamaks.

Chapter 9

Conclusions and outlook

Within the frame of research related to the tokamak device for controlling nuclear fusion on Earth (magnetically confined plasma physics), the global gyrokinetic ORB5 code and the related physics of microturbulence the code can address have been presented in this thesis. In a first stage, some basic tokamak concepts as well as a few insights into theoretical modelling of microturbulence have been recalled for the sake of completeness. The history of the ORB5 development over many years has been briefly reviewed with a particular focus on the implementation of linearized collision operators, the main code development in the frame of this work. The physical model upon which ORB5 is based, the gyrokinetic model, was then summarized. The algorithms providing the code routines from both the collisionless and collisional model equations have been detailed, including the noise-control procedures allowing to carry out relevant turbulence simulations. The noise-control procedures are especially crucial in the presence of collisions treated here with a Langevin approach which increase the numerical noise. The collision operators have been thoroughly tested and first applied to neoclassical physics studies. Careful benchmarks have been performed, comparing ORB5 results with both numerical results from other codes and analytical models and thus allowing to validate the implementation of the collision operators in the code. The rich topic of interactions between collisions and electrostatic turbulence in tokamak plasmas has then been addressed, both in Ion-Temperature-Gradient (ITG) and Trapped-Electron-Mode (TEM) regimes. The effects of electron collisions have been found to act mostly linearly on TEM regime and decrease the turbulence level through the electron detrapping process, while the effects of ion collisions in ITG regime turned out to be essentially non-linear and increase the turbulence level through interactions with zonal flows. The zonal flow dynamics in collisionless and collisional ITG turbulence simulations has been studied, emphasizing the limitation of the zonal flow shearing rate level due to Kelvin-Helmoltz-type instabilities.

Additionally, some collisionless results related to TEM turbulence have been presented. The linear simulations in TEM regime have been validated through a successful benchmark against the global GENE code. The zonal flows have been found to play a weak role in TEM turbulence saturation, at least in the temperature-gradient-driven TEM regime, in agreement with previous studies. In the TEM regime, the effects of the finite plasma size appeared to be weak in linear simulations but strong in non-linear simulations, unlike the effects of the finite plasma size in ITG regime which are important both in linear and non-linear simulations.

For the first time, a realistic non-linear global gyrokinetic ORB5 simulation, accounting for a proper magnetic equilibrium related to the TCV tokamak along with the corresponding density and temperature profiles, has been successfully carried out including a kinetic response of trapped electrons and has obtained a good agreement with GAM experimental measurements [133]. The potential of ORB5 related to further studies of realistic tokamak shots has thus been demonstrated.

The ORB5 code has proven belong to the state-of-the-art codes for studying microturbulence in tokamak plasmas. As such, it is ready to address crucial topics of current research in theoretical core plasma physics, such as a better understanding of momentum transport or global electromagnetic simulations requiring fully kinetic electron dynamics. Studies of turbulence in a realistic ITER geometry have already started to provide results of interest regarding heat transport levels in the future ITER tokamak [134]. This thesis work allows the future ORB5 users to include reliable collisional effects in different specific studies. Note that the electromagnetic solver of NEMORB, the new version of ORB5, remains to be modified in order to be compatible with the 2-weight scheme before collisional electromagnetic studies can become accessible. Moreover, non-linear benchmarks remain to be performed against other gyrokinetic codes, both in electrostatic TEM and electromagnetic regimes with and without collisions. Additionally, simulations accounting simultaneously for both electron and ion collisions remain to be carried out in the different turbulence regimes.

The main current weakness of the ORB5 code is probably the long wavelength approximation assumed by the quasi-neutrality field solver which prevents the code from studying properly microturbulence at smaller wavelengths. A new integral solver [69] is definitely required in order to further study the mixed ITG-TEM regime, of clear relevance to realistic tokamak experimental conditions [135].

Some work actually remains to be done regarding the collision operators which are (so far) not multi-ion species. Although appropriate for the single-ion plasma simulations presented in this work, the current collision operators will have to be upgraded for future simulations of multi-ion plasmas [136], taking for instance plasma impurities such as Carbon into account. Moreover, ion-electron collisions and associated drag need to be implemented for accurate parallel dynamics. Full non-linear collision operators could in principle be considered as an improvement to the current linearized operators, but the practical complexity of such non-linear operators, for a questionable benefit regarding core tokamak physics, makes them unlikely to be implemented soon in the code.

Ultimately, in order to increase the physical relevance of its transport predictions for a real tokamak device, ORB5 should be coupled to a code describing accurately the edge of tokamak plasmas. Standard gyrokinetic codes indeed rely on the core ordering $\delta n/n \sim e\phi/T \ll 1$ which essentially breaks down close to the plasma edge. Strong gradients in edge transport barriers also lead potentially to the breakdown of gyrokinetic theory. Edge plasma physics is however crucial for modelling properly the behaviour of a future fusion reactor, especially in high confinement regime (H-mode plasmas) where the associated pedestal cannot be accurately modeled by ORB5 and the current gyrokinetic codes in general.

Appendix A

Potential energy flux in turbulence simulations

The generic term *heat flux* is often used in order to qualify the quantity which is strictly the *kinetic energy flux*. Actually, the proper heat flux, as defined in Eq. (3.66), should also account for the potential energy flux [71] and the particle flux contributions. In the frame of simulations with adiabatic electrons, the total ion particle flux does vanish in order to ensure the ambipolarity condition, but the potential energy flux does not vanish in collisional runs. Here one gives an estimate of the potential energy flux magnitude compared to the kinetic energy flux magnitude, the only term usually retained in the heat flux computation. ORB5 simulations show that the net potential energy flux is due mainly to the neoclassical Maxwellian contribution:

$$Q_{\text{pot}} \approx \left\langle \frac{1}{|\nabla\Psi|} \int d^3v q \phi f_0 \frac{d\Psi}{dt} \Big|_0 \right\rangle_S, \quad (\text{A.1})$$

the two remaining contributions $\sim q\phi \delta f d\Psi/dt|_0$ and $\sim q\phi f_0 d\Psi/dt|_{E \times B}$ balancing each other. It is recalled that $d\Psi/dt_0 = \nabla\Psi \cdot (\mathbf{v}_{\nabla B} + \mathbf{v}_e)$ and $d\Psi/dt|_{E \times B} = \nabla\Psi \cdot \mathbf{v}_{E \times B}$. The potential energy flux (A.1) is inward for the considered CYCLONE case parameters, and has thus a balancing effect on the resulting outward kinetic energy flux. Considering a local Maxwellian background $f_0 = f_{LM}$, it is possible to show, by analytically expliciting the integral on the Right-Hand-Side of Eq. (A.1), that the potential energy flux arises from the poloidal variation of the electrostatic potential:

$$Q_{\text{pot}} \sim 2\pi n_0 T_0 \frac{F(\Psi)}{S(\Psi)} \int_0^{2\pi} \frac{1}{B^2} \frac{\partial \phi}{\partial \theta^*} d\theta^*, \quad (\text{A.2})$$

where $S(\Psi)$ is the flux surface defined by:

$$S(\Psi) = 2\pi \int_0^{2\pi} J_{\Psi\theta^*\varphi} |\nabla\Psi| d\theta^*, \quad (\text{A.3})$$

$J_{\Psi\theta^*\varphi} = 1/[(\nabla\Psi \times \nabla\theta^*) \cdot \nabla\varphi]$ being the Jacobian function. Note that $Q_{\text{pot}} = 0$ in simulations retaining only the flux-surface-averaged electrostatic potential ($\phi = \langle \phi \rangle_S$), according to

Eq. (A.2).

It turns out that the magnitude of the total potential energy flux is small. For CYCLONE base case simulations considering the temperature gradient $R_0/L_{T_0} = 6.9$ and adiabatic electrons, at $r/a = 0.5$ the scaling is empirically found to be a quarter of the neoclassical kinetic energy flux, with opposite direction (pointing inwards):

$$\frac{Q_{\text{pot}}}{Q_{\text{kin,neo}}} \approx -\frac{1}{4}. \quad (\text{A.4})$$

As an illustration of the ratio given by Eq. (A.4), Figure A.1 shows the time evolution of the neoclassical kinetic energy flux $Q_{\text{kin,neo}}$ and the potential energy flux Q_{pot} respectively, at mid-radius $r/a = 0.5$, for the collisionality $\nu_0^* = 0.45$ and considering the CYCLONE case parameters. It appears thus that the potential energy flux may be dropped in the heat flux computation for turbulence simulations if turbulent transport is clearly dominant compared to neoclassical transport. However, as stated in Chapter 6, the potential energy flux is *a priori* important for computing the neoclassical heat diffusivity.

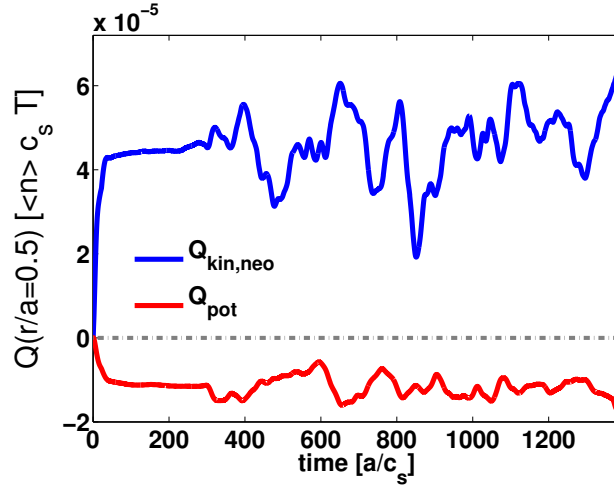


Figure A.1: Time evolution of the neoclassical kinetic energy flux $Q_{\text{kin,neo}}$ (blue) and the potential energy flux Q_{pot} (red) at mid-radius $r/a=0.5$, for CYCLONE case parameters (adiabatic electrons) and $\nu_0^* = 0.45$. The potential energy flux, pointing inwards, remains small compared to the total heat flux (neoclassical + turbulent).

Appendix B

A collisional δf PIC code for unmagnetized plasmas

B.1 Description

Although the subject of the present work is essentially the use of collisional δf Particle-In-Cell (PIC) methods in the frame of gyrokinetic simulations in toroidal geometry, the same numerical approach may be applied to much simpler physical systems for testing purposes. BIRDIE, a collisional δf PIC code for unmagnetized homogeneous plasmas, has been written from scratch, mainly for testing the collision algorithms. It features a kinetic description of electrons in a one-dimensional, unmagnetized, homogeneous plasma of length L , assuming a cold ion background. These characteristics allow it to study numerically the high frequency electron plasma waves, also called Langmuir waves, accounting for realistic collision operators. Langmuir waves typically have a real frequency $\omega \sim \omega_{pe}$, where ω_{pe} is the electron plasma frequency defined as follows:

$$\omega_{pe} = \sqrt{\frac{n_e e^2}{m_e \epsilon_0}}. \quad (\text{B.1})$$

The wavelength of a Langmuir wave is typically $\lambda \gtrsim \lambda_{De}$, where λ_{De} is the electron Debye length defined by $\lambda_{De} = v_{the}/\omega_{pe}$, $v_{the} = \sqrt{T_e/m_e}$ being the electron thermal velocity. Let f stand for the total electron distribution function. Dropping the electron index, the Fokker-Planck equation solved by BIRDIE is:

$$\frac{\partial f}{\partial t} + v_x \frac{\partial f}{\partial x} - \frac{e}{m} \mathbf{E} \cdot \frac{\partial f}{\partial \mathbf{v}} = -C[f], \quad (\text{B.2})$$

where C is a general collision operator and \mathbf{E} the perturbed electric field. One introduces the δf decomposition $f = f_M + \delta f$, where f_M is a Maxwellian:

$$f_M(v) = \frac{n}{(2\pi)^{3/2} v_{th}^3} \exp\left(-\frac{v^2}{2v_{th}^2}\right), \quad (\text{B.3})$$

where temperature $T = mv_{th}^2$ and density n are constant. Considering a Lorentz operator for electron-ion collisions and a linearized Landau operator for electron-electron collisions, as described in detail in Chapter 5, Eq. (B.2) reads in the δf formalism:

$$\frac{\partial \delta f}{\partial t} + v_x \frac{\partial \delta f}{\partial x} - \frac{e}{m} \mathbf{E} \cdot \frac{\partial \delta f}{\partial \mathbf{v}} + \nu_{ei}(v) \hat{L}^2 \delta f + C[f_M, \delta f] = \frac{e}{m} \mathbf{E} \cdot \frac{\partial f_M}{\partial \mathbf{v}} - C[\delta f, f_M]. \quad (\text{B.4})$$

The velocity space is described by the two variables (v, ξ) , where v is the norm of the velocity and $\xi = v_x/v$ is the pitch angle variable. A velocity space border $v_{\max} = 7v_{th}$ is introduced. Eq. (B.4) is solved by the δf PIC method described in detail in Chapters 3 and 4. N numerical particles, called markers, are introduced. To each marker r are associated two weights w_r and p_r defined as in Chapter 4. They allow the discretization of the distribution functions δf and f_M by linking the numerical particle distribution to the physical particle distribution:

$$\delta f(x, \mathbf{v}, t) = \sum_{r=1}^N w_r(t) \delta(x - x_r(t)) \delta(\mathbf{v} - \mathbf{v}_r(t)), \quad (\text{B.5})$$

$$f_M(x, \mathbf{v}, t) = \sum_{r=1}^N p_r(t) \delta(x - x_r(t)) \delta(\mathbf{v} - \mathbf{v}_r(t)), \quad (\text{B.6})$$

where δ stands for the Dirac function. The marker distribution g is initially chosen uniform in configuration space and pitch angle space:

$$g(x, \mathbf{v}, t = 0) = \frac{3N}{4\pi v_{\max}^3 L}. \quad (\text{B.7})$$

Marker trajectories in phase space and weight evolutions, integrated in time according to a second order scheme in Δt , are given here in normalized code units ($\lambda_{De}, \omega_{pe}, m, -e, n$):

$$\frac{dx}{dt} = v_x = v\xi, \quad (\text{B.8})$$

$$\frac{d\mathbf{v}}{dt} = E\hat{e}_x + \frac{\Delta \mathbf{v}_{\text{coll}}}{\Delta t}, \quad (\text{B.9})$$

$$\frac{dw}{dt} = pEv\xi + \frac{\Delta w_{\text{coll}}}{\Delta t}, \quad (\text{B.10})$$

$$\frac{dp}{dt} = -pEv\xi, \quad (\text{B.11})$$

where $\Delta \mathbf{v}_{\text{coll}}$ accounts for the random motion in velocity space due to collisions, as explained in detail in Sec. 5.9 for electron-ion collisions and Sec. 5.10.1 for electron-electron collisions. Δw_{coll} corresponds to the background reaction algorithm described in Sec. 5.10.2. Eqs. (B.8)-(B.11) are coupled to the Poisson equation:

$$\frac{d^2}{dx^2} \phi(x, t) = e \int \delta f(x, v, \xi, t) d^3v = -\rho(x), \quad (\text{B.12})$$

along with a periodic boundary condition $\phi(0) = \phi(L)$. Eq. (B.12) is solved by making use of a finite element method. In the frame of the δf PIC approach, the Poisson equation for electrons

reads in normalized units:

$$\frac{d^2\phi(x,t)}{dx^2} = -\sum_{r=1}^N w_r(t)\delta(x-x_r(t)). \quad (\text{B.13})$$

A regular grid of size $n_{mesh} + 1$ is introduced in configuration space and the potential is represented by a set of linear spline functions Λ_i , as shown in Figure B.1:

$$\phi(x,t) = \sum_{i=0}^{n_{mesh}} \phi_i(t)\Lambda_i(x). \quad (\text{B.14})$$

The Poisson equation becomes, making use of Eq. (B.14) in Eq. (B.13):

$$\sum_{i=0}^{n_{mesh}} \phi_i(t) \frac{d^2\Lambda_i}{dx^2} = -\sum_{r=1}^N w_r(t)\delta(x-x_r(t)). \quad (\text{B.15})$$

In order to use the finite element method of Galerkin, the system is multiplied by a test function $-\Lambda_j$ and is integrated over the whole space. It gives:

$$\begin{aligned} -\sum_{i=0}^{n_{mesh}} \phi_i(t) \int_0^L \frac{d^2\Lambda_i}{dx^2} \Lambda_j dx &= \sum_{i=0}^{n_{mesh}} \phi_i(t) \int_0^L \frac{d\Lambda_i}{dx} \frac{d\Lambda_j}{dx} dx \\ &= \sum_{r=1}^N w_r(t) \int_0^L \delta(x-x_r(t)) \Lambda_j(x) dx, \end{aligned} \quad (\text{B.16})$$

since the boundary term vanishes due to the periodic boundary condition. Eq. (B.16) is a linear system $\sum_{i=0}^{n_{mesh}} D_{ij} \phi_i = R_j$, with:

$$D_{ij} = \int \Lambda_i'(x) \Lambda_j'(x) dx, \quad (\text{B.17})$$

$$R_j = \sum_{r=1}^N w_r(t) \Lambda_j(x_r(t)), \quad (\text{B.18})$$

the notation $'$ standing for the x -derivative. The solvability condition $\int_0^L \rho(x) dx = -d\phi/dx|_0^L = 0 \implies \sum_{j=0}^{n_{mesh}} R_j = 0$, along with the periodic boundary condition, allows to choose $\phi_0 = \phi_{n_{mesh}} = 0$. The system is thus reduced to $n_{mesh} - 1$ unknown values $\phi_i, i = 1, \dots, n_{mesh} - 1$.

Building the charge density given by Eq. (B.18) is called the charge assignment. Let us write $\Delta x = L/n_{mesh}$ the width of each bin. The left and right borders of the bin i are the mesh points $i - 1$ and i respectively. The marker r in the bin i contributes to the elements R_i and R_{i-1} , relatively to its position in the bin. Namely, the fraction $|x_r(t) - x_{i-1}|/\Delta x$ of the marker charge is assigned to the element R_i , while the fraction $|x_r(t) - x_i|/\Delta x$ of the marker charge is assigned to the element R_{i-1} . At the end of the charge assignment, the charge density has been distributed over the splines.

Related to the LHS of the Poisson equation, the matrix D is symmetric and tri-diagonal, due to the linear order of the splines: On each interval, two splines overlap each other. The matrix

elements are explicitly computed as follows:

$$D_{ii} = \int_0^{\Delta x} \frac{1}{\Delta x^2} dx + \int_{\Delta x}^{2\Delta x} \frac{1}{\Delta x^2} dx = \frac{2}{\Delta x}, \quad (\text{B.19})$$

$$D_{i,i+1} = D_{i+1,i} = D_{i-1,i} = D_{i,i-1} = - \int_0^{\Delta x} \frac{1}{\Delta x^2} dx = -\frac{1}{\Delta x}. \quad (\text{B.20})$$

The other elements vanish. Note that the matrix D is time-independent and is thus built once at the beginning of the simulation, unlike the charge assignment which is performed at each time step. The described linear system is solved numerically in order to provide the potential $\phi(x, t)$. The corresponding electric field $E(x, t) = -d\phi/dx = -\sum_{i=0}^{n_{mesh}} \phi_i(t) d\Lambda_i/dx$ is used in the Fokker-Planck equation (B.2).

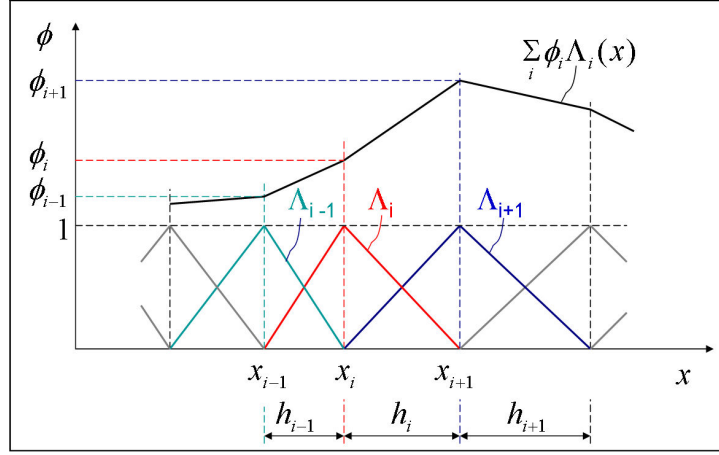


Figure B.1: Illustration of the finite element method with linear splines. In BIRDIE, an equidistant mesh is considered: $h_i = \Delta x \forall i$.

B.2 Linear studies

B.2.1 Analytical considerations

In a linear regime, the collisionless term of order δf^2 is dropped out, giving the following equation to solve:

$$\frac{\partial \delta f}{\partial t} + v_x \frac{\partial \delta f}{\partial x} + \nu_{ei}(v) \hat{L}^2 \delta f + C[f_M, \delta f] = \frac{e}{m} \mathbf{E} \cdot \frac{\partial f_M}{\partial \mathbf{v}} - C[\delta f, f_M]. \quad (\text{B.21})$$

In BIRDIE, it means practically to replace Eq. (B.9) and Eq. (B.11) by $d\mathbf{v}/dt = \Delta \mathbf{v}_{\text{coll}}/\Delta t$ and $dp/dt = 0$ respectively. A study of the collisional linear damping rate of a Langmuir wave is presented in this work. The mode $k\lambda_{De} = 0.3$ is chosen, where k is the wavenumber of the perturbation. The system size is chosen as $L = 2\pi/k$. The initial perturbation is loaded as follows:

$$\delta f(x, v, \xi, t = 0) = \alpha \cos(kx) f_M(v), \quad (\text{B.22})$$

where $\alpha = \delta n/n \ll 1$ is the perturbation parameter. A typical initial perturbation is shown in Figure B.2 (a). The perturbation (B.22) is damped by Landau wave-particle interaction, at a rate strongly affected by collisions. Although an analytical model for the damping rate accounting for self-collisions does not exist, it is possible to derive analytical values of the damping rate assuming a Lorentz model, i.e. neglecting self-collisions and retaining only the pitch angle scattering of electrons off the ions. The perturbation δf is decomposed into a sum of Legendre polynomials P_l :

$$\delta f(x, v, \xi, t) = \sum_l P_l(\xi) c_l(v, t) e^{ikx} = \delta f_k(v, \xi, t) e^{ikx}, \quad (\text{B.23})$$

where the Legendre polynomials are solutions of the following differential equation:

$$\frac{d}{d\xi} \left[(1 - \xi^2) \frac{d}{d\xi} P_l(\xi) \right] + l(l+1) P_l(\xi) = 0, \quad (\text{B.24})$$

and are thus eigenfunctions of the Lorentz operator:

$$\hat{L}^2 P_l(\xi) = l(l+1) P_l(\xi). \quad (\text{B.25})$$

Moreover, the Legendre polynomials satisfy an important orthogonality property:

$$\int_{-1}^1 P_l(\xi) P_{l'}(\xi) d\xi = \frac{2}{2l+1} \delta_{ll'}. \quad (\text{B.26})$$

Using Eq. (B.23) in order to write the Fokker-Planck equation (B.21) in x -Fourier space and neglecting self-collisions leads to:

$$\frac{\partial \delta f_k}{\partial t} + ikv \xi \delta f_k - \frac{e}{m} E_k \xi \frac{\partial f_M}{\partial v} = -\nu(v) \hat{L}^2 \delta f_k. \quad (\text{B.27})$$

The recurrence relation for the Legendre polynomials reads:

$$(l+1) P_{l+1} = (2l+1) \xi P_l - l P_{l-1}, \quad (\text{B.28})$$

Combining Eqs. (B.23) and (B.28) gives:

$$\xi \delta f_k = \sum_l c_l \left(\frac{l+1}{2l+1} P_{l+1} + \frac{l}{2l+1} P_{l-1} \right). \quad (\text{B.29})$$

Eq. (B.27) thus becomes, according to (B.29):

$$\frac{\partial \delta f_k}{\partial t} + ikv \sum_{l'} c_{l'} \left(\frac{l'+1}{2l'+1} P_{l'+1} + \frac{l'}{2l'+1} P_{l'-1} \right) - \frac{e}{m} E_k \underbrace{P_1(\xi)}_{\xi} \frac{\partial f_M}{\partial v} = -\nu(v) \hat{L}^2 \delta f_k. \quad (\text{B.30})$$

$\int_{-1}^1 d\xi P_l/2$ is applied to both sides of Eq. (B.30). It follows from the decomposition (B.23), the orthogonality property (B.26) and the Lorentz operator applied to Legendre polynomials (B.25):

$$\frac{1}{2l+1} \frac{\partial c_l}{\partial t} + ikv \left(c_{l-1} \frac{l}{2l-1} \frac{1}{2l+1} + c_{l+1} \frac{l+1}{2l+3} \frac{1}{2l+1} \right) - \frac{e}{3m} E_k \frac{\partial f_M}{\partial v} \delta_{l,1} = -\frac{\nu_l(v)}{2l+1} c_l, \quad (\text{B.31})$$

where $\nu_l(v) = \nu(v)l(l+1)$. The following system is obtained:

$$l = 0 \quad \frac{\partial c_0}{\partial t} + \frac{ikv}{3} c_1 = 0. \quad (\text{B.32})$$

$$l = 1 \quad \frac{\partial c_1}{\partial t} + ikv \left(c_0 + \frac{2}{5} c_2 \right) - \frac{e}{m} E_k \frac{\partial f_M}{\partial v} = -\nu_1(v) c_1. \quad (\text{B.33})$$

$$l = 2 \quad \frac{\partial c_2}{\partial t} + ikv \left(\frac{2}{3} c_1 + \frac{3}{7} c_3 \right) = -\nu_2(v) c_2. \quad (\text{B.34})$$

$$l > 2 \quad \frac{\partial c_l}{\partial t} + ikv \left(\frac{l}{2l-1} c_{l-1} + \frac{l+1}{2l+3} c_{l+1} \right) = -\nu_l(v) c_l. \quad (\text{B.35})$$

The system (B.32)-(B.35) for $l = 0, 1, \dots, l_{\max} = 10$ is solved numerically by introducing a velocity mesh, providing the time evolution of the Legendre coefficients c_l . The time evolution of the electric field is given by the Poisson equation in Fourier space:

$$\begin{aligned} \frac{E_k(t)}{e} &= \frac{i}{k} \int \delta f_k(v, \xi, t) d^3v = \frac{i2\pi}{k} \int \sum_l c_l(v, t) P_l(\xi) v^2 dv d\xi \\ &= \frac{i2\pi}{k} \int_0^\infty c_0(v, t) v^2 dv \underbrace{\int_{-1}^1 P_0(\xi) d\xi}_2 \simeq \frac{i4\pi\Delta v}{k} \sum_{j=0}^{N_v} (j\Delta v)^2 c_0(j\Delta v, t), \end{aligned} \quad (\text{B.36})$$

where an artificial cut-off is introduced at $v = 7v_{th}$ by the discretization of the velocity space, $\Delta v = 7v_{th}/N_v$ being the mesh width. The evolution in time of the electric field $E_k(t)$, linked to the evolution in time of the coefficient c_0 according to Eq. (B.36), provides the analytical real frequency and growth rate of the Langmuir wave, which may be compared to BIRDIE predictions.

B.2.2 Linear benchmark

The potential amplitude is defined as:

$$|\phi|(t) = \sqrt{\frac{2}{L} \int |\phi(x, t) - \langle \phi \rangle(t)|^2 dx} = \sqrt{\frac{2 \sum_{i=0}^{n_{mesh}} (\phi_i(t) - \langle \phi \rangle(t))^2}{(n_{mesh} + 1)}}, \quad (\text{B.37})$$

where n_{mesh} is the number of intervals related to the Poisson grid and where:

$$\langle \phi \rangle(t) = \frac{1}{L} \int_0^L \phi(x, t) dx. \quad (\text{B.38})$$

In the linear phase of the simulation, the potential amplitude reads:

$$|\phi|(t) = |\phi_0|e^{-\gamma t}|\cos(\omega t)|, \quad (\text{B.39})$$

where ω is the real part of the frequency and $\gamma > 0$ the imaginary part. The results of the analytical approach described in Sec. B.2.1 are found to match well BIRDIE's damping rates. Figure B.2 (b) shows how the collisionality increases the damping rate. Results from BIRDIE are compared to analytical predictions for the Lorentz model (electron-ion collisions only) using Eq. (B.36), as well as benchmarked against results from a fluid code for the full linearized collision operator. Note that the real frequency of the mode $k\lambda_{De} = 0.3$ is found to be $\omega \simeq 1.16 \omega_{pe}$ and is not significantly affected by collisions.

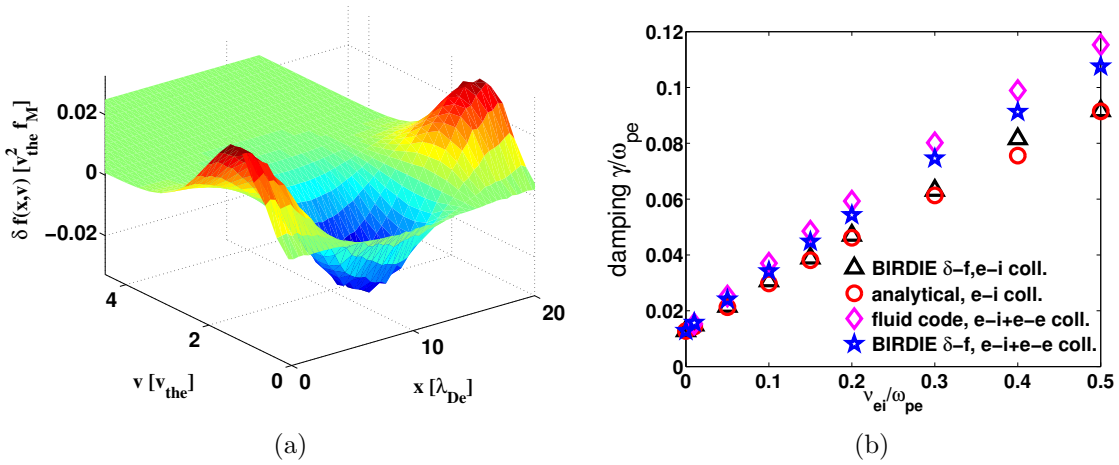


Figure B.2: (a) Typical initial perturbation $\delta f(t=0)$ in the (x, v) space. (b) $k\lambda_{De} = 0.3$. BIRDIE predictions for linear damping rates are successfully benchmarked against analytical estimates for the Lorentz model and numerical results from a fluid code for the full linearized electron collision operator. The linear Landau damping rate of a Langmuir wave is increased by electron collisions.

B.2.3 Convergence studies

The typical numerical parameters used to obtain linear results are $\Delta t = 0.005\omega_{pe}^{-1}$, $n_{\text{mesh}} = 100$, $N = 600'000$. These parameters are checked to be converged in Figure B.3 showing the collisionless linear damping rate of the mode $k\lambda_{De} = 0.3$ for different numerical parameters.

B.3 Non-linear studies

In the non-linear regime, the full Fokker-Planck equation (B.4) is solved. The non-linear term gives rise to a new and complex physics related to the Langmuir wave which is not addressed in detail here. Note that the simple case considered by the code BIRDIE, i.e. a homogeneous and unmagnetized plasma, already features a high complexity through the non-linearity of the Fokker-Planck (or Vlasov) equation. A thorough description of non-linear phenomena in the frame of the Langmuir wave physics is given in Ref. [39]. Typical numerical parameters for

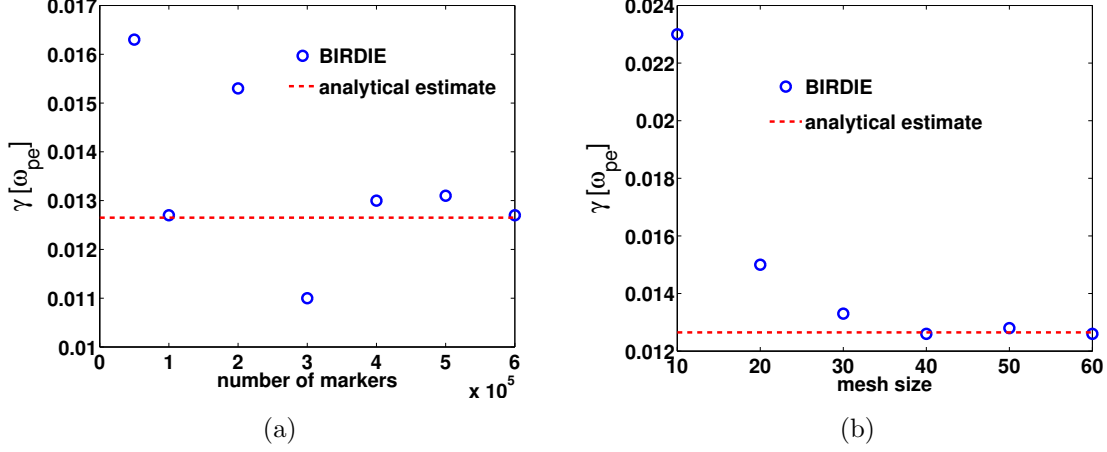


Figure B.3: Collisionless linear damping rate of the mode $k\lambda_{De} = 0.3$. BIRDIE convergence studies with respect to (a) the number of markers ($\Delta t = 0.005\omega_{pe}^{-1}$, $n_{\text{mesh}} = 100$) and (b) the mesh size in configuration space ($\Delta t = 0.005\omega_{pe}^{-1}$, $N = 600'000$).

non-linear runs are $\Delta t = 0.005\omega_{pe}^{-1}$, $n_{\text{mesh}} = 100$ and $N = 10 \times 10^6$. The considered mode is $k\lambda_{De} = 0.3$.

B.3.1 Energy conservation

The averaged energy density in BIRDIE is defined as follows:

$$\langle E \rangle(t) = \underbrace{\frac{m}{2L} \int \delta f(x, v, \xi, t) v^2 dx dv^3}_{\langle E_{kin} \rangle} + \underbrace{\frac{1}{2L} \int \rho(x, t) \phi(x, t) dx}_{\langle E_{pot} \rangle}, \quad (\text{B.40})$$

where $\rho(x, t)$ is the charge density. Making use of the Fokker-Planck equation (B.2) and using the energy conservation properties of both the Lorentz collision operator and the self-collision operator (as detailed in Sec. 5.5), the conservation of the total energy may be derived:

$$\frac{d\langle E_{kin} \rangle}{dt} = -\frac{d\langle E_{pot} \rangle}{dt}. \quad (\text{B.41})$$

The conservation property (B.41) is numerically checked in Figure B.4 (a) for $k\lambda_{De} = 0.3$, $\delta n/n = 0.05$ and no collisions. Note that the energy conservation is not ensured in linear simulations which drop the non-linear term $\sim \mathbf{E} \cdot \partial \delta f / \partial \mathbf{v}$ in Eq. (B.4).

B.3.2 Collisionless entropy conservation

The entropy production is defined in BIRDIE as:

$$\langle \delta S \rangle = \frac{1}{L} \int \frac{\delta f^2}{f_M} dx dv^3. \quad (\text{B.42})$$

Using the collisionless Vlasov equation [Eq. (B.4) with $C = 0$ and $\hat{L} = 0$], it is possible to show that:

$$\frac{d}{dt} \langle \delta S \rangle = \underbrace{\frac{e}{mL} \int \left[\frac{\delta f^2}{f_M^2} + 2 \frac{\delta f}{f_M} \right] \mathbf{E} \cdot \frac{\partial f_M}{\partial \mathbf{v}} dx d^3 v}_{D_{\text{field}}}. \quad (\text{B.43})$$

The time derivative of the quantity $\langle \delta S \rangle$ given by Eq. (B.42), computed by a finite difference approach, is compared successfully in Figure B.4 (b) to D_{field} , the RHS of Eq. (B.43).

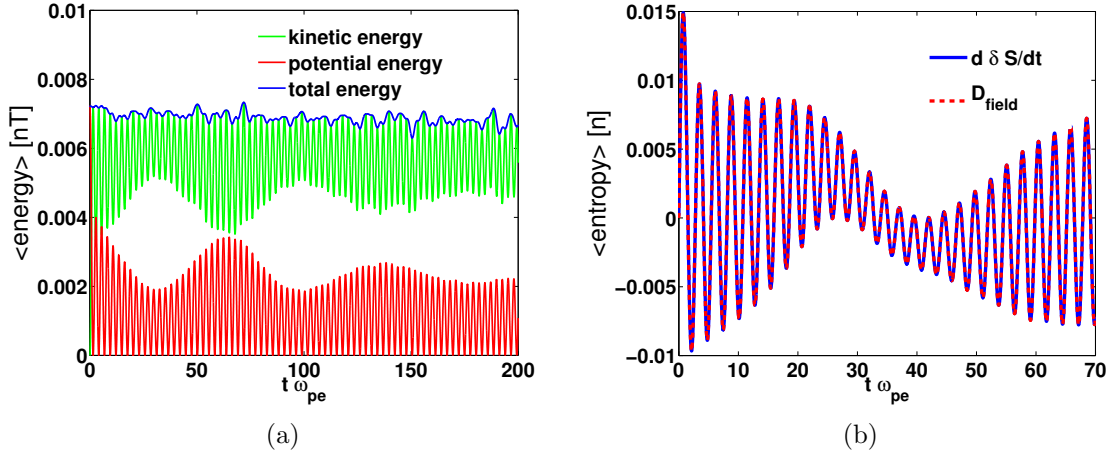


Figure B.4: (a) Exchange between kinetic and potential energy leads to the total energy conservation, as ensured by BIRDIE simulations. (b) Check for the collisionless entropy balance in BIRDIE simulations.

B.3.3 Non-linear evolution of the perturbation

The main non-linear effect affecting the evolution of a Langmuir wave is the trapping of electrons in the electrostatic potential wells. The non-linear interaction between the electron distribution function and the electrostatic Langmuir wave leads to an undamped, finite amplitude mode called a BGK wave. Choosing $\delta n/n = 0.05$ and $k\lambda_{De} = 0.3$, the long time, non-linear evolution of the wave is shown in Figure B.5, for several collisionless and collisional runs accounting for the full linearized electron collision operator. Note that collisions strongly damp the Langmuir waves and prevent the BGK mode from persisting even at moderate collisionality. The initial amplitude of the potential is computed according to the Poisson equation:

$$\frac{e|\phi|(t=0)}{T} = \frac{\delta n(t=0)}{nk^2\lambda_{De}^2} \simeq 0.55. \quad (\text{B.44})$$

It is shown in Ref. [39] that the bounce frequency ω_{be} of electrons trapped in electrostatic wells is related to the plasma frequency as follows:

$$\frac{\omega_{be}}{\omega_{pe}} = \sqrt{k\lambda_{De}} \left(\frac{\langle E_{pot}/t \rangle}{nT} \right)^{1/4}, \quad (\text{B.45})$$

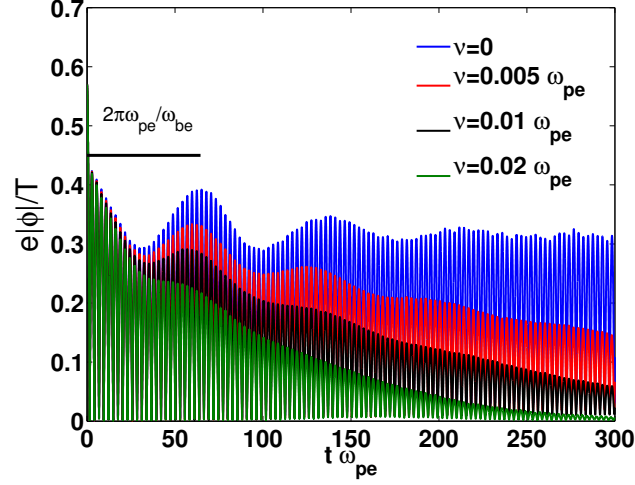


Figure B.5: Collisional effects on the non-linear evolution of the Langmuir wave amplitude. $\delta n/n = 0.05$, $k\lambda_{De} = 0.3$. The BGK modes do not persist even at moderate collisionalities.

where $\langle E_{pot} \rangle_t$ is an estimate of the time-averaged potential energy which may be given by Figure B.4 (a): $\langle E_{pot} \rangle_t/nT \approx 0.001$. Eq. (B.45) gives thus the bounce time $\tau_b\omega_{pe} = 2\pi\omega_{pe}/\omega_{be} \approx 64.5$, corresponding to the time at which a maximum of the non-linear amplitude occurs as shown in Figure B.5.

Bibliography

- [1] J D Lawson. *Proceedings of the Physical Society. Section B*, 70(1):6, 1957.
- [2] J. Nuckolls, L. Wood, A. Thiessen, and G. Zimmermann. *Nature*, 239:139–142, 1972.
- [3] M. Greenwald, J. L. Terry, S. M. Wolfe, S. Ejima, M. G. Bell, S. M. Kaye, and G. H. Neilson. *Nuclear Fusion*, 28(12):2199, 1988.
- [4] A. J. Brizard and T. S. Hahm. *Rev. Mod. Phys.*, 79:421–468, 2007.
- [5] F. Wagner, G. Becker, K. Behringer, D. Campbell, A. Eberhagen, W. Engelhardt, G. Fussmann, O. Gehre, J. Gernhardt, G. v. Gierke, G. Haas, M. Huang, F. Karger, M. Keilhacker, O. Klüber, M. Kornherr, K. Lackner, G. Lisitano, G. G. Lister, H. M. Mayer, D. Meisel, E. R. Müller, H. Murmann, H. Niedermeyer, W. Poschenrieder, H. Rapp, H. Röhr, F. Schneider, G. Siller, E. Speth, A. Stäbler, K. H. Steuer, G. Venus, O. Vollmer, and Z. Yü. *Phys. Rev. Lett.*, 49:1408–1412, 1982.
- [6] C. Mouhot and C. Villani. *Acta Mathematica*, 207:29–201, 2011.
- [7] X. Garbet, Y. Idomura, L. Villard, and T. H. Watanabe. *Nuclear Fusion*, 50(4):043002, 2010.
- [8] M. Kotschenreuther, G. Rewoldt, and W. M. Tang. *Computer Physics Communications*, 88(2-3):128–140, 1995.
- [9] F. Jenko, W. Dorland, M. Kotschenreuther, and B. N. Rogers. *Physics of Plasmas*, 7(5):1904–1910, 2000.
- [10] T. Görler, X. Lapillonne, S. Brunner, T. Dannert, F. Jenko, F. Merz, and D. Told. *Journal of Computational Physics*, 230(18):7053 – 7071, 2011.
- [11] J. Candy and R. E. Waltz. *Journal of Computational Physics*, 186(2):545 – 581, 2003.
- [12] A. G. Peeters, Y. Camenen, F. J. Casson, W. A. Hornsby, A. P. Snodin, D. Strintzi, and G. Szepesi. *Computer Physics Communications*, 180(12):2650 – 2672, 2009.
- [13] Y. Idomura, M. Ida, S. Tokuda, and L. Villard. *Journal of Computational Physics*, 226(1):244 – 262, 2007.
- [14] T. M. Tran, K. Appert, M. Fivaz, G. Jost, J. Vaclavik, and L. Villard. *Theory of Fusion Plasmas, Int. Workshop, Editrice Compositori, Società Italiana di Fisica, Bologna*, 1999.

-
- [15] S. Jolliet, A. Bottino, P. Angelino, R. Hatzky, T.M. Tran, B.F. McMillan, O. Sauter, K. Appert, Y. Idomura, and L. Villard. *Computer Physics Communications*, 177(5):409 – 425, 2007.
 - [16] T. Vernay, S. Brunner, L. Villard, B. F. McMillan, S. Jolliet, T. M. Tran, A. Bottino, and J. P. Graves. *Physics of Plasmas*, 17(12):122301, 2010.
 - [17] Z. Lin, T. S. Hahm, W. W. Lee, W. M. Tang, and R. B. White. *Science*, 281(5384):1835–1837, 1998.
 - [18] G. Jost, T. M. Tran, W. A. Cooper, L. Villard, and K. Appert. *Physics of Plasmas*, 8(7):3321–3333, 2001.
 - [19] V. Grandgirard, Y. Sarazin, P. Angelino, A. Bottino, N. Crouseilles, G. Darinet, G. Dif-Pradalier, X. Garbet, Ph. Ghendrih, S. Jolliet, G. Latu, E. Sonnendrücker, and L. Villard. *Plasma Physics and Controlled Fusion*, 49(12B):B173, 2007.
 - [20] S. Brunner, E. Valeo, and J. A. Krommes. *Physics of Plasmas*, 6(12):4504–4521, 1999.
 - [21] G. Hu and J. A. Krommes. *Physics of Plasmas*, 1(4):863–874, 1994.
 - [22] Y. Chen and S. E. Parker. *Physics of Plasmas*, 14(8):082301, 2007.
 - [23] Z. Lin, T. S. Hahm, W. W. Lee, W. M. Tang, and P. H. Diamond. *Phys. Rev. Lett.*, 83(18):3645–3648, 1999.
 - [24] G. Dif-Pradalier, V. Grandgirard, Y. Sarazin, X. Garbet, and Ph. Ghendrih. *Phys. Rev. Lett.*, 103:065002, 2009.
 - [25] P. H. Diamond, S.-I. Itoh, K. Itoh, and T. S. Hahm. *Plasma Physics and Controlled Fusion*, 47(5):R35, 2005.
 - [26] T. Vernay, S. Brunner, L. Villard, B. F. McMillan, S. Jolliet, T. M. Tran, and A. Bottino. *Physics of Plasmas*, 19(4):042301, 2012.
 - [27] T. Dannert and F. Jenko. *Physics of Plasmas*, 12(7):072309, 2005.
 - [28] F. Merz and F. Jenko. *Phys. Rev. Lett.*, 100:035005, 2008.
 - [29] D. R. Ernst, J. Lang, W. M. Nevins, M. Hoffman, Y. Chen, W. Dorland, and S. Parker. *Physics of Plasmas*, 16(5):055906, 2009.
 - [30] T. Vernay, S. Brunner, L. Villard, B. F. McMillan, S. Jolliet, A. Bottino, T. Görler, and F. Jenko. *submitted to Plasma Physics and Controlled Fusion (Varennna Workshop)*, 2012.
 - [31] A. Bottino, B. Scott, S. Brunner, B. F. McMillan, T. M. Tran, T. Vernay, L. Villard, S. Jolliet, R. Hatzky, and A. G. Peeters. *Plasma Science, IEEE Transactions on*, 38(9):2129 –2135, 2010.
-

- [32] H. Lütjens, A. Bondeson, and O. Sauter. *Computer Physics Communications*, 97(3):219 – 260, 1996.
- [33] R. A. Pitts, R. J. Buttery, and S. D. Pinches. *Physics World*, 19:20, 2006.
- [34] S. Brunner. *Global Approach to the Spectral Problem of Microinstabilities in Tokamak Plasmas Using a Gyrokinetic Model*. PhD thesis, Ecole polytechnique fédérale de Lausanne, 1997.
- [35] W. Horton. *Rev. Mod. Phys.*, 71:735–778, 1999.
- [36] Jr. W. Horton, D. I. Choi, and W. M. Tang. *Physics of Fluids*, 24(6):1077–1085, 1981.
- [37] A. Bottino. *Modelling of Global Microinstabilities in Tokamaks: Effects of ExB Flow and Magnetic Shear*. PhD thesis, Ecole polytechnique fédérale de Lausanne, 2004.
- [38] P. J. Catto. *Plasma Physics*, 20(7):719, 1978.
- [39] S. Brunner. *Lectures: Waves and Instabilities in Inhomogeneous Plasmas*. Ecole doctorale EPFL.
- [40] F. Romanelli and S. Briguglio. *Physics of Fluids B: Plasma Physics*, 2(4):754–763, 1990.
- [41] K. Miyamoto. *Plasma Physics for Nuclear Fusion*. The MIT Press, 1976.
- [42] S. I. Braginskii. *Reviews of plasma physics*, 1, 1965.
- [43] F. L. Hinton and R. D. Hazeltine. *Rev. Mod. Phys.*, 48(2):239–308, 1976.
- [44] P. Helander and D. J. Sigmar. *Collisional Transport in Magnetized Plasmas*. Cambridge University Press, 2002.
- [45] D. Bohm. *The characteristics of electrical discharges in magnetic fields*. ed A. Guthrie and R. K. Wakerling (New York: McGraw-Hill), 1949.
- [46] S. E. Parker, H. E. Mynick, M. Artun, J. C. Cummings, V. Decyk, J. V. Kepner, W. W. Lee, and W. M. Tang. *Physics of Plasmas*, 3(5):1959–1966, 1996.
- [47] P. Angelino, A. Bottino, R. Hatzky, S. Jolliet, O. Sauter, T. M. Tran, and L. Villard. *Physics of Plasmas*, 13(5):052304, 2006.
- [48] B. F. McMillan, S. Jolliet, A. Bottino, P. Angelino, T. M. Tran, and L. Villard. *Computer Physics Communications*, 181(4):715 – 719, 2010.
- [49] B. F. McMillan, S. Jolliet, T. M. Tran, L. Villard, A. Bottino, and P. Angelino. *Physics of Plasmas*, 15(5):052308, 2008.
- [50] P. Angelino. *The Role of the Electric Field in Simulations of Plasma Microturbulence*. PhD thesis, Ecole polytechnique fédérale de Lausanne, 2006.

-
- [51] S. Jolliet. *Gyrokinetic Particle-In-Cell Global Simulations of Ion-Temperature-Gradient and Collisionless-Trapped-Electron-Mode Turbulence in Tokamaks*. PhD thesis, Ecole polytechnique fédérale de Lausanne, 2009.
 - [52] L. Villard, A. Bottino, O. Sauter, and J. Vaclavik. *Physics of Plasmas*, 9(6):2684–2691, 2002.
 - [53] L. Villard, S. J. Allfrey, A. Bottino, M. Brunetti, G. L. Falchetto, V. Grandgirard, R. Hatzky, J. Nührenberg, A. G. Peeters, O. Sauter, S. Sorge, and J. Vaclavik. *Nuclear Fusion*, 44(1):172, 2004.
 - [54] L. Villard, P. Angelino, A. Bottino, S. J. Allfrey, R. Hatzky, Y. Idomura, O. Sauter, and T. M. Tran. *Plasma Physics and Controlled Fusion*, 46(12B):B51, 2004.
 - [55] P. Angelino, A. Bottino, R. Hatzky, S. Jolliet, O. Sauter, T. M. Tran, and L. Villard. *Plasma Physics and Controlled Fusion*, 48(5):557, 2006.
 - [56] P. Angelino, X. Garbet, L. Villard, A. Bottino, S. Jolliet, Ph. Ghendrih, V. Grandgirard, B. F. McMillan, Y. Sarazin, G. Dif-Pradalier, and T. M. Tran. *Phys. Rev. Lett.*, 102:195002, 2009.
 - [57] S. Jolliet, B. F. McMillan, T. Vernay, L. Villard, A. Bottino, and P. Angelino. *Physics of Plasmas*, 16(5):052307, 2009.
 - [58] B. F. McMillan, X. Lapillonne, S. Brunner, L. Villard, S. Jolliet, A. Bottino, T. Görler, and F. Jenko. *Phys. Rev. Lett.*, 105:155001, 2010.
 - [59] S. Jolliet, B. F. McMillan, T. Vernay, L. Villard, R. Hatzky, A. Bottino, and P. Angelino. *Physics of Plasmas*, 16(7):072309, 2009.
 - [60] A. Bottino, A. G. Peeters, O. Sauter, J. Vaclavik, L. Villard, and ASDEX Upgrade Team. *Physics of Plasmas*, 11(1):198–206, 2004.
 - [61] A. Bottino, O. Sauter, Y. Camenen, and E. Fable. *Plasma Physics and Controlled Fusion*, 48(2):215, 2006.
 - [62] B. F. McMillan, P. Hill, A. Bottino, S. Jolliet, T. Vernay, and L. Villard. *Physics of Plasmas*, 18(11):112503, 2011.
 - [63] A. Bottino, T. Vernay, B. Scott, S. Brunner, R. Hatzky, S. Jolliet, B. F. McMillan, T. M. Tran, and L. Villard. *Plasma Physics and Controlled Fusion*, 53(12):124027, 2011.
 - [64] R. G. Littlejohn. *Journal of Plasma Physics*, 29(01):111–125, 1983.
 - [65] J. R. Cary and A. J. Brizard. *Rev. Mod. Phys.*, 81:693–738, 2009.
 - [66] A. M. Dimits, L. L. LoDestro, and D. H. E. Dubin. *Physics of Fluids B: Plasma Physics*, 4(1):274–277, 1992.
-

- [67] J. R. Cary and R. G. Littlejohn. *Annals of Physics*, 151(1):1–34, 1983.
- [68] W. Dorland and G. W. Hammett. *Physics of Fluids B: Plasma Physics*, 5(3):812–835, 1993.
- [69] A. Mishchenko, A. Könies, and R. Hatzky. *Physics of Plasmas*, 12(6):062305, 2005.
- [70] A. M. Dimits, G. Bateman, M. A. Beer, B. I. Cohen, W. Dorland, G. W. Hammett, C. Kim, J. E. Kinsey, M. Kotschenreuther, A. H. Kritz, L. L. Lao, J. Mandrekas, W. M. Nevins, S. E. Parker, A. J. Redd, D. E. Shumaker, R. Sydora, and J. Weiland. *Physics of Plasmas*, 7(3):969–983, 2000.
- [71] P. Helander. *Plasma Physics and Controlled Fusion*, 37(1):57, 1995.
- [72] G. Dif-Pradalier, P. H. Diamond, V. Grandgirard, Y. Sarazin, J. Abiteboul, X. Garbet, Ph. Ghendrih, A. Strugarek, S. Ku, and C. S. Chang. *Phys. Rev. E*, 82:025401, 2010.
- [73] O. Sauter, C. Angioni, and Y. R. Lin-Liu. *Physics of Plasmas*, 6(7):2834–2839, 1999.
- [74] S. E. Parker and W. W. Lee. *Physics of Fluids B: Plasma Physics*, 5(1):77–86, 1993.
- [75] T. S. Hahm. *Physics of Fluids*, 31(9):2670–2673, 1988.
- [76] A. Y. Aydemir. *Physics of Plasmas*, 1(4):822–831, 1994.
- [77] S. J. Allfrey and R. Hatzky. *Computer Physics Communications*, 154, 2003.
- [78] Y. Chen and R. B. White. *Physics of Plasmas*, 4(10):3591–3598, 1997.
- [79] A. Bottino, A. G. Peeters, R. Hatzky, S. Jolliet, B. F. McMillan, T. M. Tran, and L. Villard. *Physics of Plasmas*, 14(1):010701, 2007.
- [80] Y. Idomura, S. Tokuda, and Y. Kishimoto. *Nuclear Fusion*, 43(4):234, 2003.
- [81] W. W. Lee. *Journal of Computational Physics*, 72(1):243 – 269, 1987.
- [82] I. G. Abel, M. Barnes, S. C. Cowley, W. Dorland, and A. A. Schekochihin. *Physics of Plasmas*, 15(12):122509, 2008.
- [83] A. J. Brizard, J. Decker, Y. Peysson, and F.-X. Duthoit. *Physics of Plasmas*, 16(10):102304, 2009.
- [84] M. N. Rosenbluth, W. M. MacDonald, and D. L. Judd. *Phys. Rev.*, 107:1–6, 1957.
- [85] Z. Lin, W. M. Tang, and W. W. Lee. *Physics of Plasmas*, 2(8):2975–2988, 1995.
- [86] T. Takizuka and H. Abe. *Journal of Computational Physics*, 25(3):205 – 219, 1977.
- [87] A. M. Dimits and B. I. Cohen. *Phys. Rev. E*, 49:709–721, 1994.
- [88] S. Satake, R. Kanno, and H. Sugama. *Plasma Fusion res.*, 3(S1062), 2008.

-
- [89] L. Spitzer and R. Härm. *Phys. Rev.*, 89(5):977–981, 1953.
 - [90] C. Angioni and O. Sauter. *Physics of Plasmas*, 7(4):1224–1234, 2000.
 - [91] E. A. Belli and J. Candy. *THEORY OF FUSION PLASMAS*, 1069(1):15–26, 2008.
 - [92] W. X. Wang, N. Nakajima, M. Okamoto, and S. Murakami. *Plasma Physics and Controlled Fusion*, 41(9):1091, 1999.
 - [93] W. X. Wang, F. L. Hinton, and S. K. Wong. *Phys. Rev. Lett.*, 87(5):055002, 2001.
 - [94] W. X. Wang, G. Rewoldt, W. M. Tang, F. L. Hinton, J. Manickam, L. E. Zakharov, R. B. White, and S. Kaye. *Physics of Plasmas*, 13(8):082501, 2006.
 - [95] Y. Idomura, H. Urano, N. Aiba, and S. Tokuda. *Nuclear Fusion*, 49(6):065029, 2009.
 - [96] X. Garbet, G. Dif-Pradalier, C. Nguyen, Y. Sarazin, V. Grandgirard, and Ph. Ghendrih. *Physics of Plasmas*, 16(6):062503, 2009.
 - [97] N. Winsor, J. L. Johnson, and J. M. Dawson. *Physics of Fluids*, 11(11):2448–2450, 1968.
 - [98] M. N. Rosenbluth and F. L. Hinton. *Phys. Rev. Lett.*, 80(4):724–727, 1998.
 - [99] F. L. Hinton and M. N. Rosenbluth. *Plasma Physics and Controlled Fusion*, 41(3A):A653, 1999.
 - [100] H. Sugama and T.-H. Watanabe. *Journal of Plasma Physics*, 72(06):825–828, 2006.
 - [101] K. Itoh, K. Hallatschek, and S.-I. Itoh. *Plasma Physics and Controlled Fusion*, 47(3):451, 2005.
 - [102] S. Satake, Y. Idomura, H. Sugama, and T. H. Watanabe. *Computer Physics Communications*, 181:1069–1076, 2010.
 - [103] C. S. Chang and F. L. Hinton. *Physics of Fluids*, 25(9):1493–1494, 1982.
 - [104] S. P. Hirshman and D. J. Sigmar. *Nuclear Fusion*, 21(6):001079, 1981.
 - [105] K. C. Shaing and R. D. Hazeltine. *Physics of Fluids B: Plasma Physics*, 4(8):2547–2551, 1992.
 - [106] P. Helander. *Physics of Plasmas*, 7(7):2878–2883, 2000.
 - [107] Z. Lin, W. M. Tang, and W. W. Lee. *Physics of Plasmas*, 4:1707, 1997.
 - [108] S. Satake, M. Okamoto, and H. Sugama. *Physics of Plasmas*, 9(9):3946–3960, 2002.
 - [109] A. Bergmann, A. G. Peeters, and S. D. Pinches. *Physics of Plasmas*, 8(12):5192–5198, 2001.
 - [110] R. E. Waltz, R. L. Dewar, and X. Garbet. *Physics of Plasmas*, 5(5):1784–1792, 1998.
-

- [111] R. E. Waltz, J. Candy, F. L. Hinton, C. Estrada-Mila, and J. E. Kinsey. *Nuclear Fusion*, 45(7):741, 2005.
- [112] P. Ricci, B. N. Rogers, and W. Dorland. *Phys. Rev. Lett.*, 97:245001, 2006.
- [113] B. N. Rogers, W. Dorland, and M. Kotschenreuther. *Phys. Rev. Lett.*, 85:5336–5339, 2000.
- [114] D. R. Mikkelsen and W. Dorland. *Phys. Rev. Lett.*, 101:135003, 2008.
- [115] S. Jolliet and Y. Idomura. *Nuclear Fusion*, 52(2):023026, 2012.
- [116] T. S. Hahm. *Physics of Plasmas*, 1(9):2940–2944, 1994.
- [117] P. H. Diamond, Y.-M. Liang, B. A. Carreras, and P. W. Terry. *Phys. Rev. Lett.*, 72:2565–2568, 1994.
- [118] S. J. Allfrey, A. Bottino, O. Sauter, and L. Villard. *New Journal of Physics*, 4(1):29, 2002.
- [119] A. Burckel, O. Sauter, C. Angioni, J. Candy, E. Fable, and X. Lapillonne. *Journal of Physics: Conference Series*, 260(1):012006, 2010.
- [120] G. L. Falchetto, J. Vaclavik, and L. Villard. *Physics of Plasmas*, 10(5):1424–1436, 2003.
- [121] R. E. Waltz, M. E. Austin, K. H. Burrell, and J. Candy. *Physics of Plasmas*, 13(5):052301, 2006.
- [122] J. Chowdhury, R. Ganesh, P. Angelino, J. Vaclavik, L. Villard, and S. Brunner. *Physics of Plasmas*, 15(7):072117, 2008.
- [123] Y. Xiao, I. Holod, W. Zhang, S. Klasky, and Z. Lin. *Physics of Plasmas*, 17(2):022302, 2010.
- [124] J. Lang, S. E. Parker, and Y. Chen. *Physics of Plasmas*, 15(5):055907, 2008.
- [125] Y. Xiao and Z. Lin. *Phys. Rev. Lett.*, 103:085004, 2009.
- [126] F. Hofmann, J. B. Lister, W. Anton, S. Barry, R. Behn, S. Bernel, G. Besson, F. Buhlmann, R. Chavan, M. Corboz, M. J. Dutch, B. P. Duval, D. Fasel, A. Favre, S. Franke, A. Heym, A. Hirt, C. Hollenstein, P. Isoz, B. Joye, X. Llobet, J. C. Magnin, B. Marletaz, P. Marmillod, Y. Martin, J. M. Mayor, J. M. Moret, C. Nieswand, P. J. Paris, A. Perez, Z. A. Pietrzyk, R. A. Pitts, A. Pochelon, R. Rage, O. Sauter, G. Tonetti, M. Q. Tran, F. Troyon, D. J. Ward, and H. Weisen. *Plasma Physics and Controlled Fusion*, 36(12B):B277, 1994.
- [127] Z. Lin, S. Ethier, T. S. Hahm, and W. M. Tang. *Phys. Rev. Lett.*, 88:195004, 2002.
- [128] J. Candy, R. E. Waltz, and W. Dorland. *Physics of Plasmas*, 11(5):L25–L28, 2004.

- [129] F. Romanelli and F. Zonca. *Physics of Fluids B: Plasma Physics*, 5(11):4081–4089, 1993.
- [130] S. Brunner, M. Fivaz, T. M. Tran, and J. Vaclavik. *Physics of Plasmas*, 5(11):3929–3949, 1998.
- [131] R. E. Waltz, J. M. Candy, and M. N. Rosenbluth. *Physics of Plasmas*, 9(5):1938–1946, 2002.
- [132] J. Lang, Y. Chen, and S. E. Parker. *Physics of Plasmas*, 14(8):082315, 2007.
- [133] K. de Meijere. *An experimental study of plasma fluctuations in the TCV and TEXTOR tokamaks*. PhD thesis, Ecole polytechnique fédérale de Lausanne, 2012.
- [134] L. Villard, P. Angelino, A. Bottino, S. Brunner, S. Jolliet, B. F. McMillan, T. M. Tran, and T. Vernay. *submitted to Plasma Physics and Controlled Fusion (Varennna Workshop)*, 2012.
- [135] E. Fable, C. Angioni, and O. Sauter. *Plasma Physics and Controlled Fusion*, 52(1):015007, 2010.
- [136] H. Sugama, T. H. Watanabe, and M. Nunami. *National Institute for Fusion Science*, Research report 955, 2009.

Remerciements

Ecrire une thèse, en particulier portant sur la physique des plasmas, constitue une aventure au long cours qui nécessite de nombreux soutiens extérieurs afin d'être menée à terme.

Je voudrais commencer par remercier mes deux directeurs de thèse, Stephan Brunner et Laurent Villard, dont l'aide et les apports aussi bien humains que scientifiques furent manifestement essentiels durant mon travail au CRPP.

Je pourrais faire bref en mentionnant simplement que Stephan est le meilleur physicien que j'aie jamais rencontré. Mais ce serait omettre sa disponibilité et son enthousiasme à transmettre ses vastes connaissances concernant la physique des plasmas. Tout au long de ces années, il a systématiquement guidé mes pas dans la bonne direction, en expérimenté capitaine de voilier. Stephan, un grand merci pour les heures interminables que tu as passées à corriger mes écrits scientifiques manquant parfois de la rigueur nécessaire, à m'orienter dans mon travail, à m'apprendre à programmer proprement ou à m'aider à mieux comprendre les subtilités de la gyrocinétique.

Un grand merci à Laurent d'avoir amorcé ce projet de thèse, de m'avoir soutenu constamment dans mes péripéties numériques et d'avoir partagé ses nombreuses et bonnes idées sur les pistes à explorer. Il a aussi passé beaucoup de temps à chasser le temps de calcul sur divers ordinateurs aux quatre coins du globe, afin que j'aie toujours de quoi nourrir mon insatiable appétit de coûteuses simulations. Son humanisme et ses qualités pédagogiques sont sources de motivation chez ses étudiants et doctorants, comme j'ai pu le constater pendant mes tâches d'assistantat pour ses cours.

Un merci tout particulier à Sébastien Joliet, qui n'a pas compté ses heures pour m'initier au code ORB5 avec beaucoup d'entrain, alors qu'il était lui-même en fin de thèse. Ses grandes compétences, aussi bien numériques que physiques, m'ont permis d'acquérir la motivation pour ce projet et d'affronter avec confiance les mystères d'un code gyrocinétique global. Mais surtout, Sébastien m'a légué un outil de grande qualité qu'il avait lui-même contribué à développer, ce qui est manifestement précieux pour un démarrage optimal dans un projet de thèse.

La présente thèse ne serait pas ce qu'elle est sans l'apport crucial de Ben McMillan. Il a en effet développé certaines des plus importantes routines du code avec élégance et efficacité, tout en faisant preuve d'une intuition numérique et physique exceptionnelle. De plus, il me fait l'honneur de faire partie de mon jury de thèse. Il a grandement contribué au succès de ce projet de recherche et reçoit donc mes plus sincères remerciements.

Je fais part de ma gratitude à l'égard d'Alberto Bottino, qui m'a accueilli plusieurs fois en son fief de l'IPP Garching avec bienveillance et qui m'a initié à la nouvelle version électromagnétique du code ORB5 qu'il a développée.

Le précieux travail de Trach Minh Tran, notre expert maison pour le calcul numérique et les superordinateurs, mérite d'être relevé à sa juste valeur. Non seulement il est l'initiateur du code ORB5, mais en plus il est toujours disponible et efficace concernant toutes les questions techniques liées à l'utilisation souvent complexe des différentes plateformes sur lesquelles le code ORB5 tourne. Ses qualités et son domaine de compétences en font probablement le collaborateur le plus important du groupe de théorie du CRPP, merci Minh ! Dans le registre du support informatique, je remercie également Pierre Etienne pour sa disponibilité et sa compétence.

Merci à Stefano Coda, à Per Helander et à Olivier Schneider d'avoir accepté la charge de participer à mon jury de thèse, malgré leurs nombreuses occupations respectives.

Merci à Olivier Sauter et à Jonathan Graves pour les fructueuses discussions scientifiques que j'ai eu la chance d'avoir avec eux durant ma thèse.

Un grand merci à mon collègue et ami Jonathan Rossel, qui m'a fait partager sa pertinence d'analyse sur de nombreux sujets et avec lequel j'ai passé moult bons moments, au CRPP et ailleurs, parfois devant un problème de physique ou de programmation, mais le plus souvent devant une chope de bière ou un bon verre de vin !

Merci à mon collègue de bureau Kees de Meijere pour la bonne ambiance qui a régné dans notre tanière du PPB 124, agrémentée de ses nombreux récits d'excursions dans les Alpes.

Merci au vaillant capitaine de notre non moins vaillante équipe de football, Karim Besseghir, pour son entrain dans l'organisation d'événements sportifs et ludiques toujours fort réussis !

Merci à l'éminent docteur Curchod pour les agréables pauses-café passées à parler politique, gastronomie et musique classique.

Merci à Annamaria Masetto et à Joaquim Loizu pour m'avoir accompagné en conférence aux Etats-Unis et m'avoir fait découvrir certains des aspects les plus remarquables des cultures italienne et espagnole, respectivement.

Merci à David Pffeferlé pour notre fructueuse association au sein du CRPP golf team, et pour les sympathiques parties qui en découlent.

Je ne saurais oublier les autres membres de la grande équipe des doctorants en compagnie desquels j'ai passablement erré dans les couloirs du CRPP ou à Satellite : Julien Dominski, David Wagner, Lucia Federspiel, Josef Kamleitner, Falk Braunmüller, Fabio Avino, Alexandre Bovet, Himank Anand, Joyeeta Sinha, Jonathan Faustin, Gabriele Merlo, Claudio Marini, Doohyun Kim, Vincent Vuille, Gustavo Canal, Zhouji Huang, Daniele Brunetti, sans oublier les anciens Etienne Küng, Mattia Albergante, Theodoros Panis, Francesco Piras, Andreas Pitzschke, Christian Theiler, Silvano Gnesin, Federico Felici, Christian Schlatter, Costanza Zucca. Merci pour l'agréable ambiance de travail !

Merci aux professeurs qui m'ont enseigné la physique des plasmas avec passion : Stefano Alberti, Ambrogio Fasoli, Jonathan Lister, Jean-Marc Moret, Stephan Brunner, Jonathan Graves, Ivo Furno, Stefano Coda.

Merci à Frank Jenko de m'avoir invité à sa conférence de Dresden, ainsi qu'à sa méritante escouade (Tobias Görler, Florian Merz, Hauke Dörk, Daniel Told) pour sa fructueuse collaboration. Dans un registre similaire, la collaboration avec Roman Hatzky, Ralf Kleiber et José Garcia aux instituts Max-Planck de Garching et Greifswald mérite d'être soulignée comme un point positif de cette thèse.

Merci à mes collègues du CRPP Steve Couturier, Matthieu Toussaint, Jérémie Dubray, Damien Fasel, Ugo Siravo, Pierre-François Isoz, Alexandra Krause, Francisco Sanchez, Yannis Andrèbe, Serge Barby, Robert Bertizzolo et Benoit Labit pour les agréables pauses-café, les repas en commun, les cigares de Noël ou encore les matchs de Tennis et de Pétanque.

Merci à Edith Grüter, Heidi Francelet, Roxane Tschanz, Céline Nogales, Véronique Bujard et Séverine Jaques pour leur précieuse aide administrative et organisationnelle.

Merci à mes collègues Marc-Antoine Habisreutinger et Christoph Boeckle, compagnons d'équations aussi bien que d'apéritifs, sans oublier Isabelle Udin et sa bonne humeur communicative.

Merci à Jérémie Nayak pour la relecture de quelques parties du manuscrit, ainsi qu'au Consul Simon Tinguely pour m'avoir initié à ce formidable outil qu'est \LaTeX alors que nous étions encore collégiens. Merci également à mon vieux pote Viet pour nos nombreuses soirées passées à refaire les petits mondes fribourgeois et lausannois.

Un merci tout spécial à ma petite fée Caroline, la seule étudiante en faculté des Lettres qui soit passionnée par la physique des plasmas, pour m'avoir accompagné et soutenu avec entrain durant la deuxième moitié de ce projet.

Merci à mon parrain Alois Raemy, physicien, qui m'a prodigué quelques judicieux conseils pour mes études, ainsi qu'à Gérald Jenny et Bertrand Galley, mes professeurs à Saint-Michel qui m'ont transmis leur passion pour les mathématiques et la physique.

Finalement, un grand merci à mes chers parents, Philippe et Marian, pour leur soutien constant lors de la réalisation de cette thèse et plus généralement lors de mon parcours scolaire et étudiant. Leur générosité et leur amour furent et sont encore très précieux. Merci également à mon cousin-physicien Arnaud pour nos discussions toujours intéressantes sur le monde scientifique et culturel, ainsi qu'à mes autres cousins et cousines : Guillaume, Olivia, Grégoire et Eurydice, sans oublier mes tantes Michèle et Eliane, ainsi que Dominique.

Lausanne, octobre 2012

Thibaut Vernay

Scientific publications & Conference contributions

Scientific publications in peer-reviewed journals, as first author:

- ✉ T. Vernay, S. Brunner, L. Villard, B. F. McMillan, S. Jolliet, T. M. Tran, A. Bottino, and J. P. Graves, *Neoclassical equilibria as starting point for global gyrokinetic microturbulence simulations*, Phys. Plasmas **17**, 122301 (2010).
- ✉ T. Vernay, S. Brunner, L. Villard, B. F. McMillan, O. Sauter, S. Jolliet, T. M. Tran, and A. Bottino, *Global collisional gyrokinetic simulations of ITG microturbulence starting from a neoclassical equilibrium*, J. Phys.: Conf. Ser. **260**, 012021 (2010).
- ✉ T. Vernay, S. Brunner, L. Villard, B. F. McMillan, S. Jolliet, T. M. Tran, and A. Bottino, *Synergy between ion temperature gradient turbulence and neoclassical processes in global gyrokinetic particle-in-cell simulations*, Phys. Plasmas **19**, 042301 (2012).
- ✉ T. Vernay, S. Brunner, L. Villard, B. F. McMillan, S. Jolliet, A. Bottino, T. Görler, and F. Jenko, *Global gyrokinetic simulations of TEM microturbulence*, submitted to Plasma Physics and Controlled Fusion (2012).

Scientific publications in peer-reviewed journals, as co-author:

- ✉ S. Jolliet, B. F. McMillan, T. Vernay, L. Villard, A. Bottino, and P. Angelino, *Quasi-steady and steady states in global gyrokinetic particle-in-cell simulations*, Phys. Plasmas **16**, 052307 (2009).
- ✉ S. Jolliet, B. F. McMillan, T. Vernay, L. Villard, A. Bottino, R. Hatzky, and P. Angelino, *Influence of the parallel nonlinearity on zonal flows and heat transport in global gyrokinetic particle-in-cell simulations*, Phys. Plasmas **16**, 072309 (2009).
- ✉ A. Bottino et al., *Global Nonlinear Electromagnetic Simulations of Tokamak Turbulence*, IEEE Transactions on Plasma Science **38**, 2129 (2010).
- ✉ L. Villard et al., *Gyrokinetic simulations of turbulent transport: size scaling and chaotic behaviour*, Plasma Phys. Controlled Fus. **52**, 124038 (2010).
- ✉ B. F. McMillan, P. Hill, A. Bottino, S. Jolliet, T. Vernay, and L. Villard, *Interaction of large scale flow structures with gyrokinetic turbulence*, Phys. Plasmas **18**, 112503 (2011).

- ✉ A. Bottino et al., *Global simulations of tokamak microturbulence: finite-beta effects and collisions*, Plasma Phys. Controlled Fus. **53**, 124027 (2011).
- ✉ S. Jolliet et al., *Parallel filtering in global gyrokinetic simulations*, Journal Comput. Phys. **231**, 745 (2012).
- ✉ L. Villard, P. Angelino, A. Bottino, S. Brunner, S. Jolliet, B. F. McMillan, T. M. Tran, and T. Vernay, *Global gyrokinetic ITG turbulence simulations of ITER*, submitted to Plasma Physics and Controlled Fusion (2012).

Invited participations to conferences:

- ✉ *Collisional Electrostatic Simulations of Turbulence with the Global Gyrokinetic Code ORB5*, European Fusion Theory Conference (EFTC), September 2011, Frascati, Italy.
- ✉ *Collisional effects on global gyrokinetic simulations of microturbulence in the ITG and TEM regime*, Joint Varenna-Lausanne International Workshop, Theory of Fusion Plasmas, August 2012, Varenna, Italy.

Contributed participations to conferences:

- ✉ *Collisions in Global Gyrokinetic Particle-In-Cell Simulations*, European Fusion Theory Conference (EFTC), October 2009, Riga, Latvia.
- ✉ *Collisions in Global Gyrokinetic Particle-In-Cell Code ORB5*, Workshop on Self-Organization in Turbulent Plasmas and Fluids, May 2010, Dresden, Germany.
- ✉ *Global Collisional Gyrokinetic Simulations of ITG Microturbulence Starting from a Neoclassical Equilibrium*, Joint Varenna-Lausanne International Workshop, Theory of Fusion Plasmas, August - September 2010, Varenna, Italy.
- ✉ *Collisional and Electromagnetic Simulations with the Global Gyrokinetic δf Particle-in-Cell Code ORB5*, U.S. Transport Task Force Workshop, April 2011, San Diego, California, USA.
- ✉ *Simulations of collisional Trapped-Electron-Mode turbulence with the global gyrokinetic δf Particle-in-Cell code ORB5*, Sherwood Fusion Theory Conference, April 2012, Atlanta, Georgia, USA.

Seminars:

- ✉ *Collisions in the Gyrokinetic Code ORB5: Improvements to the Langevin Approach*, Max-Planck-Institut für Plasmaphysik, Garching, Germany, June 2010.

- ✉ *Ion-Ion Collisions in the Global Gyrokinetic Code NEMORB: Some Effects on Electrostatic ITG Turbulence*, Max-Planck-Institut für Plasmaphysik, Garching, Germany, May 2011.
- ✉ *Fluid, kinetic and gyrokinetic descriptions of magnetically confined plasmas*, University of Geneva, Switzerland, March 2012.
- ✉ *Simulations of Electrostatic Trapped-Electron-Mode Turbulence with the Global Gyrokinetic Code NEMORB*, Max-Planck-Institut für Plasmaphysik, Garching, Germany, May 2012.
- ✉ *Global gyrokinetic turbulence simulations using particles*, CADMOS Workshop on Large Scale Computing, EPFL, Switzerland, September 2012.

Prizes awarded:

- ✉ Assistantship Prize, Faculté des Sciences de Base, EPFL, Switzerland, 2011.
- ✉ Graduate Student Poster Award at the 2012 Sherwood Fusion Theory Conference, April 2012, Atlanta, Georgia, USA.

Curriculum Vitae

1. Renseignements généraux

Nom : Vernay
Prénom : Thibaut
Date et lieu de naissance : 25 août 1983,
Berne
Domicile : Chemin des Rosiers 14,
1720 Corminboeuf
Originaire de : Orsières VS
Confession : catholique
Etat civil : célibataire

2. Ecoles fréquentées et formation

2007 - 2008 : Travail de Master au centre de recherches en physique des plasmas
de l'EPFL au sein du groupe *transport et gyrocinétique*
2003 - 2008 : Ecole Polytechnique Fédérale de Lausanne (EPFL), section de physique
1999 - 2003 : Collège Saint-Michel, Fribourg

3. Expérience professionnelle

2008 - 2012 : Assistant à l'EPFL. Thèse de doctorat au centre de recherches
en physique des plasmas portant sur les simulations numériques
de la turbulence dans les plasmas de fusion, sous la direction du
Prof. L. Villard et du Dr S. Brunner

4. Diplômes

2012 : Doctorat ès Sciences, section de physique, EPFL
2008 : Master of Science, section de physique, EPFL
2006 : Bachelor of Science, section de physique, EPFL
2003 : Certificat de maturité, section latin-sciences, collège Saint-Michel, Fribourg

5. Prix obtenus

- 2012 : "Graduate Student Poster Prize" obtenu à la
"Sherwood Fusion Theory Conference", Atlanta, USA
- 2011 : Prix de l'assistanat, Faculté des Sciences de Base, EPFL,
récompensant un investissement de qualité dans l'encadrement des étudiants
- 2003 : Prix "Banque cantonale de Fribourg",
meilleur résultat global aux examens de maturité, collège Saint-Michel, Fribourg
- 2003 : 2e prix au concours romand de poésie latine, gymnase de Chamblandes, Pully
- 2001 : Prix "Friedrich Dessauer",
meilleure moyenne des branches scientifiques, collège Saint-Michel, Fribourg

6. Activités professionnelles

- 2008 - 2012 : assistant, cours de physique numérique pour étudiants de 2e année,
prof. L. Villard, EPFL
- 2007 - 2008 : assistant-étudiant, cours de physique générale III pour ingénieurs,
prof. A. Pasquarello, EPFL

7. Langues

- Français : langue maternelle, connaissances très pointues
- Anglais : très bonnes connaissances écrites et orales, langue principale de travail
- Allemand : bonnes connaissances, au niveau de la maturité du canton de Fribourg

8. Compétences informatiques

- Langages : C++, Fortran, L^AT_EX
- Programmes pour ingénieurs et scientifiques : MATLAB, Mathematica
- Systèmes d'exploitation : Mac OS X, Linux, Windows

9. Activités annexes

- 2008-2012 : Diagnosticien du Jour (DdJ) sur le tokamak TCV (CRPP, EPFL)
- 2008-2012 : Guide pour les visites des installations du CRPP
- 2004-2008 : Moniteur pour la section junior du golf club Payerne